Università degli Studi di Ferrara

FACOLTÀ DI SCIENZE MATEMATICHE FISICHE E NATURALI

Dottorato di Ricerca in Fisica

Ciclo XXI

Dalitz Plot Study of the Charmless Decay $B^+ \to K_S\ \pi^+\ \pi^0$ with the *BABAR* Detector

Dottorando:
Dott. **Paolo Franchini**

Tutore:
Prof. **Roberto Calabrese**

Correlatore:
Dott. **Concezio Bozzi**

Anni Accademici 2006-2008

Contents

Introduction **v**

1 Theory Overview **1**

1.1 CP violation . . . 1

1.1.1 CP symmetry in quantum mechanics . . . 1

1.1.2 CP violation in the Standard Model . . . 9

1.2 The $B^+ \to K_S\pi^+\pi^0$ decay . . . 11

1.2.1 Experimental and theoretical status . . . 11

1.2.2 Constraints on γ angle from $B \to K\pi\pi$ modes . . . 14

1.3 Three-body decays . . . 17

1.3.1 Introduction . . . 17

1.3.2 Kinematics of the three-body decays . . . 18

1.3.3 The isobar model . . . 20

1.3.4 Mass term description . . . 22

1.3.5 Barrier factors . . . 23

1.3.6 Angular dependence and helicity angles . . . 25

1.3.7 Square Dalitz plot . . . 26

2 The *BABAR* Experiment **29**

2.1 The PEP-II Asymmetric Collider . . . 30

2.1.1 PEP-II Backgrounds . . . 33

2.2 The *BABAR* Detector . . . 34

2.2.1 Silicon Vertex Tracker (SVT) . . . 36

2.2.2 Drift Chamber (DCH) . . . 37
2.2.3 Čerenkov Light Detector (DRC) . . . 40
2.2.4 Electromagnetic Calorimeter (EMC) . . . 43
2.2.5 Instrumented Flux Return (IFR) . . . 45
2.2.6 Trigger System (TRG) and Data Acquisition (DAQ) . . . 53

3 The analysis method 55
3.1 Monte Carlo . . . 55
3.2 Reconstruction . . . 57
3.2.1 Tracking algorithms . . . 57
3.2.2 Calorimeter algorithms . . . 59
3.2.3 Particle identification . . . 59
3.2.4 Vertexing of candidates . . . 60
3.3 Discriminating variables . . . 61
3.3.1 Kinematic variables . . . 61
3.3.2 Event-shape variables . . . 63
3.3.3 Neural network . . . 67
3.4 Maximum Likelihood Fits . . . 69
3.4.1 Extended Maximum Likelihood Fits . . . 70
3.4.2 Error estimation . . . 71
3.4.3 Toy Monte Carlo . . . 71
3.4.4 Extraction of physical parameters . . . 72

4 The analysis 73
4.1 Overview . . . 73
4.2 Dependence of the discriminating variables on the DP . . . 75
4.3 Event selection . . . 75
4.3.1 Multiple candidates . . . 78
4.4 Treatment of Self Cross Feed . . . 81
4.5 Continuum Background . . . 86

4.6 $B\bar{B}$ background . . . 88
4.6.1 Determination of B background modes . . . 88
4.7 Control sample . . . 93
4.7.1 $\bar{D}^0$ shape in the Dalitz plot . . . 96
4.7.2 $B^+ \to \bar{D}^0(\to K^0_S\pi^0)\pi^+$ used as control sample . . . 98
4.8 The total likelihood . . . 98
4.8.1 The likelihood function . . . 101
4.8.2 Correlations among observables . . . 103
4.8.3 The Dalitz plot PDFs . . . 105
4.8.4 The other PDFs . . . 109
4.8.5 The fit parameters . . . 113

5 Results **117**
5.1 Decay model . . . 117
5.2 Pure toys MC tests . . . 118
5.2.1 High statistics signal-only toys . . . 118
5.3 Toys and embedded fits with realistic yields . . . 120
5.3.1 D^0 and fit stability . . . 124
5.4 Test of the fit on fully simulated MC tests . . . 127
5.4.1 Freezing the nominal fit . . . 127
5.4.2 Fit results . . . 128
5.4.3 Likelihood ratios . . . 132
5.4.4 Discriminant variables projection plots . . . 132
5.4.5 Dalitz plot projection plots . . . 132
5.5 Results on data . . . 135
5.5.1 Fit result . . . 135
5.5.2 CP blind fit . . . 136
5.5.3 Fit allowing for CP violation (nominal fit) . . . 136
5.6 Comments on the data fits . . . 138

6 Systematics **151**

6.1 Detector related effects . . . 152

6.1.1 Charged particle tracking . . . 152

6.1.2 K_S reconstruction . . . 152

6.1.3 Reconstruction of neutral particles . . . 153

6.2 Extra Resonances in the signal model . . . 154

6.3 Shape parameters . . . 154

6.4 B-background . . . 154

6.5 Lineshapes . . . 154

6.6 Continuum Dalitz plot PDF . . . 155

6.7 Fit Bias . . . 155

6.8 Systematics Summary . . . 155

6.9 Branching ratio uncertainties . . . 155

7 Conclusions **157**

7.1 Conclusions . . . 157

A Appendix **159**

A.1 Toy studies . . . 159

A.2 Systematics . . . 170

Bibliography **185**

Introduction

This thesis presents preliminary measurements of decays of B mesons in charmless final states, by using a data sample of 365 millions of $B\bar{B}$ pairs collected by the *BABAR* detector at the PEP-II Asymmetric B Factory, located at the Stanford Linear Accelerator Center.

Recently many three-body B decay modes have been observed with branching ratios of order 10^{-5}. As an example $\bar{B}^0 \to K_S K_S K_S$ ($(6.9 \pm 0.8) \times 10^{-6}$), $B^0 \to K^+\pi^-\pi^0$ ($(34.9 \pm 2.1) \times 10^{-6}$), $B^0 \to K^0\pi^+\pi^-$ ($(43.0 \pm 2.3) \times 10^{-6}$) and $B^- \to \pi^+\pi^-\pi^-$ ($(16.2 \pm 1.2) \times 10^{-6}$).

The three-body meson decays are more complicated than two-body decays as they receive resonant and non-resonant contributions. They are generally dominated by intermediate vector and scalar resonances, namely, they proceed via quasi-two-body decays containing a resonance state and a pseudoscalar meson. Indeed, most of the quasi-two-body B decays are extracted from the analysis of three-body B decays using the Dalitz plot technique, in order to study the properties of various resonances. The non-resonant contribution is usually believed to be a small fraction of the total three-body decay rate. The study of charmless hadronic B decays can make important contributions to the understanding of models of hadronic decays.

The Dalitz plot analysis of three-body B decays provides a nice methodology for extracting information on the unitary triangle in the standard model and can help the understanding of CP violation. Studies of charmless three-body decays in $B \to K\pi\pi$ system combined with theoretical assumption, allow to put constraints on γ angle of the Cabibbo-Kobayashi-Maskawa matrix.

This is the first study of the charmless decay of the charged B meson into three-body

final state $K^0_S\ \pi^+\ \pi^0$.

This thesis is organized as follows. The theory of the three-body charmless decays is reviewed in Chapter 1, together with a brief reminder of CP violation. Chapter 2 presents an overview of the *BABAR* detector used to collect the data studied in the analysis. The experimental techniques used to reconstruct events and identify particles are presented in Chapter 3. The studies performed on the Monte Carlo in order to discriminate the signal from the backgrounds are collected in Chapter 4. In Chapter 5 the steps done to validate the fitter are discussed, and the final fit on the data is presented. Chapter 6 presents the evaluation of systematic uncertainties. In Chapter 7 we show the results for branching ratios and CP asymmetries for the three-body decay under study.

The results presented in this thesis are preliminary and show the potential capabilities that can be obtained with the *BABAR* dataset. The current measurements exhibit a discrepancy between some fit results and the actual data, which is possibly due to backgrounds being not correctly estimated and/or parametrized. Further studies are under way in order to understand these discrepancies and solve them. The results shown in these thesis have not been internally reviewed by the *BABAR* collaboration; therefore, they should not be regarded as official *BABAR* results.

Chapter 1

Theory Overview

1.1 CP violation

1.1.1 CP symmetry in quantum mechanics

Discrete symmetries

Classical physics is invariant for symmetries of left-right inversion (parity) and for reversal of the time.

The symmetry under *parity* corresponds to the physical invariance of two coordinate systems with opposite sign of the space coordinates (like two rotated systems, looking each other in a mirror). A right-handed system under parity becomes left-handed. Thus the parity transformation has the same effects of a mirror reflection, and can be demonstrated that all the physics equation are invariant under this kind of transformation.

The time reversal consists of changing the sign of the time coordinate t.

For each symmetry there is a transformation, that can be associated to an operator (in this case $\mathcal{P}$ and $\mathcal{T}$). If an operator working on a function, has for result the same function with just an overall phase, this means that the function is invariant under that transformation, therefore the function owns a symmetry.

The symmetry under transformation of charge conjugation is not present in classical physics, represented by the operator $\mathcal{C}$. This symmetry, where exists, means that a so-called "antiparticle" with the opposite charge is present for each particle; this result can be assumed only in relativistic quantum mechanics, where to each particle field, can be associated a field with opposite charge quantum number: the antiparticle.

In particle physics, described by the Standard Model, the electromagnetic and strong interactions preserve P, C and T, one by one, while the weak interactions violate P and C separately. However, the composite transformation CPT is a symmetry preserved in all the universe, that means in each lagrangian field theory experimentally tested.

The parity violation in weak interactions was suggested for the first time in 1956 by Lee and Yang [2], before the experimental evidences coming from studies of pseudoscalar quantities (first of all the particle helicity). Historical experiments of great importance in testing the weak intaction were done by Garwin *et al.* and Wu *et al.* in 1957 [4], Goldhaber *et al.* in 1958 [5] who measured the neutrino helicity.

In weak interactions C and P are both violated at the same time, so at the end the symmetry under CP was considered preserved.

A first clear evidence of CP violation comes in 1964 [6] in the K_L^0 decay, who was seen to be not symmetric in the two C-conjugated decay modes, as was expected considering the neutral K_L^0 the antiparticle of itself. Therefore the K_L^0 is not eigenstate of CP transformation.

CP violation has a great theoretical importance:

- the barionic asymmetry (there is much more matter than antimatter in the observed universe), could only be generated from an initial situation in which the amount of matter and antimatter were equal, balance that has evolved after CP violating processed [7];
- elementary particles can have an electric dipole moment, who violates both P and T symmetries. In the case of T violation, CPT has to be conserved, so a CP violation is necessary at the end of the game.

In quantum mechanics the transformations P, T and C, are associated to operators $\mathcal{P}$, $\mathcal{T}$ and $\mathcal{C}$ respectively. Operators like $\mathcal{T}$ are written by exponentiation of transformation generators. A different approach should be used for $\mathcal{P}$ and $\mathcal{C}$ operators, who don't correspond to continuous transformations, since are transformation associated to finite quantum numbers. $\mathcal{P}$ and $\mathcal{C}$ operators can by defined only by not taking into account the weak interaction, since it is necessary to commute with the hamiltonian operator $\mathcal{H}$,

that generate the time translactions; operators can commute only when their relative transformations correspond to symmetries not violated in the theory described by the hamiltonian. Both P and C symmetries are not good symmetries of Nature, their operators can be defined only switching off the weak interaction, since they do not commute with the hamiltonian of the weak interaction.

$\mathcal{P}$ and $\mathcal{C}$ are unitary. They correspond to discrete transformations, therefore they can be associated to their eigenstates, that means multiplicative quantum numbers (at the opposite side, for the continuum transformation, quantum numbers are additive).

$\mathcal{T}$ is antiunitary. $\mathcal{T}$ can have two different eigenvalues, therefore it cannot be associated to any quantum number. To be very precise is not correct to say that T is conserved (nothing is conserved), but is just valid the invariance under T.

We can improperly say that CPT is conserved ("CPT theorem" that is kind of prejudice). CPT conservation means that a CP violation has to be connected to a T violation. The violations or conservations of some symmetries are related to the theory (the hamiltonian) and not to the single observables.

Strong and weak phases

The presence of complex phases in the transition amplitude is closely related to the CP violation. Only the phases that are rephasing-invariant may have a physical meaning, and in particular lead to CP violation. Those phases are in general the relative phases of the various coherent contributions to a particular transition amplitude.

Three kind of phases may arise in transition amplitudes:

- *weak* or *odd phase*: is defined to be one which has opposite signs in the transition amplitude for a process and in the transition amplitude for its CP-conjugate process;
- *strong* or *even phase*: has the same sign in the transition amplitude for its CP-conjugate process;
- *spurious phase*: is a conventional relative phase between the amplitude and the amplitude of the CP-conjugate process.

Given CP conjugated states i and $\bar{i}$, f and $\bar{f}$, g and $\bar{g}$, where for example

$$\mathcal{CP}|f\rangle = e^{i\xi_f}|\bar{f}\rangle \tag{1.1}$$

with arbitrary phase ξ_f considered equal to 1, CP violation is possible when the transition amplitudes are the sum of two or more transition amplitudes with different strong or weak phases, like

$$\langle f|T|i\rangle = A_1 e^{i(\delta_1+\phi_1)} + A_2 e^{i(\delta_2+\phi_2)} \tag{1.2}$$

where the CP-conjugate amplitude is

$$\langle \bar{f}|T|\bar{i}\rangle = A_1 e^{i(\delta_1-\phi_1+\theta)} + A_2 e^{i(\delta_2-\phi_2+\theta)} \tag{1.3}$$

where T is the transition matrix, A_1 and A_2 the modules of the transition amplitudes, and $\delta_1 \neq \delta_2$ (CP strong phases), $\phi_1 \neq \phi_2$ (CP weak phases) and θ the common spurious phase. The asymmetry between the two amplitudes is

$$\frac{|\langle f|T|i\rangle|^2 - |\langle \bar{f}|T|\bar{i}\rangle|^2}{|\langle f|T|i\rangle|^2 + |\langle \bar{f}|T|\bar{i}\rangle|^2} \tag{1.4}$$

It is possible to have CP violation even in absence of strong phases or amplitudes interference, for quantities like this

$$\langle f|T|i\rangle\langle g|T|\bar{i}\rangle - n_f n_g \langle g|T|i\rangle\langle f|T|\bar{i}\rangle = 2iA_1A_2 e^{i(\delta_1+\delta_2+\theta)}\sin(\phi_1-\phi_2) \tag{1.5}$$

where there is a relationship between the two final states f and g, like for physical states that are a superposition of two CP eigenstates.

In any case, due to CPT invariance, the total decay width of i and $\bar{i}$ has to be equal

$$\sum_f |\langle f|T|i\rangle|^2 = \sum_f |\langle \bar{f}|T|\bar{i}\rangle|^2 \tag{1.6}$$

therefore it is necessary to study CP violation using partial decay channels of the particles, since it is precluded the observation of CP-violating difference between the total decay width of a particle and its antiparticle.

Neutral meson system

The neutral mesons, interesting for the study of CP violation, decay mostly through weak interactions. Let's consider a generic neutral meson (that can be the a D^0, K^0, B_d^0 or B_s^0) P^0 with antiparticle $\bar{P}^0$, and common mass m_0, for which

- $|P^0\rangle$ and $|\bar{P^0}\rangle$ are eigenstates of strong and electromagnetic interactions with mass m_0, so they are *flavor eigenstates*[1];
- as consequence of the weak interaction, described by the non vanishing $\mathcal{H}_\mathcal{W}$, the two states oscillate between themselves before decaying.

At a certain time t it is possible to have a state that is a superposition of initial states and final states $|n_i\rangle$, where the two $|P^0\rangle$ and $|\bar{P^0}\rangle$ may decay

$$a(t)|P^0\rangle + b(t)|\bar{P^0}\rangle + \sum_n c_i(t)|n_i\rangle \tag{1.7}$$

where $c_i(t=0) = 0$ are the amplitudes of the final states.

In the Wigner-Weisskopf [8] approximation, taking into account the interaction $\mathcal{H}_\mathcal{W}$

$$|\psi(t)\rangle \simeq \psi_1(t)|P^0\rangle + \psi_2(t)|\bar{P^0}\rangle \tag{1.8}$$

where the wave function satisfies an equation equivalent to the Schrödinger equation

$$i\frac{d}{dt}\begin{pmatrix}\psi_1\\ \psi_2\end{pmatrix} = \begin{pmatrix}R_{11} & R_{12}\\ R_{21} & R_{22}\end{pmatrix}\begin{pmatrix}\psi_1\\ \psi_2\end{pmatrix} \tag{1.9}$$

where

$$\mathbf{R} = \mathbf{M} - \frac{i}{2}\mathbf{\Gamma} \tag{1.10}$$

with

$$\begin{array}{c}\mathbf{M} = \frac{1}{2}(\mathbf{R} + \mathbf{R}^\dagger),\\ \mathbf{\Gamma} = i(\mathbf{R} - \mathbf{R}^\dagger)\end{array} \tag{1.11}$$

The matrices $\mathbf{M}$ e $\mathbf{\Gamma}$ are hermitian, while the matrix $\mathbf{R}$ is anti-hermitian. The weak interaction is considered like a small perturbation with respect to the strong and electromagnetic interactions; in second-order perturbation theory the matrices $\mathbf{M}$ e $\mathbf{\Gamma}$, by sums over intermediate states n, are

$$M_{ij} = m_0\delta_{ij} + \langle i|\mathcal{H}_W|j\rangle + \sum_n P\frac{\langle i|\mathcal{H}_W|n\rangle\langle n|\mathcal{H}_\mathcal{W}|j\rangle}{m_0 - E_n}, \tag{1.12}$$

$$\Gamma ij = 2\pi\sum_n \delta(m_0 - E_n)\langle i|\mathcal{H}_W|n\rangle\langle n|\mathcal{H}_W|j\rangle \tag{1.13}$$

[1] States with a defined quark content, that are eigenstate of an effective hamiltonian that describes the strong interaction

where the operator P projects out the principal part and E_n are the energies of the states. From the second order expansion the box Feynman diagrams came out. The mass matrix has first and second order terms, therefore virtual states connect the real states.

It follows that

$$\frac{d}{dt}(|\psi_1|^2 + |\psi_2|^2) = -(\psi_1^*\psi_1^*)\mathbf{\Gamma}\begin{pmatrix}\psi_1\\ \psi_2\end{pmatrix} \tag{1.14}$$

where the left-hand side of the equation (1.14) must be negative (since the mesons decay), hence the $\mathbf{\Gamma}$ is positive definite.

The eigenstates of $\mathbf{R}$ are complex, since the matrix is not-hermitian, so they can be defined as

$$\begin{aligned}\mu_H &= m_H - \tfrac{i}{2}\Gamma_H,\\ \mu_L &= m_L - \tfrac{i}{2}\Gamma_L\end{aligned} \tag{1.15}$$

Then we define

$$\begin{aligned}\Delta m &= m_H - m_L > 0,\\ \Delta\Gamma &= \Gamma_H - \Gamma_L,\\ \Delta\mu &= \mu_H - \mu_L\end{aligned} \tag{1.16}$$

from which we can obtain

$$\Delta m = 2|M_{12}| \tag{1.17}$$

These eigenstates and eigenvectors correspond to particles with different masses m and timelifes (or decay width) Γ; hence is possible to label them taking into account one of that two characteristics: in this case they are labelled with H and L, for the heavy and for the light respectively, having in mind the mass differences. This decision is suitable for the $B^0 - \bar{B^0}$ system, where the two mass eigenstates have a relevant mass difference with respect to the lifetimes difference. For the system $K^0 - \bar{K^0}$, is better to take into account the lifetimes, being the filetime of one particle really longer in comparison with the other one (using thus labels L and S for the long-lived and short-lived respectively).

As already considered, under a CP transformation

$$\begin{aligned}\mathcal{CP}|P^0\rangle &= e^{i\xi}|\bar{P^0}\rangle,\\ \mathcal{CP}|\bar{P^0}\rangle &= e^{-i\xi}|P^0\rangle\end{aligned} \tag{1.18}$$

with arbitrary phase ξ. Hence is possible to define the two *CP eigenstates* as

$$|P_\pm\rangle = \frac{1}{\sqrt{2}}(|P^0\rangle \pm e^{i\xi}|\bar{P^0}\rangle) \tag{1.19}$$

We have a CP invariance for a theory described by an hamiltonian for the weak interaction $\mathcal{H}_{\mathcal{W}}$, if

$$(\mathcal{CP})\mathcal{H}_W(\mathcal{CP})^\dagger = \mathcal{H}_W \tag{1.20}$$

which implies that $\Gamma_{11} = \Gamma_{22}$ and analogously $M_{11} = M_{22}$. Since

$$\begin{aligned} M_{21} &= e^{2i\xi} M_{12}, \\ \Gamma_{21} &= e^{2i\xi}\Gamma_{12} \end{aligned} \tag{1.21}$$

we get $|R_{11}| = |R_{22}|$.

It is convenient to introduce the CP-violating parameters

$$\begin{aligned} \delta &= \frac{|R_{12}| - |R_{21}|}{|R_{12}| + |R_{21}|}, \\ \theta &= \frac{R_{22} - R_{11}}{\Delta\mu} \end{aligned} \tag{1.22}$$

The eigenstates $\mathbf{R}$, that are the *mass eigenvectors* (eigenvectors of the weak interaction), can be defined as follows

$$\begin{aligned} |P_H\rangle &= p_H|P^0\rangle + q_H|\bar{P^0}\rangle, \\ |P_L\rangle &= p_L|P^0\rangle - q_L|\bar{P^0}\rangle \end{aligned} \tag{1.23}$$

Unlike $|P^0\rangle$ and $|\bar{P^0}\rangle$, the mass eigenstates evolve as a function of time, according to the equation (1.9).

$$\begin{aligned} |P_H(t)\rangle &= e^{-i\mu_H t}|P_H\rangle, \\ |P_L(t)\rangle &= e^{-i\mu_L t}|P_L\rangle. \end{aligned} \tag{1.24}$$

Due to the weak interaction, described by $\mathcal{H}_{\mathcal{W}}$, these states evolve like an exponential function with defined masses m_H and m_L, and defined decay width Γ_H and Γ_L, according to eq. (1.15). The probability to observe P^0 or $\bar{P^0}$ is proportional to $e^{-\Gamma t}$. Starting with a flavor eigenstate like P^0 (that can be written in terms of mass eigenstates) produced by the strong interaction, it evolves during the time, displaying the possibility to observe a flavor eigenstate of the second kind like $\bar{P^0}$.

The phase between $|P_H\rangle$ and $|P_L\rangle$ is not defined, and it is present in the product $\langle P_H|P_L\rangle$, which gives

$$|\langle P_H|P_L\rangle|^2 = \frac{(1+\delta^2)|1-\theta^2| - (1-\delta^2)(1-|\theta|^2)}{(1+\delta^2)|1-\theta^2| + (1-\delta^2)(1+|\theta|^2)} \tag{1.25}$$

therefore from CP invariance, that oblige to have the parameters $\delta = \theta = 0$, it follows that $\langle P_H|P_L\rangle = 0$. Imposing a convention for the phases of $|P_H\rangle$ and $|P_L\rangle$ like for eq. (1.23), we have $\langle P_H|P_L\rangle = \delta$, that is real.

Since CP violation is small, assuming that CPT conserved (so $q_H/p_H = q_L/p_L = q/p$) gives

$$\begin{aligned} |P_H\rangle &= (1+\epsilon)|P^0\rangle + (1-\epsilon)|\bar{P}^0\rangle \simeq |P_+\rangle, \\ |P_L\rangle &= (1+\epsilon)|P^0\rangle - (1-\epsilon)|\bar{P}^0\rangle \simeq |P_-\rangle \end{aligned} \tag{1.26}$$

where the parameter

$$\epsilon = \frac{p-q}{p+q} \tag{1.27}$$

allows to quantify the CP violation. In presence of CP violation the mass eigenstates are not orthogonal, and are not equal to the CP eigenstates.

Classification of CP violation

If CP is conserved

$$\begin{aligned} M_{12}^* &= e^{2i\xi} M_{12}, \\ \Gamma_{12}^* &= e^{2i\xi} \Gamma_{12}, \\ \frac{q}{p} &= \pm e^{i\xi} \end{aligned} \tag{1.28}$$

and the CP eigenstates are equal to the mass eigenstates

$$\begin{aligned} \mathcal{CP}|P_H\rangle &= \pm|P_H\rangle, \\ \mathcal{CP}|P_L\rangle &= \mp|P_L\rangle \end{aligned} \tag{1.29}$$

where the sign ambiguity can be solved only by experiments. The condition to have CP invariance is

$$\left|\frac{q}{p}\right| = 1 \tag{1.30}$$

The CP transformation acts on a final state f in this straightforward way

$$\begin{aligned} \mathcal{CP}|f\rangle &= e^{i\xi_f}|\bar{f}\rangle, \\ \mathcal{CP}|\bar{f}\rangle &= e^{-i\xi_f}|f\rangle \end{aligned} \tag{1.31}$$

so for the decay amplitudes, taking into account equation (1.18), we have

$$\begin{aligned} \bar{A}_f &= e^{i(\xi_f - \xi)} A_f, \\ A_{\bar{f}} &= e^{i(\xi_f + \xi)} \bar{A}_f \end{aligned} \tag{1.32}$$

hence, avoiding the arbitrary phases ξ and ξ_f, to have CP invariance we need to satisfy the conditions

$$\begin{aligned} |A_f| &= |\bar{A}_{\bar{f}}|, \\ |A_{\bar{f}}| &= |\bar{A}_f| \end{aligned} \tag{1.33}$$

hence the decay rate of $P^0 \to f$ and $\bar{P}^0 \to \bar{f}$ must be equal.

At the end from equations 1.28 and 1.32 follows that

$$arg\left(\frac{p^2}{q^2}A_f\bar{A}_f^*A_{\bar{f}}\bar{A}_{\bar{f}}^*\right) = 0 \tag{1.34}$$

There are tree species of CP violation:

- *indirect* CP violation: CP violation in the mixing between the flavor eigenstates, when 1.30 does not hold;
- *direct* CP violation: CP violation in the decay amplitudes, when 1.33 does not hold;
- *interference* CP violation: CP violation in the phase mismatch between the mixing parameters (p, q) and the decay amplitudes, when 1.34 does not hold.

To summarize, CP violation arises always from an interference between phases, phases of the elements M_{12} and Γ_{12} (indirect), phases of two decay amplitudes (direct), or phase of p/q and the phases of the decay amplitudes (interference).

1.1.2 CP violation in the Standard Model

The charged current term of the electro-weak lagrangian (mediated by the $W^{\pm}$ boson), written for the mass eigenstates of just one quark family, is

$$\mathcal{L}_W^q = \frac{g}{\sqrt{2}}(W_\mu^+\bar{u}_L\gamma^\mu V d_L + W_\mu^-\bar{d}_L\gamma^\mu V^\dagger u_L) \tag{1.35}$$

where V is an element of the Cabibbo-Kobayashi-Maskawa (CKM) matrix [11] [12]. For three quark families

$$V = \begin{pmatrix} V_{ud} & V_{us} & V_{ub} \\ V_{cd} & V_{cs} & V_{cb} \\ V_{td} & V_{ts} & V_{tb} \end{pmatrix} \tag{1.36}$$

It is a unitary matrix[2], with 4 independent parameters and one phase that, as observed for the first time by Kobayashi and Maskawa, generates CP violation [12]. There is not an analog matrix for the neutral currents, since flavor changing neutral currents do not exists at the tree level.

There is CP violation in the Standard Model, if, and only if, any of the rephasing-invariant functions of the CKM matrix is not real.

[2] $V^\dagger V = VV^\dagger = 1$.

Unitarity Triangle

Taking into account the unitarity conditions of the CKM matrix, the following relations hold

$$\begin{aligned} V_{ud}V_{us}^* + V_{cd}V_{cs}^* + V_{td}V_{ts}^* = 0, \\ V_{us}V_{ub}^* + V_{cs}V_{cb}^* + V_{ts}V_{tb}^* = 0, \\ V_{ud}V_{ub}^* + V_{cd}V_{cb}^* + V_{td}V_{tb}^* = 0. \end{aligned} \tag{1.37}$$

these are sums of three complex quantities, that can be represented in the complex plane as sides of a triangle; the lenghts of the sides are invariant, so the triangle does not modify its shape under a rephasing of all the phases.

From experimental measurements of V_{ij}, the triangles coming out from the first two equations of 1.37 have a side much shorter than other two, these triangles are connected to CP violation in the K and B_s system respectively.

The most interesting triangle, related with the physics of the B_d meson, is the third one built from the orthogonality condition between the first and the second columns of the matrix. It is the so called "Unitarity Triangle"[13].

Choosing a convention for the phases and rescaling the triangle by dividing each side by $|V_{cd}V_{cb}^*|$, we obtain the triangle of Figure 1.1. The inner angles of the triangle are

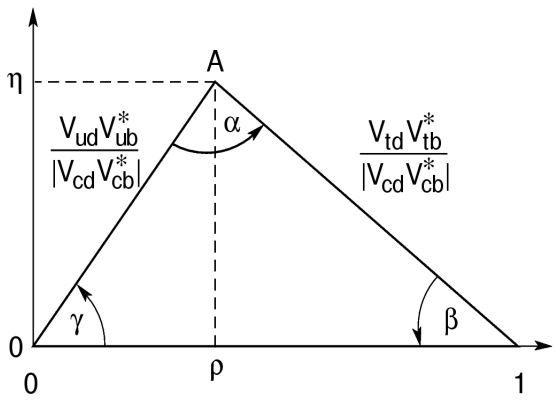

Figure 1.1: Unitarity triangle rescaled.

$$\begin{aligned}\alpha &= \arg\left(-\frac{V_{td}V_{tb}^*}{V_{ud}V_{ub}^*}\right),\\ \beta &= \arg\left(-\frac{V_{cd}V_{cb}^*}{V_{td}V_{tb}^*}\right),\\ \gamma &= \arg\left(-\frac{V_{ud}V_{cb}^*}{V_{cd}V_{cb}^*}\right).\end{aligned} \tag{1.38}$$

Wolfenstein parametrization

The first parametrization of the CKM matrix was put forward by Kobayashi and Maskawa using the three Euler angles, writing the matrix like a product of three rotations.

In 1983 it was realized that the bottom quark b decays predominantly to the charm quark c, so $|V_{cb}| \gg |V_{ub}|$; then it was noticed by Wolfenstein that $|V_{cb}| \sim |V_{us}^2|$, and [14] a parametrization in which unitarity only holds approximately was introduced, writing

$$V = \begin{pmatrix} 1-\lambda^2/2 & \lambda & A\lambda^3(\rho - i\eta) \\ -\lambda & 1-\lambda^2/2 & A\lambda^2 \\ A\lambda^3(1-\rho-i\eta) & -A\lambda^2 & 1 \end{pmatrix} + \mathcal{O}(\lambda^4) \tag{1.39}$$

involving the parameters λ, A, ρ and η, where $\lambda = \sin\theta_C \simeq 0.22$ is small and serves as an expansion parameter, that is a function of the Cabibbo angle θ_C, $A \simeq 0.82$ and η rapresent the CP violation phase. We have CP violation if $\eta \neq 0$, that means a triangle area not equal to zero.

In the Wolfenstein parametrization the CKM matrix elements satisfy these relations

$$\begin{aligned}\frac{V_{ud}V_{ub}^*}{|V_{cd}V_{cb}|} &= \rho + i\eta,\\ \frac{V_{cd}V_{cb}^*}{|V_{cd}V_{cb}|} &= -1,\\ \frac{V_{td}V_{tb}^*}{|V_{cd}V_{cb}|} &= 1 - \rho - i\eta.\end{aligned} \tag{1.40}$$

1.2 The $B^+ \to K_S\pi^+\pi^0$ decay

1.2.1 Experimental and theoretical status

The $B^+ \to K_S\pi^+\pi^0$ decay[3] proceeds via quasi-2-body channels, $B^+ \to K^{*+}\pi^0$, $B^+ \to K^{*0}\pi+$ and $B^+ \to \rho^+ K_S^0$, or via the non resonant 3-body decay. The K^* and ρ resonances decay into $K\pi$ and $\pi\pi$ final states respectively. Many resonances overlap in

[3] unless otherwise stated, charge conjugate modes are implied

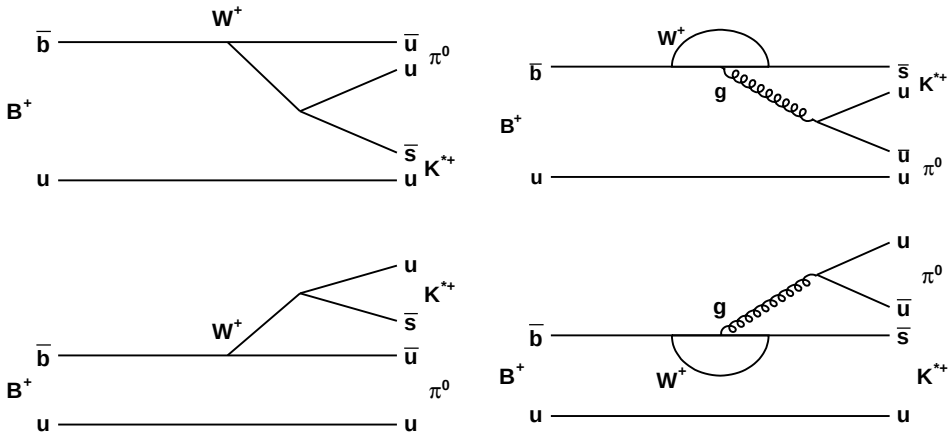

Figure 1.2: Trees (left column) and penguins (right column) Feynman diagrams, where the first row are the colour suppressed and the second row the colour favoured diagrams.

Mode	PDG avg. [40]	*BABAR*	ref.	Belle	ref.	CLEO	ref.	New avg.
$K^*(892)^0\pi^+$	10.9 ± 1.8	$10.8 \pm 0.6^{+1.1}_{-1.3}$	[15]	$9.7 \pm 0.6^{+0.8}_{-0.9}$	[16]	$7.6^{+3.5}-3.0 \pm 1.6$	[17]	10.0 ± 0.8
$K^*(892)^+\pi^0$	6.9 ± 2.4	$6.9 \pm 2.0 \pm 1.3$	[18]			$7.1^{+11.4}_{-7.1} \pm 1.0$	[17]	6.9 ± 2.3
$K_0^*(1430)^0\pi^+$	47 ± 5	$32.0 \pm 1.2^{+10.8}_{-6.0}$	[15]	$51.6 \pm 1.7^{+7.0}_{-7.4}$	[16]			$45.2^{+6.2}_{-6.3}$
$K_2^*(1430)^0\pi^+$	< 6.9	$5.6 \pm 1.2^{+1.8}_{-0.8}$	[15]	< 6.9	[19]			$5.6^{+2.2}_{-1.4}$
$K^*(1410)^0\pi^+$	< 45			< 45	[19]			< 45
$K_0^*(1680)^0\pi^+$	< 12	< 15	[20]	< 12	[19]			< 12
$K^0\pi^+\pi^0$ (N.R.)	< 66					< 66	[21]	< 66
$K_S^0\rho^+$	8.0 ± 1.5	$8.0^{+1.4}_{-1.3} \pm 0.6$	[22]			< 48	[23]	$8.0^{+1.5}_{-1.4}$

Table 1.1: Compilation of the $B^0 \to K_S^0\pi^+\pi^0$ results. Snapshot of December 2008. B^+ Branching Fractions (decays with kaons) ($\times 10^6$). (UL 90% CL).

phase space, therefore is required an amplitude (Dalitz plot) analysis of the 3-body final states (see section 1.3). Measurements existing up to now are included in table 1.1. While all final states can be reached via colour allowed penguin diagram and annihilation diagrams, the $B^+ \to K^{*+}\pi^0$ can also proceed through color allowed and color suppressed tree and penguin graphs (Figure 1.2) with CKM factors λ^4 and λ^2 respectively. The gluonic penguin processes are favored by color and CKM. The electroweak penguin transitions might be sizeable as well.

The most important decays channel that contribute to the final 3-body state are listed in table 1.2.1 together with the branching fraction prediction; table 1.1 shows the correspondingly measured branching fractions.

The charmless decays $B \to K\pi\pi$ are dominated by $b \to s$ penguin transition. Under

Mode	Model	ref.	B.F. prediction
$\rho(770)^{\pm}K^0$	QCDF	[24]	10.27±1.96
	global fit	[25]	6.08±0.79
	HMChPT	[26]	$1.3\ ^{+3.0}_{-0.9}$
$K^*(892)^{\pm}\pi^0$	QCDF	[24]	5.25±0.83
	global fit	[25]	7.00±4.49
	HMChPT	[26]	$1.5^{+0.3}_{-0.3}$
	FSI	[27]	$12.4^{+1.5}_{-0.8}$
$K^*(892)^0\pi^{\pm}$	QCDF	[24]	8.90±1.59
	global fit	[25]	10.64±0.82
	HMChPT	[26]	$1.5^{+0.4}_{-0.3}$
	FSI	[27]	$22.5^{+2.8}_{-0.9}$
$K^*(1430)^{\pm}\pi^0$	HMChPT	[26]	$5.5^{+1.6}_{-1.4}$
$K^*(1430)^0\pi^{\pm}$	HMChPT	[26]	$5.2^{+1.6}_{-1.4}$
$K^0\pi^{\pm}\pi^0$	HMChPT	[26]	$10.0^{+7.1}_{-3.7}$

Table 1.2: Theoretical predictions ($\times 10^6$) for various models of the signal model of the Dalitz analysis, together with a global fit. The models listed are: QCD factorization (QCDF), heavy meson chiral perturbation theory (HMChPT) and final-state interaction (FSI).

the factorization approach [26], the decay amplitude consists of three distinct factorizable terms: the current-induced process, the transition process and the annihilation process.

Recently, Belle has measured the direct CP violations $B^- \to K\pi$ decay [28] that for the charge B is

$$A_{CP}(B^- \to K^-\pi^0) = \frac{\Gamma(B^- \to K^-\pi^0) - \Gamma(B^+ \to K^+\pi^0)}{\Gamma(B^- \to K^-\pi^0) + \Gamma(B^+ \to K^+\pi^0)} = +0.07 \pm 0.03 \pm 0.01, \quad (1.41)$$

and the average of the current experimental data of *BABAR* , Belle, CLEO and CDF by the Heavy Flavor Averanging Group (HFAG) [29] is

$$A_{CP}(B^- \to K^-\pi^0) = 0.050 \pm 0.025 \quad (1.42)$$

A difference is observed between direct CP violations in charged and neutral modes, that by the HFAG average is

$$\Delta A = A_{CP}(B^- \to K^-\pi^0) - A_{CP}(\bar{B}^0 \to K^-\pi^+) = 0.147 \pm 0.028 \quad (1.43)$$

at 5σ level; however, recent calculations based on the QCD factorization approach (QCDF), the perturbative QCD approach (pQCD) and the soft-collinear effective theory

(SCET), predicted that $A_{CP}(B^- \to K^-\pi^0)$ and $A_{CP}(\bar{B}^0 \to K^-\pi^+)$ are close to each other. The mismatch between theory and experiment is maybe due to the limited understanding of the strong dynamics in B decays, but equally possibly due to new physics effects.

Even recent theoretical estimations within the QCDF framework give $A_{CP}(B^- \to K^-\pi^0) = -0.109 \pm 0.008$ [24], very close to $A_{CP}(\bar{B}^0 \to K^-\pi^+)$, but still in sharp contrast to experimental data. So it is very hard to accommodate the measured large difference ΔA in the SM with the available approaches for hadron-dynamics in B decays, even varying the value of the effective gluon mass that enter in the models. This could be an indication of new sources of CP violation beyond the SM. Using a set of FCNC effective NP operators ($b \to su\bar{u}$ and $b \to sd\bar{d}$) the results are more consistent with the experimental data for $A_{CP}(B^- \to K^-\pi^0)$.

1.2.2 Constraints on γ angle from $B \to K\pi\pi$ modes

The current methods to measure γ rely on the interference between the colour-allowed $B^- \to D^0K^-$ and the colour-suppressed $B^- \to \bar{D}^0K^-$ decay modes resulting in direct CP violation. They are theoretically very clean, as only tree amplitudes are involved, but their sensitivity to γ is governed by the rather small relative magnitude of the two amplitudes, denoted r_B: $0.05 \lesssim r_B \lesssim 0.3$, depending on the D meson decay channel. As a consequence, γ is the most poorly determined angle of the unitarity triangle, $(78 \pm 12)^\circ$ using only direct determinations (c.f. $\beta = (22.0 \pm 0.8)^\circ$ with the full fit) [30]. Therefore, any independent determinations of the angle γ should be exploited in order to reduce the statistical uncertainty. Although a first proposal on using the charmless three-body decays $B \to K\pi\pi$ to extract the unitarity triangle angle γ via isospin relations was made in 2002 [31], the more recent ideas in [32] [33] are both far more accurate in their estimations of the theoretical uncertainties of their methods, and more convenient experimentally.

The paper by Ciuchini, Pierini and Silvestrini [33] exploits the use of the phase-extraction capabilities of the Dalitz plot analysis technique, similarly to what Lipkin-Nir-Quinn-Synder proposed to measure α in $B^0 \to \rho\pi \to \pi^+\pi^-\pi^0$ [34]. They start by relating the ratio of the amplitudes for the decays $B^+ \to K^{*+}\pi^0$ and $B^+ \to K^{*0}\pi^+$ and their CP conjugates to γ through isospin, and then cleverly take advantage of the Dalitz

plot to determine the phase difference between the two B flavours.

Isospin ensures that amplitudes with the same topology are approximately equal for the two modes. Neglecting for simplicity the electro-weak penguin contribution, it is possible to write the amplitudes using isospin symmetry, in terms of Renormalization Group Invariant complex parameters, and obtain for our channel (factorizing out their CKM elements and grouping them accordingly):

$$\sqrt{2}A(K^{*+}\pi^0) = V_{tb}^*V_{ts}P_1 - V_{ub}^*V_{us}(E_1 + E_2 + A_1 - P_1^{GIM}), \tag{1.44}$$

$$A(K^{*0}\pi^+) = -V_{tb}^*V_{ts}P_1 + V_{ub}^*V_{us}(A_1 - P_1^{GIM}), \tag{1.45}$$

where unitary triangle relations have been used to separate the penguin amplitude into CKM-favoured (P_1) and CKM-suppressed (P_1^{GIM}) contributions; A_1 is the disconnected annihilation and E_1 (E_2) the connected (disconnected) emission topologies. Recalling that the amplitude for the C-conjugate B^- process is obtained simply by complex-conjugating the CKM factors, we can use the previous isospin relations to cancel out the penguin terms:

$$A^+ = A(K^{*0}\pi^+) + \sqrt{2}A(K^{*+}\pi^0) \tag{1.46}$$

$$= -V_{ub}^*V_{us}(E_1 + E_2), \tag{1.47}$$

$$A^- = A(\bar{K}^{*0}\pi^-) + \sqrt{2}A(K^{*-}\pi^0) \tag{1.48}$$

$$= -V_{ub}V_{us}^*(E_1 + E_2), \tag{1.49}$$

whose ratio is

$$R^{\mp} = \frac{A^-}{A^+} = \frac{V_{ub}V_{us}^*}{V_{ub}^*V_{us}} = e^{-2i\gamma} \tag{1.50}$$

that provides a clean determination of the weak phase γ.

$A^{\pm}$ can be extracted from the 3-body decay chains $B^{\pm} \to K^{*\pm}(\to K_S\pi^{\pm})\pi^0$ and $B^{\pm} \to K^{*0}(\to K^0\pi^0)\pi^{\pm}$ entering the $K_S\pi^{\pm}\pi^0$ Dalitz plot. Electric charge forbids the extraction of the relative phase of the two Dalitz plots amplitudes $A(K^{*\pm}\pi^0)$ and $A(K^{*0}\pi^{\pm})$ in a straightforward way. One possibility is to use the penguin-dominated channel $K^{*0}\pi^+$ to fix the phase difference between the amplitudes in the two Dalitz plots. In this way an independent, albeit more uncertain, determination of γ can be obtained from $R^{\mp}$. In any

case the determination of γ is not as theoretically clean as the one obtained from the neutral B decays, using similar isospin relations that bring to a ratio

$$R^0 = \frac{\bar{A}^0}{A^0} = \frac{V_{ub}V_{us}^*}{V_{ub}^*V_{us}} = e^{-2i\gamma} \tag{1.51}$$

where

$$A^0 = A(K^{*+}\pi^-) + \sqrt{2}A(K^{*0}\pi^0) \tag{1.52}$$

$$\bar{A}^0 = A(K^{*-}\pi^+) + \sqrt{2}A(\bar{K}^{*0}\pi^0). \tag{1.53}$$

In the above discussion, the so-called electroweak penguins (obtained by exchanging the gluon in the penguin diagrams by a photon) have been ignored. These result in isospin-breaking effects due, among other things, to the different electric charges of the u and d quarks, and precision measurements must take these into account. By considering the full (weak, strong and electromagnetic) effective Hamiltonian for the transition, the authors of [11] give the following final expression:

$$R^{\mp} = e^{-i(2\gamma + \arg(1+k_{EW}))} \times (1+\Delta) \tag{1.54}$$

where Δ is the theoretically bound ($\lesssim 0.05$) and k_{EW} is

$$k_{EW} = \frac{3}{2}\frac{C_+^{EW}}{C_+}\left(1 + \frac{1-\lambda^2}{\lambda^2(\bar{\rho} - i\bar{\eta}) + \mathcal{O}(\lambda^2)}\right) \tag{1.55}$$

with C_+^{EW} and C_+ being, respectively, the coefficients of the electroweak and normal QCD 4-quark operators in the effective theory. The experimental results for both R^0 and $R^{\mp}$ can be translated into allowed regions in the $\bar{\rho} - \bar{\eta}$ plane.

That model was tested using the $B^0 \to K^+\pi^-\pi^+$ and $B^0 \to K_S\pi^+\pi-$ decays to fix the relative phase of neutral B decays, but the determination of the UT parameters can be improved with the experimental measurements of $R^{\mp}_{K^*\pi}$ and $R^{\mp}_{K^*(1430)\pi}$, for which the Dalitz decay $B^{\pm} \to K_S\pi^{\pm}\pi^0$ will be worthwile.

That model can be sensitive to new physics, since is reasonable to assume that new physics effects only enter at the loop level. There are three possible scenarios:

- the new physics could affect the coefficients of QCD penguin operators, therefore the analysis of R^0 is unaffected, while the phase of new physics would modify the $R^{\mp}$

equation (1.54), producing a discrepancy between the constraints on the UT obtained from R^0 and $R^{\mp}$;

- the new physics modifies the electro-weak penguin coefficients, leading to a modification of k_{EW}, so the constraint on the UT obtained using the SM value for k_{EW} could be inconsistent with the SM UT fit result;

- the new physics could produce contributions to electro-weak penguin operators or give raise to new operators that cannot be eliminated, and one would observe $|R^{0,\mp}| \neq 1$.

The second paper, due to Gronau, Pirjol, Soni and Zupan [32], extends the previous work and thoroughly studies the isospin structure of all the amplitudes and effective field theory operators involved in the decay. These also involve a more detailed evaluation of the electroweak penguin amplitudes, thus providing similar formulae for more general cases.

1.3 Three-body decays

1.3.1 Introduction

The aim of the present work is to study the structures arising in the three-body decay $B^+ \to K^0_S \pi^+ \pi^-$. In this section we explore some of the consequences of the kinematics of the decay and discuss the parametrization employed. The general features of the decay of a particle can be discussed based on elementary concepts of quantum mechanics. The transitions of an initial state into a final state is an application of the standard time-independent perturbation theory:

$$c_{fi} = \frac{\langle \psi_f | V_{int} | \psi_i \rangle}{E_i - E_f} \tag{1.56}$$

which is the amplitude c_{fi} to find a system, whose initial state is i, in a final state f when an interaction potential V_{int} connecting them is introduced, where ψ_i and ψ_f describe the initial and final states in the absence of the interaction and E_i and E_f are their energies. The transition can happend directly, $\langle \psi_f | V_{int} | \psi_i \rangle \equiv V_{fi} \neq 0$, or it may involve intermediate

"virtual" states j, also called resonances, in which case the transition amplitude can be approximated by:

$$c_{fi} = \sum_{j \neq i,f} \left(\frac{V_{fi}V_{ji}}{(E_f - E_i)(E_j - E - i)} - \frac{V_{fi}V_{ff}}{(E_f - E_i)^2} \right). \tag{1.57}$$

Both equations display a similar form, involving the *vertex factors* V_{jk} and the *propagators* $(E_j - E_k)^{-1}$. The former represents the "strength" with which the interaction connects the two states, while the latter is related to the overlap of the two states:

$$\langle E'|E\rangle = \int dt \langle E'|t\rangle\langle t|E\rangle = \int dt e^{iE't} e^{-iEt} \propto \frac{1}{E' - E}. \tag{1.58}$$

If the final state is degenerate, the probability to observe the transition has to be summed over all the states sharing the same quantum numbers:

$$c_{fi} = \int c_{fi}(E_f)\rho(E_f)dE_f \tag{1.59}$$

where $\rho(E_f)$ is the *density of final states* or *phase space factor*.

In the following subsections we discuss in detail the peculiarities of the densities of states for three-body decays, the vertex factors and the propagators.

1.3.2 Kinematics of the three-body decays

In the decay of the pseudo-scalar B meson, with mass m_B into three more pseudo-scalar particles with masses m_1, m_2, m_3 and with four-momenta p_B, p_1, p_2, p_3, there are several kinematical constraints that reduce to two the number of degrees of freedom needed to specify the final state. Defining the invariant mass squared of a pair of particles as $m_{ij}^2 \equiv (p_i + p_j)^2$ we get

$$m_{12}^2 + m_{23}^2 + m_{31}^2 = m_B^2 + m_1^2 + m_2^2 + m_3^2 \tag{1.60}$$

so that one of the $m_{ij}^2$is linearly dependent on the other two. Furthermore, in the B rest frame,

$$m_{ij}^2 = (p_B - p_k)^2 = m_B^2 + M_k^2 - 2m_n E_k \tag{1.61}$$

$$= (p_i + p_j)^2 = m_i^2 + m_j^2 + 2E_iE_j - 2|\vec{p}_i||\vec{p}_j|\cos\theta_{ij} \tag{1.62}$$

where the last equation indicates that the angles between the momenta of the final state particle are known once their energies are determined. The two equations (1.61) and (1.62) imply that the knowledge of two quantities, customarily chosen from among the m_{ij}^2, are sufficient to specify the state of the system, up to its overall orientation.
A Dalitz plot [35] [36] is produced when a two-dimensional scatter plot is made in two of the m_{ij}^2 variables, say $m_{13}^2 \equiv x$ and $m_{23}^2 \equiv y$. For a given value of m_{jk}^2 the maximum of m_{ij}^2 is attained when the particle i and j are flying back-to-back, and the minimum when they are at rest in the ij center-of-mass system, i.e. their directions are parallel.
Similarly, for events close to the edges of the Dalitz plot, one of the m_{ij}^2 takes a small value while the other two have rather large values, whereas in the center the invariant masses of the three pairs of particles take approximately the same values. This implies that in the latter case, the directions of the three particles are distributed quite isotropically, and that they carry similar energies, whereas in the former case, one of the particles in the final state is back to back to the other two, which move in parallel, giving the event a strong directionality. It is also worth noting that, for an event lying near the corners of the Dalitz plot, one of the particles is slow, as can be seen from (1.62).

Now it is possible to discuss the *phase space factor*. The summation should be done over all momenta in the final state, but application of the kinematical constraints noted before should enable us to write is as a function of only two of the energies or squared invariant masses:

$$\rho(m_{13}^2, m_{23}^2) dm_{13}^2 dm_{23}^2 = \frac{d^3p_1 d^3p_2 d^3p_3}{E_1 E_2 E_3} \delta(p_1 + p_2 + p_3 - p_B) \tag{1.63}$$

where the energies in the denominator of the right-hand side have been introduced to ensure the Lorentz invariance. Integration over p_3 yields

$$\frac{d^3p_1 d^3p_2}{E_1 E_2 E_3} \delta(E_1 + E_2 + E_3 - m_B) = \frac{p_1^2 dp_1 d\Omega_1 p_2^2 d\Omega_{1-2}}{E_1 E_2 E_3} \delta(E_1 + E_2 + E_3 - m_B) \tag{1.64}$$

where Ω_1 and Ω_{1-2} are the solid angles for the direction of $\vec{p}_1$, and for the direction of $\vec{p}_2$

with respect to $\vec{p}_1$. Since the B is a scalar, the angles should be integrated over, giving

$$\frac{p_1^2 dp_1 (4\pi) p_2^2 dp_2 (2\pi d\cos\theta_{1-2})}{E_1 E_2 E_3} \delta(\sum_{i=1}^{3} E_i - m_B) = 8\pi^2 \frac{dE_1 dE_2 p_1 p_2 d\cos\theta_{1-2}}{E_3} \delta(\sum_{i=1}^{3} E_i - m_B). \tag{1.65}$$

Noting

$$E_3^2 = p_1^2 + p_2^2 + 2p_1 p_2 \cos\theta_{1-2} + m_3^2 \Longrightarrow E_3 dE_3 = p_1 p_2 d\cos\theta_{1-2}, \tag{1.66}$$

substituting it and integrating the δ-function gives

$$\int 8\pi^2 dE_1 dE_2 dE_3 \delta(E_1 + E_2 + E_3 - m_B) = 8\pi^2 dE_1 dE_2 = \frac{4\pi^2}{m_B^2} dm_{23}^2 dm_{13}^2. \tag{1.67}$$

Therefore, the density of final states is constant when expressed in terms of the m_{ij}^2 variables. In other words, the decay rate (the probability of decay per unit time) has the form

$$d\Gamma \propto |\mathcal{M}|^2 dm_{13}^2 dm_{23}^2 \tag{1.68}$$

where $\mathcal{M}$ encodes all the dynamical information about the decay, containing the vertex factors and the propagators.

We observe that, according to eq. (1.68), a constant term $|\mathcal{M}|^2$ results in a uniform distribution over the Dalitz plot, and that any departure is due to dynamical effects, i.e. a non-trivial $|\mathcal{M}|^2$.

1.3.3 The isobar model

The isobar model [37] [38] approximates $\mathcal{M}$ as a sum of terms with individual couplings and propagators, each representing a resonance in one pair of particles:

$$\mathcal{M}(m_{13}^2, m_{23}^2) = \sum_{j=1}^{N} c_j F_j(m_{13}^2, m_{23}^2) \tag{1.69}$$

where N is the number of intermediate states considered, c_j are the complex amplitudes describing the coupling of the B meson to the particular resonant final state (i.e. the vertex factors) and $F_j(m_{13}^2, m_{23}^2)$ are the propagators, that are products of several terms:

$$F_j(m_{13}^2, m_{23}^2) = R_j(m) \times B_L^B(|\vec{p}|r) \times B_L^{res}(|\vec{q}|r) \times Z_j^L(\vec{p}, \vec{q}), \tag{1.70}$$

where the different terms are: first, the mass-dependent part of the propagator, second and third, factors that account for the difficulty of slow decay products to conserve the angular momentum due to the spin of the resonance and last, the term that describes the angular distribution. $\vec{p}$ and $\vec{q}$ are the momenta of the bachelor particle and one of the daughters respectively, r is the effective range. The conventions adopted for these are described in detail in the following sections, a good reference being [39]. World averages [40] are used for the parameters characterizing each resonant state (e.g. mass, width).

A *Dalitz* or *amplitude analysis* aims to extract the complex couplings c_j from the data, when a given model for the resonant structure has been proposed. Note that, since the decay rate depends on $\mathcal{M}$ (1.68), eq. (1.69) implies that bilinear terms in $F_j(m^2_{13}, m^2_{23})$ will appear in the model of the distribution over the Dalitz plot. These terms, proportional to $F^*_j F_k$, represent, and are sensitive to, the interference between two resonances j and k, thus allowing for the relative phase between c_j and c_k to be determined.

In charged decays to CP eigenstates, one expects the same resonances to be present in the B^+ and the B^- decays in the same amounts, up to direct CP violanting effects. Therefore a parametrization of the complex coupling c_j and $\bar{c}_j$ appearing in the B^+ and B^- amplitudes ($\mathcal{A}$, $\bar{\mathcal{A}}$, respectively) that reflects that fact is preferred instead of using for example separate magnitudes and phases for each flavor.

A Dalitz analysis extracts all non-trivial information from the data; no physically meaningful aspect of the decay is left unmodelled. Therefore the CP asymmetry must be parametrized in terms of the c_j.

$$A_{CP_j} = \frac{|\bar{c}_j|^2 - |c_j|^2}{|\bar{c}_j|^2 + |c_j|^2}. \tag{1.71}$$

The relative weight of a given resonance in the decay is usually quoted in terms of the *isobar fit fraction*:

$$FF_j = \frac{\iint_{DP} |c_j F_j(m^2_{13}, m^2_{23})|^2 dm^2_{13} dm^2_{23}}{\iint_{DP} |\sum_j c_j F_j(m^2_{13}, m^2_{23})|^2 dm^2_{13} dm^2_{23}}, \tag{1.72}$$

where the DP integration domain means the integral must be calculated over the whole phase space.

The approximation in eq. 1.69 neglects rescattering of the final state particles and is

known to lead to unitary violation whenever the overlapping of two resonances is sizable. One alternative is the use of the so-called K-matrix, too complex to be used in the present analysis. The main source of systematic uncertainties in the model is the term R_j from eq. 1.70, since its precise function form in not well known for some components as the higher K^* resonances.

1.3.4 Mass term description

In this section the mass term distributions (or *lineshape* distributions) used to parametrize the resonances accounted in the nominal signal model of the decay studied in this analysis are presented. The parameters used for the different intermediate states are included in Table 1.3.

Breit-Wigner distribution:

The most common parametrization of the mass term is the Breit-Wigner formula, that arises for the overlap between a state of energy E and a resonant state with mass m_R and decay width Γ_R, and therefore gives the amplitude for a system in the first state to be in the second state:

$$\langle E|R\rangle = \int dt e^{iEt} e^{-t(im_R+\Gamma_r/2)} \propto \frac{1}{(E-m_R)-i\Gamma/2} \tag{1.73}$$

Relativistic Breit-Wigner distribution:

An obvious improvement is making the Breit-Wigner equation relativistic [41]:

$$R_j(m) = \frac{1}{(m_R^2-m^2)-im_R\Gamma(m)}, \tag{1.74}$$

in which the variation of the width with the energy is taken into account via

$$\Gamma(m) = \Gamma_R \left(\frac{q}{q_0}\right)^{2L+1} \left(\frac{m_R}{m}\right) B_L^2(|\vec{q}|r) \tag{1.75}$$

where L is the angular momentum quantum number of the resonance, B_L are the barrier factors, r is the radius of the barrier factors and $\vec{q}$ is the momentum of one of the daughters in the resonance rest frame and $q_0 = q(m = m_R)$. The Relativistic Breit-Wigner is used for the resonances $K^*(892)^{\pm,0}$.

Gournaris-Sakurai distribution:

The Gournaris-Sakurai formula is a parametrization of the P-wave scattering amplitude for a broad resonance decaying to two pions [42]:

$$R_j(m) = \frac{1 + d\Gamma_R/m_R}{m_R^2 + f(m) - m^2 - im_R\Gamma(m)} \tag{1.76}$$

where $d = f(0)/(\Gamma_R m_R)$ is a constant [43] and $\Gamma(m)$ is the same of the relativistic Breit-Wigner distribution (1.75), and where

$$f(m) = \Gamma_R \frac{m_R^2}{q_R^3}\left[q^2\Big(h(m) - h(m_R)\Big) + \Big(m^2 - m_R^2\Big)q_0^2\frac{dh}{dm}\Big|_{m_R}\right]. \tag{1.77}$$

and

$$h(m) = \frac{2}{\pi}\frac{q}{m}\ln\left(\frac{m + 2q}{2m_\pi}\right). \tag{1.78}$$

The Gournaris-Sakurai distribution is used for the $\rho(770)^{\pm}$.

LASS distribution:

For the $K\pi$ S-wave resonances, which dominate for resonance masses $m_{K\pi}$ below 1.8 GeV/c^2, an effective-range parametrization was used to describe the slowly increasing phase as a function of the $K\pi$ mass. The parametrization as in the LASS experiment [44] tuned for B decays is:

$$R_j(m) = \frac{m}{q\cot\delta_B - iq} + e^{2i\delta_B}\frac{m_R\Gamma_R\frac{m_R}{q_0}}{(m_R^2 - m^2) - im_R\Gamma_R\frac{q}{m}\frac{m_R}{q_0}}, \tag{1.79}$$

where

$$\cot\delta_B = \frac{1}{aq} + \frac{1}{2}rq. \tag{1.80}$$

a is the scattering length and r the effective range of the resonance. The LASS distribution is used for the $K_0^*(1430)^{\pm,0}$ resonances.

1.3.5 Barrier factors

The Blatt-Weisskopf barrier or penetration factors [45] (the B_L terms in eq. (1.70)) are motivated by the consideration of the Schrödinger equation in spherical polar coordinates. An effective potential, dubbed "centrifugal barrier", arises from the vanishing of the

Intermediate state	Lineshape	Parameters
	Nominal model	
Non resonant	Constant	
$\rho^+(770)$	GS	$r = 5.3^{+0.9}_{-0.7}$ $(\mathrm{GeV}/c)^{-1}$
$K^*(892)^+$	RBW	$r = 3.6 \pm 0.6$ $(\mathrm{GeV}/c)^{-1}$
$K^*(892)^0$	RBW	$r = 3.6 \pm 0.6$ $(\mathrm{GeV}/c)^{-1}$
$K_0^*(1430)^+$	LASS	$m_R = 1412 \pm 3$ MeV/c^2
$K_0^*(1430)^0$		$\Gamma_R = 294 \pm 6$ MeV
		$a = 2.07 \pm 0.10$ $(\mathrm{GeV}/c)^{-1}$
		$r = 3.32 \pm 0.34$ $(\mathrm{GeV}/c)^{-1}$
	Additional resonances	
$\rho(1450)$	GS	$m_R = 1439$ MeV/c^2
		$\Gamma_R = 550$ MeV
$\rho(1700)$	GS	$m_R = 1795$ MeV/c^2
		$\Gamma_R = 278$ MeV
$K_2^*(1430)^{+,0}$	RBW	
$K^*(1680)^{+,0}$	RBW	

Table 1.3: The *nominal model* for the decay $B^+ \to K\pi^+\pi^0$ comprises a nonresonant part and five intermediate states. The resonances masses and widths as well as the barrier range parameters r are from PDG2008 [40], except for the LASS shape [44]. We use the same LASS parameters for both neutral and charged $K\pi$ systems. *Additional resonances* that may contribute are included in extended models which we study to estimate the systematic uncertainties.

wavefunction at the origin when the orbital angular momentum is non-zero, both in the decay of the B meson to a $J \neq 0$ resonance and in the subsequent decay of the resonance to two pseudoscalar particles. Physically, it means that particles emitted very close to the center need too large momenta to account for all the angular momentum of the resonance. A correction is thus needed to the usual Breit-Wigner lineshapes, that can be derived from the transmission coefficients for the centrifugal potential.

Empirically, an effective radius r is needed to describe the shape of the barrier correctly.

The factors are:

$$B_{L=0}(z) = 1, \tag{1.81}$$

$$B_{L=1}(z) = \sqrt{\frac{1+z_0^2}{1+z^2}}, \tag{1.82}$$

$$B_{L=2}(z) = \sqrt{\frac{z_0^4+3z_0^2+9}{z^4+3z^2+9}}, \tag{1.83}$$

where $z = (|\vec{q}|r)^2$ and z_0 is the value that z takes when $\vec{q}$ is evaluated at the resonance pole mass.

1.3.6 Angular dependence and helicity angles

It can be argued that the distribution of decays through a scalar resonance will uniformly populate the band of mass associated to the intermediate state, since the lack of spin means there is no preferred direction for the daughters of the resonance. For a vector intermediate state, however, a privileged direction exists, and their distribution is not obvious. It can be calculated though, by evaluating the propagator for $B \to R \to abc$, where R is the resonance of a given spin J. The vectorial nature of the intermediate state ($J = 1$) is accounted for by the sum over its helicity states λ [39]:

$$\sum_{\lambda} \langle ab|R_\lambda\rangle\langle cR_\lambda|B\rangle. \tag{1.84}$$

The first factor represents the probability of finding the decay daughters a and b in a given state of relative motion:

$$\langle ab|R\rangle \sim (p_a - p_b)_\nu. \tag{1.85}$$

The second factor can be regarded as the probability of B turning into c by emitting a vector particle R. Since the emission of hard particles (large momentum) is suppressed, states with the momenta of c and B as parallel as possible are favoured

$$\langle cR|B\rangle \sim (p_B + p_c)_\mu. \tag{1.86}$$

Finally, using standard techniques of quantum field theory, the sum over the helicity states can be performed, giving

$$Z^1 = (p_B + p_c)_\mu \left(-g^{\mu\nu} + \frac{p_R^\mu p_R^\nu}{m_{ab}^2} \right) (p_a - p_b)_\nu \tag{1.87}$$

$$= \left(m_{bc}^2 - m_{ac}^2\right) + \frac{(m_B^2 - m_c^2)(m_a^2 - m_b^2)}{n_{ab}^2} \tag{1.88}$$

$$= -2\vec{p} \cdot \vec{q} \tag{1.89}$$

$$= -2|\vec{p}||\vec{q}|cos\theta_{ac} \tag{1.90}$$

where $\vec{p}$ and $\vec{q}$ are, respectively, the momenta of c and a in the resonance rest frame. The angle θ is the *helicity* angle of the resonances. For completeness, the expression for tensor resonances ($J = 2$) is

$$Z^2 = \frac{4}{3} \left[3(\vec{p} \cdot \vec{q})^2 - (|\vec{p}||\vec{q}|)^2 \right]. \tag{1.91}$$

The formulae for Z^j used here are known as *Zemach tensors* [46].

1.3.7 Square Dalitz plot

Charmless B decays proceed mostly through low mass resonances, such as $\rho^0(770)$, $K^*(892)$ and $K_0^*(1430)$. That implies that the most populated areas of the Dalitz plot are close to the edges, where the resonances recoil against energetic bachelor particles. Furthermore, the combinatorial nature of background events means that their density also peaks around the edges. Clearly, the binning of the histograms used to characterize the two dimensional distributions will be problematic, as fine binning is needed around the edges, and coarse binning around the center. Instead of using variable binning, we introduce another set of variables to parametrize the final state phase space. All input histograms will be expressed in terms of these variables:

$$m' = \frac{1}{\pi} \arccos \left(2 \frac{m - m_{min}}{m_{max} - m_{min}} - 1 \right), \tag{1.92}$$

$$\theta' = \frac{1}{\pi}\theta, \tag{1.93}$$

where m and θ are respectively the invariant mass and the helicity angle of the $K_s^0\pi^0$ system; $m_{max} = m_B - m_{\pi^+}$ and $m_{min} = m_{K_s^0} + m_{\pi^0}$ are the kinematic limits of m. The

range of both the new variables is between 0 and 1. The effect of the transformations in (1.92) and (1.93) is a magnification of the areas of interest, as can be seen in Figure 1.3.

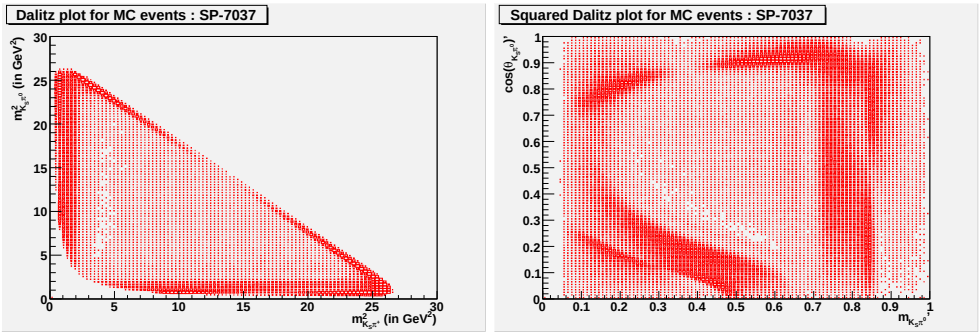

Figure 1.3: Nominal (left) and square (right) Dalitz plot for Monte Carlo model of the 3-body decay.

The calculation of the jacobian J

$$dm^2_{K^0_s\pi^+} dm^2_{K^0_s\pi^0} \rightarrow |\det J| dm' d\theta'. \tag{1.94}$$

is necessary to transform from one set of variables to another one.

Chapter 2

The *BABAR* Experiment

The *BABAR* experiment at PEP-II B factory [47, 48] has been optimized for CP violation studies and searches for rare B meson decays. The PEP-II B factory is an high luminosity ($\mathrm{L} \gtrsim 3 \times 10^{33}\mathrm{cm}^{-2}\mathrm{s}^{-1}$) e^+e^- collider operated at the center-of-mass (CM) energy of 10.58 GeV, on the $\Upsilon(4S)$ resonance. This resonance decays almost exclusively ($> 96\%$) in a $B^0\bar{B}^0$ or a B^+B^-pair with equal probabilities, giving a clean environment characterized by a good signal-to-noise ratio ($\sigma_{b\bar{b}}/\sigma_{tot} \approx 0.28$) and low track multiplicity per event (≈ 11). In addition, events reconstruction and background rejection benefit by the kinematic constraint on the momentum and energy, of each B, in the CM frame.

From December 2007 until February 2008, PEP-II operated at the resonance of $\Upsilon(3S)$, taking 30 fb^{-1} of data. In the very last period, just before the final shutdown, a scan of other Υ resonances, up to $\Upsilon(5S)$, was performed. Data taking ended in April 2008 with a total recorded luminosity of 531 fb^{-1}.

In PEP-II, the electron beam of 9 GeV collides head-on with the positron beam of 3.1 GeV resulting in a Lorentz boost for the $\Upsilon(4S)$ of $\beta\gamma = 0.56$ in the laboratory frame.

The asymmetry of the machine is motivated by the need of separating the decay vertexes of the two B mesons, a crucial point for the determination of the CP asymmetries. The boost allows the separation and reconstruction of the decay vertexes of both B mesons, the determination of their relative decay length measured in the center-of-mass frame, the difference of their decaying time and thus the measurement of time dependent asymmetries. Nevertheless other stringent requirements on the detector are placed in order to measure the very small branching ratios of B mesons to CP eigenstates:

- large and uniform acceptance down to small polar angles relative to the boost direction;
- excellent reconstruction efficiency down to 60 MeV/c for charged particles and 20 MeV for photons;
- very good momentum resolution to separate small signals from background;
- excellent energy and angular resolution to detect photons coming from π^0 and η decays, and from radiative decays in the range from 20 MeV to 4 GeV;
- very good vertex resolution, both transverse and parallel to the beam direction;
- efficient electron and muon identification, with low misidentification probabilities for hadrons. This feature is crucial for tagging the B flavor, for the reconstruction of charmonium states and also important for the study of decays involving leptons;
- efficient and accurate identification of hadrons over a wide range of momenta for B flavor-tagging and for the reconstruction of exclusive states;
- low-noise electronics and a reliable, high bandwidth, data-acquisition and control system;
- detailed monitoring and automated calibration;
- an on-line computing and network system that can control, process and store the expected high volume of data;
- detector components that can tolerate significant radiation doses and operate reliably under high background conditions.

2.1 The PEP-II Asymmetric Collider

The PEP-II B factory is part of the accelerator complex at SLAC, shown in Figure 2.1. The electron beam is produced by the electron gun near the beginning of the two-mile long linear accelerator (the "linac"). The gun consists of a thermally heated cathode filament held under high voltage. Large numbers of electrons are "boiled off" the cathode,

accelerated by the electric field, collected into bunches, and ejected out of the gun into the linac. The electron bunches are accelerated in the linac with synchronized radio-frequency (RF) electromagnetic pulses generated in RF cavities through which the beam passes by a series of 50 Megawatt klystron tubes (klystrons generate the pulses with their own lower energy electron beams passing through resonant cavities). The steering, bending, and focusing of the beam is carried out with magnets throughout the acceleration cycle.

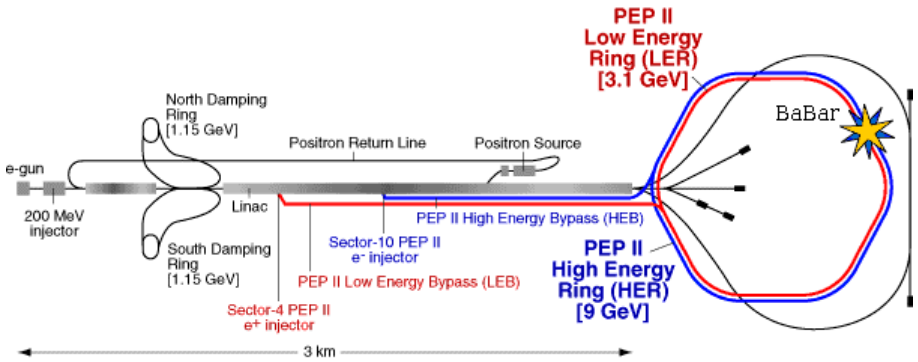

Figure 2.1: A schematic depiction of the B factory accelerator complex ad SLAC.

After acceleration to an energy of approximately 1 GeV, the electron beam is directed to a damping ring, where the beam is stored for some time. As it circulates in the ring, it loses energy through synchrotron radiation and is continuously re-accelerated by RF cavities. The radiation and careful re-acceleration has the effect of reducing the emittance, or spatial and momentum spread of the beam, a necessary step in high-luminosity collisions. The "damped" beam is then re-directed to the linac and accelerated to 8.9 GeV.

Half of the generated electron bunches are used for the generation of the positron beam. They are accelerated to approximately 30 GeV, extracted from the linac and directed onto a tungsten target, producing electromagnetic showers that contain large numbers of electron-positron pairs. The positrons are separated electromagnetically from the electrons, collected into bunches, accelerated, and sent through the return line to the source end of the linac. The positron beam is then accelerated and shaped like the electron beam through the linac and its own damping ring, culminating in an energy of 3.1 GeV.

After reaching their respective collision energies, the electron and positron beams are

extracted from the linac, and directed to the PEP-II storage rings, the High-Energy Ring (HER) for electrons and Low-Energy Ring (LER) for the positrons, both housed in the same tunnel of 2.2 km circumference. As they circulate, the are focused further by a complex of magnets and accelerated by RF cavities to compensate the synchrotron-radiation losses. In the interaction region IR-2 (one of twelve such regions), where the *BABAR* detector is located, they are brought to a collision after a final-focus system squeezes the beams to the smallest possible emittance. During data taking, each ring contains about 1600 circulating bunches colliding every 5 ns. The collisions are then analyzed by the *BABAR* detector. About 10% of the time the beams are collided at an energy 40 MeV below the $\Upsilon(4S)$ resonance for calibration of the backgrounds, as no B mesons are produced then since this energy is below the $b\bar{b}$ threshold. As data is collected, the collision and other losses reduce the currents in the rings, necessitating re-injection of electron and positron bunches. Initially in the life of the B factory from 1999-2002, data was taken for about an hour or two while the currents diminished, and then additional current was injected into the rings for a few minutes. Data could not be taken during injection due to the large backgrounds in the detector and the resulting danger to instrumentation. (The detector would have to be put into a "safe" but non-operational state during injection, with, for example, all high-voltage components ramped down to a lower, safer potential). Starting in 2003, a new scheme for injection, called "trickle" injection, was developed, wherein new bunches are continuously injected at a rate large enough to replenish beam losses but low enough to not damage the detector. This has allowed more efficient operation of the B-factory with 30% more integrated luminosity for a given highest instantaneous luminosity.

The PEP-II collider was designed for an instantaneous luminosity of 3×10^{33} cm^{-2}s^{-1}, but has reached values of 1.2×10^{34} cm^{-2}s^{-1} due to improvements in the RF cavities, beam-shaping cavities and magnet systems. The increased luminosity comes from larger beam currents (up to 3 A in the LER and 2 A in the HER) and reduced emittance. With these specifications and trickle injection, the machine generates hundreds of pb^{-1} of integrated luminosity daily during normal operations and has integrated hundreds of fb^{-1} throughout its operating lifetime. Figure 2.2 shows the total integrated and recorded

luminosity.

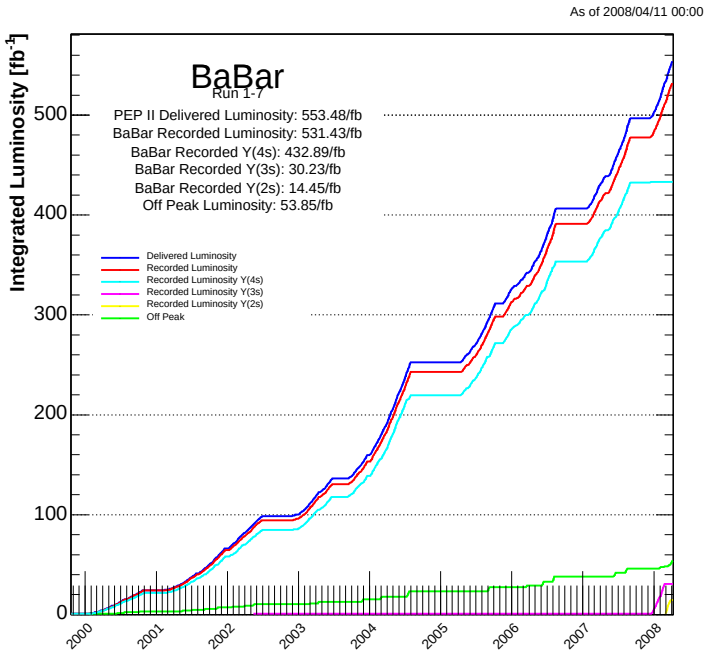

Figure 2.2: PEP-II delivered and *BABAR* recorded total (red line) integrated luminosity in the data taking period of 1999-2008 (Run1-Run7). The recorded luminosities for the other Υ resonances and for the off peak data are also shown.

2.1.1 PEP-II Backgrounds

Different factors should be taken into account when trying to set an acceptable background that allows a smooth and safe *BABAR* detector operation. Main constraints are:

- Radiation levels in EMC and SVT sub-detectors;
- Current tolerated by DCH;
- L1 trigger rate;
- Other subsystems occupancy.

Simulations, data analysis and dedicated measurements of the various background sources, on their impact on data taking and on detector performance have contributed to form

a detailed knowledge of different background-related underlying phenomena and made possible their tuning and reduction. PEP-II main background sources [49] are:

- *synchrotron radiation* in the proximity of the interaction region. A strong source of background (many kW of power) is due to the beam deflections in the interaction region. This component is limited by channeling the radiation out of the *BABAR* acceptance with a proper design of the interaction region and the beam orbits, and placing absorbing masks before the detector components.
- *interaction* between *beam particles* and *residual gas* in either ring can have two different origins: beam-gas bremsstrahlung and Coulomb scattering. Both these two types of interaction causes an escape of the beam particle from their orbit. This background represents the primary source of radiation damage for the inner vertex detector and the principal background for the other detector components.
- *electromagnetic showers generated by beam-beam collisions.* These showers are due to energy degraded e^+ and e^- produced by radiative Bhabha scattering and hitting the beam pipe within a few meters of the IP. This background is proportional to the luminosity of the machine.

2.2 The *BABAR* Detector

The *BABAR* detector is a large, multi-purpose hermetic detector with several components. *BABAR* operated from October 1999 until April 2008, recording a total of 596 millions of $B\bar{B}$ pairs.

As shown in Figure 2.3 the detector consists of two endcaps and a cylindrical barrel hugging the beam pipe along the z direction and roughly symmetric in the azimuth ϕ. The right-handed coordinate system is defined with the z axis pointing in the e^- direction, x pointing horizontally away from the center of PEP-II rings, and y pointing upwards. The geometrical center is offset from the beam-beam interaction point towards polar angles to maximize the geometric acceptance for the boosted $\Upsilon(4S)$ decays.

The sub-detectors are arranged in layers of increasing distance from the beam pipe. The silicon vertex tracker (SVT), the innermost detector, is used for vertexing particle

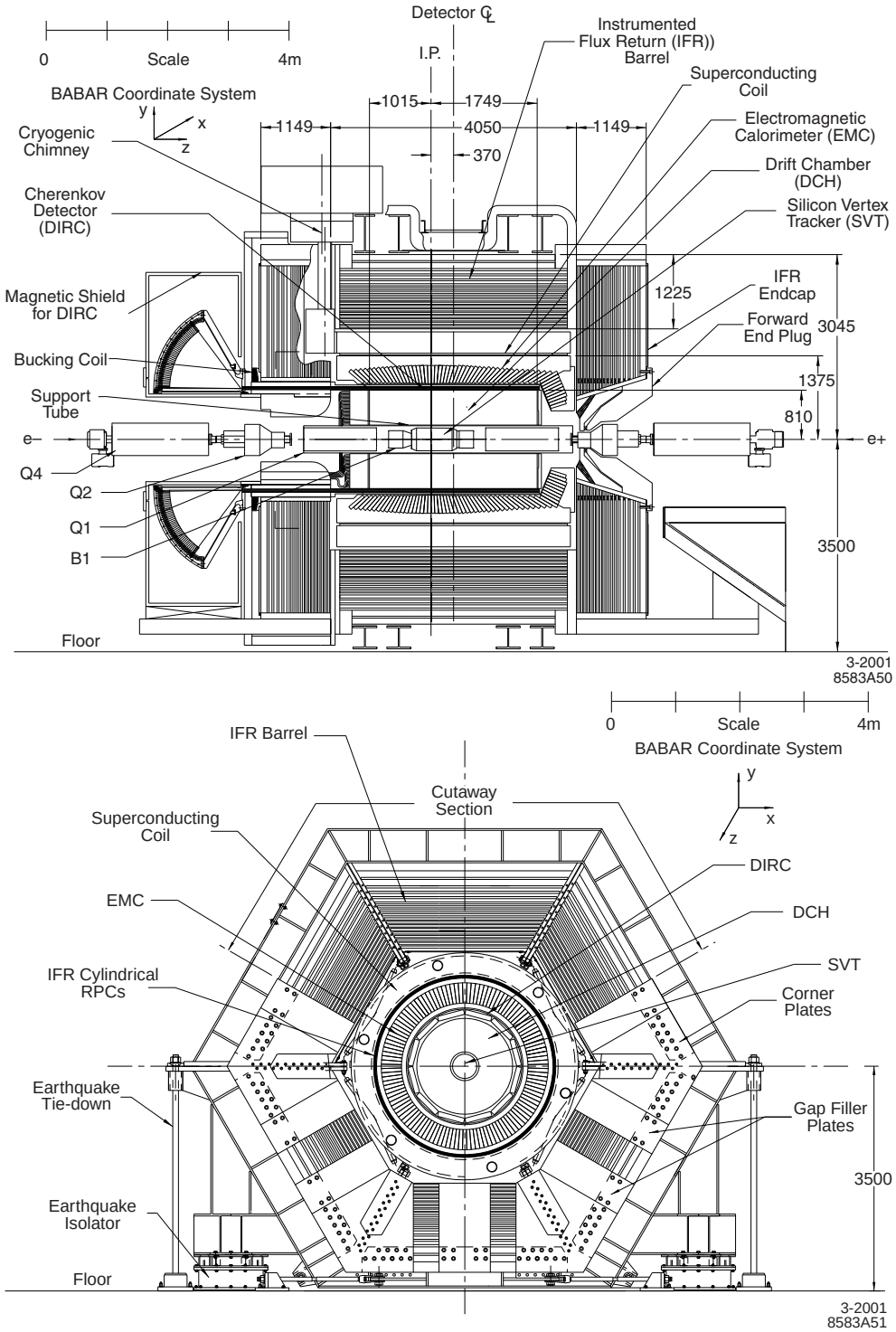

Figure 2.3: Longitudinal (top) and end (bottom) views of the *BABAR* detector. Units are mm.

decays and is the main source of information on the polar angle of charged particles. The Drift Chamber (DCH) is the main device for measuring charged-particle momenta with good resolution through gaseous wire-chamber technology. A Detector of Internally Reflected Čerenkov Light (DRC) is used to separate pions from kaons, while a crystal Electromagnetic Calorimeter (EMC) is used for energy measurement of photons and electrons and for electron identification. These components are placed within a 1.5 Tesla solenoidal magnet that provides the magnetic bending of charged particles needed to measure their momenta. Outside the magnet is the Instrumental Return Flux (IFR), which is used for the identification of muons and long-lived neutral hadrons. The detector signals are processed through detector electronics, and examined by a trigger system that selects physically interesting collision data to be stored. Various online and offline reconstruction procedures are employed to convert the data into a format amenable to analysis for the study of relevant B decays and other processes.

2.2.1 Silicon Vertex Tracker (SVT)

The SVT consists of five layers of double-sided silicon sensors segmented in both the z and ϕ directions, designed to measure accurately the positions and decay vertexes of B mesons and other particles. This measurement is most accurate at small distances from the interaction point, as the trajectory of the particles farther away is affected by multiple scattering within the detector. Thus, the first three layers are located as close to the beam pipe as possible. The outer two layers are closer to the Drift Chamber to facilitate matching of SVT tracks with DCH tracks. They also provide pattern recognition in track reconstruction, and the only tracking information for charged particles with transverse momenta below 120 MeV/c, as these may not reach the Drift Chamber. The SVT covers 90% of the solid angle in the CM frame. Figure 2.4 shows schematic views of the SVT.

The silicon sensors are 300 μm-thick high-resistivity n-type silicon wafers, with n^+ and p^+ strips running orthogonally on opposite sides. As high-energy particles pass through the sensor they displace orbital electrons, producing conducting electrons and positive holes that then migrate under the influence of an applied depletion voltage. The resulting electrical signal is read-off from the strips, amplified and discriminated with respect to a

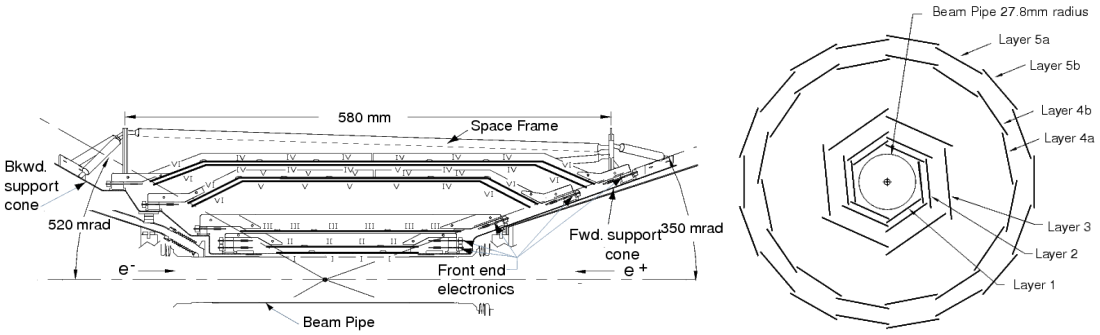

Figure 2.4: Schematic view of the SVT: longitudinal section (left) and transverse section (right).

signal threshold by front-end electronics. The time over threshold of the signal is related to the charge of the signal and is read out by the data acquisition system for triggered events. The position resolution is in the 10 μm-50 μm range, depending on the orientation of the strip (ϕ or z) and the layer number.

The SVT is water-cooled and monitored for temperature, humidity and position variations. Local and global position alignment is performed frequently in the offline reconstruction software. As the SVT has to withstand a lifetime integrated radiation dose of 2 Mrad, the sensors have a high threshold for radiation damage. Nevertheless, they are easily damaged by high instantaneous or integrated doses and an extensive system of radiation monitoring with PIN and diamond diodes can abort the beams if dangerous level develop. Up to 2007 the monitoring systems have prevented any significant damage from occurring and the SVT has performed extremely well, with an average track reconstruction efficiency of 97%.

2.2.2 Drift Chamber (DCH)

The Drift Chamber is the main tracking device. It supplies high precision tracking for charged particles with transverse momenta p_T above $\approx$ 120 MeV/c, and provides also particle identification by measuring track ionization losses as function of position (dE/dx), in particular for tracks with momenta less than 700 MeV/c.

The inner wall of the Drift Chamber is placed close to the SVT outer wall to facilitate track-matching between the two devices. The chamber is 2.8 m long and consists of 40 cylindrical layers of 12 mm by 19 mm hexagonal cells, each consisting of six field wires

at the corners and one field wire in the center as shown in Figure 2.5 and Figure 2.6.

The field wires are grounded, while the sense wire is held at high voltage, typically

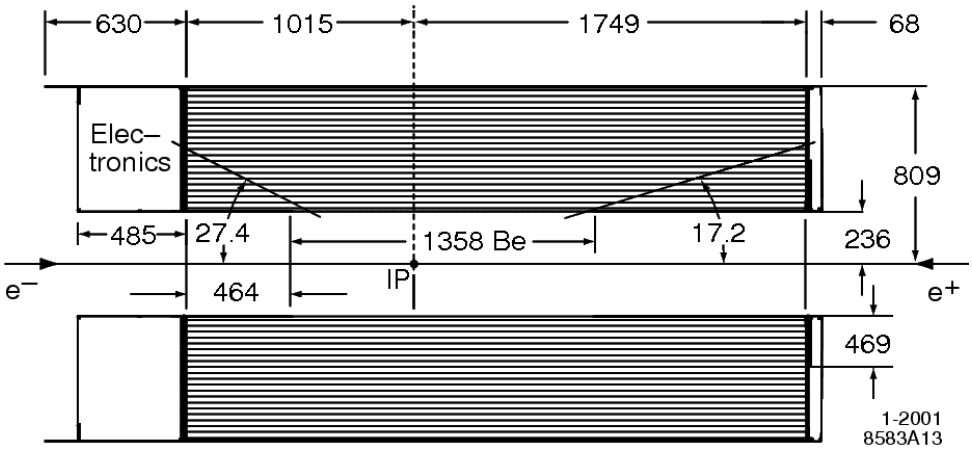

Figure 2.5: Longitudinal section of the DCH. Dimensions are in mm. The chamber center has an offset of 370 mm from the interaction point (IP).

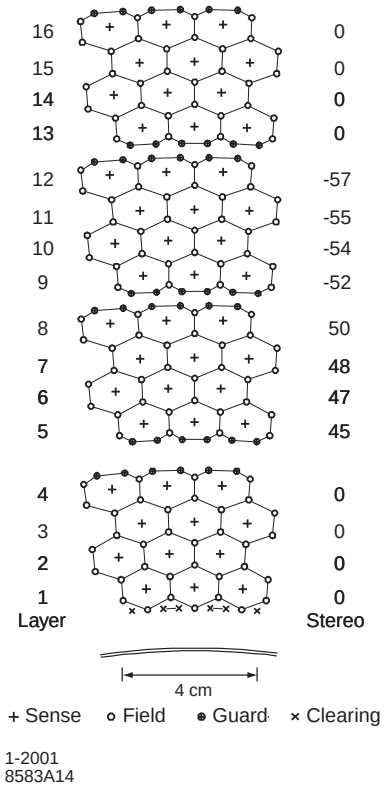

Figure 2.6: Layout of the four innermost super-layers.

around 1900 V. The space around the wires is filled with gas mixture containing 80% helium and 20% isobutane. High-energy particles ionize the gas as they traverse it, and the liberated electrons are then accelerated toward the sense wires, ionizing additional electrons, which are in turn accelerated themselves and result in the formation of a gas avalanche of electric charge. The avalanche collects on the sense wire with drift times of 10-500 ns and the charge and timing information of the signal is read-off through electronic circuits AC-coupled to the wire. The gain relative to the charge of primary ionization is about 5×10^4. The grounded field wires produce a uniform electric field in the cell with evenly distributed isochrones, or contours of equal drift time, as shown in Figure 2.7. "Stereo" wires in 24 of the 40 layers are placed at small angles with respect to the z direction in order to provide longitudinal information. The chamber has a typical position resolution of 140 μm.

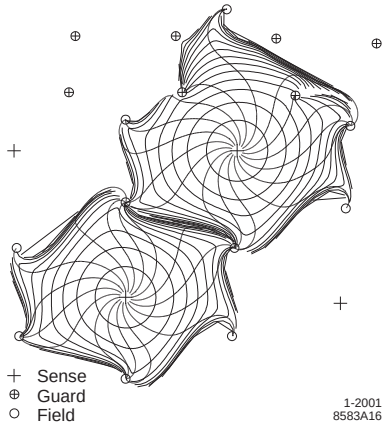

Figure 2.7: Isochrones in a typical DCH cell.

Isobutane has large molecules with rotational degrees of freedom that can absorb electrical energy, and its presence in the gas mixture limits the growth of the avalanche in order to protect the chamber from damaging levels of accumulated charge. The choice of the gas mixture is motivated by considerations of aging and avalanche size as well as minimizing multiple scattering in the chamber, which is accomplished by choosing helium as the primary gas component and aluminum as the lightweight material for the multiple field wires. The gas is circulated to flush out any degraded component, with one full volume of fresh gas (5.2 m^3) added every 36 h. In addition, the water content of the gas is

maintained by a water bubbler at 3500 ± 200 ppm and oxygen is removed with a catalytic filter, both measures designed to prevent Malter-effect discharges in the gas that would degrade the performance and aging behavior of the chamber.

The DCH has demonstrated excellent performance throughout the life of *BABAR* with track-reconstruction efficiencies at the 95% level. This includes the effect of disconnecting a fraction of the wires in superlayers 5 and 6 that were damaged during the commissioning phase. The $\mathrm{d}E/\mathrm{d}x$ response, with a resolution of about 7%, is shown in Figure 2.8, and a new calibration in 2006 has improved the PID potential of this capability for high-energy tracks. The achieved resolution on transverse momentum is $\sigma_{p_T} \,/\, p_T \;=\; (0.13 \,\pm\, 0.01)\% \,\times\, p_T + (0.45 \pm 0.03)\%$ where p_T is given in units of GeV/c.

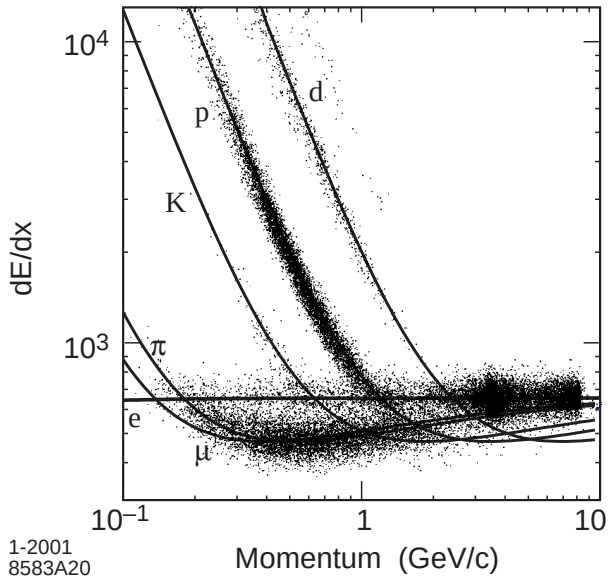

Figure 2.8: $\mathrm{d}E/\mathrm{d}x$ in the DCH as a function of track momentum for different particles: protons, kaons, pions, muons and electrons.

2.2.3 Čerenkov Light Detector (DRC)

The DIRC (Detector of Internally Reflected Čerenkov) is the main PID sub-detector at *BABAR* , providing $\pi - K$ separation of 2.5σ or more over the momentum range 700 MeV/c - 4.2 GeV/c. It is thin and light, minimizing the size and the impact on performance of the EMC that is located outside the DRC in the radial direction. Čerenkov devices detect light radiated by particles that move faster than the speed of light in a given medium,

with the Čerenkov angle θ_C of the radiated photons given by

$$\cos(\theta_C) = \frac{1}{n\beta} = \frac{c}{nv}, \tag{2.1}$$

where n is the index of refraction of the medium and v is the particle's velocity. For a given momentum, particles of different mass will have different velocities, differentiating particle-mass hypotheses for a track and thus different PID hypotheses.

The DRC consists of 144 bars made of fused silica running along the z direction, with dimensions of 17 mm by 35 mm and 4.9 m in length. The silica serves as the Čerenkov radiator, with the high index of refraction of $n = 1.437$ and as a waveguide, with a low attenuation length. A charged particle passing through radiates Čerenkov photons, which then propagate to the longitudinal end of the bar, trapped within by total internal reflections at the flat boundaries of the bar. Each reflection preserves the original Čerenkov angle. At the end of the bars, the photons pass through a standoff box filled with purified water that has a similar refractive index of $n = 1.346$, so that refraction at the silica-water boundary is minimized. The water must be highly transparent as the photons pass through about one meter of water in the standoff box, so it is filtered, de-gassed, de-ionized, exposed to UV radiation to prevent the growth of bacteria, and treated with a reverse-osmosis unit.

The rear surface of the standoff box is instrumented with 12 sectors of 896 photo-multiplier tubes (PMTs) each, which collect the photons, convert them to electrons with photo-cathodes and amplify the signal using the gas-avalanche principle. As the standoff box is located outside the solenoid magnet, it is possible to limit the magnetic field in its volume to about 1 Gauss with a bucking coil that counteracts the field of the solenoid. Thus, conventional PMTs, which do not tolerate high magnetic fields, can be used. To limit the number of PMTs, there is only one standoff box, located at the backward end of the detector to exploit the forward boost environment of the collisions. The forward ends of the silica bars have mirrors perpendicular to the axis of the bars, so that forward-pointing photons are reflected and reach the backward end of the bars as well. The detector is depicted schematically in Figure 2.9. The total photon detection efficiency is at the 5% level, with the average number of detected photons ranging from 20 at normal

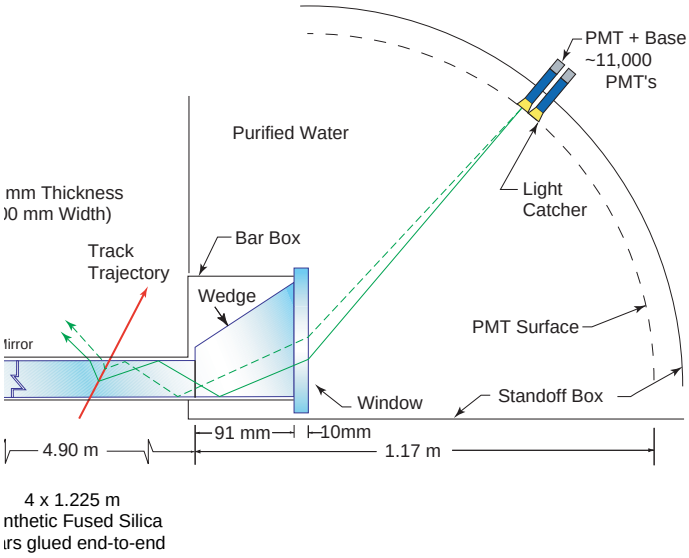

Figure 2.9: DRC scheme: radiation area and imaging region.

track incidence to 65 at large polar angles.

As the Čerenkov angle of the emitted photons is preserved, it can be reconstructed from the PMT signals, the timing information and the track momentum vectors obtained by matching the signal with tracks from the DCH and SVT. The resolution on the single-photon Čerenkov angle $\theta_{C,\gamma}$ is 10.2 mrad, while the resolution that can be obtained for a track from all its radiated photons is

$$\theta_{C,track} = \frac{\theta_{C,\gamma}}{\sqrt{N_\gamma}} \tag{2.2}$$

where N_γ is the number of detected photons. This yields typical track angular resolutions of 3 mrad.

The DRC is intrinsically a three-dimensional imaging device, giving the position and arrival time of the PMT signals. The three-dimensional vector pointing from the center of the bar end to the center of the PMT is computed and then is extrapolated (using Snell's law) into the radiator bar in order to extract, given the direction of the charged particle, the Čerenkov angle. Timing information is used to suppress background hits and to correctly identify the track emitting the photons. Figure 2.10 shows light rings reconstructed by the DRC.

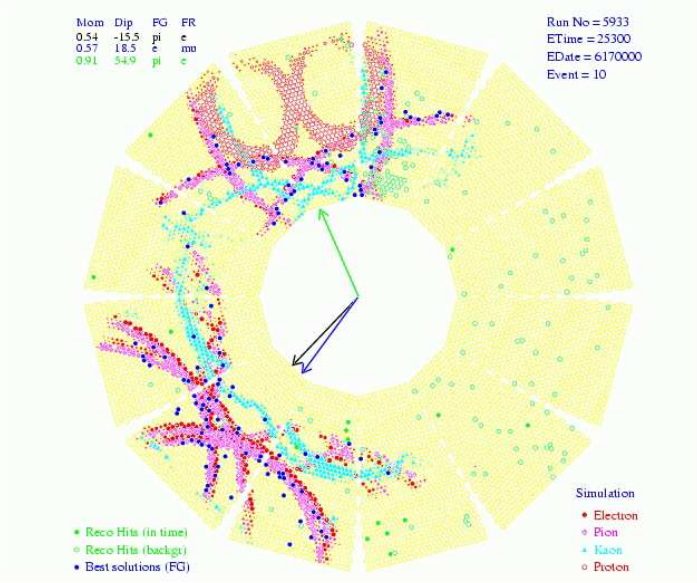

Figure 2.10: Čerenkov light ring reconstruction using the DRC.

2.2.4 Electromagnetic Calorimeter (EMC)

The electromagnetic calorimeter has been designed to measure with excellent resolution the energy and angular distribution of electromagnetic showers with an energy in the range from 20 MeV (for photons from decays of slow π^0 or η^0) to 4 GeV (for photons and electron from weak processes). An efficient and pure selection of electrons is necessary for B flavor tagging via semileptonic decays, for the reconstruction of vector mesons like J/ψ, or of several exclusive final states of B and D mesons. Furthermore QED processes like $e^+e^- \rightarrow e^+e^-(\gamma)$ and $e^+e^- \rightarrow \gamma\gamma$ need to be efficiently detected because they are useful for calibration and luminosity determination.

The EMC (Figure 2.11) is made of 6580 CsI Tallium activated crystals (Figure 2.12) The transverse segmentation is at the scale of Molière radius to optimize the angular resolution while limiting the number of crystals and readout channels. The crystals serve as radiators for the traversing electrons and photons, with a short radiation length of 1.85 cm. The crystal scintillate under the influence of the showers and the light is passed through total internal reflection to the outer face of the crystal, where it is read out by

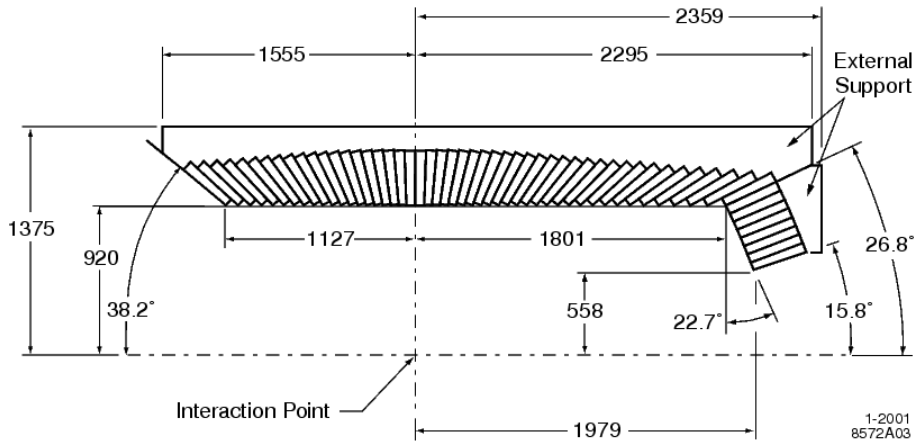

Figure 2.11: EMC longitudinal section (top-half only, dimension in mm) showing how the 56 crystal rings are placed. Detector has an axial symmetry along z axis.

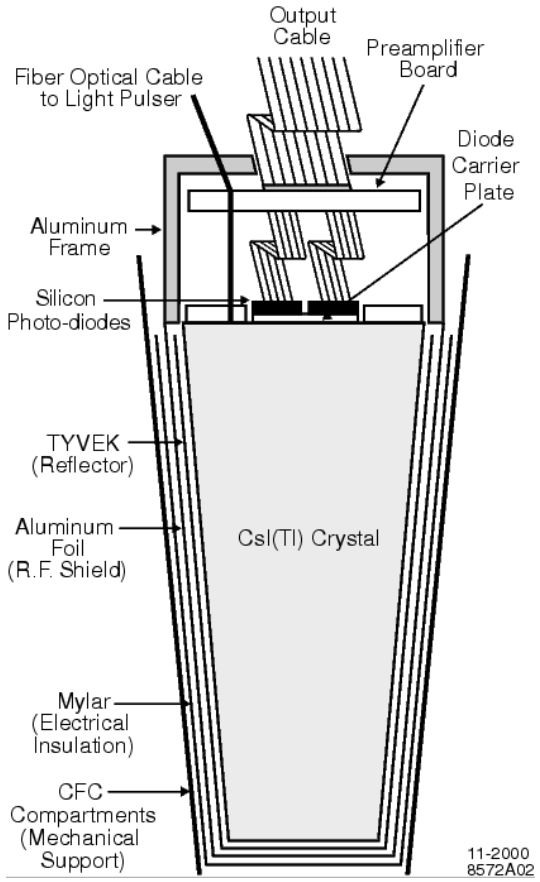

Figure 2.12: EMC crystal scheme.

silicon PIN diodes. As these diodes are well suited for operation in the high magnetic fields in the EMC, part of the motivation for the crystal choice was that the frequency spectrum of CsI(Tl) is detected by silicon PIN sensors with the high quantum efficiency of 85%. The EMC is cooled by water and Flourinert coolant and monitored for changes in the environmental and radiation conditions and for changes in the light response of individual crystals.

The energy response of the EMC is calibrated using low-energy photons from a radioactive source and high-energy photons from radiative e^+e^- Bhabha events. As electromagnetic showers spread throughout several crystals, a reconstruction algorithm is used to associate activated crystals into clusters and either to identify them as photon candidates or to match individual maxima of deposited energy to extrapolated tracks from the DCH-SVT tracker. Additional PID is obtained from the spatial shape of the shower. The energy and angular resolutions are determined to be

$$\frac{\sigma_E}{E} = \frac{(2.32 \pm 0.30)\%}{\sqrt[4]{E(\mathrm{GeV})}} \oplus (1.85 \pm 0.12)\%, \tag{2.3}$$

$$\sigma_\theta = \sigma_\phi = \frac{(3.87 \pm 0.07)\ \mathrm{mrad}}{\sqrt{E(\mathrm{GeV})}} \oplus (0.00 \pm 0.04)\ \mathrm{mrad}. \tag{2.4}$$

In both cases, the first term is due to fluctuations in the number of photons and to electronic noise of the photon detector and electronics, while the second term arises from the non-uniformity of light collection, leakage and absorption due to materials between and in front of the crystals and calibration uncertainties. Figure 2.13 shows the agreement between data and simulation of the angular resolution of the EMC and its π^0 reconstruction performance.

2.2.5 Instrumented Flux Return (IFR)

The IFR is the primary muon detector at *BABAR* and is also used for the identification of long-lived neutral hadrons (primarily K_L^0). The IFR is divided into a hexagonal barrel, which covers 50% of the solid-angle in the CM frame, and two endcaps (Figure 2.14). Originally it consisted of layers of steel of varying thickness interspersed with Resistive

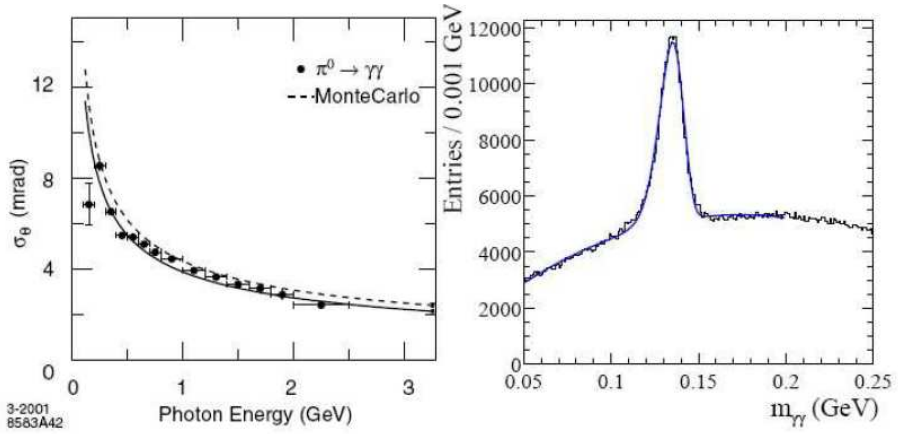

Figure 2.13: Left: angular resolution in the EMC as function of photon energy. The solid curve is a fit to Eq. 2.4. Right: the reconstructed diphoton peak at the π^0 mass region.

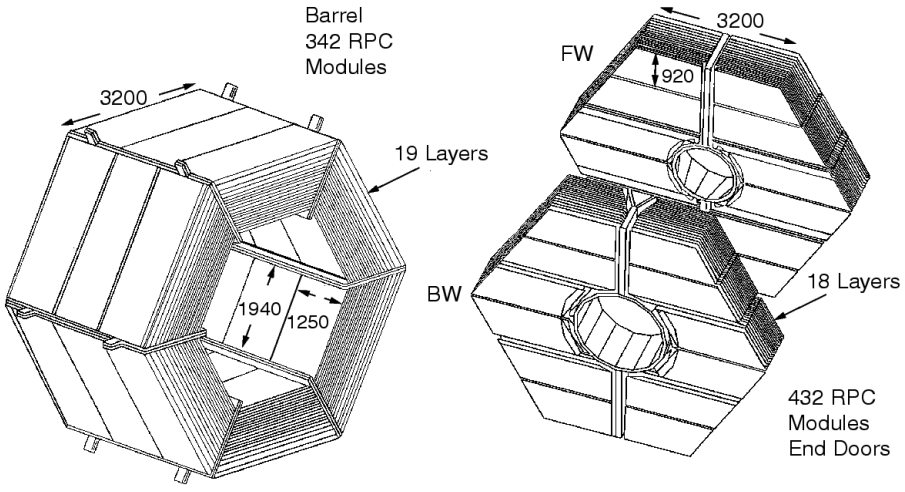

Figure 2.14: Overview of the original IFR Barrel sectors and forward and backward end-doors.

Plate Chambers (RPCs), 19 layers in the barrel and 18 in each endcap[1]. The steel serves as a flux return for the solenoidal magnet as well as a hadron absorber, limiting pion contamination in the muon ID. RPCs were chosen as they were believed to be a reliable, inexpensive option to cover the 2000 m^2 of instrumented area in this outermost region of *BABAR* with the desired acceptance, efficiency and background rejection for muons down to momenta of 1 GeV/c.

The RPCs detect high energy particles through gas-avalanche formation in high electric field. The chambers consist of 2 mm-thin bakelite sheets kept 2 mm apart by an array of spacers located every 10 cm (Figure 2.15). The space between is filled with a non-

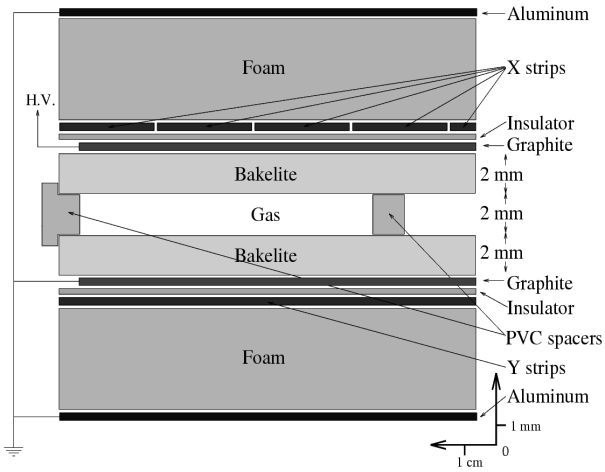

Figure 2.15: Planar RPC section with HV connection scheme.

flammable gas mixture of 56.7% argon, 38.8% freon 134a and 4.5% isobutane, while the sheets are held at a potential of 7600V. The inside surface of the bakelite is smoothed with a linseed-oil coating so that the electric field is uniform, thus preventing discharges in the gas and large dark currents. The RPCs operate in streamer mode, wherein the avalanche grows into a streamer, a mild, controlled form of electrical discharge in the gas. The streamer charge is read out in both ϕ and z directions by aluminum strips located outside and capacitively coupled to the chamber. The streamer is kept from producing electrical breakdown of the gas by the quenching action of the freon and isobutane molecules, as described for the DCH.

[1] Additional cylindrical RPCs were placed just outside the solenoid magnet to improve the matching between IFR and EMC showers

In streamer mode, the gas gain is at the 10^8 level. The factor 10-1000 increase in gain over avalanche mode greatly simplifies the readout electronics. Moreover, the charge of the streamer is independent of the primary-ionization charge, resulting in an effectively digital signal with high efficiency. Initially, the RPCs performed over 90% efficiency as expected geometrically from inactive space in the detector, resulting in a muon detection efficiency of 90% for a pion misidentification rate of 6–8% in the momentum range of $1.5 < p < 3.0$ GeV/c, as shown in Figure 2.16.

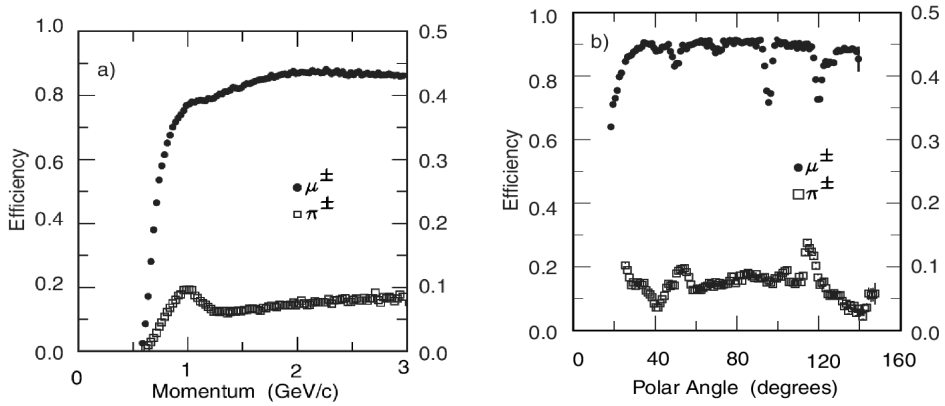

Figure 2.16: Initial muon-identification performance of *BABAR* RPCs.

Shortly after the start of data-taking with *BABAR* in 1999, the performance of the RPCs started to deteriorate rapidly. Numerous chambers began drawing dark currents and developing large areas of low efficiency. The overall efficiency of RPCs started to drop and the number of non-functional chambers (with efficiency less than 10%) rose dramatically (Figure 2.17), deteriorating muon ID. The problem was traced to insufficient curing and R&D of the linseed-oil coating and to the high temperature at which the RPCs were operated initially. Uncured oil droplets would form columns under the action of the strong electric field and the high temperature (up to 37 C), bridging the bakelite gap and resulting in large currents and dead space. Various remediation measures were attempted, including flowing oxygen through the chambers to cure the oil and introducing water cooling of the IFR, but they did not solve the problem. Extrapolating the efficiency trend showed a clear path towards losing muon ID capability at *BABAR* within a couple of years of operations, so an upgrade of the IFR detector was deemed necessary by the

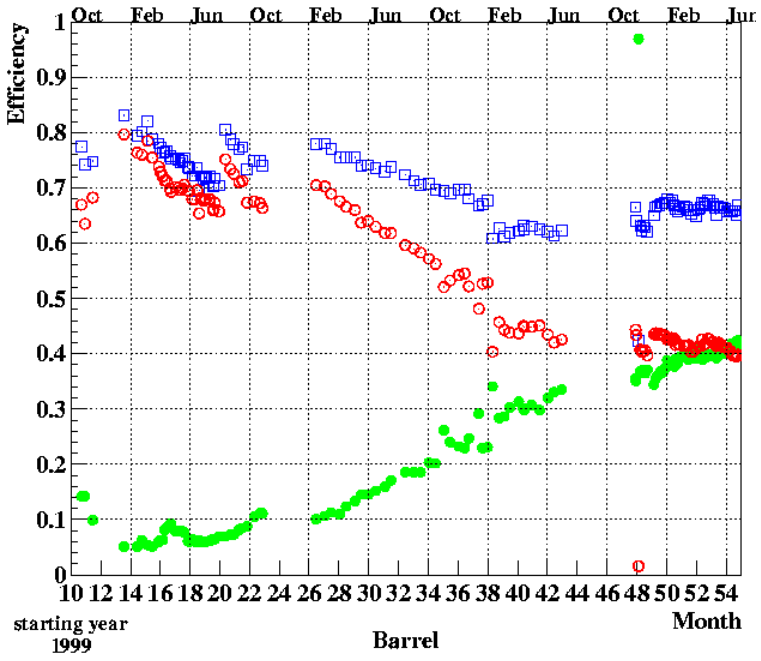

Figure 2.17: Deterioration with time of the average RPC efficiency (red). The green dots show the fraction of RPCs with efficiency lower than 10%; the blue squares the deterioration of the RPC with efficiency higher than 10%.

collaboration.

The forward endcap was retrofitted with new improved RPCs in 2002. The new chambers were screened much more stringently with QC tests and had a much thinner linseed-oil coating that was properly cured and tested. They have performed well since then. The backward endcap was not retrofitted, as its acceptance in the CM frame is small. In the barrel, the collaboration decided to upgrade the detector with Limited Streamer Tube (LST) technology. The RPCs were removed and replaced by 12 layers of LSTs and 6 layers of brass to improve hadron absorption. (The last layer of RPCs is inaccessible, so the old chambers there were disconnected from all utilities but kept in place). Since the author was partially involved in this upgrade, this project will be described in more detail than the other components of the detector.

The LSTs consist of a PVC comb of eight 15 mm by 17 mm cells about 3.5 m in length, encased in a PVC sleeve, with a 100 μm gold-plated beryllium-copper wire running down the center of each cell (Figure 2.18). The cells in the comb are covered with graphite,

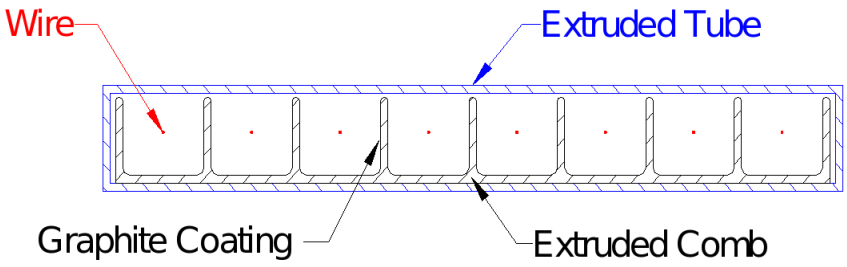

Figure 2.18: The mechanical structure of *BABAR* LSTs, with 8 cells.

which is grounded, while the wires are held at 5500 V and held in place by wire holders located every 50 cm. The gas mixture consists of 3.5% argon, 8% isobutane, and 88.5% carbon dioxide. Like the RPCs, the LSTs are operated in streamer mode. The signal is read off directly from the wires through AC-coupled electronics with a granularity of two wires per channel in the ϕ direction, and from strips running perpendicular to the tubes and capacitively coupled to the wires, the strip pitch is 35 mm). After mechanical assembly, the tubes were conditioned under progressively higher applied voltages to burn off dirt accumulated during construction. Only tubes that could hold the operational voltage without drawing excessive currents were accepted.

One of the crucial performance characteristics of the LSTs was the "singles'-rate", or counting-rate, plateau. As the streamer signals are effectively digital, given a constant incident flux of particles, the chamber should show a counting-rate plateau over a range of applied voltage where the charge of every streamer is above the read-out threshold (Figure 2.19). The width of this plateau provides the operational tolerance of the applied HV: minimizes fluctuations of the gas gain, and therefore of the efficiency, due to pressure or voltage fluctuations. Defects in the surface of the graphite or dirt accumulated on the wire can result in large discharges in the tube (including the Malter effect) that raise the singles' rate and spoil the plateau (Figure 2.19 right). In addition, a short plateau is an indication of poor aging behavior. Thus, the quality of the plateau is a powerful QC test.

The LSTs were constructed at PolHiTech, an Italian company located in Carsoli, outside Rome. The construction and QC procedures outlined above were conducted under

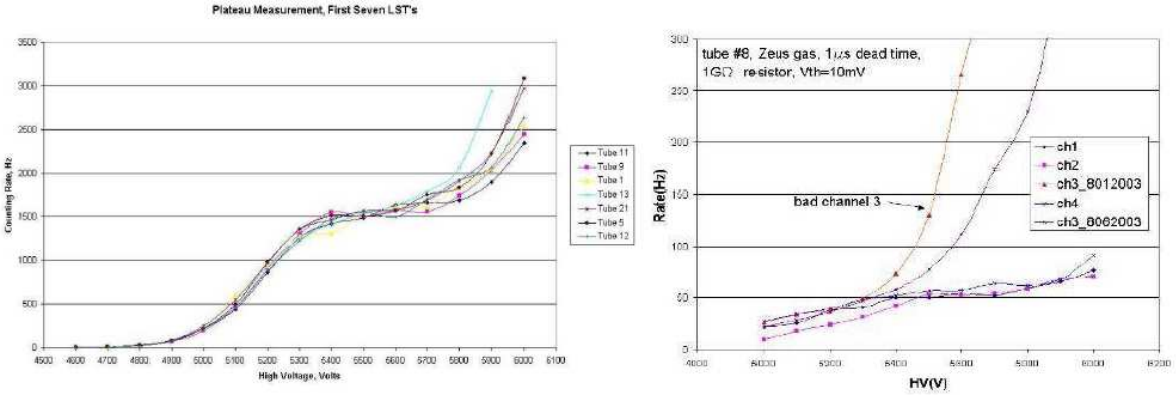

Figure 2.19: Left: a singles' rate plateau seen versus applied voltage for several LSTs. Right: defects in the chamber can spoil the plateau.

the supervision of *BABAR* personnel. After all QC tests, the tubes were held under high voltage for a month to verify that no premature aging behavior occurred. Thereafter, they were assembled into modules of two to three tubes at Princeton University and The Ohio State University and then shipped to SLAC for the installation, which occurred in two stages: two sextants of the hexagonal barrel in summer 2004 and the remaining four sextants in fall 2006. QC procedures were performed at every step to make sure that only the best tubes were installed in the detector.

The project involved the manufacture of 1500 LSTs including contingency, with more than 1200 installed in the detector. It also implied the design and fabrication of custom read-out electronics (done by INFN Ferrara in Italy), HV power supplies (The Ohio State University) and gas system (SLAC). The project was completed successfully, safely and ahead of schedule. After installation, the tubes have performed very well since 2005 in two sextants and since the beginning of 2007 in all sextants, with failure rate below 0.5% for both the tubes and z-strips. The efficiencies of all layers are at the geometrically expected level of 90%. Regular testing of singles'-rates with cosmic rays has shown a continuous excellent behavior of LSTs and long single's-rate plateaus (Figure 2.20). Figure 2.21 shows efficiency maps for all the six barrel sextants instrumented with LSTs.

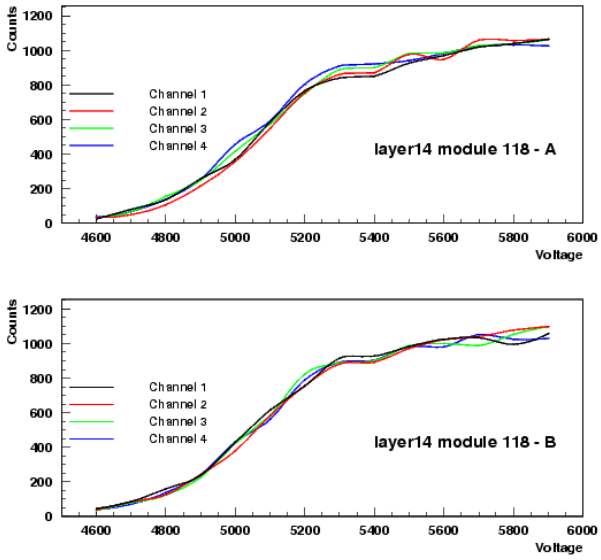

Figure 2.20: Singles' rate measurements with cosmic rays for some of the installed LST modules.

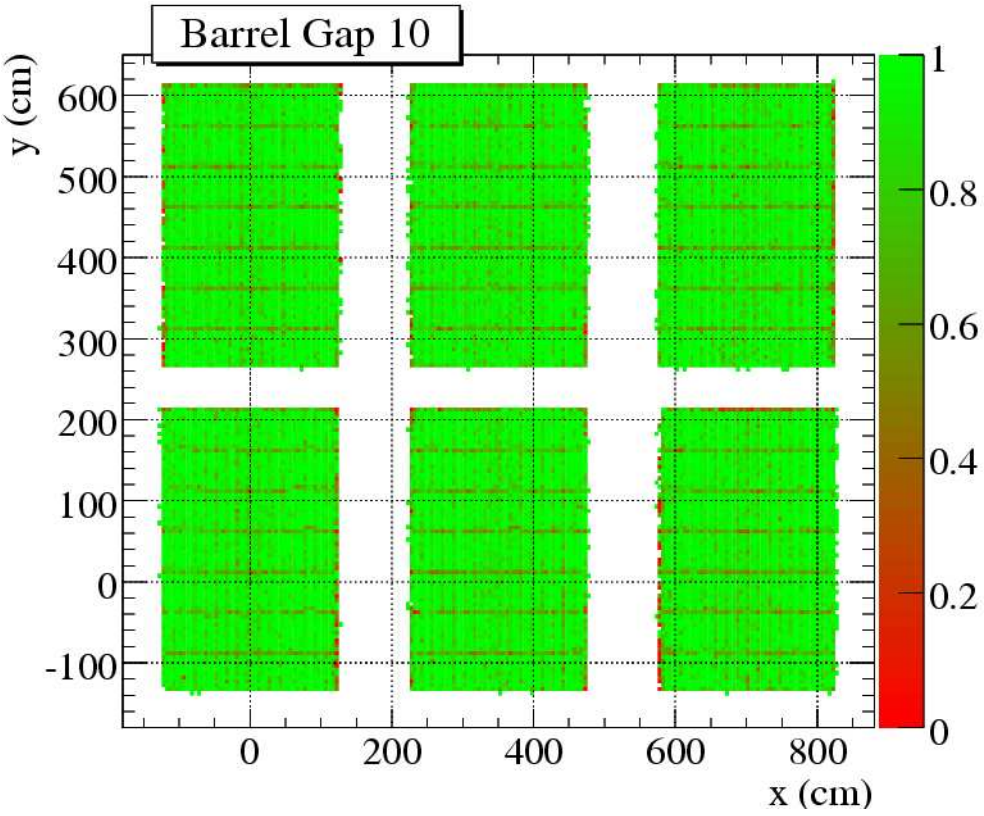

Figure 2.21: Efficiency map: each rectangle represents one sextant.

2.2.6 Trigger System (TRG) and Data Acquisition (DAQ)

The basic requirements for the trigger system is the selection of events of interest with a high, stable and well-understood efficiency while rejecting background events and keeping the total event rate under 1 kHz. At design luminosity, beam-induced background rates are typically about 20 kHz each for one or more tracks in the Drift Chamber with $p_T >$ 120 MeV/c or at least one EMC cluster with $E > 100$ MeV.

The total trigger efficiency is required to exceed 99% for all $B\bar{B}$ events and at least 95% for continuum events. Less stringent requirements apply to other event types, *e.g.* $\tau^+\tau^-$ events should have a 90-95% trigger efficiency, depending on the specific $\tau^\pm$ decay channels.

The *BABAR* trigger system is implemented as a two-level hierarchy. The Level 1 (L1) is hardware based, consisting in several dedicated microprocessor systems that analyze data from the front-end electronics (FEEs) of the DCH, EMC and IFR to form primitive physics objects used to make the trigger decision. These include tracks of minimum transverse momentum that penetrate to a particular depth into the DCH and energy clusters in the EMC above set thresholds. The selections are optimized to maintain nearly perfect $B\bar{B}$ efficiency while removing most of the beam-induced backgrounds in the process of reducing the data collection rate from about 20 kHz to a few kHz, which can be processed by the next trigger level. Some "prescaled" events of random beam-beam crossing and special event types are also collected for efficiency, diagnostic and background studies. The trigger decision is made and communicated within the 12.8 μs buffer limit of the FEEs. The L1 trigger has greater than 99.5% efficiency for $B\bar{B}$ processes.

After an L1 accept decision, the L1 output is passed on to the Level 3 (L3) trigger, which consist of software based algorithms run on a farm of PCs. The L3 triggers also has access to the complete event data and refines the L1 decision with more sophisticated selections, such as requirements on a track's distance of closest approach to the interaction point or the total invariant mass of an event. It maintains the $B\bar{B}$ selection efficiency at more than 99% while reducing the data rate to about 200 Hz. Each event corresponds to about 30 kB of detector information.

An event that results in an L3 accept decision is processed by the data-acquisition electronics and event-building software. In this process, charged tracks are reconstructed from DCH and SVT information and extrapolated to the outer part of the detector, incorporating knowledge of the distribution of material in the detector and the magnetic field. The momentum of tracks is measured from the sagitta in the curves of the tracks. PID is refined with DRC, EMC and IFR as well as with attempts to match objects in those sub-detectors with tracks in the DCH. Fundamental physical objects reconstructed in the detector are also used to assemble candidates for composite particles. Lists of particle candidates as well as the original digitized data is stored on tape in collections that are retrieved later for high-level analysis by individual groups of users.

Throughout event reconstruction various calibrations such as alignment constants and energy-scale adjustments in the EMC are applied to detector information to refine reconstruction performance. Calibration information is updated frequently during data taking to keep it consistent with running conditions. Data-quality scripts monitor detector behavior and various physics processes to verify that the collected data is not compromised by deviations from expected behavior of the detector or accelerator. A parallel system based on the EPICS slow-control environment is used to monitor and control the detector elements for all subsystems. Detector, accelerator and environmental conditions are recorded in another "ambient" database. The entire data-taking process is supervised at all times by at least two *BABAR* shifters on the detector side and several accelerator operators on the PEP-II side.

Chapter 3

The analysis method

3.1 Monte Carlo

Simulated data, usually referred to as Monte Carlo data, or simply MC, are essential to understand detector effects (e.g. efficiency, misreconstruction of signal), backgrounds and any systematic effects that could afflict our analysis procedure. The simulation of the physics mechanisms that operate in e^+e^- collisions within *BABAR* 's energy regime and the way that their products interact with the detector and are handled by the reconstruction software does not need to be perfect in order to make a measurement. However, the more detailed and faithful it is, the more effective we are at discarding any systematic problems in the data analysis, e.g. efficiency evaluations.

Often, it is most useful to be able to trace the behaviour of single particles within an event through the whole process, and for this reason information about each of them is carried along all the phases of simulation, from the production, to the later stages of track-fitting, cluster-matching and vertexing. The comparison between the reconstructed information about the event and its generator-level counterpart (*truth-matching*) can be realized in a variety of ways. In *BABAR* , the approach adopted consists of assessing the fidelity of the reconstructed data only after the full reconstruction has been completed, without any such assessment in the intermediate stages, e.g. after the track-finding.

The `EvtGen` package [50] is responsible for the physics simulation, providing an accurate representation of subtle phenomena such as mixing and interference (necessary for the correct modelling of CP-violation) or the angular distributions of the decay products

in non-trivial situations like pseudoscalar-to-vector-vector decays, for instance. The vast majority of B decays are generated by `EvtGen`, with the remaining generic B decays to hadronic final states (for which there is no specific model) and the continuum events ($e^+e^- \rightarrow q\bar{q},\ q = u, d, s, c$) being produced via an interface to `JETSET` [51]. Charmless 3-body decays are modelled in detail by `EvtGen` using the Isobar approximation (Section 1.3.3) with the lineshapes and angular dependencies described in Sections 1.3.4 and 1.3.6. The output of this stage is a list of particles, the 4-vectors specifying their kinematics, and the (potentially displaced) vertexes for the products of the decays.

The simulation of the interaction of these decay products with the detector as they propagate through it is carried out by software based on `GEANT4` [52], and requires a detailed model of the instrument, both in geometric and material terms. Processes like rescattering or photon conversions, for instance, as well as a detailed account of the energy lost and deposited by the particles in the different parts of the detector (e.g. the gas that fills the Drift Chamber, or a crystal in the calorimeter) are the concern at this stage. Each of these interactions with the detector is recorded as a "gHit".

In the following stage, these "gHits" are used to simulate the data read out from the electronics of the detector, the trigger and the data acquisition system. Typical electronic noise and machine backgrounds characterizing a certain period of running of the experiment are then added. These are obtained by recording the detector's state at regular intervals ($\sim$ 1 Hz) during normal operations, and, due to their essentially random nature, they are unlikely to represent any physics event.

Finally, the simulated detector's electronic output is run through the same version of *BABAR* 's reconstruction software that is used on real data.

A related, widely used term, is *toy MC*, by which we refer to events simulated with the highly simplified model employed in the analysis to extract the relevant physics quantities from signal and background. Only a few of the relevant variables are usually taken into account and many of their possible correlations are neglected. Detector response effects are also often ignored, or modelled in a highly abstract manner, avoiding all the details of the passage of the particles through the detector and the reconstruction software.

3.2 Reconstruction

The reconstruction of events is performed in two stages. The first one, known as Offline Prompt Reconstruction, consists of finding and reconstructing tracks and calorimeter clusters from hits in the Drift Chamber and the Silicon Vertex Tracker, and crystals with energy deposits in the Electromagnetic Calorimeter, respectively. Čerenkov photons and dE/dx information are also processed at this stage and abstracted into "particle identification selectors". The second part of the process deals with the reconstruction of composites, objects that are not directly observed in the detector but can be inferred from the properties and correlations of their decay products, the best example being a B meson. "Candidates" for composites are formed from combinations of tracks and neutral objects, allowing the important vertexing of the B meson.

3.2.1 Tracking algorithms

Due to the axial magnetic field in which the inner parts of the detector are immersed, charged tracks follow helices and are described by five parameters, which we take to be defined at the point of closest approach (POCA) to the z-axis:

- d_0, the distance in the xy plane to the z-axis,
- z_0, the coordinate along the z-axis,
- ϕ_0, the azimuthal angle of the POCA,
- λ, the dip angle of the track with respect to the transverse (xy) plane. It is related to the cylindrical polar angle θ via $\theta = \pi/2 - \lambda$,
- ω, the (signed) curvature of the track, whose sign and magnitude are related, respectively, to the charge of the associated particle and its transverse momentum, $\omega \propto 1/p_t$.

The tracks are fitted using a Kalman filter technique [53], that essentially fits each vertex independently, and iteratively and recursively propagates the changes in the parameters to the neighbouring vertexes. Although the result is a global fit, the local character of

each step of the algorithm allows corrections to be made that model the fine detail of the material distribution of the detector, the slight inhomogeneities of the magnetic field or the energy loss of low momentum tracks.

The algorithm starts from the Dch hits found by the Level 3 Trigger to form a track, and further hits are added if they are observed to be consistent with that track. Once the process is finished, the remaining hits in the Dch are searched for tracks that may not have originated at the beamspot (like K_S^0 or Λ, that live long enough to have their decay vertexes outside the SVT), or may not be energetic enough to traverse the whole chamber. Afterwards, SVT hits are examined and added to the existing DCH tracks if possible, and are otherwise searched to locate any low momentum, SVT-only tracks.

The reconstructed tracks are then classified and stored in lists according to different selection criteria.

In the present analysis, the K_S candidates are required to meet the conditions of the `KsDefault` list, that means the following conditions:

- a charged track;
- mass inside the window 472.67 MeV, 522.67 MeV];
- POCAMass inside the window [0.45 GeV, 0.55 GeV].

The $\pi^{\pm}$ candidates are required to have the `GoodTracksVeryLoose` requirements:

- a charged track;
- 0 GeV $< p_T <$ 10 GeV;
- maximum DOCA[1] in xy plane equal to 1.5 cm;
- DOCA with z axis less than 10 cm.

The π^0 candidates are required to met the the `pi0LooseMass` conditions:

- built from two photons;
- mass windows of [90.0 MeV, 165.0 MeV];
- constraint on the vertex.

[1] Distance of closest approach

3.2.2 Calorimeter algorithms

The interactions of particles in the Electromagnetic Calorimeter typically result in *showers*, with the deposited energy spreading over neighbouring crystals. Each group of crystals, known as a *cluster*, might be due to the impact or passage of more than one particle and hence present energy distributions with several maxima. The aim of the calorimeter reconstruction routines is to locate and extract the right shape of the clusters, and to identify and correctly assign the energy to all the maxima within them.

The algorithm first looks for crystals with energies greater than 10 MeV, that will be used as 'seeds' for cluster formation. Surrounding crystals containing above 1 MeV themselves, or being neighbors of other crystals with more than 3 MeV are added to the cluster. Local maxima are found by standard methods, and are assigned a fraction of the energy of each crystal in the cluster that depends on the ratio of the distance from the crystal to the maximum, and the Molière radius.

Finally, tracks are projected onto the calorimeter, and if their position and entrance angle are consistent with one of the maxima, they are linked and considered as a single particle in the following reconstruction routines. The remaining maxima are assumed to be neutral objects and placed in lists of neutral particles like `pi0LooseMass`.

3.2.3 Particle identification

There are five common types of charged, long-lived particles that can be tracked in the *BABAR* detector: electrons, muons, pions, kaons and protons. Their correct identification is paramount for the physics goals of a B Factory, and this can be achieved thanks to the different ways in which those particles interact with each part of the detector. Information from all the sub-detectors (SVT, DCH, EMC, DIRC and IFR) is gathered to form probability density functions (see chapter 4) that represent the likelihood of a track belonging to a certain species. Since electrons and muons can often be separated easily from the other types of particles by their behaviour in the Electromagnetic Calorimeter and the Instrumented Flux Return, respectively, and protons are quite scarce, we will focus on the kaon-pion separation.

The likelihood for kaon and pion hypotheses is constructed as the product of the PDFs from the SVT, the DCH and the DIRC for the given particle hypothesis, where the first two contribute with measurements of the rate of energy loss (dE/dx) and the last one, with an estimation of the angle with respect to the track at which photons are emitted in the quartz bars of the DIRC. For both the DCH and the SVT, the measured energy loss of each track is compared with the Bethe-Bloch [40] expectation by forming the pull (see Section 3.4.3), which is parametrized with a gaussian for the DCH, and a gaussian with asymmetric widths for the SVT. The DIRC suffers from long non-gaussian tails that prevent the use of a similar method, so a binned likelihood is calculated instead with the help of MC. This likelihood depends on the angle of the Čerenkov photons with respect to the track, and also on the number of photons, since the latter is a function of the momentum and type of the particle, and it helps to improve the identification of low momentum tracks.

Once the likelihoods for the different particle hypotheses have been calculated, cuts on their values are applied, and the track is entered into different lists according to the criteria satisfied: `VeryLoose`, `Loose`, `Tight` and `VeryTight` for pions, and `NotPion`, `VeryLoose`, `Loose`, `Tight` and `VeryTight` in the case of kaons.

3.2.4 Vertexing of candidates

Candidates for composite particles are first formed from all the possible combinations of tracks and neutral objects matching the decay daughters of the particle. These candidates are then required to meet some kinematical criteria, and are subsequently vertexed. For instance, in the reconstruction of the charmless decays $B^+ \to K^0_S\pi^+\pi^0$, any intermediate state like $K^*(892)^+$ or ρ^+, is governed by the strong force and have such short lifetimes that their decay daughters may be assumed to originate from the B meson. Hence, there can only be candidates for the K^0_S and the B mesons.

Once a kinematical candidate has been found, its decay vertex is calculated by means of a geometric fit, in which the tracks of the daughters are required to emerge from a common vertex. Such is the task of the `TreeFitter` package, which performs a global fit to the whole decay chain by applying the Kalman filter technique. First, the K^0_S is built

from the two oppositely charged decay pions, imposing mass and beam constraints, and a K^0_S vertex is determined by using `TreeFitter`. Then, the B candidate is fitted by adding the π^+ and the π^0 to the K^0_S, applying momentum, mass and energy constraints.

3.3 Discriminating variables

The small branching fractions of charmless B decay modes like the one studied in this thesis ($\mathcal{B}(B^+ \to K^0_S\pi^+\pi^-) \sim 10^{-6}$) and the high cross sections for the undesired processes $e^+e^- \to q\bar{q}$ ($q = u, d, s, c$, where $\sigma_{udsc} \sim 3.2 \times \sigma_{b\bar{b}}$), make the use of background-rejecting variables unavoidable. By making use of the differences between the distributions of signal and background events in these variables, statistical separation of the two species can be attained. These differences can be taken advantage of in two ways. If the densities of events for the two types peak at different points of the range in the variable considered, a"cut" on the variable may be imposed, rejecting all events that lie on one side of the cut value, and enriching the sample with signal events. The other approach consists of accepting all events, and assigning each of them a weight or probability of belonging to each species based on their value for the discriminating variable.

In the present analysis, a mixed strategy has been followed: loose cuts are applied on the three discriminating variables, m_{ES}, ΔE and on the output of a neural network (see below), but their distributions are also used in the fit to help determine the number of events of each species. We now proceed to describe in detail the variables mentioned above.

3.3.1 Kinematic variables

Two kinematic variables, largely uncorrelated [54], are defined to help discriminate signal and background: the *energy-substituted mass*, m_{ES}, and the *energy difference*, the difference between the reconstructed center-of-mass energy of the B candidate and half the

total center-of-mass energy, ΔE:

$$m_{ES} = \sqrt{\left(\frac{s/2 + \vec{p}_i \cdot \vec{p}_B}{E_i}\right)^2 - \vec{p}_B^2}, \tag{3.1}$$

$$\Delta E = E_B^* - \frac{\sqrt{s}}{2}, \tag{3.2}$$

where $\vec{p}_B$ is the momentum of the B candidate, $\sqrt{s}$ denotes the center-of-mass-energy and

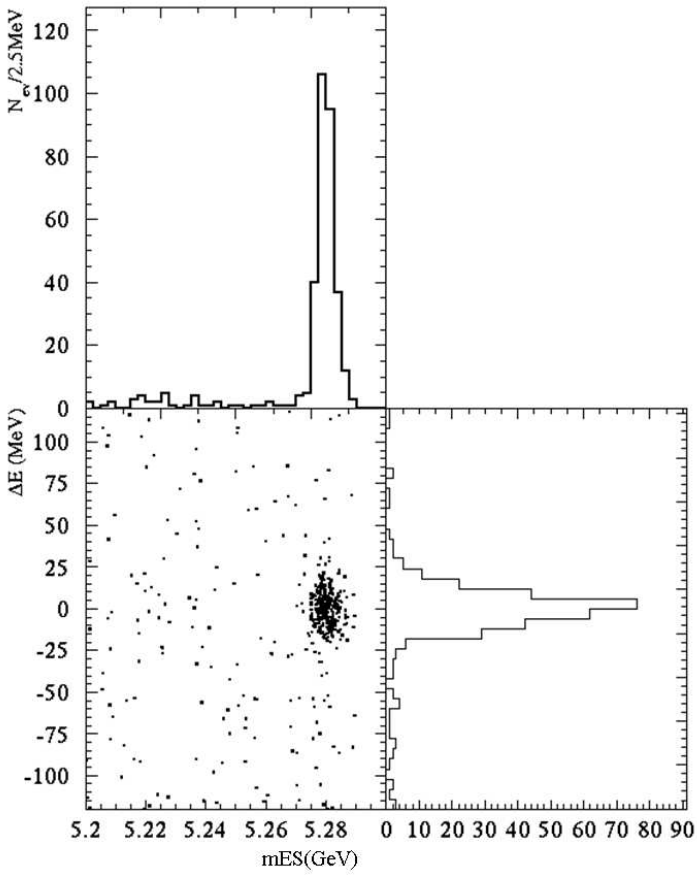

Figure 3.1: Example of m_{ES} and ΔE distributions for signal events.

$(E_i, \vec{p}_i) = p_i$ is the four-momentum of the initial state (the electron-positron system). The mass of the B candidate calculated from the kinematic constraints, m_{ES}, is used rather than simply $\sqrt{E_B^2 - \vec{p}_B^2}$. The reason is that the candidate is formed from a number of tracks and neutral objects whose energies are not as accurately measured as are the beam conditions. Therefore, a great improvement in the mass resolution is achieved by using

our knowledge of the initial kinematics. Since the electron and the positron annihilate creating a $B\bar{B}$ pair, and the masses of the particle and of the antiparticle are equal:

$$\begin{aligned} p_B^2 = p_{\bar{B}}^2 = (p_i - p_B)^2 = p_i^2 + p_B^2 - 2p_i p_B \\ 0 = p_i^2 - 2p_i p_B \\ s/2 = -E_i E_B + \vec{p}_i \cdot \vec{p}_B \\ m_B = \sqrt{E_B^2 - \vec{p}_B^2} = \sqrt{\left(\frac{s/2 + \vec{p}_i \cdot \vec{p}_B}{E_i}\right)^2 - \vec{p}_B^2} = m_{ES}. \end{aligned} \tag{3.3}$$

Thus, for signal events, m_{ES} yields the mass of the B meson and shows a clean peak. For continuum events, composed of light quarks, the only way of reaching the B rest mass is by artificially associating random tracks. As a consequence, their distribution displays the slowly varying shape that one could expect from their combinatorial nature. In this analysis a variable m'_{ES} is used instead of m_{ES}, where:

$$m'_{ES} = m_{ES}\sqrt{\frac{s_0}{s}} \tag{3.4}$$

that is the energy-substituted mass is rescaled by the actual center-of-mass energy s_0.

The idea behind ΔE is different and complementary to that of m_{ES}. Whereas the latter is by construction independent of the mass hypotheses for each of the tracks, ΔE depends strongly on them. If, for example, a kaon is misidentified as a pion, its energy $\sqrt{\vec{p}^2_{\text{measured}} + m^2_{\text{hypothesis}}}$, and consequently that of the B candidate, will be smaller and the event will be shifted towards negative values of ΔE. In contrast, the distribution for signal events peaks at zero as expected, making ΔE especially helpful in isolating backgrounds from misreconstructed B decays.

3.3.2 Event-shape variables

Event-shape variables, also known as topological variables, aim to exploit the angular correlations among the decay products in $B\bar{B}$ and $q\bar{q}$ events to further help the separation of the two species. In $q\bar{q}$ events ($e^+e^- \to q\bar{q}$, $q = u, d, s, c$), known as *continuum*, the small amount of energy invested in the rest masses of the quarks means that most of the available center-of-mass energy will be carried as kinetic energy. This, in turn, implies that the event will have a two-jet-like structure, roughly following a $(1 + \cos^2\theta)$ dependence, where θ is the cent re-of-mass angle of a jet with respect to the beam axis. This is as

predicted by lowest order Feynman diagrams for the quantum electrodynamical (QED) process of annihilation of an electron-positron system to produce a fermion-antifermion pair. Indeed, since the typical energy scale for strong interactions is far smaller than the available kinetic energy, $\Lambda_{QCD} \ll m_B - m_{q\bar{q}}$, hadronization and other QCD effects are not expected to alter greatly the expected QED angular dependence.

The $e^+e^- \rightarrow \Upsilon(4S) \rightarrow B\bar{B}$ process, in contrast, is characterized by the decay of the vector resonance $\Upsilon(4S)$ into two pseudo-scalars, resulting in a $\sin^2\theta$ distribution, where θ is the angle between the momentum of one of the B mesons and the beam axis. Furthermore, the reaction is barely allowed kinematically, with very little of the cent re-of-mass energy converting into kinetic energy of the B mesons. Their average momenta, $\sim$ 340 MeV/c, are in fact smaller than the typical momenta of their daughters, $\sim$ 1-2 GeV/c, which means that the decay products of a bottom meson will not be boosted enough to follow the flight direction of their parent. Hence the angular distribution of the decay products will be poorly preserved. Since the B mesons are pseudo-scalars, they decay isotropically and the distributions of their daughters in the $\Upsilon(4S)$ cent re-of-mass frame will be approximately spherical.

We will now describe a few variables that put to good use the differences explained above. In the definitions that follow, it is useful to distinguish between the reconstructed B side of the event, and the *Rest Of the Event* (ROE), that comprises all tracks, composites and neutral objects that do not make up the B candidate.

Angle between the B momentum and the beam axis

As noted before, the distribution of the B momentum direction with respect to the beam axis for $B\bar{B}$ events has a parabolic shape, $\sin^2\theta_{B_{\rm mom}} = 1 - \cos^2\theta_{B_{\rm mom}}$. For continuum events, in contrast, kinematically appropriate B candidates can only be formed from random combinations of tracks (often referred to as combinatorial background) and as a consequence, $\cos^2\theta_{B_{\rm mom}}$ will also take random values. Hence, the distribution is expected to be uniform (see Figure 3.3).

Thrust Axis variables

The *thrust axis* of a collection of particles is defined as the direction in which the sum of the projections of the momenta of the particles is maximized:

$$\text{thrust axis } \hat{n} : max \sum_i |\hat{n} \cdot \vec{p}_i| \tag{3.5}$$

where the i index runs over all the particles in the collection, and $|\hat{n}| = 1$. Given the spherical nature of B decays, the thrust axis of a true B candidate is essentially random. For continuum events, however, which are strongly collimated, the above definition ensures that the thrust axis approximates the direction along which the pair of quarks was emitted, even when the tracks are selected artificially to form a kinematical B candidate.

Several variables can be defined employing the thrust axis, such as the cosine of the angle between the thrust axis of the B candidate and the z axis, $\cos\theta_{B_{\text{thrust}}}$ (Figure 3.3), or the cosine of the angle between the thrust axes of the B candidate and the rest of the event.

Sphericity

As with thrust, sphericity provides a good separation of $q\bar{q}$ events and and events without that jet structure. Sphericity is a measure of the sum of the squares of transverse momenta for each track with respect to the event axis [63]. Defined over the interval (0,1), with highly directional events having low sphericity, and isotropic events corresponding to sphericity equal to 1. Sphericity is defined as

$$S = \frac{3}{2}(\lambda_2 + \lambda_3), \tag{3.6}$$

where λ_2 and λ_3 are the two larger eigenvalues of the diagonalized sphericity tensor

$$S^{\alpha\beta} = \frac{\sum_i p_i^\alpha p_i^\beta}{\sum_i \vec{p}_i^2} \tag{3.7}$$

where α, $\beta = 1, 2, 3$ corresponds to the x, y, z component respectively.

The ROE and Legendre polynomials

We can take further advantage of the marked differences in the angular distributions of the momentum flow in signal events ($\propto \sin^2\theta$) and continuum events ($\propto 1 + \cos^2\theta$) to

refine the selection criteria. Since our analysis explores the whole allowed phase space of a three-body decay, we cannot make use of the signal-side angular information on that aspect without biasing our sample, but we can exploit the fact that the other B in the event behaves statistically, but independently, in the same way. Furthermore, a good way of characterizing the angular correlations of the rest of the event is to calculate the components of the momentum distribution in the basis formed by the *Legendre polynomials*. Indeed, a calculation of the expectation values of the Legendre polynomials for the signal and background momentum distributions enables us to identify the order of the polynomials with the largest separation power. These turn out to be the zeroth and the second order, whose expectation values are non-zero and different. The remaining orders have vanishing expectation values. They are defined as follows:

$$L_0 = \sum_i^{ROE} p_i, \tag{3.8}$$

$$L_1 = \sum_i^{ROE} p_i \cos\theta_i, \tag{3.9}$$

$$L_2 = \sum_i^{ROE} \frac{1}{2}(3\cos^2\theta_i - 1), \tag{3.10}$$

where p_i and θ_i are the momentum and the angle with respect to the beam axis of the i-th track or neutral object in the rest of the event.

It should be noted that the intrinsic symmetry inherent to continuum events, due to their jet-like structure, leads to correlations between the values of their ROE and signal-side quantities. Since the signal side state is completely characterized by giving its Dalitz-plot coordinates, correlations between these and some discriminating variables, such as the Legendre polynomials evaluated from the ROE, should be expected for these events.

Tagging variable

Algorithms are used to determine ("to tag") the flavor of the B meson candidates. This is achieved by examining the decay products of the meson when it decays into a flavor-specific state.

The *BABAR* tagging algorithm [55] first removes from the event the tracks and neutral objects belonging to the fully reconstructed B meson. The remnants are analyzed by a Neural Network, which assigns to the event an overall (signed) probability, the magnitude representing the confidence in the estimation, and the sign indicating the flavor of the meson. The inputs to the Neural Network are themselves the results of other NNs, which are optimized to find any of nine distinct processes that would uniquely identify the flavor of their parent B meson, and are hence known as "sub-taggers".

The variable used in this analysis containing the tagging output is called `Not4Tag`.

3.3.3 Neural network

A multivariate analyzer technique is adopted, in order to define a single variable to be used the selection and in the fit. The event-shape variables L_0, L_2, thrust of the ROE, $\cos\theta_{B_{\rm mom}}$, $\cos\theta_{B_{\rm thrust}}$, the sphericity of the ROE, together with a tagging configuration (`Not4Tag` multiplied by the charge of the pion) are used to build a Neural Network, taking advantage of the `TMVA` package [56].

Comparison between the Neural Network and a Fisher discriminant were also made, and the performance of the Neural Network was seen to be slightly better to that of the Fisher (see Figure 3.2).

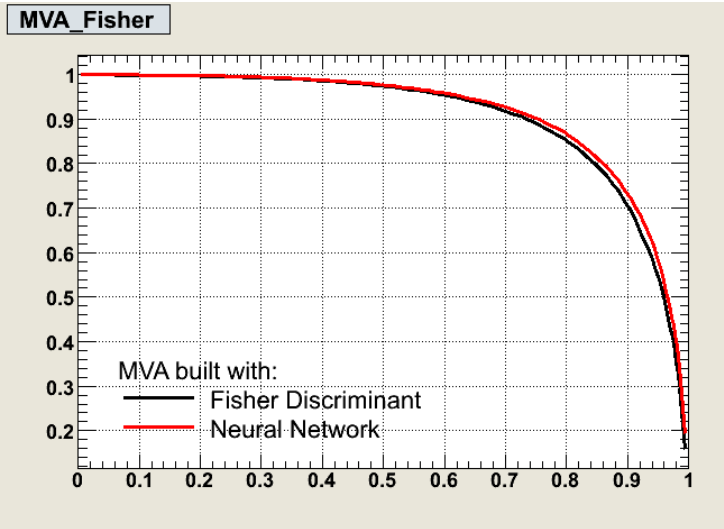

Figure 3.2: NN and Fisher comparison: efficiency versus rejection power.

Figure 3.4 shows the Neural Network distribution for the signal events and for the $q\bar{q}$ events.

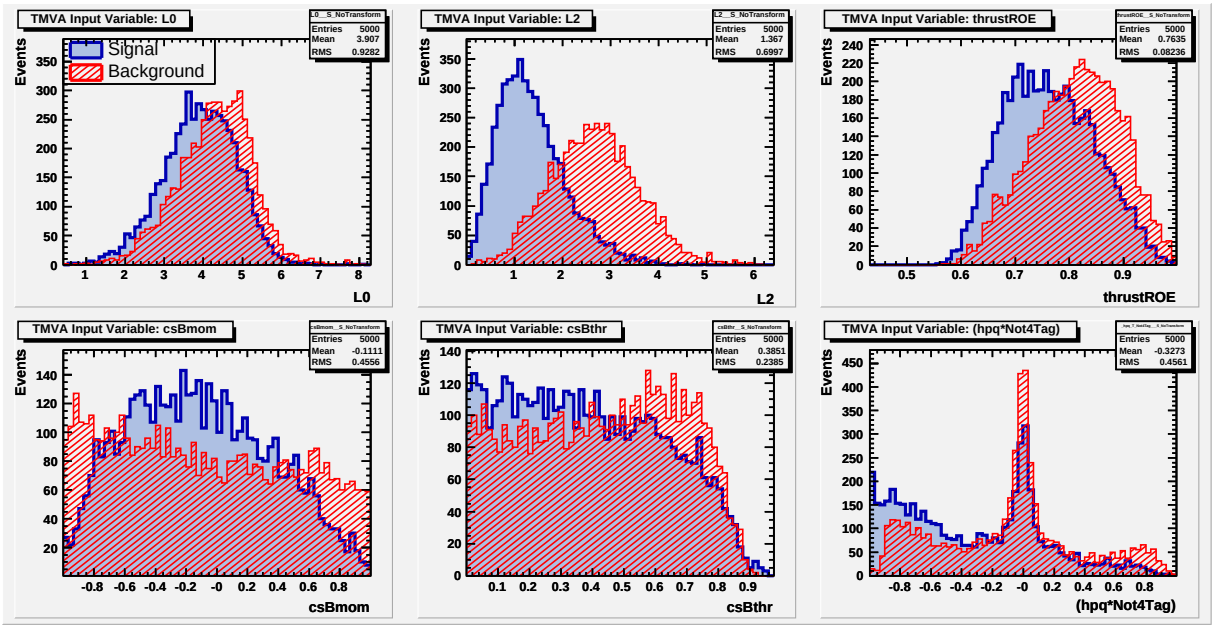

Figure 3.3: (Top) L_0, L_2, thrust of the ROE, (Bottom) $\cos\theta_{B_{\rm mom}}$, $\cos\theta_{B_{\rm thrust}}$, tagging configuration

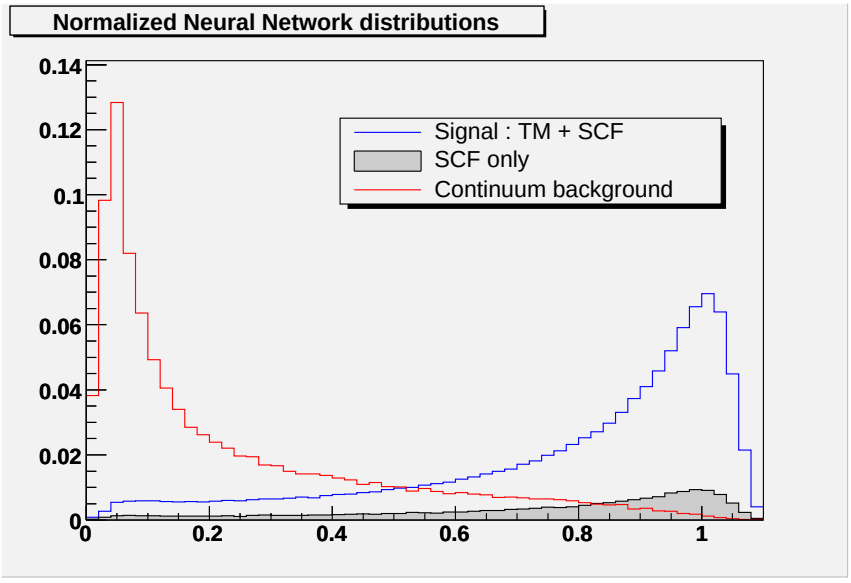

Figure 3.4: signal events (blue), $q\bar{q}$ events (red), misreconstructed signal events (gray).

3.4 Maximum Likelihood Fits

Maximum likelihood fitting is a powerful method to estimate the parameters that characterize a given statistical distribution from a data sample representing it. A more complete discussion can be found in [57] and [58].

The distribution taken by the outcomes of a sampling experiment (i.e. the values of a random variable x) can usually be described by a functional form $\mathcal{P}(x;\vec{a})$ whose shape is determined by some parameters $\vec{a}$. If the function $\mathcal{P}(x;\vec{a})$ is normalized, it is said to be a *Probability Density Function* (PDF) for x. Given a set of N measurements of the random variable, the problem consists of having the best possible estimations for the values of the parameters $\vec{a}$ that characterize the PDF. The estimations provided by the maximum likelihood method are attained by seeking the values of $\vec{a}$ that maximize the so-called likelihood function:

$$\mathcal{L}(\vec{a}) = \prod_{i=1}^{N} \mathcal{P}(x_i;\vec{a}) \tag{3.11}$$

Intuitively, the likelihood function represents the probability of drawing the N measurements of the random variable given a certain set of values for the parameters $\vec{a}$, so optimizing this probability should yield the parameter values that best describe the sample. In the simple case in which the data follow gaussian distributions, it can be proved that the methods of maximum likelihood and the time-honored least squares are equivalent. The former, though, is not limited to binned distributions.

The PDFs can be quite complicated, reflecting several hypotheses for the source of the measurement (e.g. whether it is signal or background), or the fact that the outcome of the experiment requires several random variables to be described:

$$\mathcal{P}(i;\vec{a}) = \sum_{j=1}^{M} \mathcal{P}_j(x_i, y_i;\vec{a}) = \sum_{j=1}^{M} \mathcal{Q}(x_i;\vec{a}_{\mathcal{Q}})\mathcal{R}(y_i;\vec{a}_{\mathcal{R}}) \tag{3.12}$$

where M is the number of hypotheses, x_i and y_i are the outcomes of the i-th experiment and in the last equality it has been assumed that the two random variables are uncorrelated and, therefore, that their joint PDF $\mathcal{P}$ can be written as a product of their individual PDFs $\mathcal{Q}$ and $\mathcal{R}$.

A crucial point to the maximum likelihood method is the assumption that the PDFs are normalized. If this were not the case, the results would be distorted or meaningless, since changes to the parameters could increase the normalization without increasing the probability, leading the optimization process to converge on incorrect values, or even pushing the global maximum to infinity. Therefore, recalculation of the norms of the PDFs is often necessary on each iteration of the fit.

Eq. 3.11 is not usually applied in that form, but with a slight modification to ease its computation. Taking logarithms, it can be rewritten as

$$\ell = -\log \mathcal{L} = -\sum_{i=1}^{N} \log \mathcal{P}(x_i; \vec{a}), \tag{3.13}$$

where the sum of logarithms is far more manageable in terms of machine precision than the previous product. The minus sign has been introduced so that the optimization of the likelihood function is performed by minimizing ℓ. In our likelihood fitting package, derived from `RhoPiTools` package [59], this is carried out numerically via an interface to `Minuit` [60] [61] through `ROOT` [62].

3.4.1 Extended Maximum Likelihood Fits

In particle physics, the number of events observed in an experiment is often unknown *a priori* and can be considered to be one of the outcomes of the measurement. In that case, the likelihood function must be appropriately modified to include the probability, given by the Poisson distribution, of having N occurrences when ν is the expected value:

$$\mathcal{L}(\nu, \vec{a}) = \frac{e^{-\nu}\nu^N}{N!} \prod_{i=1}^{N} \mathcal{P}(x_i; \vec{a}) = \frac{e^{-\nu}}{N!} \prod_{i=1}^{N} \nu \mathcal{P}(x_i; \vec{a}), \tag{3.14}$$

which, dropping constant factors, is generalized for M species or hypotheses by

$$\mathcal{L}(\vec{n}, \vec{a}) = e^{-\sum_{k=1}^{M} n_k} \prod_{i=1}^{N} \left(\sum_{j=1}^{M} n_j \mathcal{P}_j(x_i; \vec{a}) \right), \tag{3.15}$$

where n_j is the number of events for the hypothesis j.

3.4.2 Error estimation

There are several ways of calculating the errors on the estimations of parameters returned by a maximum likelihood fit, each of them involving different assumptions. Usually, the standard deviation σ, calculated as the square-root of the variance, is taken as the error on a parameter. In the large sample limit, the covariance matrix, and hence the errors, can be computed by inverting the matrix of the second derivatives of the likelihood function with respect to the parameters evaluated at the maximum:

$$\left(V^{-1}\right)_{ij} = -\left.\frac{\partial^2 \log \mathcal{L}}{\partial a_i \partial a_j}\right|_{\vec{a}=\vec{a}^0} \tag{3.16}$$

where $\vec{a}^0$ are the values returned by the fit.

Another method consists of defining the errors σ_i by the points $a_i^0 \pm \sigma_i$ in which the logarithm of the likelihood drops by 1/2:

$$\ell(a_i^0 \pm \sigma_i) = \ell(a_i^0) + \frac{1}{2} = \ell_{max} + \frac{1}{2}. \tag{3.17}$$

This prescription is inspired by the fact that, when the second derivatives of the likelihood can be considered constant in the range given by $a_i^0 \pm \sigma_i$, the shape of the function at the minimum is well approximated by a gaussian, as can easily be seen by making a Taylor expansion of ℓ. The definition of the error then reduces to that of the width of the gaussian.

Finally, an assumption-free procedure consists of generating a large sample of MC experiments using the values returned from the fit, fitting them again, and calculating the standard deviation of the results for the estimated parameter.

3.4.3 Toy Monte Carlo

A good way to identify and assess potential problems in the maximum likelihood fit is to generate a large number of MC experiments with given PDFs, and fit them using the same PDFs, in line with the procedure described at the end of the previous section. This simple check enables us to evaluate any bias due to low statistics, a defective likelihood or a mistake in the calculations, and to correct it in the latter cases. This toy MC (see Section 5.2) is generated using Von Neumann's acceptance-rejection method [58] with

our fitting package, and should result in gaussian distributions around the true value. Furthermore, the so-called *pull* distribution can be constructed by evaluating

$$\text{pull} = \frac{a_i^{\text{true}} - a_i^{\text{fit}}}{\sigma_i^{\text{fit}}}, \tag{3.18}$$

where the numerator is referred to as the "residual". These pull distributions should be gaussian in shape, centred around zero, and with a unit width.

3.4.4 Extraction of physical parameters

The signal model is built in terms of amplitudes and phases. The physical parameters we are interested in are partial yields and CP asymmetries. These parameters are non-trivial functions of the fit parameters.

In order to estimate their mean values and errors out of the fit result, we use a Lagrange Multiplier approach [66]: call X_i $(i = 1, N)$ the N parameters estimated in the fit, and $f(X_i)$ the physical parameter one is interested in (i.e. a CP asymmetry). Then one defines a χ^2 function as

$$\chi^2(f) = \sum_{i,j} \left(X_i - X_i^{\text{fit}}\right) \mathcal{C}_{ij}^{-1} \left(X_j - X_j^{\text{fit}}\right) + \left(\frac{f - F(X_i)}{\sigma_f}\right)^2, \tag{3.19}$$

where X_i^{fit} are the fitted values, $\mathcal{C}$ is the fit covariance matrix. The first term in the R.H.S. is such that χ^2 will be minimum (in fact, zero) when the fit parameters X_i are equal to those obtained from the fit. The second term is a penality defined to ensure that, for a given value of the test parameter f, the χ^2 function will be minimal for the best possible agreement between the f value and the function $F(X_i)$. One can then scan different values of the parameter f and fit the X_i parameters to evaluate the variation of $\chi^2(f)$. The "error" σ_f is an (arbitrary) small parameter, typically adapted to the scan step size.

The (unnormalised) likelihood distribution for the parameter f will be given by $\mathcal{L}(f) = \exp\left(-\frac{1}{2}\chi^2\right)$, and the confidence level by $\text{CL}(f) = \texttt{PROB}(\chi^2, 1)$. One can then infer the $1-\sigma$ $(2-\sigma)$ intervals by looking for the f values for which $CL = 32\%$ (5%), and they take correctly into account the (potentially) non-trivial correlations between the fit parameters and the physical quantity one is interested in.

Chapter 4

The analysis

The next three chapters discuss the analysis of $B^+ \to K^0_S\pi^+\pi^0$ in detail. This chapter shows the construction of the likelihood, and develops the methodology. A careful examination of all the species of events and ways of characterizing them is made, as well as of all the variables used to differentiate them.

Chapter 5 presents the tests performed to ensure that the complex fit is handled correctly, describes how the for the Dalitz structure is explored. Chapter 6 shows the evaluation of systematic uncertainties. Chapter 7 finally comments on the results obtained.

4.1 Overview

A Dalitz or amplitude analysis aims to extract the relative magnitudes and phases of structures contributing to a three-body decay. In this analysis, this is achieved by performing an unbinned extended maximum likelihood fit to the data sample.

The analysis was performed on an integrated luminosity of 347.47 fb^{-1}, which translates into a data sample of 364.8×10^6 $B\bar{B}$ pairs. A further 36.60 fb^{-1} of *off-peak* data were used for background characterization purposes.

Events are selected if the candidates found in them satisfy a number of deliberately moderately loose kinematic and event-shape requirements. Essentially, they are demanded to have a mass close to that of the B meson, decay in a rather isotropic way, and pass some loose PID requirements (Section 4.3).

The efficiency of these selection criteria and of the reconstruction process is modelled carefully, as it varies over the Dalitz plot and thus distorts the observed shapes of any structures.

Another reconstruction effect, the migration of the recorded position of badly reconstructed signal events over the Dalitz plot, is examined in Section 4.4. Its importance grows in the corners, where the resonances overlap and hence where most of the sensitivity to the relative phases between resonances lie. In an attempt to partially recover the lost information, simulated signal events are used to characterize the misreconstruction and statistically track down their point of origin.

There are background events in addition to signal in our sample, and they need to be accounted for. To that end, a detailed study of the number of background events and their distributions in the Dalitz plot and all other variables has been carried out (Section 4.5, Section 4.6). Two types of background are considered:

- *Continuum events.* They are by far the most numerous, in fact outweighing the signal due to the loose selection criteria. These are, however, very different kinematically from signal, and an effective separation between the two is attained with the help of the Neural Network described in Section 3.3.3.

- $B\bar{B}$ *background.* By this generic name we refer to true $B\bar{B}$ events where a B meson decaying to different channels from $K^0_S\pi^+\pi^0$ is misreconstructed as signal. This background is expected to be only a fraction of signal, but it shares many of the characteristics of signal, their distributions peaking close to or at the same point as that of true $B^+ \to K^0_S\pi^+\pi^0$ events. A careful modelling is needed, and $B\bar{B}$ background events are further split into 8 categories.

As mentioned above, to maximize our ability to separate background events from signal, and hence reduce the statistical uncertainty of our measurements, background discriminating variables are used. Rather than a harsh cut that optimizes the signal significance in the sample (like $N_{\rm signal}/\sqrt{N_{\rm signal}+N_{\rm background}}$), loose selection requirements were applied with the idea of separating signal and background on a statistical basis by including the variables in the fit.

The specific and generic B-decay and $q\bar{q}$ continuum Monte Carlo (MC) samples that were used to characterize signal and background are listed in Table 4.1.

4.2 Dependence of the discriminating variables on the Dalitz-plot coordinates

As mentioned in Section 3.4, the joint PDF for two uncorrelated variables can easily be constructed as the product of their individual PDFs. If the variables are correlated, the joint PDF does not factorize, and a more complicated dependence has to be considered.

For signal, any dependence of m'_{ES} on the Dalitz plot position was found to be negligible, instead ΔE exhibits a strong dependence, that is mitigated by using the corrected variable

$$\Delta E' = \frac{2\Delta E - (\Delta E_{\rm max} + \Delta E_{\rm min})}{\Delta E_{\rm max} - \Delta E_{\rm min}} \tag{4.1}$$

with $\Delta E_{\rm min} = -0.25 + 0.005 \times m^2_{K^0_S\pi+}$ and $\Delta E_{\rm max} = 0.15 + 0.002 \times m^2_{K^0_S\pi+}$, that follows the π^0 momentum dependent offset and resolution in ΔE over the Dalitz plot (Figure 4.1).

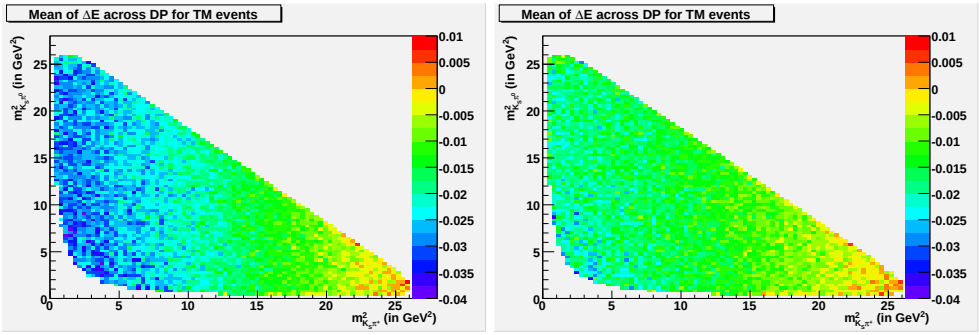

Figure 4.1: Dalitz plot maps of the average of ΔE before (left) and after (right) the correction is applied.

4.3 Event selection

The selection criteria are applied to the data in several stages. In a first stage B candidates are formed by requiring that they decay to final state particles belonging to lists described in Section 3.2.1. Next, they are asked to pass three very basic cuts:

- $m_{ES} > 5.2$ GeV,

Sample	events ($\times 10^3$)	$\mathcal{L}$ (fb^{-1})
Monte Carlo		
nominal signal model:		
$B^+ \to K_S\pi^+\pi^0 N.R.$	3518	11699631
$B^+ \to K^{*+}(892)\pi^0$	1	159015
$B^+ \to K^{*0}(892)\pi^+$	175	80511
$B^+ \to K_0^*(1430)^{+/0}\pi^{0/+}$	175	16408
$B^+ \to \rho^+ K_S^0$	175	
$B^+ \to K_s\pi^+\pi^0$	3165	
extra resonances:		
$B^+ \to \rho^+(1450)K_S^0$		
$B^+ \to \rho^+(1710)K_S^0$		
$B^+ \to K_2^{*+}(1430)\pi^0$		
$B^+ \to K_2^{*0}(1430)\pi^+$		
$B^+ \to K^{*+}(1680)\pi^0$		
$B^+ \to K^{*0}(1680)\pi^+$		
backgrounds:		
$B^0\overline{B}^0$	567264	540.3
B^+B^-	574668	547.3
$\bar{D}^0\pi^+$; $\bar{D}^0 \to K_S^0\pi^0$ (control)	350	215997
$B^+ \to K_S^0\pi^+$	350	
$B^0 \to \pi^-\pi^+$	1754	
$B^0 \to K_S^0\pi^0, B_b^0 \to X$	3518	
$B^+ \to K_S^0 K^{*+}, K^{*+} \to K^+\pi^0$	175	
$B^+ \to K^+K^{*0}, K^{*0} \to K_S^0\pi^0$	175	
$B^+ \to \bar{D}^0 K^+$	350	
$B^+ \to D^0\pi^+$	350	
$B^+ \to \bar{D}^0\rho^+$	1754	
$B^+ \to \bar{D}^{*0}\pi^+, \bar{D}^{*0} \to \bar{D}^0\gamma,$	350	
$B^+ \to \bar{D}^{*0}\pi^+, \bar{D}^{*0} \to \bar{D}^0\pi^0,$	350	
$B^+ \to D_s(D_s \to K_S^0\pi^+)\pi^0$	208	
$B^+ \to D_p(D_p \to \pi^+\pi^0)K_S^0$	208	
$q\bar{q}$ $(q = u, d, s)$	767138	367.1
$c\bar{c}$	778374	598.7
Real data		
on-peak	5250840	347.5
off-peak	496241	36.6

Table 4.1: Data samples. For Monte Carlo samples, we give the total number of simulated events without any selection cut and the equivalent integrated luminosity. In a specific Monte Carlo event the B decays to the specified final state and the B decays inclusively. All $\bar{D}^0$ (resp. K_S^0) mesons in a specific channel decay to $K_S^0\pi^0$ (resp. $\pi^+\pi^-$). *N.R.* means *non-resonant*. The signal Dalitz model is a complete nominal model with the amplitudes and phases specified in Table 5.1. The B-background $B^+ \to \bar{D}^0\pi^+(\bar{D}^0 \to K_S^0\pi^0)$ (*control sample*) which has the same final state as the signal is classified as background because it is not a charmless decay.

- 4.99 GeV $< E^* <$ 5.59 GeV,
- -0.45 GeV $< \Delta E <$ 0.45 GeV.

In the second stage, additional cuts are used to select signal events and reject background from continuum and other Bdecays. We impose no restriction to the Dalitz plot variables in their range for signal events which have been correctly reconstructed (Truth Matched, TM) simulated signal events. No optimization is done: the cuts are chosen very loose by inspecting distributions in the *signal region* and the *sidebands* defined in the (m'_{ES}, ΔE) plane by:

- $m'_{ES} < 5.27$ GeV/c^2 and $m'_{ES} > 5.29$ GeV/c^2 (*Grand Sideband*),
- $|\Delta E'| > 1$ (ΔE *Sideband*),
- both of above cuts (*Total Sideband*).

In the following stage, the PID likelihoods for the tracks, some quality related variables for the K_S, the π^+ and the π^0 are calculated.
For the K_S candidate:

- the mass requirement is tightened to $|m_{K^0_S} - m^{\rm PDG}_{K^0_S}| < 10$ MeV/c^2, where $m^{\rm PDG}_{K^0_S} =$ 497.614 MeV/c^2;
- the cosine of the angle between the momentum of the K^0_S and the line that joins its decay vertex with that of the B candidate, $\cos(\alpha_{K^0_S})$, must be greater than 0.995;
- the lifetime significance, $\tau_{K^0_S}/\sigma(\tau_{K^0_S})$, where $\tau_{K^0_S}$ the measured K^0_S proper time, is required to be greater than 5.0, thus rejecting combinatorial background.

For the π^+ candidate :

- the transverse momentum of the track, p_T has to be greater than 0.1 GeV/c^2;
- the track is requested to have more than 12 hits in the Drift Chamber;
- the π^+ candidate has to fail PID requirements for electrons, muons, kaons and protons.

For the π^0 candidate:

- it must be made of two photons each with $0.01 < \text{LAT} < 0.6$, where LAT is the lateral energy distribution of the photons;
- for each $E_{\gamma,\text{LAT}} > 50$ MeV;
- the invariant mass $m_{\gamma\gamma}$ has to be within $0.11\ \text{GeV/c}^2 < m_{\gamma\gamma} < 0.16\ \text{GeV/c}^2$.

An acceptable $B^+ \to K_S\pi^+\pi^0$ candidate must obey:

- $|\Delta t| < 10$ ps, where Δt is the time difference computed from the difference in z-axis between its vertex and the vertex of the rest of the events;
- $\sigma_{\Delta t} < 5$ ps;
- $5.27\ \text{GeV} < m'_{ES} < 5.29\ \text{GeV}$;
- $|\Delta E'| < 1$,

where the last two cuts define the *Signal region*. A few remarks are that:

- the neutral correction are applied for all kinematical calculations;
- no two-body veto is applied; this means that the abundant $B^+ \to \bar{D}^0(\to K^0_S\pi^0)\pi^+$ decay is kept and used a data control data,

Last but not least a cut is applied on the Neural Network variable at 0.8 (see Figure 3.3.3). Plots showing the cuts on signal and background MC, are in Figure 4.2.

The efficiency of each of these cuts, as well as the overall efficiency, have been evaluated from resonant and non-resonant MC, and are shown in Table 4.3.

4.3.1 Multiple candidates

When an event with multiple candidates passes the full selection, the best candidate is chosen to be the one with the smallest $\chi^2(m_{K^0_S}, m_{\pi^0})$:

$$\chi^2 = ((m^{\text{CAND}}_{\pi^0} - m^{\text{PDG}}_{\pi^0})/\sigma_{m_{\pi^0}}))^2 + ((m^{\text{CAND}}_{K^0_S} - m^{\text{PDG}}_{K^0_S})/\sigma_{m_{K^0_S}}))^2. \quad (4.2)$$

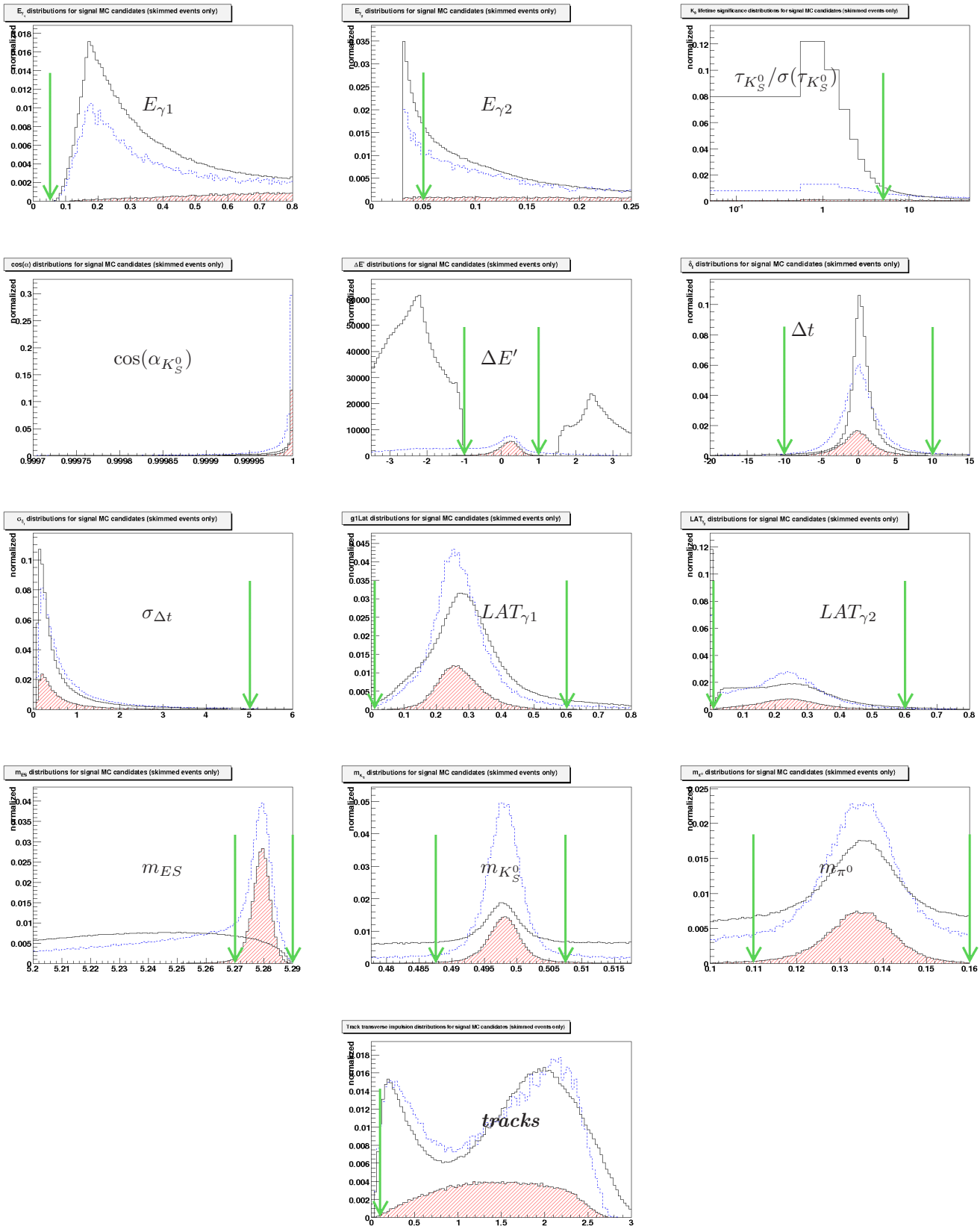

Figure 4.2: Distributions of discriminating variables for $B^+ \to K_S^0\pi^+\pi^0$ candidates for signal and background events. Blue/dashed line: all candidates reconstructed in the signal region in the purely non-resonant signal Monte Carlo. Red shaded histogram: truth-matched candidates only. Black/solid line: all candidates from on-peak data reconstructed in the sidebands (background distributions). For all variables except m_{ES} and ΔE, the *Total Sideband* is used, for m_{ES} the ΔE *Sideband* is used and for ΔE, the *Grand Sideband* is used.

Cut applied	$N.R.$	$K^{*0}\pi^+$	$K^0_S\rho^+$	$K^{*+}\pi^0$
Skim Efficiency	52.6%	59.5%	52.4%	55.5%
Preselection	71.4%	65.6%	68.4%	61.0%
$p_T > 0.1\,\mathrm{GeV}/c$	100.0%	100.0%	100.0%	100.0%
12 hits in DCH	98.8%	100.0%	100.0%	100.0%
$-1.0 < \Delta E' < 1.0$	84.3%	88.3%	91.0%	93.2%
$5.27 < m'_{ES} < 5.29\,\mathrm{GeV}/c^2$	88.2%	85.1%	86.0%	85.7%
$0.01 < \mathrm{LAT}_\gamma < 0.6$	96.5%	93.6%	94.6%	98.0%
$E_{\gamma,LAB} > 50$ MeV	97.8%	94.7%	95.6%	98.9%
$0.11 < \mathrm{m}_{\pi^0} < 0.16\,\mathrm{GeV}$	98.6%	97.7%	97.8%	98.9%
$\lvert \mathrm{m}_{K^0_S} - \mathrm{m}^{PDG}_{K^0_S} \rvert < 10\,\mathrm{MeV}$	93.6%	93.1%	94.1%	91.6%
$\cos(\alpha_{K^0_S}) > 0.995$	96.9%	96.8%	98.1%	95.4%
$\tau_{K^0_S}/\sigma(\tau_{K^0_S}) > 5$	97.5%	97.6%	98.3%	97.5%
$\lvert \Delta t \rvert < 10$ ps	97.9%	98.4%	97.6%	96.8%
$\sigma_{\Delta_t} < 5$ ps	98.2%	98.5%	98.2%	98.1%
electron PID veto	99.9%	100.0%	99.9%	99.7%
muon PID veto	97.9%	97.0%	98.4%	99.0%
kaon PID veto	98.4%	97.7%	98.4%	98.6%
proton PID veto	98.8%	98.4%	98.9%	99.3%
sub-total efficiency	20.7%	20.2%	20.6%	20.3%
$NN > 0.8$	62.2%	59.4%	59.4%	60.7%
total efficiency	**12.9%**	**12.0%**	**12.2%**	**12.3%**
SCF fraction	7.2%	33.2%	34.2%	16.8%

Table 4.2: Summary of selection efficiency for signal modes in the Monte Carlo. The efficiency of a given cut is relative to the sample selected with all previous cuts applied. The cut on NN is applied after selection of the best candidate. Some of the selected events are mismeasured as explained in Section 4.4, their fractions in the selected samples are given at the bottom of the table.

The chosen χ^2 method has the advantage to increase the signal efficiency in corners of the Dalitz plot (where the interference occur) and to enrich the reconstructed sample in the actual signal decays. For multi-candidate events (Figure 4.3) which on average comprise

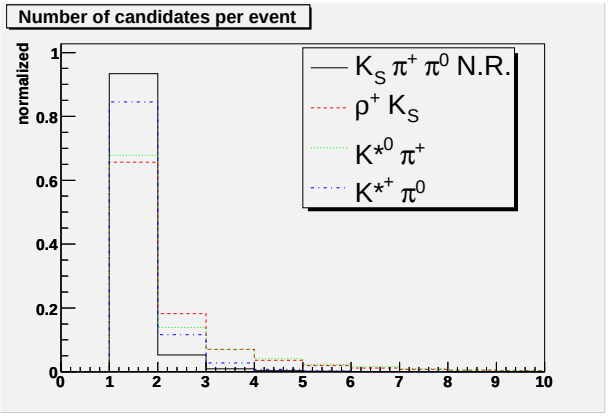

Figure 4.3: Candidate multiplicity for selected events (non-resonant and resonant modes).

respectively 2.98 candidates per event for the signal Dalitz model and 2.46 for the non resonant MC, the true decay combination is reconstructed in 37% (respectively 50.4%) of the cases.

4.4 Treatment of Self Cross Feed

Misreconstructed signal events, also called Self-Cross-Feed (SCF), are a non negligible part of the data sample. A simulated signal event is classified as truth matched (TM) if the two pions and the K^0_S of the selected candidate are matched with the right particles at the generator level. In addition to this, we require that the mothers of the matched generator level particles are the expected ones (depending on the specific signal MC mode). While the TM events with a TM candidates are accurately reconstructed, the (SCF) events migrate, i.e. in the Dalitz plot their reconstructed location is far from their generated location. Figure 4.4 shows that the generated locations of the SCF events are where there are soft particles which are easily mismeasured, in particular in the kinematical corners of the Dalitz plot.

For most non-TM events, we have access to the full Monte Carlo truth information

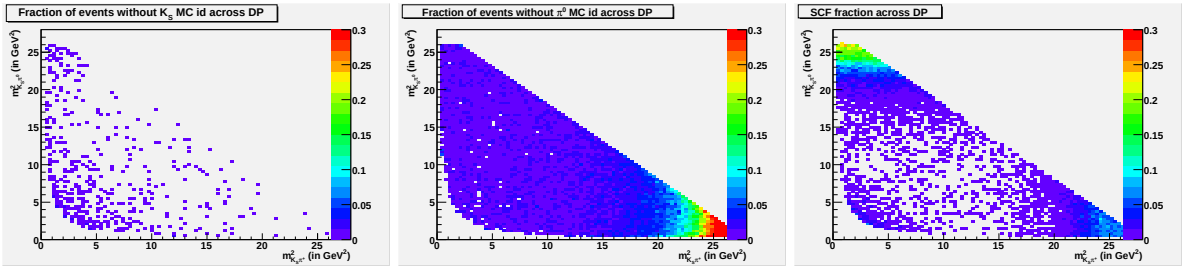

Figure 4.4: Location of the generated SCF events in the Dalitz plot; from left to right: the K^0_S-SCF cluster in the soft K^0_S corner, the π^0-SCF in the soft π^0 corner, and the True-SCF in all three soft particle corners.

(the *Lund-Id*s[1]) for all 3 candidates in the selected combination. However, a few events miss at least one Lund-Id, and are therefore undecidable. An algorithm has been devised to classify them. Fig. 4.5 can help follow the steps. We make the following distinction among the non-TM events:

- *True-SCF*: all the Lund-Id are available and at least one does not refer to a particle from the generated signal event.

- K^0_S-(resp. π^0)-*SCF*: the Lund-Id sequence is incomplete for the K^0_S (resp. for the π^0 or for both the K^0_S and the π^0).

  Two categories are enough as it never happens that the π^+ Lund-Id is missing. Further studies show that the misreconstruction of the composite particles is

  - either γ, γ-*SCF*, a random association of particles from the same or from different B ancestors (combinatorial γ ray),
  - π, π-*SCF*, a random association of particles from the same or from different B ancestors (charged pion pairing),
  - or *Quasi*-K^0_S or *Quasi*-π^0, a Lund-Id sequence which includes an extra soft particle (e.g. from a merged EMC cluster),

Figure 4.6 shows the migration both in the nominal and square Dalitz plot for all category of events, by using arrows from the generated to the reconstructed positions

[1] Each particle is identified with a number, and all the decay chain information are present.

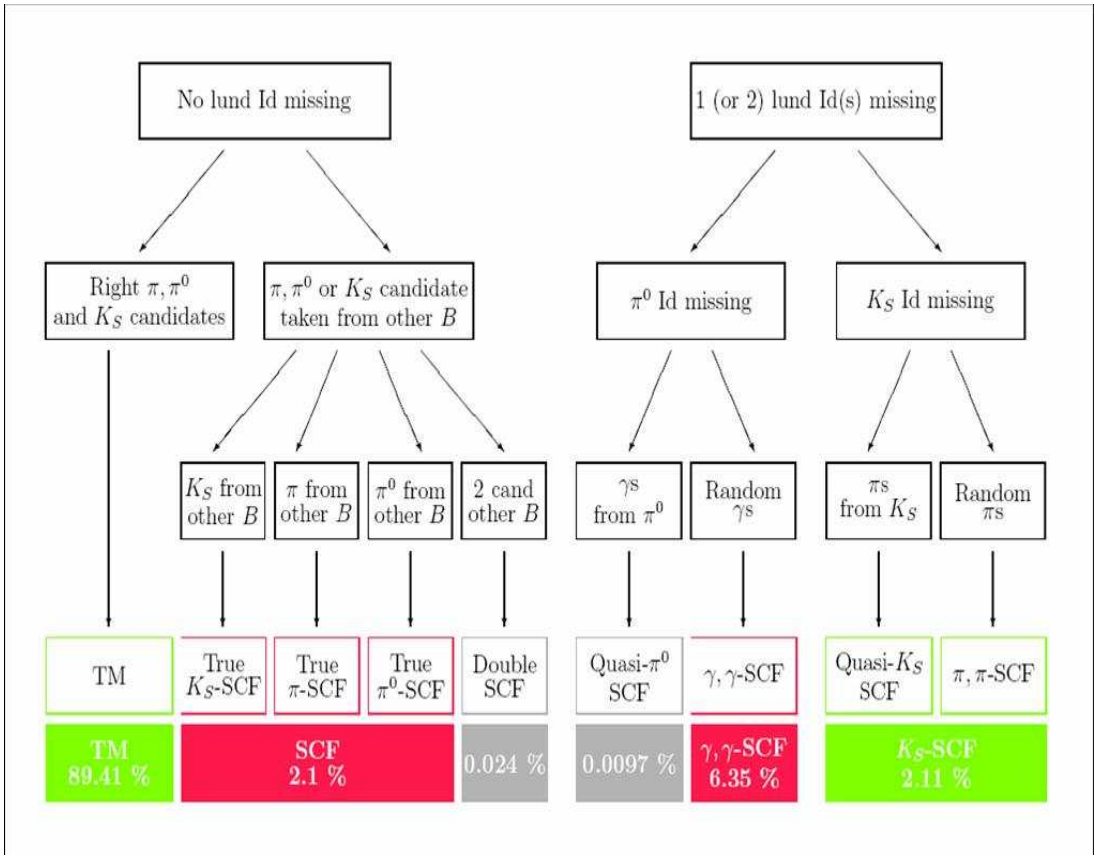

Figure 4.5: Signal components organigram.

in the Dalitz plot. In this figure, classic-SCF denotes inclusively all the events where 2 selected particles come from the signal B-meson.

We use the migration features to finalize two mutually exclusive signal event categories, the TM and the SCF operational categories. They are shown in light/green (resp. dark/red) on the organigram of Figure 4.5.

As expected, the TM events do not migrate. The K^0_S-SCF events do not show much migration either. When we later use a 40×40 grid to quantify the migration, these remain confined within one bin. Hence these two classes of events are grouped into the TM category. It also is convenient to merge these events as the K^0_S-SCF m_{ES} and ΔE distributions are very similar to those of the (TM) radiative events (Figure 4.7).

The selection efficiency (Table 4.3) split into the TM and SCF categories is shown over the Dalitz plot in Figure 4.8.

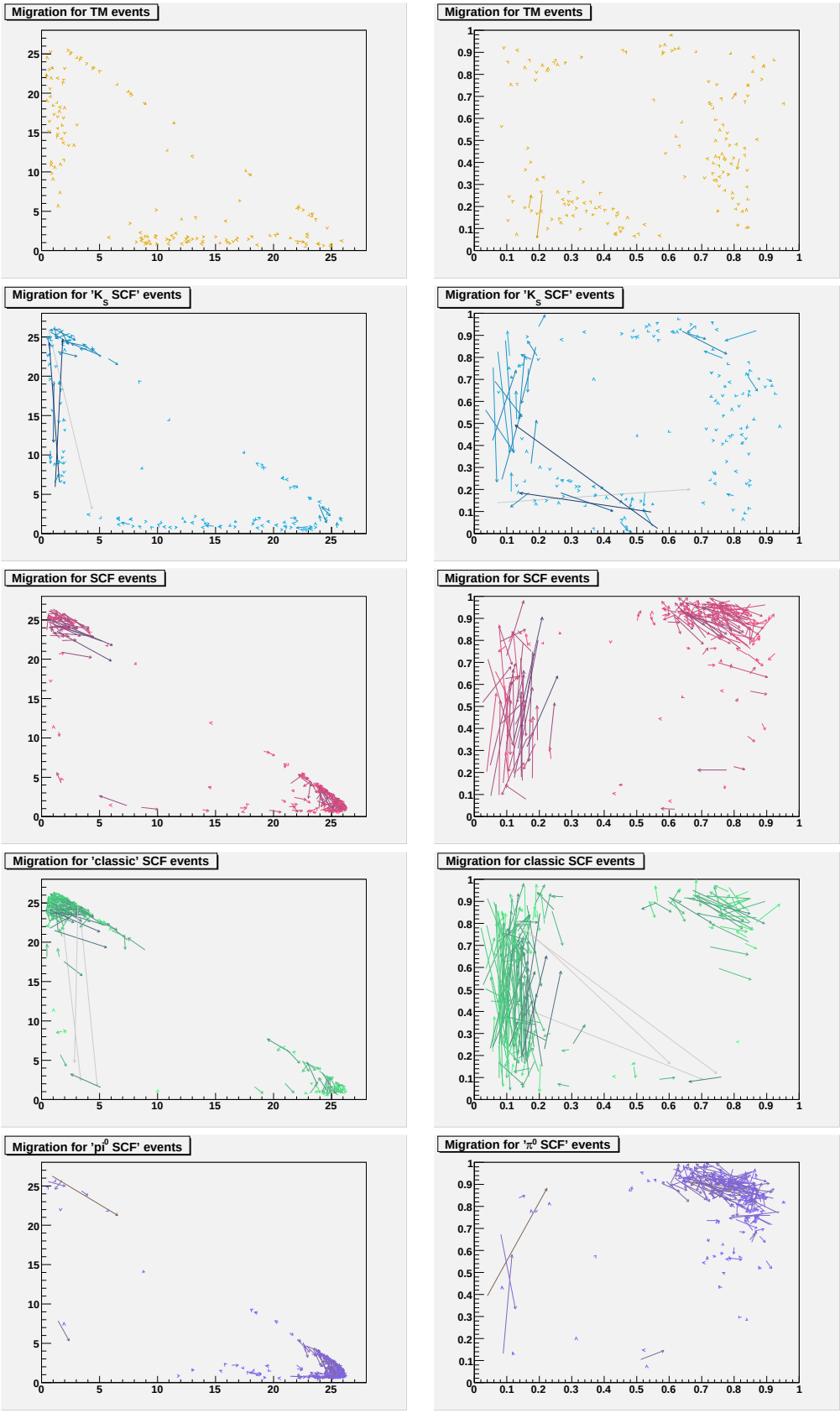

Figure 4.6: Arrows Dalitz plot (left: normal, right: square) for TM and SCF categories (True, Classic, π^0 and K_S).

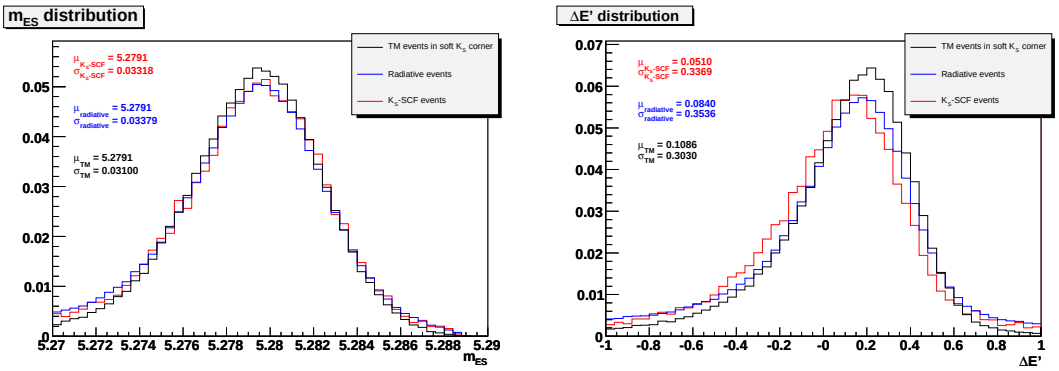

Figure 4.7: m_{ES} (left) and $\Delta E'$ (right) distributions for K_S-SCF (red), radiative events (blue) and TM events (black) from the soft K_S corner.

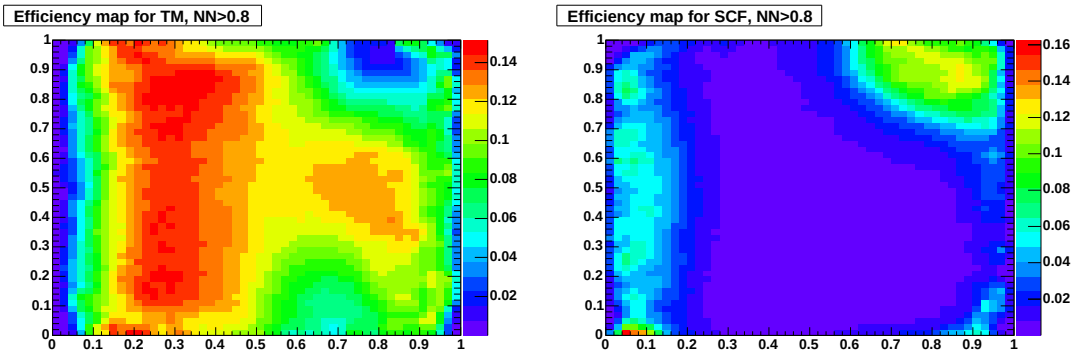

Figure 4.8: Square Dalitz plot distributions of the efficiency for TM (left) and SCF (right) events from the non resonant Monte Carlo. Their sum is the global efficiency $\varepsilon(m'_{ES}, \theta')$.

4.5 Continuum Background

As stated before, in any charmless analysis, the main source of background comes from $e^+e^- \to q\bar{q}$ events ($q = u, s, c, d$). In order to reduce this contamination, we use the different topology of the events: due to the small portion of available phase space, final state particles in a $B\bar{B}$ event are isotropically distributed, while $e^+e^- \to q\bar{q}$ events have a typical jet-like structure. Many variables can be defined to quantify that difference in event shape. Since all of them use the same starting information (particle's flight direction in the $\Upsilon(4S)$ rest frame), they have to be correlated. Because of this, a Multivariate Analyzer technique is usually adopted, in order to define a single variable to be used in selection and fit.

The study pursued to use a Neural Network built with the `TMVA` tool to reject many of the continuum events, as explained in Section 3.3.3.

Studies performed on fast parametrized Monte Carlo toy studies show that, when applying no cut on NN, the fit gives biased results, the signal being drowned in the continuum background. Hence we apply a final cut $NN > 0.8$ in the event selection as already stated. This requirement is applied after the best candidate in the event is chosen, and it was verified that this procedure is not impaired by any correlation between NN and the two variables ($m_{K^0_S}$ and m_{π^0}) being used to select the best candidate. How the efficiency and purity of the selected sample depend on the cut is summarized in Table 4.3 and Table 4.4.

Sample	no cut	$NN > 0.2$	$NN > 0.4$	$NN > 0.6$	$NN > 0.8$
TM efficiency		94.8%	88.0%	78.8%	63.3%
SCF efficiency		92.6%	83.7%	72.4%	54.7%
Continuum efficiency		36.0%	19.1%	10.1%	3.8%
Signal / Continuum ratio	0.010	0.026	0.046	0.077	0.163

Table 4.3: Efficiencies for each component for different values of cuts applied on NN. The signal efficiencies are evaluated by using the signal Dalitz model.

In order to use NN as a fit observable, we apply a mapping $NN \to NN'$ to smooth the peaks shown in Figure 3.4 and obtain gaussian-like distributions. The method [64],

Sample	no cut on NN	$NN > 0.2$	$NN > 0.4$	$NN > 0.6$	$NN > 0.8$
N.R.	8.27%	8.08%	7.90%	7.64%	7.19%
signal model	22.83%	22.23%	21.65%	20.86%	19.48%

Table 4.4: Fraction of SCF depending on cut applied on NN, evaluated on different Monte Carlo samples.

uses the reciprocal function of the sigmoid function[2]:

$$NN' = log\left(\frac{\frac{NN-NN_{\text{min}}}{NN_{\text{max}}-NN_{\text{min}}}}{1-\frac{NN-NN_{\text{min}}}{NN_{\text{max}}-NN_{\text{min}}}}\right) = log\left(\frac{NN-NN_{\text{min}}}{NN_{\text{max}}-NN}\right) \tag{4.3}$$

with $NN_{\text{min}} = 0.2$, low enough to keep a sufficient number of offpeak events to build a PDF and $NN_{\text{max}} = 1.03$, above the highest value seen in data and MC. We study the correlations that need to be controlled. The input variables to the Neural Network were chosen to avoid correlations with the Dalitz variables for signal events. In contrast, some of them are correlated with the Dalitz plot for the continuum background events and NN' depends on the variable

$$\Delta_{\text{Dalitz}} \equiv \min\left(\sqrt{m^2_{K^0_S\pi^+} - m^2_{K^0_S\pi^+,\text{min}}}, \sqrt{m^2_{K^0_S\pi^0} - m^2_{K^0_S\pi^0,\text{min}}}, \sqrt{m^2_{\pi^+\pi^0} - m^2_{\pi^+\pi^0,\text{min}}}\right). \tag{4.4}$$

The Dalitz plot maps of Δ_{Dalitz} are shown on Figure 4.9, and the correlation of NN and NN' with Δ_{Dalitz} on Figure 4.10.

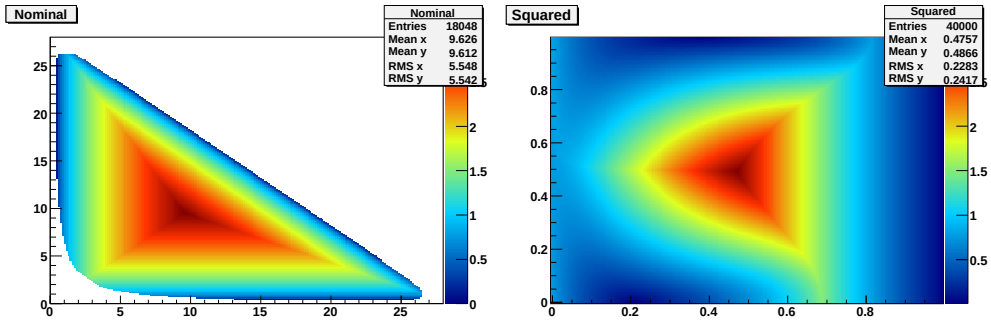

Figure 4.9: Δ_{Dalitz} plots. Left: classic Dalitz plot. Right: square Dalitz plot.

[2] $f(x) = \log(x/(1-x))$

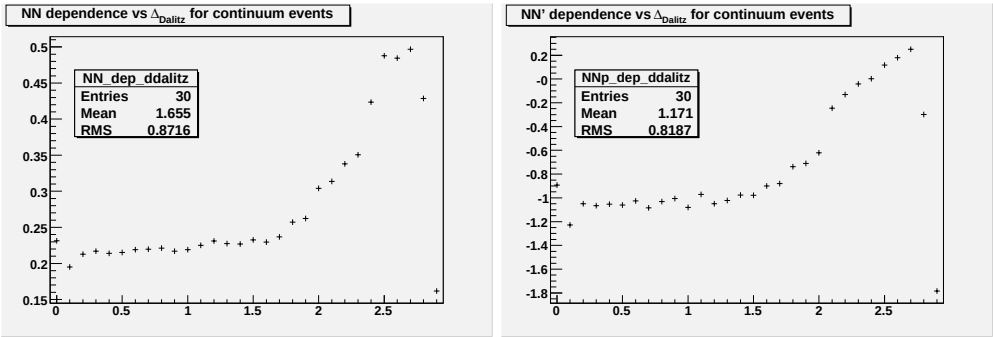

Figure 4.10: NN and NN' versus Δ_{Dalitz} Continuum plots.

4.6 $B\bar{B}$ background

Since no invariant mass cuts ("vetoes") are being applied on the Dalitz plot, and because of the presence of a π^0, the decay $B^+ \to K^0_S\pi^+\pi^0$ suffers from large cross-feed from other charmed and charmless B decays. Some of these B background modes have unknown branching fractions. Moreover, they can exhibit CP-violating asymmetries. We study the cross-feed from other Bdecays using MC simulation.

The strategy followed in this analysis aims at classifying B-background events in a small number of classes which exhibit similar behavior in the distributions of the variables being used in the fit.

We classify the B background modes according to their multplicity (two-, three- and four-body final states), and to the reason of misreconstructing the decay. Separate PDFs are built for each of these classes. The features of these PDFs differ significantly due to the rather different decay kinematics of the modes included in each of background classes.

4.6.1 Determination of B background modes

B background modes are identified by means of the study of B^+B^- and $B\bar{B}$ generic Monte Carlo samples (respectively 574.7×10^6 and 567.3×10^6, of generated events). The result of the study is presented in Tables 4.5 and 4.6. The branching fractions have been taken from either the PDG [40], HFAG [29] or the generation values in the *BABAR* Monte Carlo [50]. In the latter case the numerical value of the uncertainty on the branching

fraction is taken to be the same as that of the central value.

Decay mode	Efficiency	Branching fraction	Expected number of events
$D^0\pi^+$	$(1.432 \pm 0.016) \times 10^{-3}$	$(4.84 \pm 0.15) \times 10^{-3}$	2655 ± 92
$\bar{D}^{*0}\pi^+$	$(3.8 \pm 0.09) \times 10^{-4}$	$(5.19 \pm 0.26) \times 10^{-3}$	759 ± 42
$\bar{D}^0\rho^+$	$(9.3 \pm 0.3) \times 10^{-5}$	$(1.34 \pm 0.18) \times 10^{-2}$	477 ± 66
$\bar{D}^{*0}\rho^+$	$(9.9 \pm 0.9) \times 10^{-6}$	$(9.8 \pm 1.7) \times 10^{-3}$	37 ± 7
$\bar{D}^0K^+$	$(1.32 \pm 0.17) \times 10^{-4}$	$(4.02 \pm 0.21) \times 10^{-4}$	20 ± 3
$\bar{D}^{*0}K^+$	$(1.7 \pm 0.6) \times 10^{-5}$	$(4.16 \pm 0.33) \times 10^{-4}$	2.7 ± 1.0
$\bar{D}^0\nu_\mu\mu^+$	$(9.7 \pm 1.9) \times 10^{-7}$	$(2.15 \pm 0.22) \times 10^{-2}$	8.0 ± 1.8
$\bar{D}^{*0}\nu_\mu\mu^+$	$(1.6 \pm 0.5) \times 10^{-7}$	$(5.29 \pm 0.19) \times 10^{-2}$	3.1 ± 1.0
$\bar{D}_0^{*0}\pi^+$	$(2.5 \pm 0.5) \times 10^{-5}$	$(6.1 \pm 1.9) \times 10^{-4}$	5.8 ± 2.1
$\bar{D}_2^{*0}\pi^+$	$(8.7 \pm 3.0) \times 10^{-6}$	$(3.4 \pm 0.8) \times 10^{-4}$	1.1 ± 0.5
$D_s\pi^0$	$(9.6 \pm 2.0) \times 10^{-4}$	$(1.6 \pm 0.5) \times 10^{-5}$	5.9 ± 2.2
$\bar{D}^0\pi^+\pi^0$	$(1.0 \pm 0.4) \times 10^{-5}$	$(5.0 \pm 5.0) \times 10^{-4}$	2.0 ± 0.8
$X_{su}\gamma$	$(3.3 \pm 0.3) \times 10^{-4}$	$(3.55 \pm 0.29) \times 10^{-4}$	45 ± 6
$K^{*+}\gamma$	$(2.20 \pm 0.22) \times 10^{-3}$	$(4.03 \pm 0.26) \times 10^{-5}$	34 ± 4
$K^0\pi^+$	$(2.25 \pm 0.29) \times 10^{-3}$	$(2.31 \pm 0.10) \times 10^{-5}$	20 ± 3
$a_1^+K^0$	$(3.4 \pm 0.5) \times 10^{-3}$	$(3.49 \pm 3.49) \times 10^{-5}$	45 ± 45
$a_1^+\pi^0$	$(6.3 \pm 1.2) \times 10^{-4}$	$(2.64 \pm 2.64) \times 10^{-5}$	6.4 ± 6.4
$a_1^0\pi^+$	$(2.8 \pm 0.8) \times 10^{-4}$	$(2.04 \pm 0.58) \times 10^{-5}$	2.2 ± 0.8
$a_1^+\bar{D}^0$	$(1.7 \pm 0.4) \times 10^{-6}$	$(4.0 \pm 4.0) \times 10^{-3}$	2.6 ± 2.6
$K^{*+}f_0$	$(1.6 \pm 0.4) \times 10^{-3}$	$(5.2 \pm 1.3) \times 10^{-6}$	3.2 ± 1.0
$K_0^*(1430)^+\bar{K}^0$	$(7.4 \pm 1.8) \times 10^{-3}$	$(2.0 \pm 2.0) \times 10^{-6}$	5.7 ± 5.7
$K^{*+}\bar{K}^0$	$(5.2 \pm 1.2) \times 10^{-3}$	$(3.0 \pm 3.0) \times 10^{-6}$	6 ± 6
$K^+\pi^0$	$(8.7 \pm 2.7) \times 10^{-3}$	$(1.0 \pm 1.0) \times 10^{-6}$	3.3 ± 3.3
$K^0\rho^+\pi^0$	$(2.6 \pm 0.5) \times 10^{-3}$	$(1.0 \pm 1.0) \times 10^{-5}$	10 ± 10
$K^{*0}\rho^+$	$(1.9 \pm 0.4) \times 10^{-3}$	$(9.2 \pm 1.6) \times 10^{-6}$	6.7 ± 1.9
$K^{*+}\rho^0$	$(9.5 \pm 2.9) \times 10^{-4}$	$(6.1 \pm 6.1) \times 10^{-6}$	2.2 ± 2.2
$\pi^+\pi^0\pi^0$	$(7.7 \pm 1.6) \times 10^{-4}$	$(2.6 \pm 2.6) \times 10^{-5}$	7.7 ± 7.7
$K^{*0}\pi^+\pi^0$	$(1.5 \pm 0.4) \times 10^{-3}$	$(1.0 \pm 1.0) \times 10^{-5}$	5.7 ± 5.7
$\rho^+\rho^0$	$(7.5 \pm 2.1) \times 10^{-4}$	$(1.82 \pm 0.20) \times 10^{-5}$	5.3 ± 1.6
$\rho^+\pi^0$	$(7.3 \pm 2.3) \times 10^{-4}$	$(1.09 \pm 0.15) \times 10^{-5}$	3.0 ± 1.0
$K^0\pi^+\pi^0\pi^0$	$(1.04 \pm 0.30) \times 10^{-3}$	$(1.0 \pm 1.0) \times 10^{-5}$	4.0 ± 4.0
$K^0\bar{K}^0K^+$	$(1.1 \pm 0.4) \times 10^{-4}$	$(4.60 \pm 0.52) \times 10^{-5}$	1.9 ± 0.8
Small contribution modes	-	-	133.0
TOTAL EXPECTED			4331.2

Table 4.5: Background modes found in B^+B^- Monte Carlo (574.7×10^6 of generated events).

For each event, the true B mesons that give birth to each of the reconstructed daughters are looked for. These may not be the same for the three particles that make up the B candidate. The decay mode of the B meson that contributes the highest number of reconstructed daughters to the B candidate is taken to be the decay channel that causes this particular background event. Down in the tables we have the "Small contribution

Decay mode	Efficiency	Branching fraction	Expected number of events
$D^-\rho^+$	$(1.71 \pm 0.04) \times 10^{-4}$	$(7.5 \pm 1.2) \times 10^{-3}$	490 ± 80
$D^{*-}\rho^+$	$(7.7 \pm 1.0) \times 10^{-6}$	$(6.8 \pm 0.9) \times 10^{-3}$	20 ± 4
$\bar{D}^0\rho^0$	$(1.3 \pm 0.2) \times 10^{-4}$	$(2.9 \pm 1.1) \times 10^{-4}$	15 ± 6
$D^-\pi^+$	$(3.87 \pm 0.11) \times 10^{-4}$	$(2.68 \pm 0.13) \times 10^{-3}$	397 ± 23
$D^{*-}\pi^+$	$(1.84 \pm 0.08) \times 10^{-4}$	$(2.62 \pm 0.13) \times 10^{-3}$	185 ± 12
$D_0^{*-}\pi^+$	$(3.1 \pm 1.2) \times 10^{-5}$	$(2.0 \pm 2.0) \times 10^{-4}$	2.4 ± 2.4
$\bar{D}^0\pi^0$	$(4.7 \pm 0.4) \times 10^{-4}$	$(2.61 \pm 0.24) \times 10^{-4}$	46.8 ± 5.7
$\bar{D}^{*0}\pi^0$	$(1.57 \pm 0.22) \times 10^{-4}$	$(1.7 \pm 0.4) \times 10^{-4}$	10.2 ± 2.8
$\eta_c K_S^0$	$(8.5 \pm 1.1) \times 10^{-5}$	$(5.0 \pm 1.0) \times 10^{-4}$	16.3 ± 3.9
$\eta_c(2S)K_S^0$	$(5.1 \pm 1.4) \times 10^{-5}$	$(2.4 \pm 2.4) \times 10^{-4}$	4.7 ± 4.7
$J/\psi K_S^0$	$(6.2 \pm 1.1) \times 10^{-5}$	$(4.36 \pm 0.17) \times 10^{-4}$	10.4 ± 1.9
$\chi_{c0}K_S^0$	$(6.3 \pm 2.0) \times 10^{-5}$	$(1.4 \pm 1.4) \times 10^{-4}$	3.4 ± 3.4
$\chi_{c1}K_S^0$	$(4.6 \pm 1.3) \times 10^{-5}$	$(1.95 \pm 0.20) \times 10^{-4}$	3.4 ± 1.1
$D^-\nu_\mu\mu^+$	$(4.7 \pm 1.4) \times 10^{-7}$	$(2.08 \pm 0.18) \times 10^{-2}$	3.7 ± 1.2
$D^{*-}\nu_\mu\mu^+$	$(1.4 \pm 0.5) \times 10^{-7}$	$(5.29 \pm 0.19) \times 10^{-2}$	3.1 ± 1.0
$D_0^{*-}\nu_\mu\mu^+$	$(2.6 \pm 0.7) \times 10^{-6}$	$(4.5 \pm 4.5) \times 10^{-3}$	4.4 ± 4.4
$D_0^{*-}\nu_e e^+$	$(4.5 \pm 0.9) \times 10^{-6}$	$(4.5 \pm 4.5) \times 10^{-3}$	7.8 ± 7.8
$D_2^{*-}\pi^+$	$(1.2 \pm 0.3) \times 10^{-5}$	$(9.0 \pm 9.0) \times 10^{-4}$	4.1 ± 4.1
$D^-\pi^+\pi^0$	$(1.4 \pm 0.5) \times 10^{-5}$	$(5.0 \pm 5.0) \times 10^{-4}$	2.7 ± 2.7
D^-K^+	$(4.0 \pm 1.3) \times 10^{-5}$	$(2.0 \pm 0.6) \times 10^{-4}$	3.0 ± 1.4
$\bar{D}^0\bar{K}^0$	$(2.0 \pm 0.6) \times 10^{-4}$	$(5.2 \pm 0.7) \times 10^{-5}$	4.0 ± 1.4
$\eta' K_S^0$	$(2.15 \pm 0.24) \times 10^{-3}$	$(3.25 \pm 0.16) \times 10^{-5}$	26.7 ± 3.3
$f_0 K_S^0$	$(8.1 \pm 1.1) \times 10^{-3}$	$(5.8 \pm 0.9) \times 10^{-6}$	18.0 ± 3.7
$\rho^0 K_S^0$	$(4.6 \pm 0.4) \times 10^{-2}$	$(2.7 \pm 0.5) \times 10^{-6}$	48 ± 10
$K^{*+}\rho^-$	$(4.5 \pm 0.4) \times 10^{-3}$	$(1.2 \pm 1.2) \times 10^{-5}$	20 ± 20
$K_0^*(1430)^+\rho^-$	$(1.28 \pm 0.24) \times 10^{-3}$	$(2.0 \pm 2.0) \times 10^{-5}$	9.8 ± 9.8
$K^{*0}\rho^0$	$(1.2 \pm 0.3) \times 10^{-3}$	$(5.6 \pm 1.6) \times 10^{-6}$	2.7 ± 1.0
$\rho^+ K^0\pi^-$	$(1.9 \pm 0.4) \times 10^{-3}$	$(1.0 \pm 1.0) \times 10^{-5}$	7.1 ± 7.1
$\rho^- K^0\pi^+$	$(1.4 \pm 0.4) \times 10^{-3}$	$(1.0 \pm 1.0) \times 10^{-5}$	5.4 ± 5.4
$\rho^0 K^0\pi^0$	$(2.6 \pm 0.7) \times 10^{-3}$	$(5.0 \pm 5.0) \times 10^{-6}$	5.1 ± 5.1
$\rho^+\rho^-$	$(2.6 \pm 0.9) \times 10^{-4}$	$(2.42 \pm 0.31) \times 10^{-5}$	2.5 ± 0.9
$a_1^0 K^0$	$(7.0 \pm 0.8) \times 10^{-3}$	$(7.0 \pm 7.0) \times 10^{-6}$	18.7 ± 18.7
$a_1^+\pi^-$	$(2.4 \pm 0.5) \times 10^{-4}$	$(3.17 \pm 0.37) \times 10^{-5}$	2.9 ± 0.7
$a_1^+ D^-$	$(1.8 \pm 0.4) \times 10^{-6}$	$(6.0 \pm 3.3) \times 10^{-3}$	4.1 ± 2.5
$K^0\pi^0$	$(6.1 \pm 0.7) \times 10^{-3}$	$(9.9 \pm 0.6) \times 10^{-6}$	23.1 ± 2.9
$K^{*+}\pi^-$	$(8.5 \pm 0.8) \times 10^{-3}$	$(9.8 \pm 1.1) \times 10^{-6}$	32 ± 5
$K^0\pi^+\pi^-$	$(2.44 \pm 0.29) \times 10^{-3}$	$(3.1 \pm 1.0) \times 10^{-6}$	2.9 ± 1.0
$K^{*0}\pi^0$	$(5.2 \pm 1.6) \times 10^{-3}$	$(0.4 \pm 1.3) \times 10^{-7}$	0.8 ± 0.8
$K^{*+}\pi^-\pi^0$	$(1.4 \pm 0.4) \times 10^{-3}$	$(1.0 \pm 1.0) \times 10^{-5}$	5.4 ± 5.4
$K^{*0}\bar{K}^0$	$(1.8 \pm 0.7) \times 10^{-3}$	$(1.9 \pm 1.9) \times 10^{-6}$	1.3 ± 1.3
$K^0\bar{K}^0\pi^0$	$(1.3 \pm 0.8) \times 10^{-3}$	$(2.0 \pm 2.0) \times 10^{-6}$	1.0 ± 1.0
ϕK_S^0	$(3.1 \pm 0.8) \times 10^{-3}$	$(4.2 \pm 0.5) \times 10^{-6}$	5.1 ± 1.4
$K_S^0 K_S^0$	$(2.8 \pm 0.6) \times 10^{-2}$	$(4.8 \pm 1.0) \times 10^{-7}$	5.1 ± 1.6
$\pi^+\pi^-\pi^0$	$(6.2 \pm 1.5) \times 10^{-4}$	$(2.4 \pm 2.4) \times 10^{-5}$	5.7 ± 5.7
$X_{sd}\gamma$	$(7.1 \pm 1.4) \times 10^{-5}$	$(3.55 \pm 0.29) \times 10^{-4}$	9.6 ± 2.1
Small contribution modes	-	-	147.5
TOTAL EXPECTED			1651.6

Table 4.6: Background modes found in $B^0\bar{B}^0$ Monte Carlo (567.3×10^6 of generated events).

Decay mode	Category #1	Category #2	Category #3	Category #4	Category #5	Category #6	Category #7
$\bar{D}^0\pi^+$	0	0	198 (2.4%)	7 (0%)	1 (0%)	309 (3.8%)	270 (3.3%)
$\bar{D}^{*0}\pi^+$	817 (40.5%)	0	24 (1.2%)	4 (0.2%)	660 (32.7%)	164 (8.1%)	349 (17.3%)
$\bar{D}^0\rho^+$	745 (52%)	0	27 (2%)	0	0	435 (30%)	225 (16%)
$\bar{D}^{*0}\rho^+$	13 (12%)	0	2 (2%)	0	0	81 (72%)	16 (14%)
$\bar{D}^0K^+$	0	0	0	0	50 (81%)	4 (6%)	8 (13%)
$\bar{D}^0\nu_\mu\mu^+$	12 (48%)	0	0	0	0	6 (24%)	7 (28%)
$X_{su}\gamma$	0	0	9 (7.5%)	4 (3%)	0	106 (89%)	0
$K^{*+}\gamma$	0	0	0	12 (12%)	0	90 (88%)	0
$K^0\pi^+$	0	0	0	26 (42%)	0	36 (58%)	0
$a_1^+K^0$	0	0	16 (41%)	0	0	23 (59%)	0
$a_1^+\pi^0$	0	0	4 (14%)	0	0	24 (86%)	0
$D^-\rho^+$	0	959 (64.3%)	112 (7.5%)	0	0	419 (28.2%)	0
$D^{*-}\rho^+$	0	3 (5%)	15 (25%)	0	0	40 (68%)	1 (1%)
$\bar{D}^0\rho^0$	37 (84%)	0	0	0	0	4 (9%)	3 (7%)
$D^-\pi^+$	0	0	452 (36.8%)	0	0	776 (63.2%)	0
$D^{*-}\pi^+$	363 (62%)	0	36 (6%)	0	0	106 (18%)	81 (14%)
$\bar{D}^0\pi^0$	0	0	80 (52%)	0	0	72 (47%)	2 (1%)
$\bar{D}^{*0}\pi^0$	0	0	8 (17%)	0	0	40 (83%)	0
$\eta_cK^0_S$	0	0	52 (90%)	0	0	6 (10%)	0
$J/\psi K^0_S$	0	0	30 (97%)	0	0	1 (3%)	0
$\eta' K^0_S$	1 (1%)	0	35 (45%)	0	0	41 (53%)	1 (1%)
$f_0K^0_S$	0	0	11 (20%)	0	0	44 (80%)	0
$\rho^0K^0_S$	0	0	70 (51.0%)	0	0	63 (46%)	3 (2%)
$K^{*+}\rho^-$	0	0	64 (63%)	0	0	37 (37%)	0
$a_1^0K^0$	0	0	58 (73%)	0	0	21 (27%)	0
$K^0\pi^0$	0	0	8 (10%)	75 (90%)	0	0	0
$K^{*+}\pi^-$	0	0	26 (21%)	0	0	100 (79%)	0
$X_{sd}\gamma$	0	0	8 (32%)	0	0	17 (68%)	0

Table 4.7: Main B background modes followed by the number of events of each of them being used in the making of the PDFs of a given category. Between parentheses, the percentage of that mode that goes into each category.

modes": events in which the Monte Carlo truth information is insufficient to reconstruct the decay chain, together with channel with less than 10 events contributing.

Except for the mode $B^+ \to \bar{D}^0 (\to K_S\pi^0)\,\pi^+$, which is modelled with exclusive MC, the PDFs for the rest of the Bbackground are built from the generics samples. After removing the events from the D mode mentioned above, and the signal events ($\rho^+K_S^0$, $K^*(892)^+\pi^0$, $K^*(892)^0\pi^+$, $K_0^*(1430)^+\pi^0$, $K_0^*(1430)^0\pi^+$ and $K_S^0\pi^+\pi^0$ non-resonant) from the generics samples, the remaining events are classified in different categories, according to whether the reconstructed event shares the kinematical characteristics of a D decay, and to whether all reconstructed particles in the B candidate come from the same B meson or not.

The fractions of events from the most important B background modes that go in each category are presented in Table 4.7. The categories themselves are:

- *Category #0*: $B^+ \to \bar{D}^0\pi^+$ events where the D decays in $K_S^0\pi^0$.
- *Category #1*: the 3 reconstructed daughters come from the same B meson, that has more actual daughters than the 3 forming the B candidate. The event involves a $\bar{D}^0$, $\bar{D}^{*0}$ or D^{*-}. This category is mostly made up by events from $\rho^+\bar{D}^0$, $\bar{D}^{*0}\pi^+$ and $D^{*-}\pi^+$.
- *Category #2*: as in category #1, except that D^+ decays are involved. Mostly $B^0 \to \rho^+D^-$ decays.
- *Category #3*: the 3 reconstructed daughters come from the same B meson, that has more actual daughters than the 3 forming the B candidate. Contrary to the previous categories, distributions don't show narrow peaks around the D mass. This category is mostly made up by Bdecays into $D^-\pi^+$, $\bar{D}^0\pi^0$, $\bar{D}^0\pi^+$, ρ^+D^-, $\rho^0K_S^0$, $K^{*-}\rho^+$ and $\eta_cK_S^0$ decays.
- *Category #4*: 2 of the reconstructed daughters come from a charmless Bdecay mode with two bodies in the final state or a mode with similar kinematics. Mostly made up by Bdecays into $K^0\pi^0$, $K^0\pi^+$, $K^{*-}\gamma$ and $X_{s,u}\gamma$, where $X_{s,u}$ is an inclusive final state containing the charm or lighter quarks, respectively.

- *Category #5*: $B^+ \to \bar{D}^0 h$ decays where the D doesn't decay in $K^0_S\pi^0$, and the 3 reconstructed daughters come from the same B. Mostly made up by decays to $\bar{D}^{*0}\pi^+$ and $\bar{D}^0 K^+$.

- *Category #6*: events in which one of the 3 reconstructed daughters comes from the other B. Mostly made up by events containing a Bdecay into $D^-\pi^+$, $\bar{D}^0\pi^+$, $\rho^+ D^-$, $\rho^+\bar{D}^0$, $\bar{D}^{*0}\pi^+$, $X_{su}\gamma$, $D^{*-}\pi^+$, $K^{*-}\pi^+$, $K^{*-}\gamma$, $\rho^+\bar{D}^{*0}$ or $\rho^0 K^0_S$.

- *Category #7*: events with a D^0 in which the missing D daughters worsen greatly the resolution about the D mass peak. Mostly made up by events from $\bar{D}^0\pi^+$, $D^{*0}\pi^+$, $\rho^+\bar{D}^0$ and $D^{*-}\pi^+$.

The distributions of m_{ES}, $\Delta E'$ and NN' as well as in the Dalitz plot for categories from #1 to #7 are shown respectively in Figure 4.11 and Figure 4.12. After proper normalization, they represent the PDFs used in the fit (Section 4.8) for the B-background components. Background classes #3 and #6 presents scattered points in the Dalitz plot and were furthermore smeared with an algorithm averaging among nearest neighbor points. The Dalitz plot-PDF for class #4 is smoothed using two dimensional histogram.

The expected yields for each background class are reported in Table 4.8.

Category #	Expected yield
0	2425
1	726
2	322
3	593
4	46
5	267
6	1266
7	366

Table 4.8: B-backgrounds expected yields by category.

4.7 Control sample

The decay $B^+ \to \bar{D}^0\pi^+$ ($\bar{D}^0 \to K^0_S\pi^0$) is both Cabibbo and color allowed. Since the final state involves the same particles as in the signal case, this mode represents a large irreducible background. We expect about 3000 such events in the selected sample. This

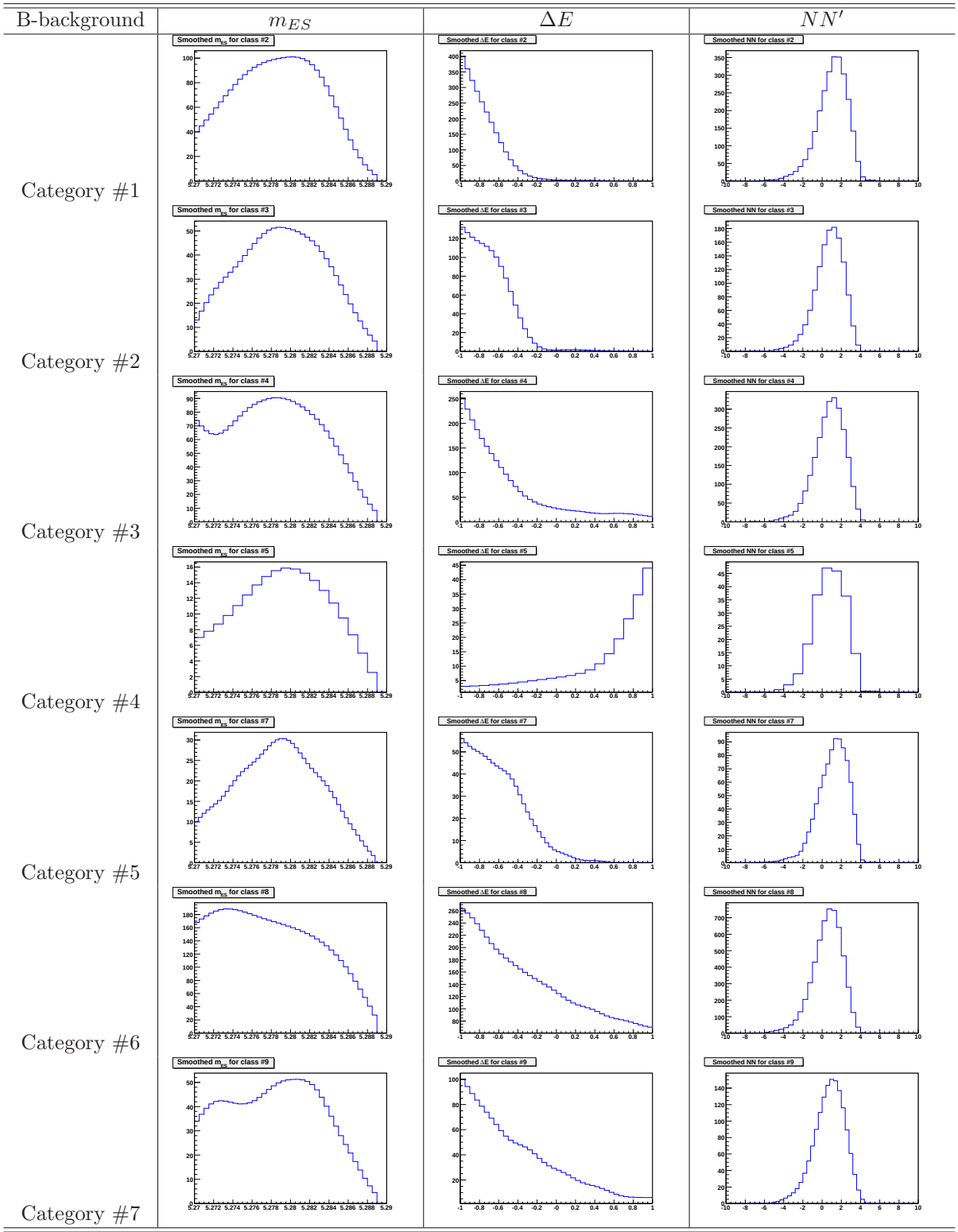

Figure 4.11: m_{ES}, ΔE and NN' plots for the B-backgrounds categories.

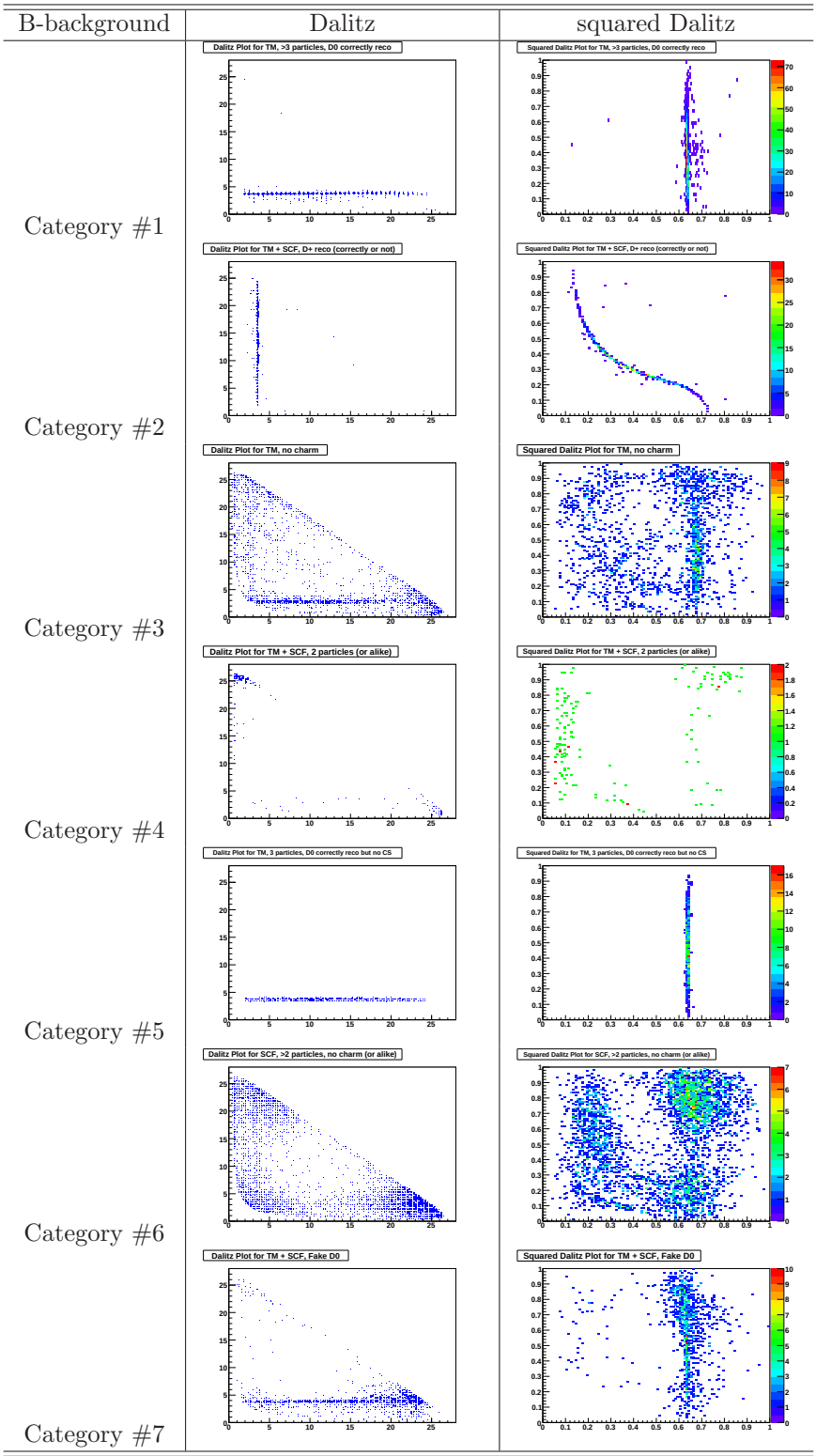

Figure 4.12: Dalitz plot distributions (left: classic; right: square) for the B-backgrounds categories.

background does not interfere since the $\bar{D}^0$ decays far away with respect to the K_S. To restrict to charmless events only, we could veto this channel by cutting on the $K^0_S\pi^0$ invariant mass around the $\bar{D}^0$ mass. We prefer to keep these events for several reasons. They can stabilize the fit by providing accurate determinations of PDF parameters from a kinematically constrained source of events. We therefore include this channel as class #0 of the B-background. Extreme care is to be taken to model the relative PDFs since this component is abundant.

4.7.1 $\bar{D}^0$ shape in the Dalitz plot

Figure 4.13 shows how this channel populates the Dalitz plot. The resolution on the $\bar{D}^0$ mass depends on the energy of the π^0. It is wider in the soft π^0 corner, a place where SCF prevails ($f^{\bar{D}^0}_{SCF} = 10.9\%$ on average) as can be seen on Figure 4.14. The $\bar{D}^0$ invariant mass peak widens as slices closer to the soft π^0 corner (high θ') are looked at. These features

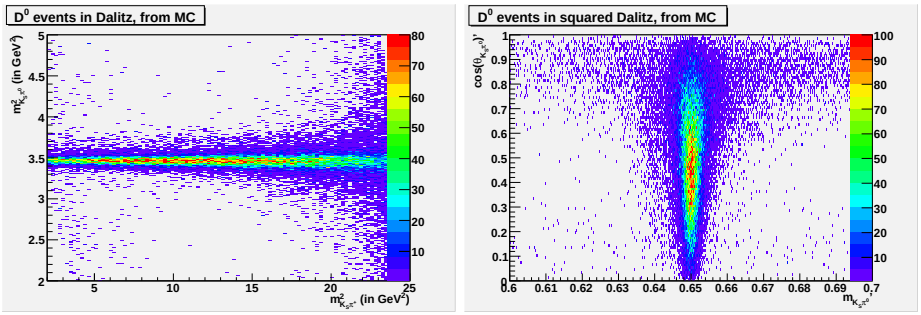

Figure 4.13: Dalitz plots for D^0. Left: classic Dalitz plot; right: square Dalitz plot.

are accommodated by a PDF summing the TM and SCF contributions. The TM term is the product of a θ' PDF by an m' PDF which is the sum of a gaussian and a Breit Wigner, both θ'-dependent. The TM θ' PDF consist of a 6th-order polynomial in θ'. The SCF PDF is a smoothed histogram (see Figure 4.15 and 4.16).

The other PDFs (for m'_{ES}, $\Delta E'$ and NN') are those of the signal. They thus can constrain the fit when some of their parameters are left free to vary. Figure 4.17 shows that the m'_{ES} and $\Delta E'$ $\bar{D}^0$ PDF are the same as the signal, the latter being compared in the relevant $\mathrm{m}_{K^0_S\pi^0} = \mathrm{m}_{\bar{D}^0}$ region.

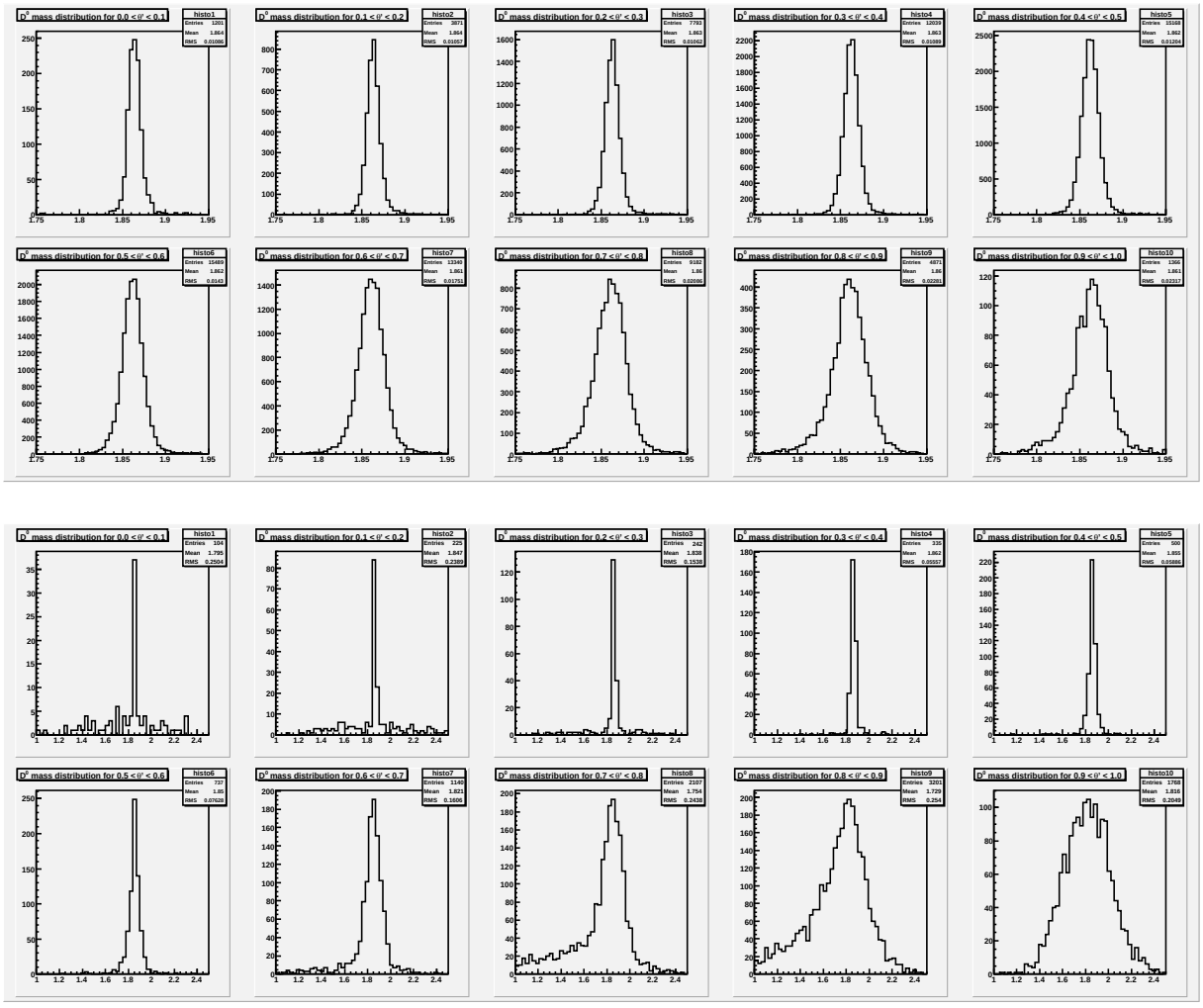

Figure 4.14: $\bar{D}^0$ invariant mass distributions for TM (bottom two rows) and SCF (top two rows) in θ' slices. Notice the different x-axis scales for the two groups of plots. The slices are, from top left to bottom right of each group: $0 < \theta' < 0.1$, $0.1 < \theta' < 0.2$, $0.2 < \theta' < 0.3$, $0.3 < \theta' < 0.4$, $0.4 < \theta' < 0.5$, $0.5 < \theta' < 0.6$, $0.6 < \theta' < 0.7$, $0.7 < \theta' < 0.8$, $0.8 < \theta' < 9.1$ and $0.9 < \theta' < 1$.

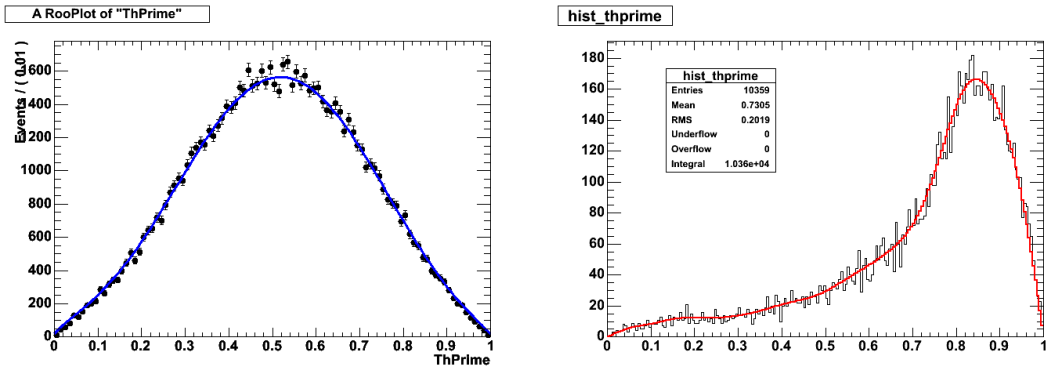

Figure 4.15: θ' distributions (points/histogram) and resulting PDFs (lines) for $B^+ \to \bar{D}^0\pi^+$ TM (left) and SCF (right) MC events.

4.7.2 $B^+ \to \bar{D}^0(\to K^0_S\pi^0)\pi^+$ used as control sample

To compare the PDFs on data and MC, a specific full Montecarlo sample has been used. For on-peak data, $\bar{D}^0$ candidates are required to be within 3σ of the $\bar{D}^0$ mass. In addition we require $NN > 0.8$ and $m^2_{K^0_S\pi^+} < 20\,\mathrm{GeV}/c^2$ in order to avoid the soft π^0 corner of the Dalitz plot. A 2-dimensional fit in the $(m'_{ES}, \Delta E')$ plane is performed, by using a double gaussian for m_{ES} and the sum of a gaussian and a bifurcated gaussian[3] for $\Delta E'$. The projections of the fit to the MC and data are shown in Figures 4.18 and 4.19.

Table 4.9 show the fitted parameters (the means μ and the widths σ of the double gaussian, and the bifurcated gaussian) for m_{ES} and $\Delta E'$, and the resulting differences between MC and on-peak data, in terms of bias and relative ratios. There are some differences between data and MC.

4.8 The total likelihood

We perform an unbinned extended maximum likelihood fit to determine the total $B^+ \to K^0_S\pi^+\pi^0$ event yield, the magnitudes $c_j, \bar{c}_j$ and the phases $\phi_j, \bar{\phi}_j$ of the complex

[3] an asymmetry gaussian distribution with a single mean and two different left and right widths:

$$f(x) = \begin{cases} e^{-\frac{1}{2}(\frac{x-\mu}{\sigma_l})^2} & x \geq \mu \\ e^{-\frac{1}{2}(\frac{x-\mu}{\sigma_r})^2} & x < \mu \end{cases}$$

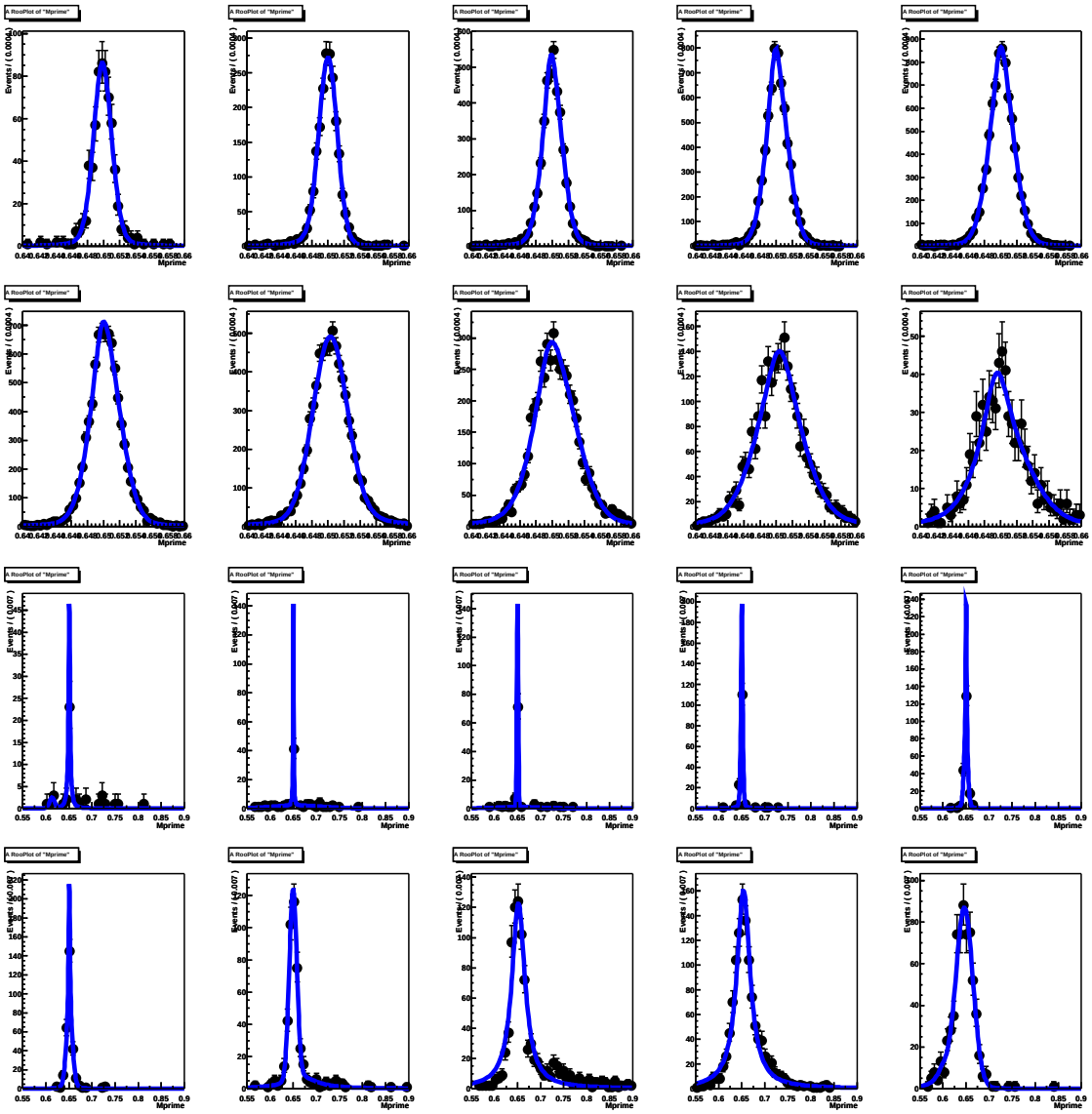

Figure 4.16: m' distributions for TM (top two rows) and SCF (bottom two rows) $B^+ \to \bar{D}^0\pi^+$ events, in the same θ' slices as in Figure 4.14.

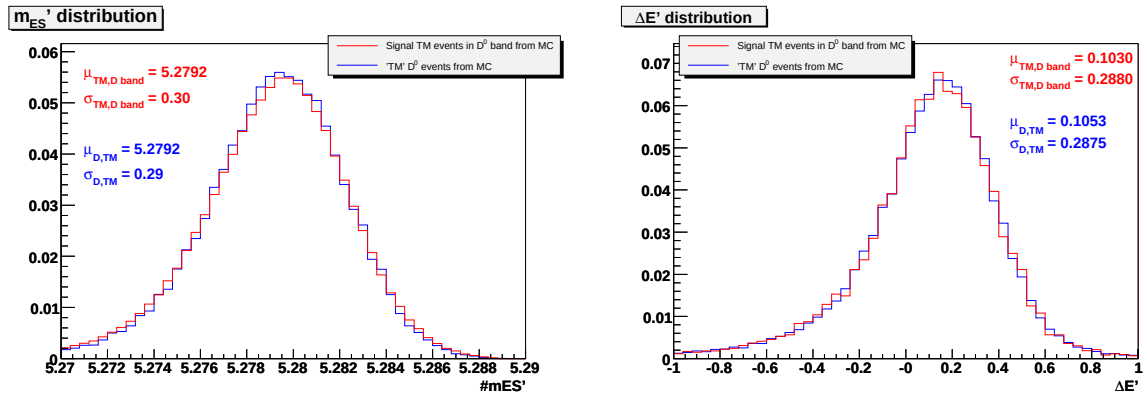

Figure 4.17: m'_{ES} (left) and $\Delta E'$ (right) PDFs for signal MC in the $\bar{D}^0$ band (red) and in $\bar{D}^0$ MC (blue).

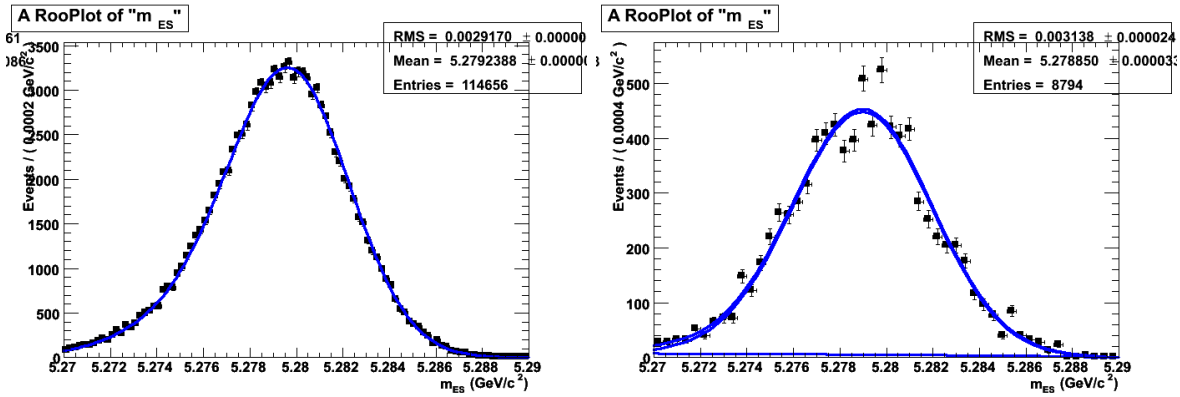

Figure 4.18: m_{ES} distribution for signal MC (left) and on-peak data (right); the fit result is superimposed.

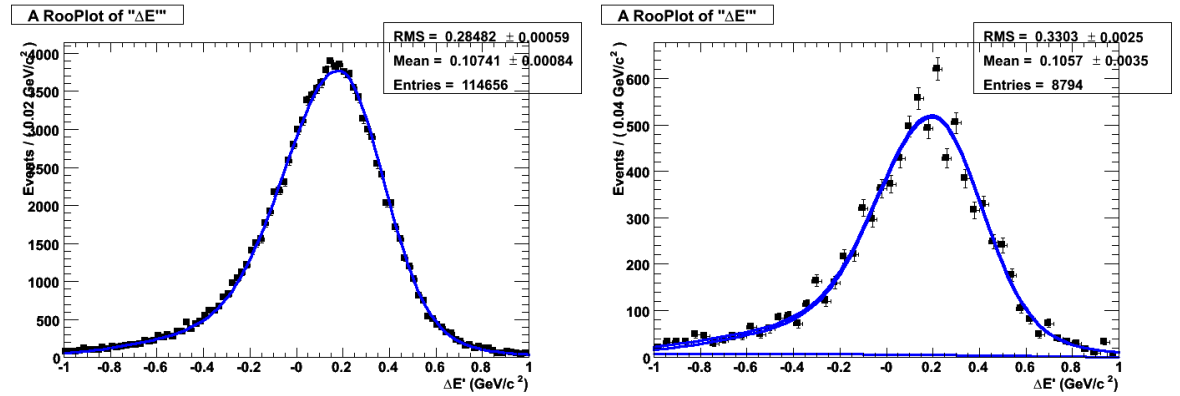

Figure 4.19: $\Delta E'$ distribution for signal MC (left) and on-peak data (right); the fir result is superimposed.

m_{ES}				
Variable	MC Control sample [GeV]	On Peak data [GeV]	data-MC [MeV]	data/MC
μ_1	5.27626 ± 0.00046	5.27381 ± 0.00275	-2.45	
μ_2	5.27980 ± 0.00004	5.27901 ± 0.00005	-0.79	
σ_1	0.00320 ± 0.00014	0.00484 ± 0.00113		1.51
σ_2	0.00255 ± 0.00002	0.00300 ± 0.00004		1.18
fraction	0.16863 ± 0.03050	0.03819 ± 0.01235	-0.13044	
μ_{tot}	5.27920	5.27813	-1.07	
σ_{tot}	0.00401	0.00515		1.28
$\Delta E'$				
Variable	MC Control sample	On Peak data	data-MC	data/MC
μ_1	-0.03977 ± 0.00553	-0.05542 ± 0.02881	0.01565	
μ_2	0.18705 ± 0.00233	0.20448 ± 0.00937	0.01743	
σ_1	0.46313 ± 0.00133	0.51587 ± 0.00484		1.11
σ_{2l}	0.23261 ± 0.00203	0.23490 ± 0.00852		1.01
σ_{2r}	0.18623 ± 0.00184	0.20314 ± 0.00810		1.09
fraction	0.23347 ± 0.00419	0.28748 ± 0.02010	0.05401	
μ_{tot}	0.11409	0.12604	0.01195	
σ_{tot}	0.41474	0.47804		1.15

Table 4.9: Differences between data and signal MC for the fit to D^0 control sample in m_{ES} and $\Delta E'$.

isobar coefficients of the decay amplitude:

$$\mathcal{A}(m^2_{K^0_S\pi^+}, m^2_{K^0_S\pi^0}) = \sum_j c_j e^{i\phi_j} F_j(m^2_{K^0_S\pi^+}, m^2_{K^0_S\pi^0}), \tag{4.5}$$

and similarly for the $B^- \to K^0_S\pi^-\pi^0$ decay:

$$\overline{\mathcal{A}}(m^2_{K^0_S\pi^-}, m^2_{K^0_S\pi^0}) = \sum_j \bar{c}_j e^{i\bar{\phi}_j} F_j(m^2_{K^0_S\pi^-}, m^2_{K^0_S\pi^0}) \tag{4.6}$$

where $F_j(m^2_{K^0_S\pi^\pm}, m^2_{K^0_S\pi^0})$ is the propagator defined in eq. 1.70. The fit uses the variables m'_{ES}, $\Delta E'$, m', θ' and NN', to discriminate signal from background.

4.8.1 The likelihood function

The selected on-resonance data sample is assumed to consist of signal, continuum-background and background due to other B decays. Accordingly the likelihood function of event i is written:

$$\mathcal{L}_i = \mathcal{L}_i^{\text{sig}} + \mathcal{L}_i^{q\bar{q}} + \sum_c \mathcal{L}_{c,i}^{\text{Bbkg}}, \tag{4.7}$$

where the sum over c runs over all the B-background classes listed in Section 4.6. All background likelihood functions have the same expression:

$$\mathcal{L}_i^{\rm bkg} = N^{\rm bkg}\frac{1}{2}(1 - q_i^{\pi}A^{\rm bkg})\mathcal{P}_i^{\rm bkg}, \tag{4.8}$$

where q_i^{π} is the pion charge in event i, and $A^{\rm bkg}$ is the charge asymmetry.

We consider $B^+$and B^-separately to build the signal likelihood function.

$$N^{\rm sig} = N^{\rm sig+} + N^{\rm sig-}, \tag{4.9}$$

$$\mathcal{L}_i^{\rm sig} = \mathcal{L}_i^{\rm sig+} + \mathcal{L}_i^{\rm sig-}. \tag{4.10}$$

Each part has two terms, one for the TM and one for the SCF events:

$$\mathcal{L}_i^{\rm sig+} = \mathcal{L}_i^{\rm TM+} + \mathcal{L}_i^{\rm SCF+} \tag{4.11}$$

$$= N^{\rm sig+}\left[(1 - \bar{f}^{\rm SCF})\mathcal{P}_i^{\rm TM+} + \bar{f}^{\rm SCF}\mathcal{P}_i^{\rm SCF+}\right], \tag{4.12}$$

and similarly for $\mathcal{L}_i^{\rm sig-}$. The fraction $\bar{f}^{\rm SCF}$ of SCF-events averaged over the Dalitz plot, assumed to be the same for both flavors, is discussed below. The fit maximizes the extended likelihood function[4]:

$$\mathcal{L} = e^{-N^{\rm tot}}\prod_{i=1}^{N}\mathcal{L}_i, \tag{4.13}$$

where N is the size of the data sample and $N^{\rm tot} = N^{\rm sig} + N^{q\bar{q}} + \sum_c N_c^{\rm Bbkg}$, is the expected number of events.

The five-dimensional probability density functions (PDF) $\mathcal{P}$ are the products of the four PDFs of the measured discriminating variables $v = \{m', \Delta E', NN', (m', \theta')\}$,

$$\mathcal{P} = \prod_{k=1}^{4}\mathcal{P}(v_k). \tag{4.14}$$

The correlations among the measurements are handled by building conditional PDFs where appropriate (between NN' and the Dalitz variables for the continuum, and between $\Delta E'$ and the Dalitz variables for TM signal events). Systematic uncertainties account for the correlations we neglect.

[4]The canceling factors $1/N^{\rm tot}$ in eq. 4.8 and eq. 4.9, and $N^{\rm tot}$ in eq. 4.13 required for the likelihood functions to be properly normalized have been omitted for simplicity.

A total of 37 parameters are varied in the fit (see Section 4.8.5). A summary of the PDF parametrization is given in Table 4.10. The PDF written in red are the ones for which a Dalitz plot dependence has been handled.

		m_{ES}	$\Delta E'$	NN	Dalitz plot
Signal					
	TM	GG	$BG+G$	$2BG+G$	6 res. DP model
	SCF	SH	SH	$2G+2BG$	6 res. DP model
Continuum		$Argus$	$P2$	$2BG$	2D-SH
B-backgrounds	TM	GG	$BG+G$	$2BG+G$	GG∗$P6$
including:		(same ones as signal)			(different than TM)
$B^{\pm} \to D^0\pi^{\pm}$	SCF	SH	SH	$2G+BG$	GG∗$P6$
$D^0 \to K_s\pi^0$		(same ones as signal)			(different than TM)
Other B-backgrounds		SH	SH	SH	2D-SH

Table 4.10: Summary of the PDFs used. The PDFs written in red are Dalitz plot dependent. SH means smoothed histogram, BG bifurcated gaussian, GG double gaussian, P2 a 2-nd order polynomial function and P6 a 6-th order polynomial function.

4.8.2 Correlations among observables

The TM Dalitz plot maps of the mean and standard deviations are shown

- of the *kinematical variables* m_{ES}, ΔE (a wider cut than in the selection is used $|\Delta E| < 250$ MeV), $\mathrm{m}_{K^0_S}$ and m_{π^0},
- of the *shape variables* L_0, L_2, and NN,
- of the *decay time variables* Δt and $\sigma_{\Delta t}$,

are shown in Figure 4.20, 4.21 and 4.22 respectively. A significant correlation between $\Delta E'$ and the Dalitz plot variables needs to be accounted for in the signal PDF. The shape variables are not correlated with the Dalitz plot for signal, but we have seen a sizeable correlation for the continuum background in Figure 4.10 which has to be dealt with when building the PDF. The time variables show a significant correlation and have not been used in the fit.

In Figure 4.23 we show the correlations between m'_{ES}, $\Delta E'$ and NN. None of them is high enough to require a specific PDF parameterization. The correlation coefficients of the fit observables are summarized in Figure 4.24 for TM, SCF and continuum events.

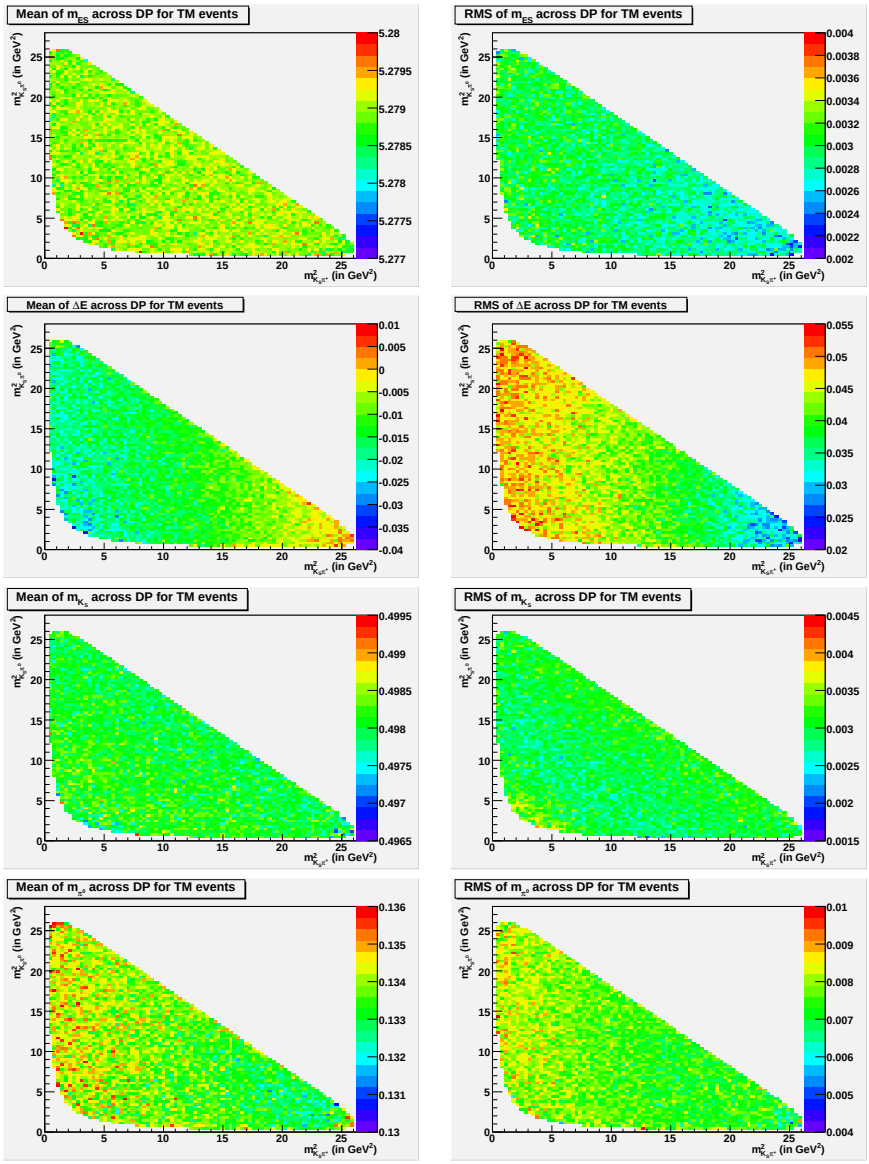

Figure 4.20: Distributions of the mean (left) and standard deviation (right) across the Dalitz plot for: m_{ES} (first row), ΔE (second row), m_{K_S} (third row) and m_{π^0} (fourth row). TM signal events.

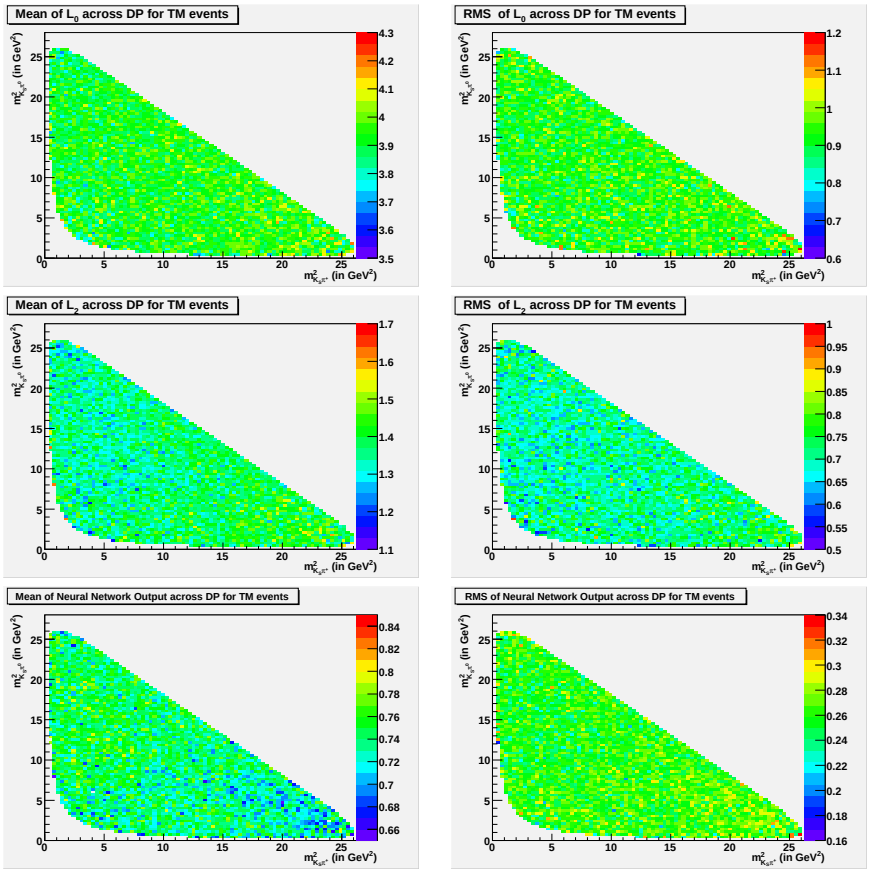

Figure 4.21: Distributions of mean (left) and standard deviation (right) across the Dalitz plot for: L_0 (first row), L_2 (second row) and the Neural Network output (third row). TM signal events.

4.8.3 The Dalitz plot PDFs

The B^+ and B^- Dalitz plots are independent. However, since the backgrounds are similar (and mostly CP-symmetric), we get a more robust procedure by fitting them simultaneously. It is enough to describe only the B^+ Dalitz plot PDF[5]. A change from $\mathcal{A}$ to $\overline{\mathcal{A}}$ gives the B^- PDF.

In the next section we show the PDF for each component (signal and background) of the likelihood function.

[5] We drop the superscript in $\mathcal{P}^+$ in the following.

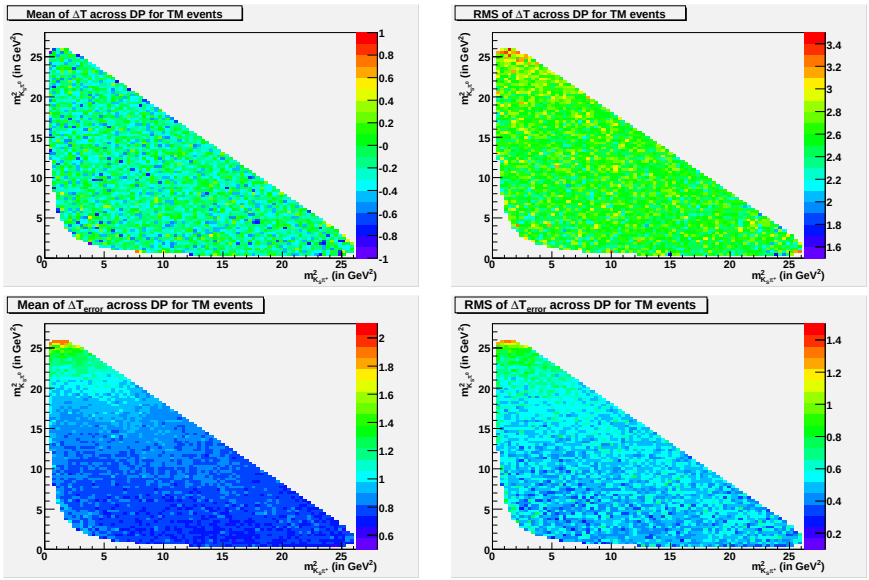

Figure 4.22: Distributions of mean (left) and standard deviation (right) across the Dalitz plot for: Δt (first row)and $\sigma_{\Delta t}$ (second row). TM signal events.

Signal

The signal Dalitz model has been described in Section 1.3. The free parameters are the magnitudes c_j and phases ϕ_j defined, in equations 4.5 and 4.6 for all the intermediate states of the signal model given in the upper part of Table 1.3.

We choose to measure phases relatively to the $K^*(892)^+\pi^0$ final state; the phases of this and its charge conjugate channel are therefore fixed to zero. The amplitude of $B^+ \to K^*(892)^+\pi^0$ is also fixed but not that of $B^- \to K^*(892)^-\pi^0$ in order to be sensitive to direct CP-violation.

The normalization of the component signal PDFs:

$$\mathcal{P}_i^{\mathrm{TM}} \propto \varepsilon_i(1 - f_i^{\mathrm{SCF}})|detJ_i||\mathcal{A}_i|^2, \tag{4.15}$$

$$\mathcal{P}_i^{\mathrm{SCF}} \propto \varepsilon_i f_i^{\mathrm{SCF}} \left[|detJ_i||\mathcal{A}_i|^2 \otimes R_{SCF,i}\right], \tag{4.16}$$

is model dependent, where J is the jacobian matrix of the mapping to the square Dalitz plot (see Section 1.3.7). The symbol $\otimes$ stands for a convolution and the R matrix is described below (eq. 4.21). The normalization requires the computation of the integrals

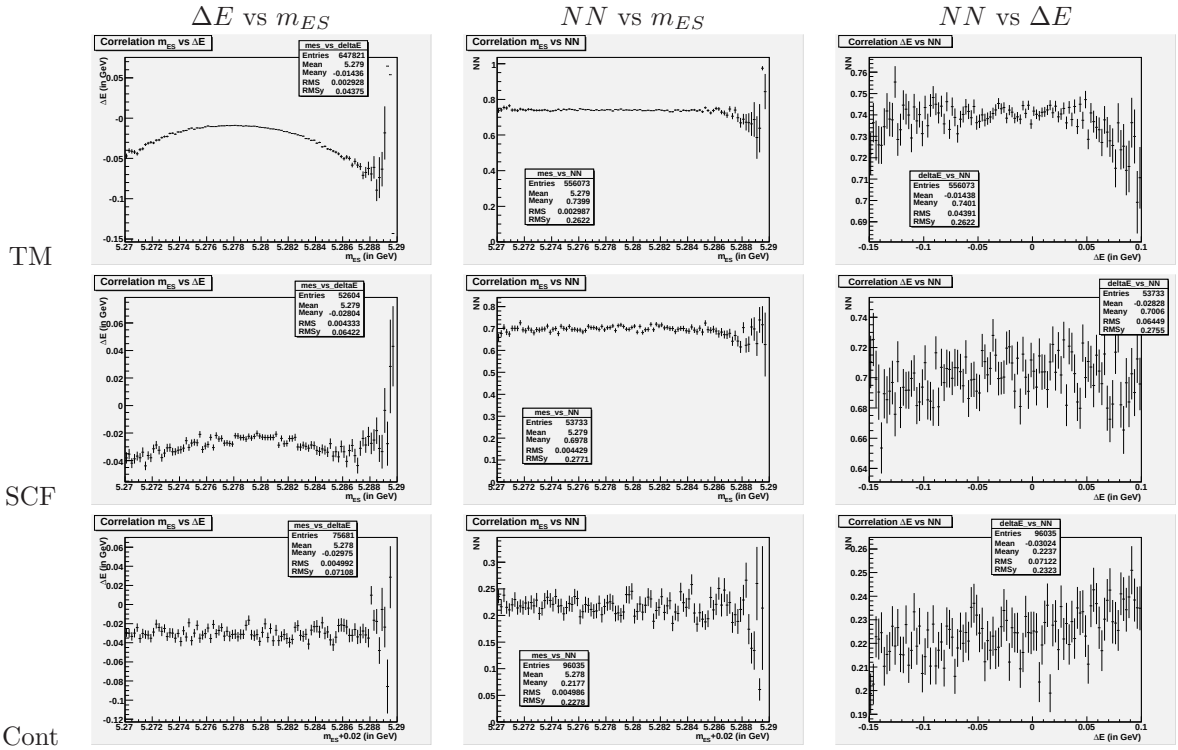

Figure 4.23: Profile plots between m_{ES}, $\Delta E'$ and NN for TM (top), SCF (middle) and Continuum (bottom).

(we drop the i index)

$$\int_0^1 dm' \int_0^1 d\theta' \; \varepsilon(1 - f^{\mathrm{SCF}})|\mathrm{det}J|F_k F_l^*, \tag{4.17}$$

$$\int_0^1 dm' \int_0^1 d\theta' \; \varepsilon f^{\mathrm{SCF}}|\mathrm{det}J|F_k F_l^*, \tag{4.18}$$

and

$$\int_0^1 dm' \int_0^1 d\theta' \; \varepsilon|\mathrm{det}J|F_k F_l^*, \tag{4.19}$$

where the notations of eq. 4.5 are used. The integrations over the square Dalitz plot are performed numerically. The weight

$$\overline{f}^{\mathrm{SCF}} = \frac{\int_0^1 dm' \int_0^1 d\theta' \; \varepsilon f^{\mathrm{SCF}}|\mathrm{det}J||\mathcal{A}|^2}{\int_0^1 dm' \int_0^1 d\theta' \; \varepsilon|\mathrm{det}J||\mathcal{A}|^2} \tag{4.20}$$

in eq. 4.9 ensures that the total signal PDF is normalized. The PDF normalization depends on the decay dynamics and is computed iteratively. In practice the computation

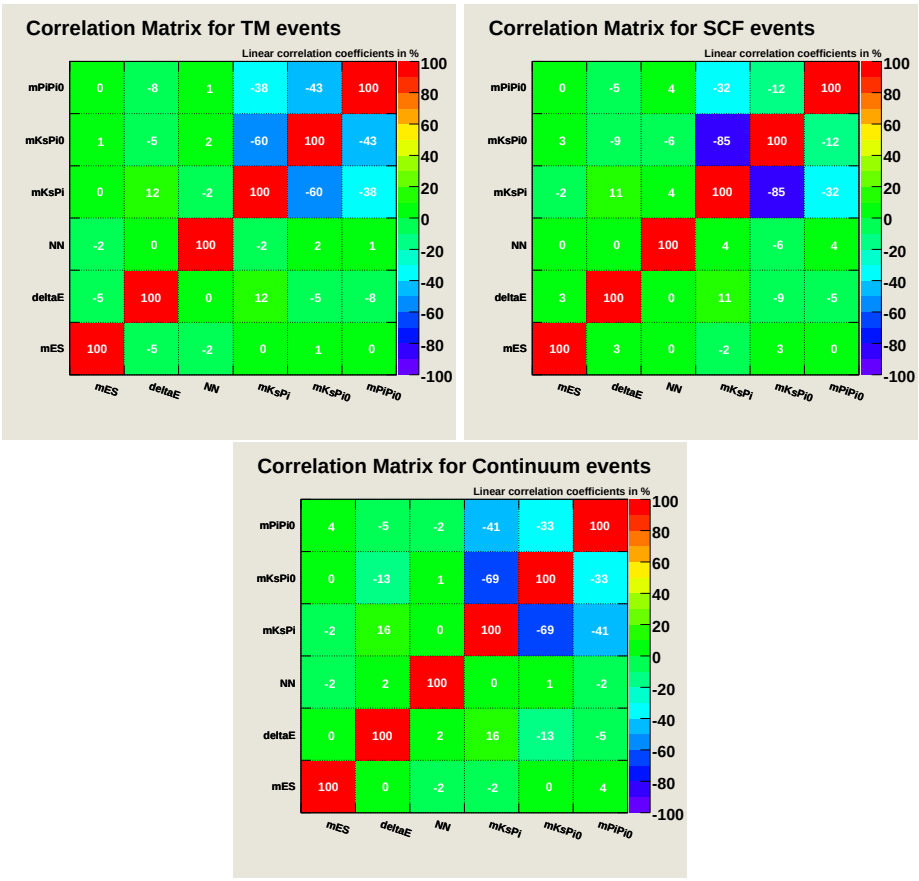

Figure 4.24: Tables showing the correlations between variables. Top left: TM events, top right: SCF events, bottom: continuum events.

of $\overline{f}^{\rm SCF}$ rapidly converges to a value which we fix after a few exploratory fits on the signal only model. The fit works properly even if we leave the fraction of SCF floating.

Studies in simulation have shown that the experimental resolutions of m' and θ' need not be introduced in the TM signal PDF. In contrast, misreconstructed events often incur large migrations, when the reconstructed $(m'_r,\ \theta'_r)$ are far from the true values $(m'_t,\ \theta'_t)$. We use the Monte Carlo simulation to compute a normalized two-dimensional resolution function $R^{\rm SCF}(m'_r, \theta'_r; m'_t, \theta'_t)$, with

$$\int_0^1 dm'_r \int_0^1 d\theta'_r R^{\rm SCF}(m'_r, \theta'_r; m'_t, \theta'_t) = 1. \qquad (4.21)$$

$R^{\rm SCF}$ is convolved with the signal model in the expression of $\mathcal{P}^{\rm SCF}$ (eq. 4.16). A grid with 40 bins in m' and 40 bins in θ' is used to compute the already shown (Figure. 4.8) TM and

SCF efficiency maps as well as the migration matrix $R^{\rm SCF}$ (a $40 \times 40 \times 40 \times 40$ array) in the Monte Carlo. Each element of the migration matrix is the probability that an event generated in bin (i, j) is reconstructed in bin (i', j'); to compute the $R^{\rm SCF}$ all the SCF events from the signal Dalitz model Monte Carlo have been used.

Backgrounds

After the very tight cut on the NN', there were not enough events in the offpeak sample to build a PDF. Therefore it was decided to use also the onpeak *Grand Sideband* by adding it to the offpeak sample, after subtracting the contribution due to B-background. The latter was estimated by using MC events. We avoided to use the $q\bar{q}$ MC, since there are known discrepancies with respect to the offpeak data. The square Dalitz plot was divided into 4 zones (see Figure 4.25) in order to better parametrize the structures; for each zone a 2-dimensional smoothed histogram was built. After this step all the 4 zones were merged together in order to obtain a single 2-dimensional histogram used as PDF for the continuum. The bottom plots of Figure 4.25 show a good agreement between the obtained PDF and the data for the m' and θ' distributions.

The B background Dalitz PDFs were shown in Figure 4.21 except for the $B^+ \to \bar{D}^0\pi^+$ (class #0) which is described by the 2-dimensional analytical parametrization explained in Section 4.7.

4.8.4 The other PDFs

Signal

- *TM*: the m_{ES} PDF for TM-signal events is a double gaussian function. The mean and the width of the narrower gaussian are free parameters in the fit. The fitted PDF on the N.R. Monte Carlo is shown on Figure 4.26.

  After the transformation $\Delta E \longrightarrow \Delta E'$, the residual correlation with the Dalitz plot (Figure 4.20) needs to be modeled. We parametrize $\Delta E'$ with the sum of a gaussian and a bifurcated gaussian whose parameters vary across the Dalitz plane: means and widths that vary linearly as a function of $m^2_{K^0_S\pi^+}$. A two step fitting procedure is employed, first, the parameters of the $\Delta E'$ PDF are obtained in slices of $m^2_{K^0_S\pi^+}$ in

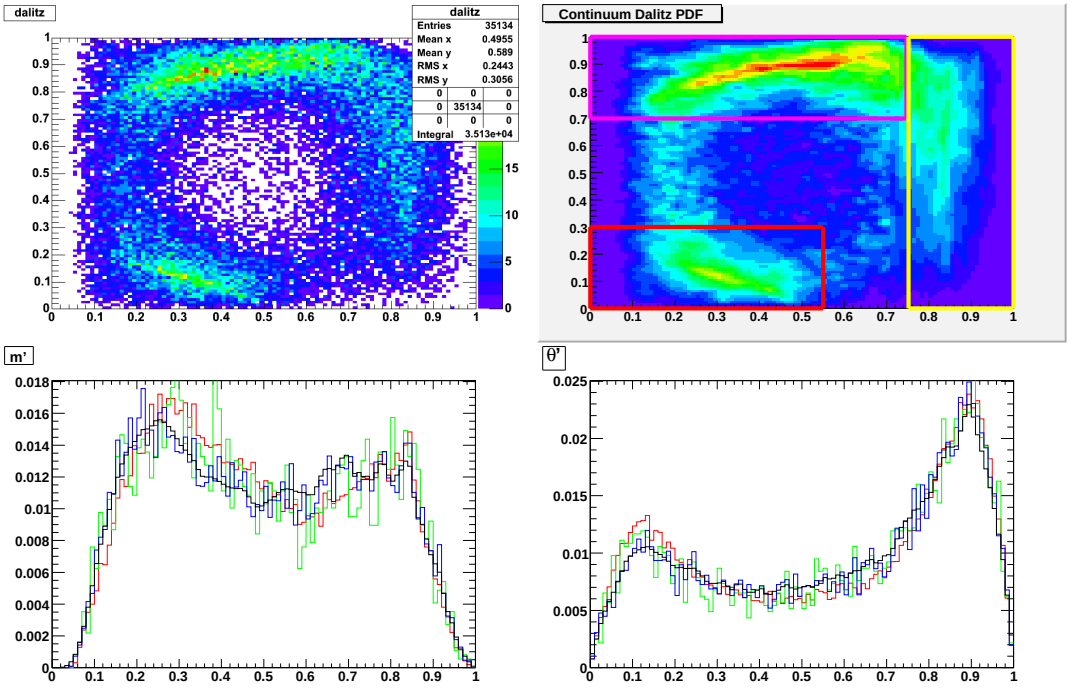

Figure 4.25: Top left: square Dalitz plot for a sample of offpeak and onpeak sideband data, obtained as described in the text; top right: resulting PDF, obtained by smoothing the previous histogram in four regions. Bottom: m' (left) and θ' (right) projections for $q\bar{q}$ MC (red), offpeak (green) and onpeak sideband (blue) data. The black lines corresponds to the PDF derived from the latter two samples.

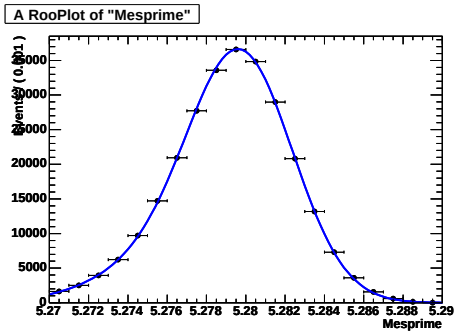

Figure 4.26: m'_{ES} PDF for signal TM events.

the Dalitz plot; then, a linear fit to the $m^2_{K^0_S\pi^+}$ dependence is performed with the results shown in Figure 4.27.

The TM NN' distribution is uncorrelated with all fit observables. The sum of a gaussian distribution plus two bifurcated gaussians adequately fits the non resonant

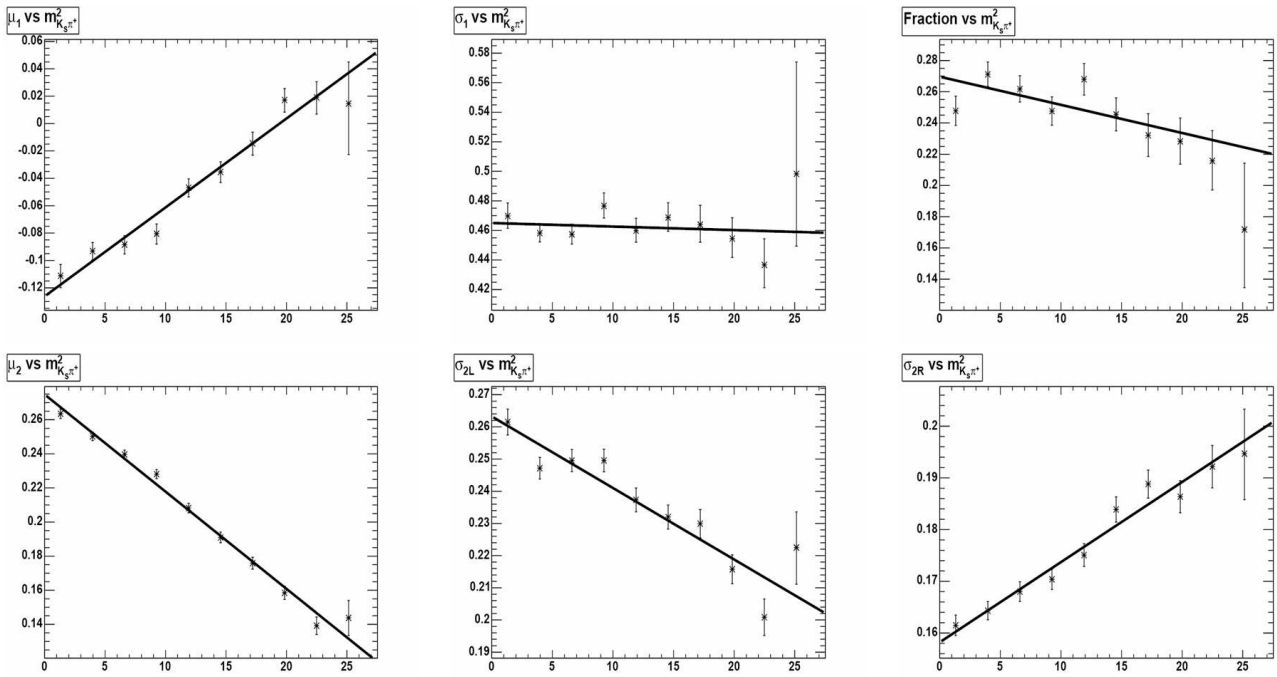

Figure 4.27: Distributions of the $\Delta E'$ PDF parameters as a function of $m^2_{K^0_S\pi^+}$. The PDF is the sum of a gaussian and a bifurcated gaussian. The plots represent respectively: the mean (top left) and standard deviation (top middle) of the gaussian, the mean (bottom left) and standard deviations (bottom middle and bottom right) of the bifurcated gaussian, and the relative fraction (top right) between the two functions. The distributions are fitted with straight lines.

MC as shown on Figure 4.28 (left).

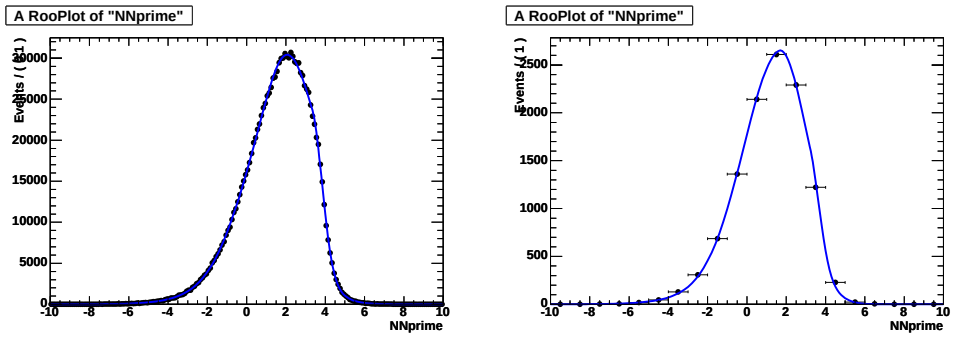

Figure 4.28: NN' PDFs for TM (left) and SCF (right) signal events.

- *SCF*: we saw in Section 4.4 that different types of events are merged in the SCF category. We use smoothed histograms built with the signal model MC, shown as the blue (solid) curves in Figure 4.29.

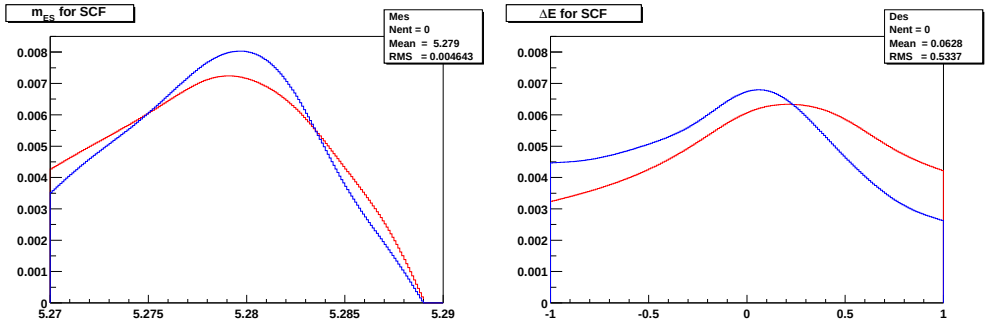

Figure 4.29: m_{ES} (left) and $\Delta E'$ (right) PDFs for SCF events. The blue PDFs are built on the signal Dalitz model and subsequently used in the fit. The red PDFs are obtained from the non resonant signal MC. There are significant differences, since the various types of SCF populate the two models differently.

As for the TM, the SCF NN' distribution is uncorrelated with all fit observables. The SCF NN' PDF is the double bifurcated gaussian fitted on the non resonant MC shown on Figure 4.28 (right).

Continuum background

The m'_{ES} and $\Delta E'$ PDF are respectively an Argus function and a second order polynomial. They are built by using the offpeak data and the $q\bar{q}$ MC samples. They are shown on Figure 4.30

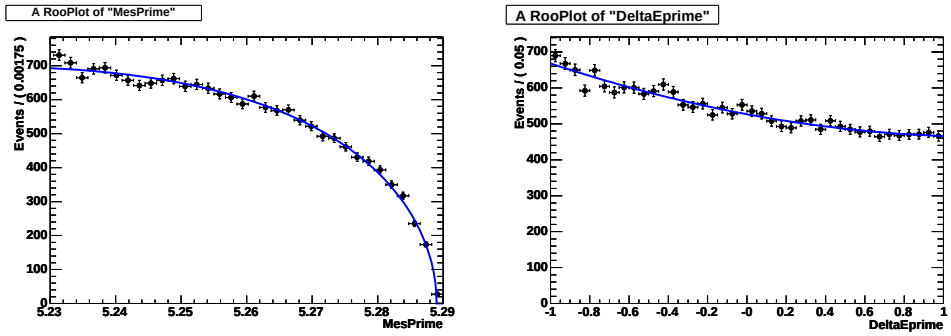

Figure 4.30: Continuum PDFs. Left: Argus function for m'_{ES}. Right: Second order polynomial for $\Delta E'$.

Neural Network correction for continuum events

The dependence of the NN across the Dalitz plot, described in Section 4.5, is taken into account by using a double bifurcated gaussian as a PDF, where all the parameters are second order polynomial functions of Δ_{Dalitz}. The PDF is built on $q\bar{q}$ MC (where enough events are available). Initially a range $\Delta_{\text{Dalitz}} < 2$ was considered and linear fits were performed for the first 6 slices. When the fit was attempted on a full Monte Carlo sample we found that it was necessary to enlarge the range and use quadratic fits. The results are shown in Figure 4.31.

B **background**

The PDF were already described in Section 4.6. The PDFs used for m_{ES}, $\Delta E'$ and NN' are smoothed histograms (Figure 4.11). The PDFs used for the square Dalitz plot are 2-dimensional smoothed histograms (Figure 4.12).

4.8.5 The fit parameters

The following parameters are varied in the fit:

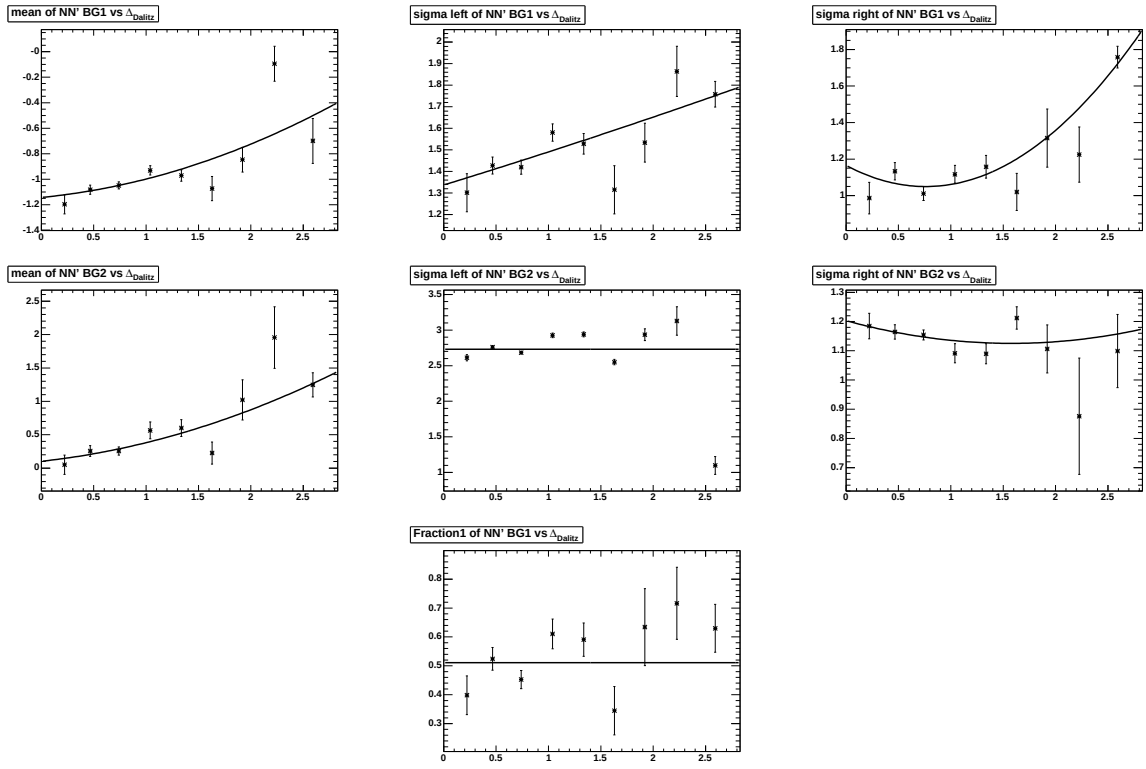

Figure 4.31: Distributions of the NN' PDF parameters as a function of Δ_{Dalitz}. The PDF is the sum of two bifurcated gaussians. The plots represent respectively: the mean (first row left) and standard deviations (first row middle and right) of the first bifurcated gaussian, the mean (second row left) and standard deviations (second row middle and right) of the second bifurcated gaussian and the relative fraction (bottom) between the two functions. The distributions are fitted with 2nd order polynomial.

- 10 yields for signal (N_{sig}), continuum ($N_{q\bar{q}}$) and for the 8 B background classes; the signal yield is the sum of the TM and SCF contributions while their relative proportion is kept fixed;
- 1 CP-asymmetry for the continuum events, A_{CP};
- 2 parameters related to narrow particle masses: the mass and mass resolution for the B;
- 3 parameters of the m_{ES} and $\Delta E'$ PDFs for the continuum events: slope of the Argus function, slope and intercept of the $\Delta E'$ polynomial function;
- 21 isobar amplitudes and phases. There are 6 intermediate states (5 resonances and a non-resonant term) and two Dalitz plots. We fix one reference amplitude, that of $B^+ \to K^{*+}(892)\pi^0$ and two phases for the latter and its conjugate. Therefore we end up with 11 magnitudes and 10 phases to be determined by the fit.

Chapter 5

Results

5.1 Decay model

The default decay model is the signal model already mentioned and shown in Table 1.3, with the amplitudes c_j and phases ϕ_j of Table 5.1. These parameters are also used to generate the Monte Carlo nominal model of the $B^+ \to K^0_S\pi^+\pi^0$ decay, which is needed to evaluate the efficiencies and to build the PDFs for the signal. The model used is CP conserving, i.e., it has equal isobar coefficients for the B^+ and B^- decays. The interferences are destructive (isobar phase difference within 30 degrees from π radians) between the $K_S\rho^+$ and each of the $K^*(892)\pi$ channels as well as between the $K^*_0(1430)^0\pi^+$ and each of the $K^*(892)\pi$.

Resonance	Amplitude c	Phase ϕ	FF
$\rho(770)^{\pm}$	1.45	151.83	0.238
$K^*(892)^{\pm}$	0.747	0.00	0.057
$K^*(892)^0$	1.00	-52.33	0.105
$K^*(1430)^{\pm}$	38.3	149.82	0.219
$K^*(1430)^0$	45.86	-76.39	0.315
N.R	15.1	-141.13	0.070

Table 5.1: Amplitude and Phase Parameters. The phases are referenced to that of the $B^+ \to K^(892)^+\pi^0$ component and chosen to lie between $\pm\pi$. The isobar fit fractions are computed according to eq. 1.72. The same isobar parameter values are used to model the B^+ and the B^- decays, hence the CP-asymmetries are equal to zero by construction.

The expected yields for each component of the signal and of the backgrounds is shown in Table 5.2.

Component	Expected yields
Signal (TM + SCF)	1206
SCF only	239
Continuum	7405
B-background (without D^0)	6011
D^0	2425

Table 5.2: Expected yields in the analysis by component.

5.2 Pure toys MC tests

A standard procedure to check the correct behaviour of the fit is to generate toy MC (see Section 3.4.3) according to some given PDFs ("pure toys"), employ the same PDFs to fit those simulated data, and compare the resulting values with those used to generate the data by producing pull plots for all the parameters that are estimated by the fit.

5.2.1 High statistics signal-only toys

As a first study, we determine whether the decay model can be fit without intrinsic degeneracies. To this end we perform scans on high statistics (10 times the data) toy samples. We perform one-dimensional scans of all the isobar phase angles ϕ in turn, as they are the sources of potential degeneracies. All other parameters are frozen to their default values. 36 scan steps in ϕ are made to span the $[-180°, +180°]$ interval in ϕ. At each step, 100 toy samples with 10000 events each are generated. For each toy, we record the phase ϕ_{rec} where we found the minimum of the negative logarithm of the likelihood value of the fits, NLL$\equiv -\ln(\mathcal{L})$ (see Section 3.4). When $\phi_{rec}(\phi)$ is multivalued, there is a degeneracy. We start with a simple model with two resonances only and add more resonances up to the full signal model.

Two resonances

Trigonometric ambiguities lead to fit degeneracies. They can be seen on Figure 5.1 (top left) for a model with the $K^*(892)^0\pi^+$ and the $K_S\rho^+$ resonances, where we see that the *wrong* solution is picked up for negative phases for the complete model (including SCF). The degeneracy is stronger for a model with $K^{*+}\pi^0$ and $K^*(892)^0\pi^+$ (Figure 5.1 (top

right)) which do not overlap much in phase space, than for a model with $K^{*+}\pi^0$ and $K_S\rho^+$ (Figure 5.1 (bottom)).

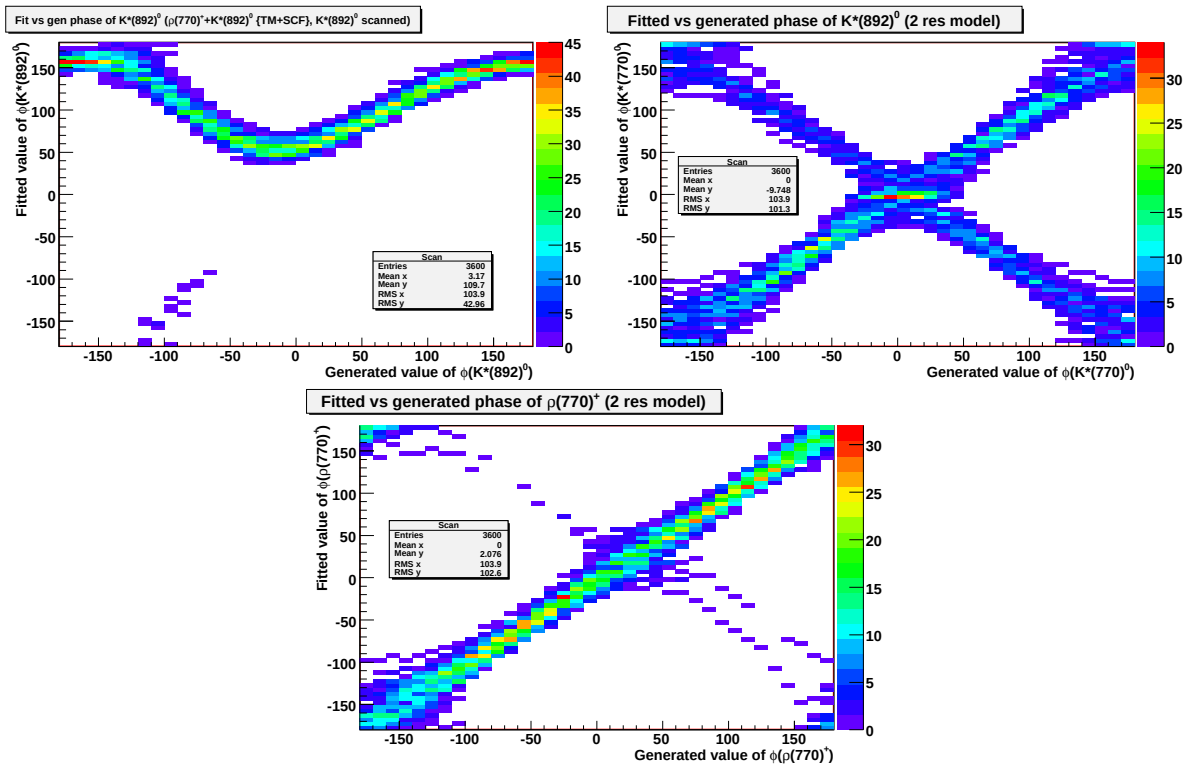

Figure 5.1: Phases resulting from the fit as a function of the generated phase. Two-resonance models: (Top left) $B^+ \to K^{*0}\pi^+$ and $K^0_S\rho^+$, (Top right) $B^+ \to K^{*0}\pi^+$ and $K^{*+}\pi^0$, and (Bottom) $B^+ \to K^{*+}\pi^0$ and $K^0_S\rho^+$.

Three and Four resonances

The results obtained on models with three and four resonances are shown in Figure 5.2 and 5.3. By comparing Figure 5.2 (left) with 5.1 (top right) we see that the maximum likelihood is obtained for the wrong $(\phi_{K^{*0}} - \phi_{K^{*+}})$ phase difference when the ρ is added to the model with the two $K^*(892)$ resonances. If we compare it to Figure 5.1 (top left), we see that the results are similar, wrong in half of the $(\phi_{K^{*0}} - \phi_{\rho^+})$ range. Comparing Figure 5.2 (right) to Figure 5.1 (bottom) we see the result degrades (the curve is thicker, the uncertainty on the reconstructed phase is larger) but remains acceptable (the correct solution is chosen). The Dalitz signal model has a destructive interference in the soft π^0

corner which is hard to be eliminated with only three resonances.

Scans for other models with three resonances including the $K_0^*(1430)^{0,+}$, are shown on Figure 5.3. Scans for four-resonance models show that when more components are added, the degeneracies get removed.

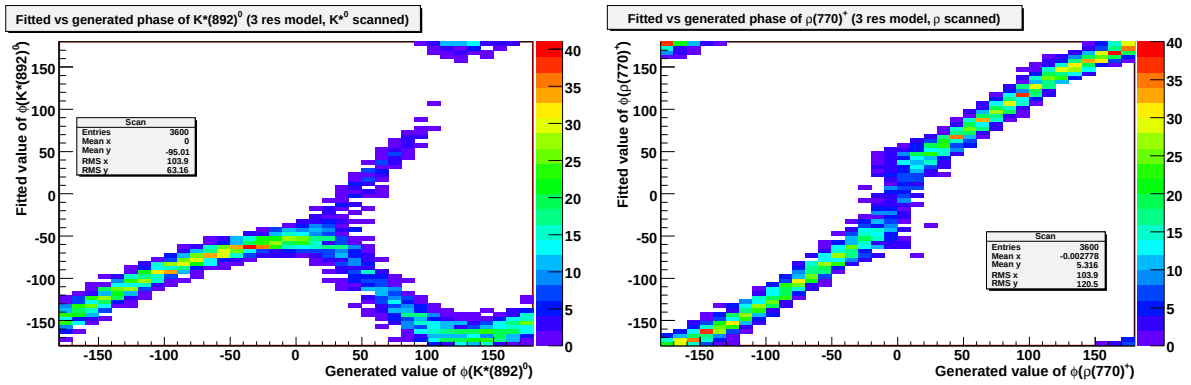

Figure 5.2: Phases resulting from the fit as a function of the generated phase. Three-resonance models with $B^+ \to K^{*0}\pi^+$, $K^{*+}\pi^0$, and $K_S\rho^+$: (Left) scan of the K^{*0} phase, (Right) scan of the ρ^+ phase.

Nominal model with six resonances

The six resonance nominal model is exempt of intrinsic degeneracies. All the scans presented in Figure 5.4 indicate that the likelihood function is maximum for the correct phase angle values. In conclusion, the likelihood function associated to the nominal B decay model does not present intrinsic degeneracies. With high statistics, the decay model can be fit.

5.3 Toys and embedded fits with realistic yields

In this section we study samples with the statistics we expect in the real data by performing a toy MC study were we generate and fit with a fit model which includes only the nominal signal decay model and add components one at a time as follows:

- signal only;
- signal only and $B^+ \to \bar{D}^0\pi^+$ ($\bar{D}^0 \to K_S^0\pi^0$);

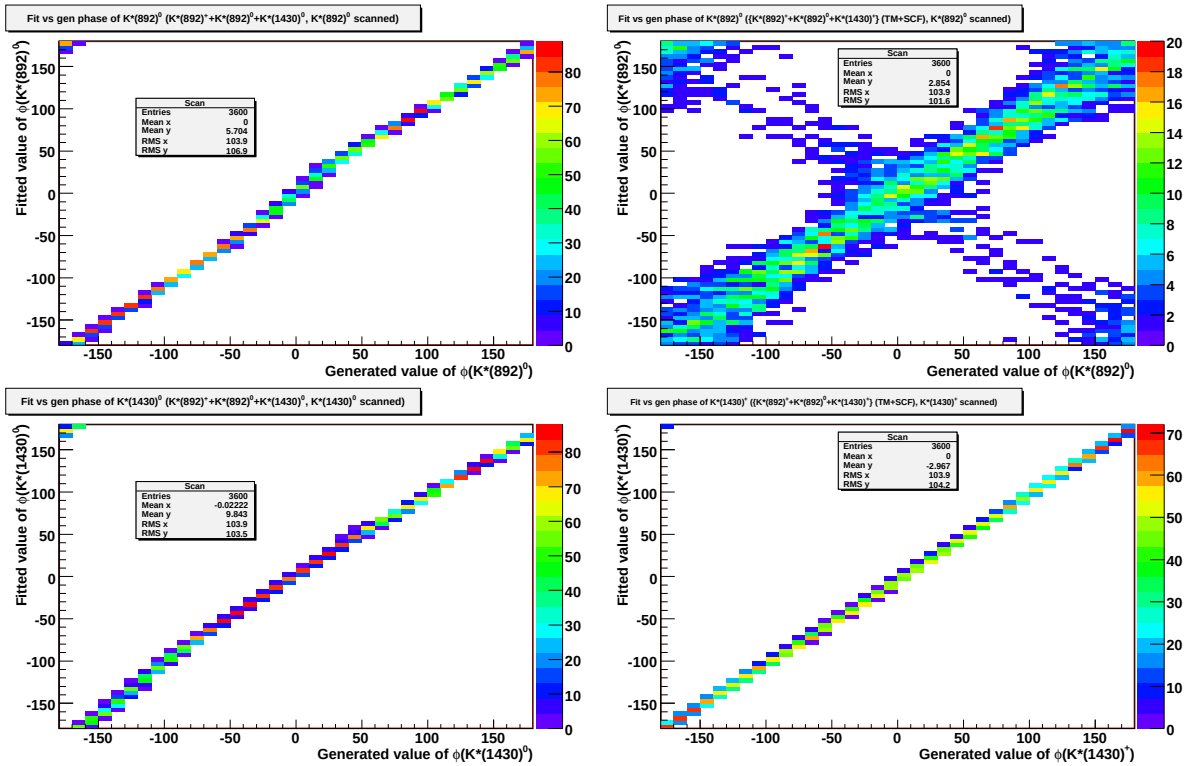

Figure 5.3: Phases resulting from the fit as a function of the generated phase. Three-resonance models with $B^+ \to K^*(892)^0\pi^+$, $K^*(892)^0\pi^0$, and $(K\pi)_0^{*0}(1430)$ (left) / $(K\pi)_0^{*+}(1430)$ (right): (Top) scan of the $K^*(892)^0$ phase, (Bottom) scan of the $(K\pi)_0^*(1430)$ phase.

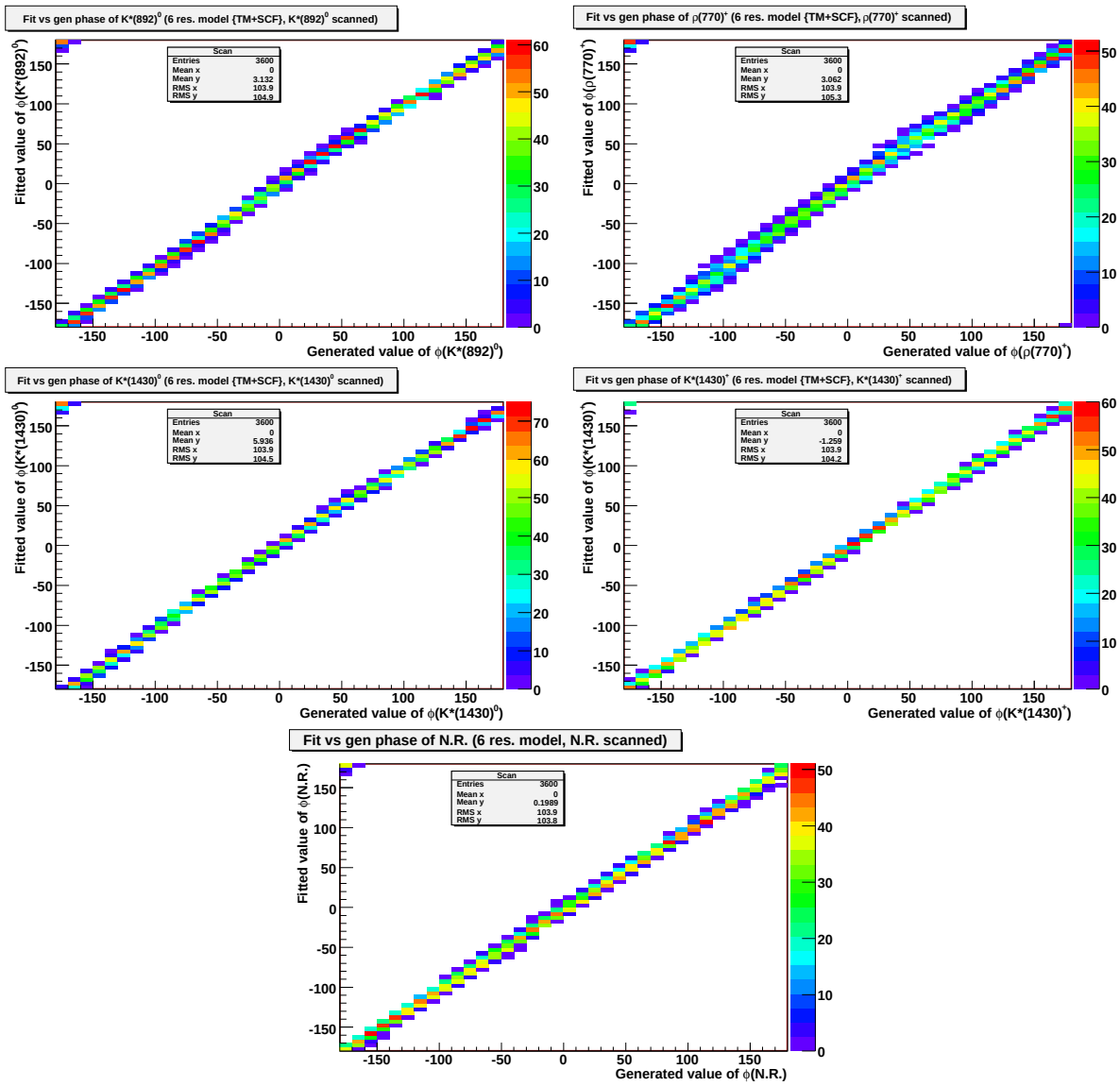

Figure 5.4: Phases resulting from the fit as a function of the generated phase. Nominal six-resonance model: (Top left) scan of the $K^*(892)^0$ phase, (Top right) scan of the ρ^+ phase, (Middle left) scan of the $(K\pi)_0^{*0}(1430)$ phase, (Middle right) scan of the $(K\pi)_0^{*+}(1430)$ phase, (Bottom) scan of the $N.R.$ phase.

- the latter and the B backgrounds;
- signal and the continuum background;
- the latter and $B^+ \to \bar{D}^0\pi^+$ ($\bar{D}^0 \to K^0_S\pi^0$);
- the latter and the B backgrounds.

We refer to the last case as the *full toy* study.

In each case, we generate 500 samples that are:

- *independent* by changing the seeds of the random number sequence.
- *poissonized*: prior to the generation of a sample the input yields are determined from Poisson distributions with means equal to the expected yields in the data (Table 5.2).
- *randomized* an appropriate number of times. To randomize means to fit a given sample starting from enough different input values of the fit parameters to make sure that the fit converges to the absolute minimum value of the negative loglikelihood function. *Full toy* (resp. *embedded*) fits are randomized 31 (resp. 29) times, in order to be sure that the fit reaches the absolute NLL minimum.

All fits are performed by keeping $f_{\rm SCF}$ and all PDF shape parameters fixed. We use two kind of samples:

- *pure toys* samples to construct pseudo experiments through the generation of events along the PDFs used in the fit. With *pure toys* we check the self consistency of the fit algorithm.
- *embedded fit* samples where we use fully generated and reconstructed signal events and toy MC events for backgrounds. With *embedded fits* we check the quality of the reconstruction, in particular the reliability of the SCF modeling.

We obtain three distributions for each parameter (isobar amplitudes, isobar phases and yields): the *residual* (reconstructed - generated value), the *standard deviation*, and the *pull* (residue/standard deviation) distributions. An example of these plot are in Appendix A.1

for the embedded fits with the full model (see from Figure A.1 to A.4). Tables showing the pulls for amplitudes and phases for all toy studies are presented in Appendix A.1.

The detailed results for all the studied validation samples are given in [65]. The fit machinery works satisfactorily. In the *embedded fits* for the full fit model, the maximum deviation of a pull mean from zero is 0.75 standard deviations for the yield of the category #4 of the B-background. The signal yield is also biased by 0.5 standard deviations σ. Looking at these results we decided after the toy MC studies to fix the yield of the B-background in category #1 because it is correlated with the yield of the continuum background. The pull widths for the yields are between 0.96 and 1.13. The pull widths for the amplitudes are between 0.8 and 1.01, most differing form 1.00 by less than 10%. There are no significant biases for the phase angles. The pulls are more scattered and on the high side between 0.98 and 1.30. The relative uncertainties on the yields are consistent with Poisson errors and the signal to noise ratio. The phases are measured with precisions between 17 and 56 degrees. The most difficult to determine are those of the neutral ($K\pi$) resonances.

We summarize the outcome of the validation studies by showing in Table 5.3, which also shows the degradation of the uncertainties on the fit parameters as the fit model gets more and more complex. In particular, the presence of the continuum background significantly degrades the precision on the phase measurements, which gets further degraded by the introduction of B backgrounds.

5.3.1 D^0 and fit stability

The stability of the fit with respect to the high $B^+ \to \bar{D}^0\pi^+$ yield is studied by using Toy MC with a model incorporating TM only signal and the $B^+ \to \bar{D}^0\pi^+$ channel and performing scans of all the analytical parameters of the TM PDFs (see Figure 5.5). We see that for each parameter the minimum of the NLL is unique, therefore the fitter is stable with respect to the choice of the PDF parameters.

Fit	Signal		Signal+D^0	Signal+Cont.		Full fit	
	T	E	T	T	E	T	E
ρ^+ (amp)	0.20	0.18	0.18	0.27	0.28	0.27	0.33
ρ^- (amp)	0.19	0.18	0.19	0.28	0.29	0.27	0.31
ρ^+ (phase)	22.21	17.92	24.74	42.21	38.55	51.09	42.61
ρ^- (phase)	23.78	17.35	24.09	43.60	32.74	51.88	39.16
K^{*-} (amp)	0.13	0.13	0.12	0.20	0.19	0.18	0.18
K^{*0} (amp)	0.16	0.14	0.15	0.22	0.21	0.21	0.23
$\bar{K}^{*0}$ (amp)	0.16	0.16	0.15	0.21	0.22	0.20	0.24
K^{*0} (phase)	31.41	24.25	32.28	51.28	46.14	60.77	59.55
$\bar{K}^{*0}$ (phase)	26.14	23.95	32.28	53.59	45.10	64.73	55.49
$K^*(1430)^+$ (amp)	5.60	5.35	5.50	8.08	8.37	7.89	9.43
$\bar{K}^*(1430)^-$ (amp)	5.25	5.06	5.07	7.79	7.67	7.81	8.80
$K^*(1430)^+$ (phase)	11.42	10.75	12.29	17.83	16.74	18.78	18.84
$\bar{K}^*(1430)^-$ (phase)	11.30	10.84	11.83	17.50	17.80	17.93	17.89
$K^*(1430)^0$ (amp)	6.08	5.61	5.82	8.32	8.63	8.08	9.55
$\bar{K}^*(1430)^0$ (amp)	6.19	5.15	6.05	8.71	8.63	8.94	9.94
$K^*(1430)^0$ (phase)	30.85	22.73	31.14	50.05	45.81	59.36	59.66
$\bar{K}^*(1430)^0$ (phase)	26.15	23.16	31.96	54.38	43.55	64.32	56.92
$N.R.$ (amp)	3.19	3.17	3.22	5.02	4.84	5.23	5.97
$\overline{N.R.}$ (amp)	3.04	3.06	3.29	4.67	4.87	5.54	5.27
$N.R.$ (phase)	17.79	14.98	18.13	31.20	31.20	36.55	42.64
$\overline{N.R.}$ (phase)	16.08	16.13	16.84	36.80	29.29	39.10	36.21

Table 5.3: Uncertainties on the fitted parameters (standard deviation of the residues σ_{res}) for different and increasingly complex fit models. For each sample type, we show the toys (T) and the embedded (E) fit results when applicable.

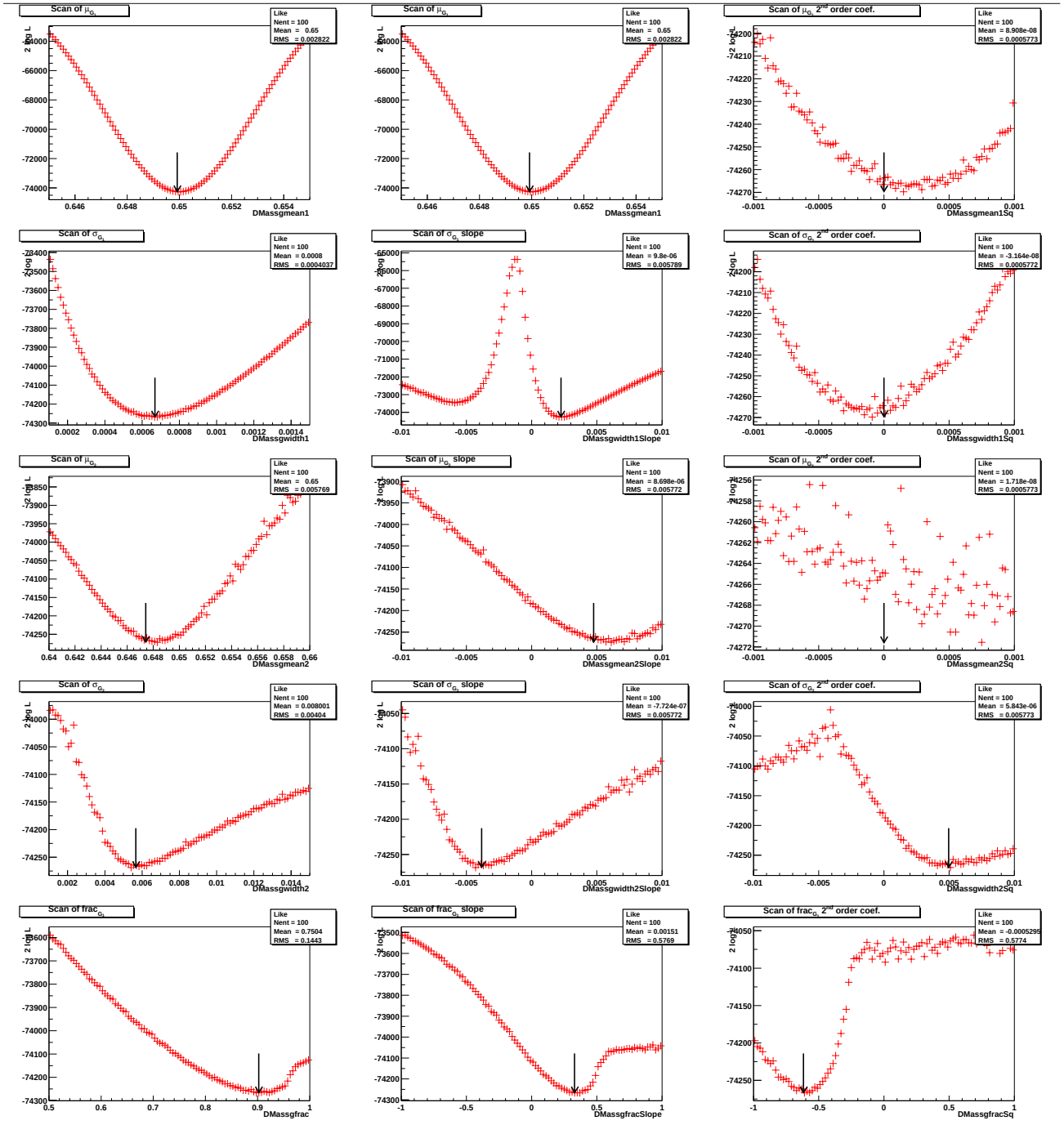

Figure 5.5: Likelihood scans on TM part of the D^0 parameterization on a $TM + D^0$ pure toy. For each parameter of the PDFs, we see the NLL values obtained varying the initial value.

5.4 Test of the fit on fully simulated MC tests

A realistic dataset of simulated events is built, by combining signal, continuum and B background Monte Carlo samples with an equivalent luminosity equal to the collected luminosity of the real onpeak data. The signal MC is generated according to the signal model studied with the pure toys.

14624 events are retained by the selection procedure and submitted to the fitter.

5.4.1 Freezing the nominal fit

With respect to the validation studies, two modifications appear to be necessary to properly fit the datasized-full MC sample:

- when trying to let free all parameters, unphysical yields for two of the B-background categories (#1 and #5) show up as well as correlations between them and the signal and continuum yields. For this reason, the yield for category #1 is kept fixed in the nominal fit;

- by looking at the projection plots of the discriminant variables, it is necessary to adjust the shape of the continuum NN PDF.

The fit function depends on 37 parameters listed in Section 4.8.5. Various fit configurations are explored and described in the forthcoming tables which show the result.

After the study presented in this section we changed slightly the nominal fit configuration to take into account:

- the actual continuum cross section which in and up to this section was underestimated because the effect of a cut on m_{ES} was overlooked. The correct expected continuum yield is 8250 events and not 7045 and the total expected yield 15274.

- that the B-background was unduly modeled by unsmoothed histograms taken from the very same generic $B\bar{B}$ Monte Carlo that is used to build the full MC sample.

When we fit the data we fix the yields of the B-background categories (# 1, 3, 6 and 7). Therefore the number of free parameters in the nominal fit configuration is reduced to 33.

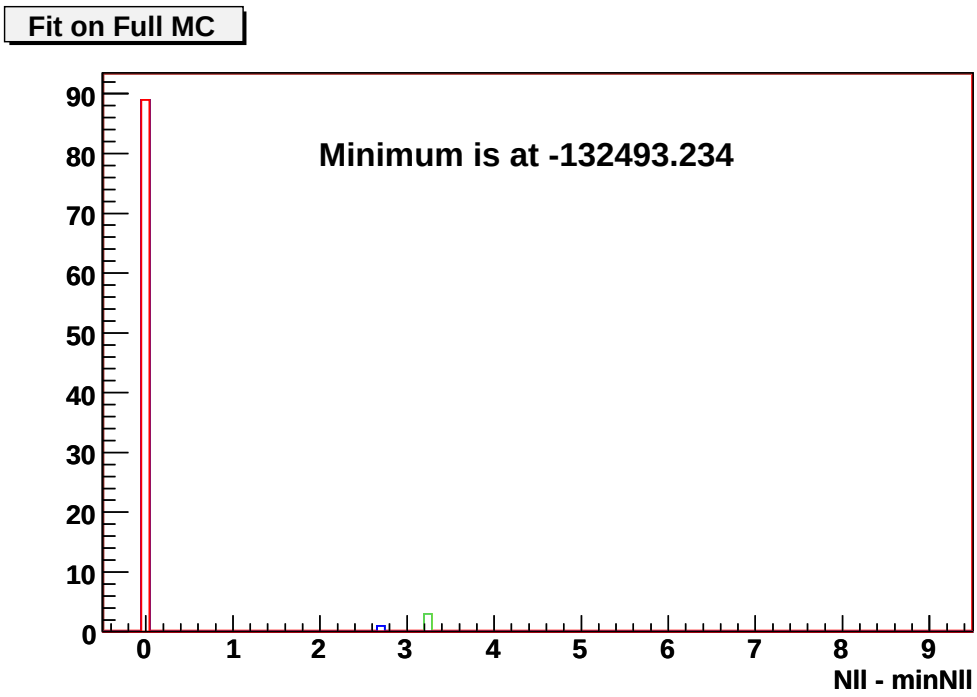

Figure 5.6: Distribution of $NLL_{\rm min}$ for the fits attempted with randomized input parameters. The origin is $NLL_{\rm bestfit}$, i.e. the value associated to the fit on the full Monte Carlo sample that is retained as the solution.

We also used smeared Dalitz plot PDFs for the B-background categories (#3, 4 and 6) with broad patterns in (m', θ'). More details are given in Section 4.6. We have checked that the final fitter on a corrected full MC sample gives similar results to those we are about to describe below.

5.4.2 Fit results

The NLL distribution of the randomized[1] fit is shown in Figure 5.6. We see a single solution (only one NLL minimum). We postpone the study of potential multiple solution of the fit on the real data in case they occur. The value of the NLL corresponding to the best fit ($NLL_{\rm bestfit}$) is well within the range covered by the validation fits (Figure 5.7). The correlation between the fit parameters is given in Figure 5.8. Most of the correlations are small, except of for some couples of resonances and of phases.

The parameters and their fitted values are collected in Table 5.4. The fit fractions

[1] the fits are performed randomizing the starting values for the fit parameters.

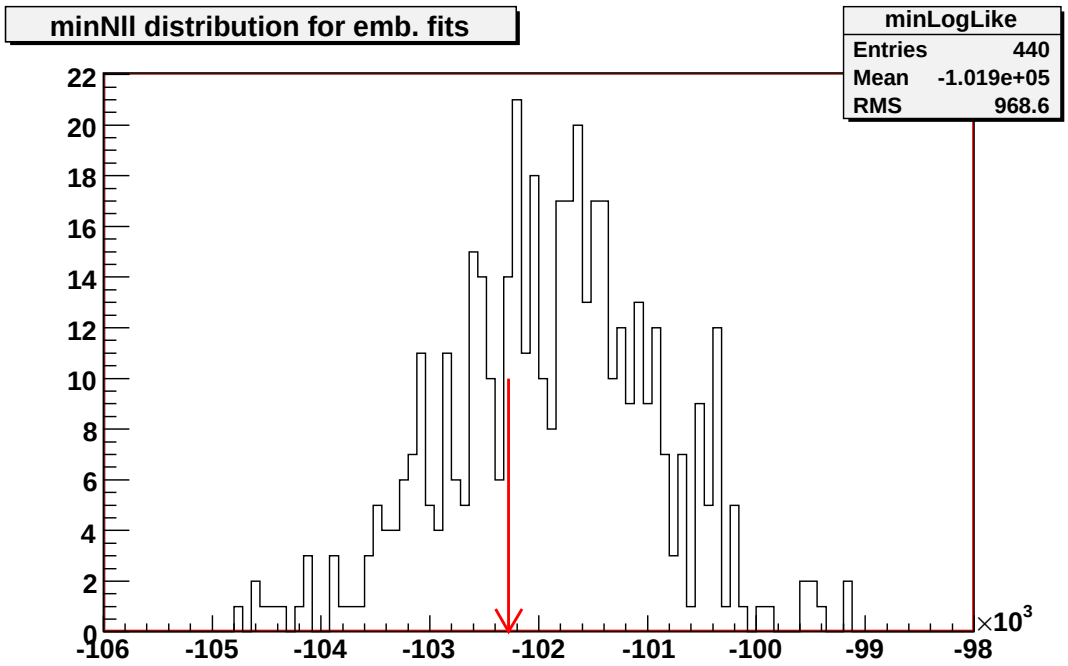

Figure 5.7: Distribution of NLL_{bestfit} for the embedded fits. The red arrow indicates the NLL_{bestfit} value for the fit on the full Monte Carlo sample .

and CP-asymmetries, obtained by using a Lagrange multiplier method (see Table 5.5) (described in Section 3.4.4) are compared to the initial values of signal Dalitz model in Table 5.1. The fitting fraction sum up to 1.03, a value which differs from 1.00 because of the interferences in the Dalitz plot (see eq. 1.71). To show the details of the agreement of the fit with the simulated data, we show in the following, likelihood ratio plots, Dalitz mass spectra and the distributions of the discriminating variables m'_{ES}, $\Delta E'$ and NN'. In all plots, the fitted sample appear as points with error bars. The distributions from the various components, obtained from one high statistics (1 Million events) toy Monte Carlo pseudoexperiment are shown as histograms. The various colors show the continuum (yellow), B background (green), $\bar{D}^0$ background (blue), signal self cross feed (black), and truth-matched events (red) respectively.

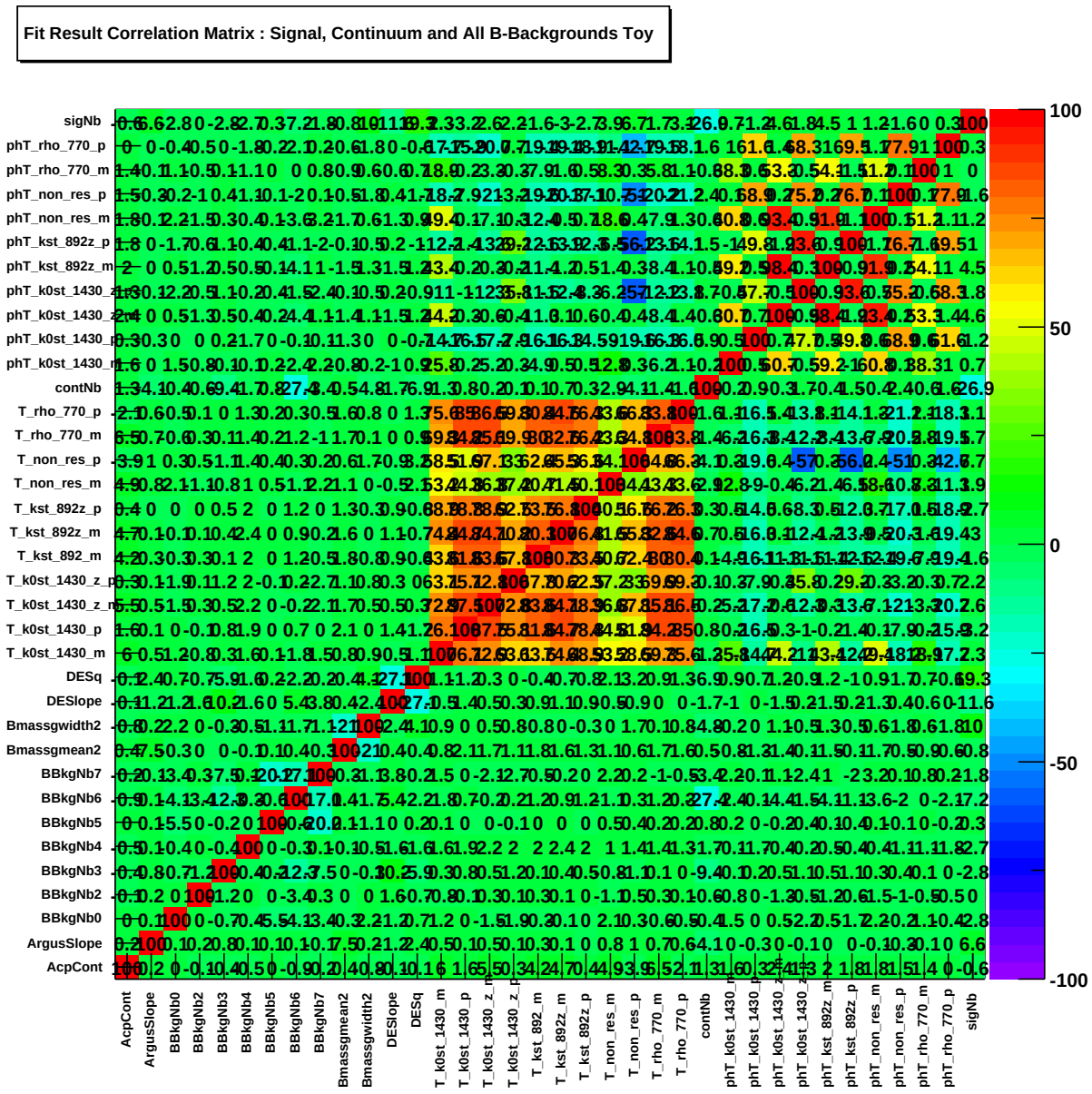

Figure 5.8: Correlation matrix for the best fit on a data-sized Monte Carlo sample.

Floating Parameter	Gen. Value	Final Value	Error
Signal yield	1206	1.2145e+03	5.76e+01
Continuum yield	7405	7.2856e+03	1.07e+02
Continuum A_{CP}	0.0	-1.4539e-03	1.39e-02
Category #0 yield	2425.0	2.4591e+03	5.34e+01
Category #2 yield	330.0	3.2065e+02	1.97e+01
Category #3 yield	624.0	6.6958e+02	4.07e+01
Category #4 yield	51.0	5.7403e+01	9.99e+00
Category #5 yield	239.0	2.1942e+02	2.81e+01
Category #6 yield	1317.0	1.2720e+03	6.68e+01
Category #7 yield	357.0	3.5342e+02	3.78e+01
Argus slope	-2.0938e+01	-1.5301e+01	6.22e+00
B mass (MeV/c^2)	5.2799e+00	5.2796e+00	6.85e-05
B mass width (MeV/c^2)	2.6218e-03	2.5053e-03	5.28e-05
ΔE slope (GeV/$c^{2^{-1}}$)	-1.9221e-01	-1.7754e-01	2.37e-02
ΔE intercept	7.6595e-02	3.4709e-02	4.61e-02
$K^*(1430)^-$ (amp)	3.830e+01	2.8433e+01	5.37e+00
$K^*(1430)^+$ (amp)	3.830e+01	3.3417e+01	6.70e+00
$\bar{K}^*(1430)^0$ (amp)	4.586e+01	3.7725e+01	6.03e+00
$K^*(1430)^0$ (amp)	4.586e+01	2.8413e+01	5.48e+00
$K^*(892)^-$ (amp)	7.470e-01	5.5765e-01	1.31e-01
$\bar{K}^*(892)^0$ (amp)	1.000e+00	7.6787e-01	1.47e-01
$K^*(892)^0$ (amp)	1.000e+00	7.6619e-01	1.42e-01
$\overline{N.R.}$ (amp)	1.510e+01	1.5427e+01	3.81e+00
$N.R.$ (amp)	1.510e+01	1.1122e+01	6.33e+00
ρ^- (amp)	1.450e+00	1.1699e+00	1.86e-01
ρ^+ (amp)	1.450e+00	1.0555e+00	1.81e-01
$K^*(1430)^-$ (phase)	1.498e+02	-2.2559e+02	1.62e+01
$K^*(1430)^+$ (phase)	1.498e+02	1.3512e+02	2.08e+01
$\bar{K}^*(1430)^0$ (phase)	-7.639e+01	-1.1060e+02	3.88e+01
$K^*(1430)^0$ (phase)	-7.639e+01	2.5310e+02	6.85e+01
$\bar{K}^*(892)^0$ (phase)	-5.233e+01	-8.4295e+01	3.86e+01
$K^*(892)^0$ (phase)	-5.233e+01	-4.2189e+01	6.08e+01
$\overline{N.R.}$ (phase)	-1.411e+02	-1.7731e+02	3.00e+01
$N.R.$ (phase)	-1.411e+02	2.6987e+02	5.47e+01
ρ^- (phase)	-2.817e+01	-7.4285e+01	2.89e+01
ρ^+ (phase)	-2.817e+01	3.2113e+02	3.76e+01

Table 5.4: Result of the fit on the data-sized MC. The fit parameters are compared to their input values which were chosen to be equal to those of the signal model used in the MC generation.

Resonance	FF	A_{CP}
$\rho(770)^{\pm}$	0.235981	-0.102498
$K^*(892)^{\pm}$	0.075007	0.284282
$K^*(892)^0$	0.103336	-0.00218122
$K^*(1430)^{\pm}$	0.241789	0.160129
$K^*(1430)^0$	0.280395	-0.276122
N.R	0.092647	-0.31604

Table 5.5: A_{CP}'s and FF's derived from the datasized full MC fit result.

5.4.3 Likelihood ratios

We define

$$R \equiv \frac{(\mathcal{L}_{\text{TM}} + \mathcal{L}_{\text{SCF}})}{\mathcal{L}_{\text{TM}} + \mathcal{L}_{\text{SCF}} + \mathcal{L}_{\text{continuum}} + \mathcal{L}_{\text{B-backgrounds}}} \tag{5.1}$$

where $\mathcal{L}$ is the likelihood function of an event and it is split between all components (or groups of components). Since there is no *background-free* area in the parameter space, R is never higher than 0.92. The distribution of R for various configurations (linear and logarithmic scales) are shown on Figure 5.9 to emphasize the regions dominated by signal and backgrounds.

5.4.4 Discriminant variables projection plots

The m'_{ES}, $\Delta E'$ and NN' distributions presented on Figure 5.10. The left plots show all events, the right ones show events surviving a cut on R[2], tuned to maximize the $\frac{\text{signal}^2}{\text{signal+background}}$, ratio to enrich the sample in signal events. There is good agreement between the fit model and the input simulated data.

5.4.5 Dalitz plot projection plots

On Figure 5.11 we show in turn the $K^0_S\pi^+$, $K^0_S\pi^0$ and the $\pi^+\pi^0$ invariant mass spectra. For each meson pair, we show the full kinematical range, the restricted range between threshold and 1.6 GeV/c^2 to see the range where the resonances are located, without and with signal enrichment. A zoom on the $K^0_S\pi^0$ mass in the region of the $\bar{D}^0$ is shown on Figure 5.12.

[2] R is computed by excluding the plotted variable from the likelihood.

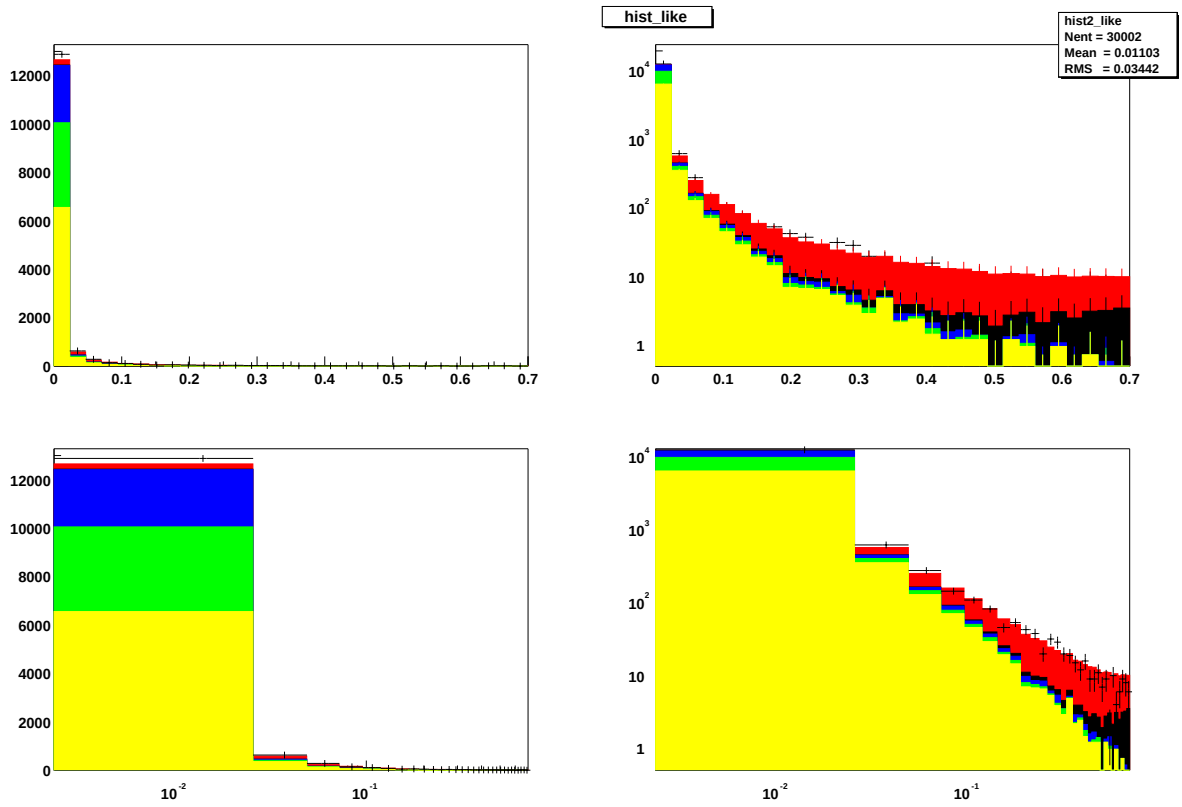

Figure 5.9: Full MC fit likelihood ratio. The simulated data is shown as point with error bars. The color code depicts the continuum (yellow), B background (green), $\bar{D}^0$ (blue), signal self cross feed (black), and truth-matched events (red) respectively. Linear (left) and logarithmic (right) scales for the y axis, and linear (top) and logarithmic (bottom) scales for the x axis illustrate the regions where the signal dominates over the background and vice versa.

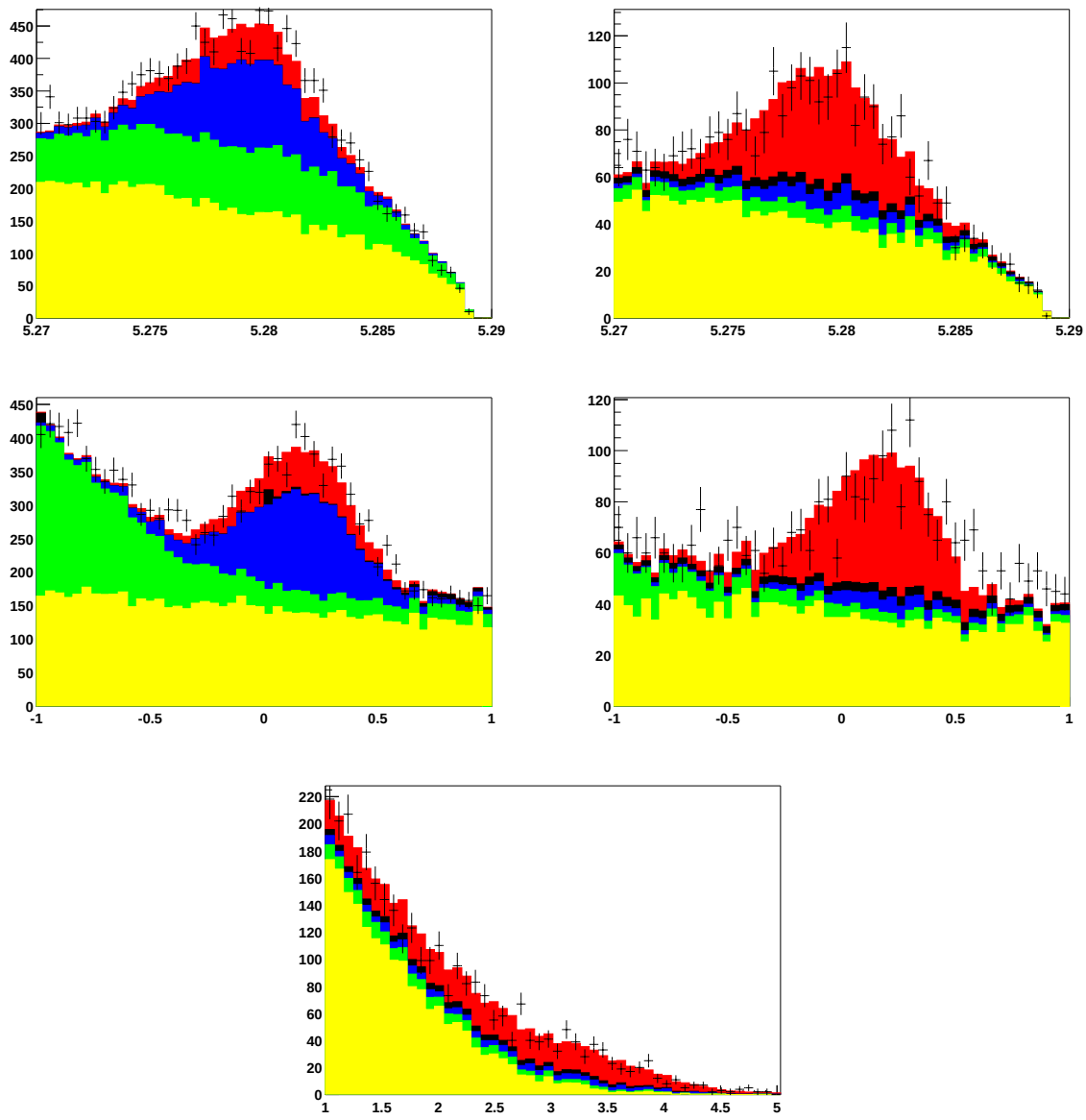

Figure 5.10: Full MC fit results. (top) m_{ES}, (middle) $\Delta E'$ and (bottom) NN' distributions. The simulated data is shown as points with error bars (all available data on the left, after a cut on R (computed after excluding the plotted variable) to enhance signal on the right). The color code depicts the continuum (yellow), B background (green), $\bar{D}^0$ (blue), signal self cross feed (black), and truth-matched events (red) respectively.

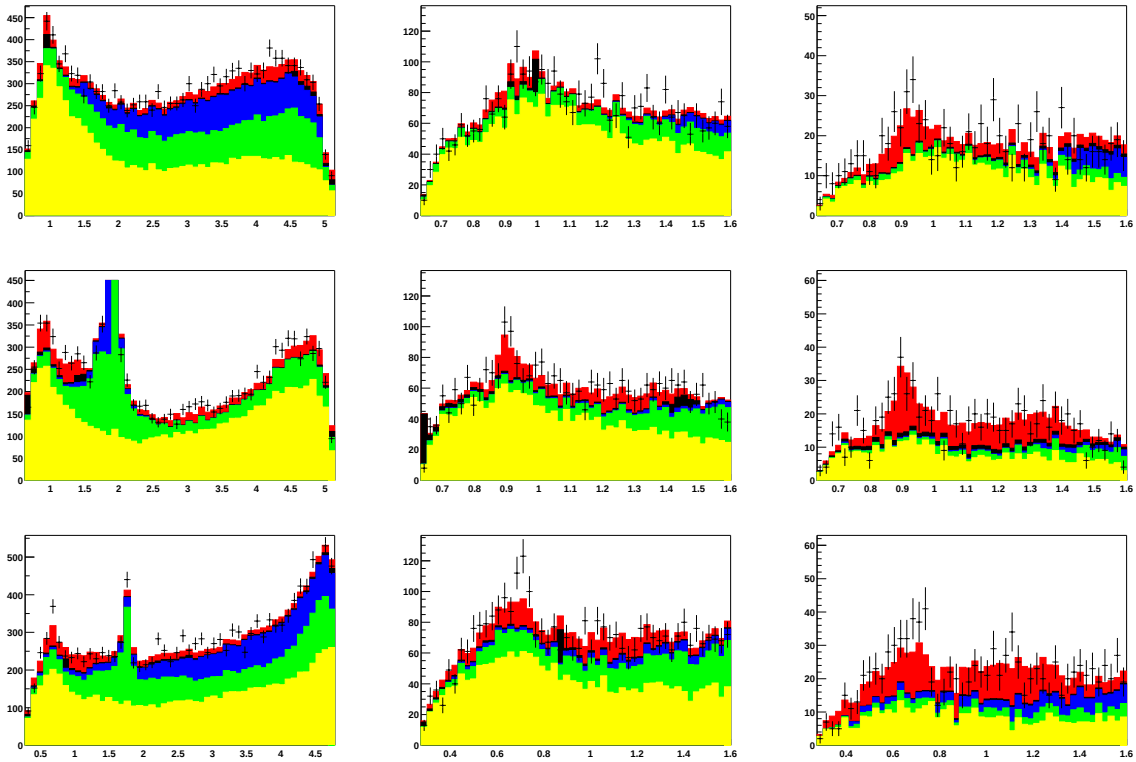

Figure 5.11: Full MC fit results. (Top) $K^0_S\pi^+$ invariant mass all events (left), $m \leq 1.6$ GeV/c^2 (center) and for a sample enriched in signal by a cut on R (right). (Middle) the same for the $K^0_S\pi^0$ invariant mass. (Bottom) the same for the $\pi^-\pi^0$ invariant mass.
The data are shown as point with error bars. The color code depicts the continuum (yellow), B background (green), $\bar{D}^0$ (blue), signal self cross feed (black), and truth-match (red) respectively. The $\bar{D}^0$ mass peak which sticks out of the middle-left plot is shown in detail in Figure 5.12.

5.5 Results on data

5.5.1 Fit result

To look at the real data, we follow a blinding procedure as follows. We try first a CP-blind fit where we impose the $B^+$and the B^-decays to be identical, by using a single set of isobar amplitudes and phases for both. After inspection of the results, if the projection plots shows an acceptable goodness of the fit, we *unblind* the fit for CP quantities.

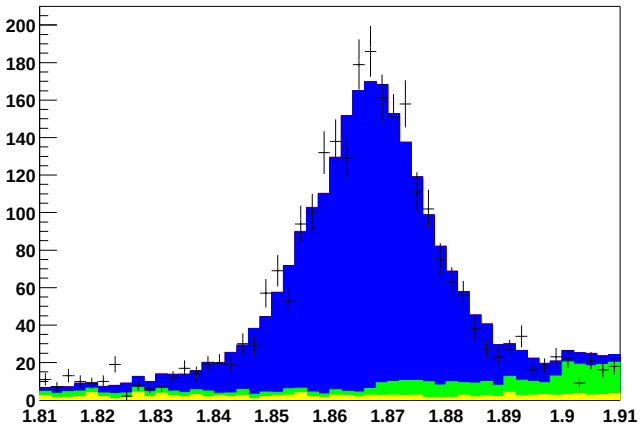

Figure 5.12: Full MC fit results. $K^0_S\pi^0$ invariant mass zoomed in the $\bar{D}^0$ mass region. The color code depicts the continuum (yellow), B background (green), $\bar{D}^0$(blue), signal self cross feed (black), and truth-matched events (red) respectively.

5.5.2 CP blind fit

The NLL distribution for 100 fits where the starting values of the fit parameters have been randomly chosen is shown in Figure 5.13. There are two solutions separated by 0.2 units of NLL. The numerical results are shown in Table 5.6. All the yields are consistent with expectation. Fixing the highest B-background yields (classes #3 and #6) far away from the nominal values, does not change dramatically the fitted parameters for signal and continuum. The fit is thus stable against wrong estimates of the B-background yields. The correlation tables for the two solutions are very similar, hence we only show that for *solution-1* in Figure 5.14. The projection plots are presented in Figure 5.15 (likelihood ratio), Figure 5.16 (m'_{ES}, $\Delta E'$ and NN'), Figure 5.17 (Dalitz invariant mass spectra), and Figure 5.18 ($m_{K^0_S\pi^0}$ in detail in the region of the $\bar{D}^0$).

5.5.3 Fit allowing for CP violation (nominal fit)

The NLL distribution for 100 fits obtained by varying the starting values of fit parameters, is shown in Figure 5.19. There are two solutions separated by half a unit of NLL. The numerical results are shown in Table 5.7, the FF and A_{CP} parameters in Table 5.8. The correlation tables for the two solutions are very similar, hence we only show that for

	Solution-1		Solution-2	
Floating Parameter	Final Value	Error	Final Value	Error
Signal yield	1.2274e+03	7.50e+01	1.2430e+03	7.84e+01
Continuum yield	8.1515e+03	1.17e+02	8.1439e+03	1.20e+02
Continuum A_{CP}	-2.8501e-02	1.25e-02	-2.8683e-02	1.25e-02
Category #0 yield	2.5333e+03	5.45e+01	2.5273e+03	5.44e+01
Category #1 yield	726.0 (fixed)			
Category #2 yield	3.2075e+02	1.98e+01	3.2256e+02	1.98e+01
Category #3 yield	593.0 (fixed)			
Category #4 yield	8.7027e+00	7.37e+00	7.5842e+00	7.23e+00
Category #5 yield	2.3802e+02	2.89e+01	2.3521e+02	2.88e+01
Category #6 yield	1266.0 (fixed)			
Category #7 yield	366.0 (fixed)			
Argus slope	-6.0554e+00	6.40e+00	-5.0001e+00	4.50e+01
B mass (MeV/c^2)	5.2794e+00	7.26e-05	5.2794e+00	7.43e-05
B mass width (MeV/c^2)	2.6831e-03	5.47e-05	2.6893e-03	5.49e-05
ΔE slope (GeV/$c^{2^{-1}}$)	-2.7874e-01	2.47e-02	-2.7992e-01	2.47e-02
ΔE intercept	2.0444e-01	5.13e-02	2.0768e-01	5.18e-02
$K^*(1430)^+$ (amp)	4.5268e+01	6.01e+00	3.2433e+01	5.27e+00
$K^*(1430)^0$ (amp)	3.1683e+01	5.13e+00	4.0782e+01	5.35e+00
$K^*(892)^0$ (amp)	8.1385e-01	1.27e-01	7.0753e-01	1.28e-01
N.R. (amp)	1.3384e+01	2.99e+00	1.5210e+01	3.51e+00
ρ^+ (amp)	9.5696e-01	1.42e-01	9.4123e-01	1.52e-01
$K^*(1430)^+$ (phase)	-3.5157e+02	1.37e+01	-2.0767e+01	1.41e+01
$K^*(1430)^0$ (phase)	1.0760e+02	3.12e+01	-1.3220e+02	3.26e+01
$K^*(892)^0$ (phase)	-3.5677e+02	3.40e+01	-2.7536e+02	3.51e+01
N.R. (phase)	-1.1063e+02	3.01e+01	1.2694e+02	2.99e+01
ρ^+ (phase)	-3.4852e+02	2.86e+01	-6.8667e+01	3.48e+01

Table 5.6: Result of the CP-blind fit on data. The two almost degenerate solutions have $NLL_1 = -137569.0$, and $NLL_2 = -137568.8$.

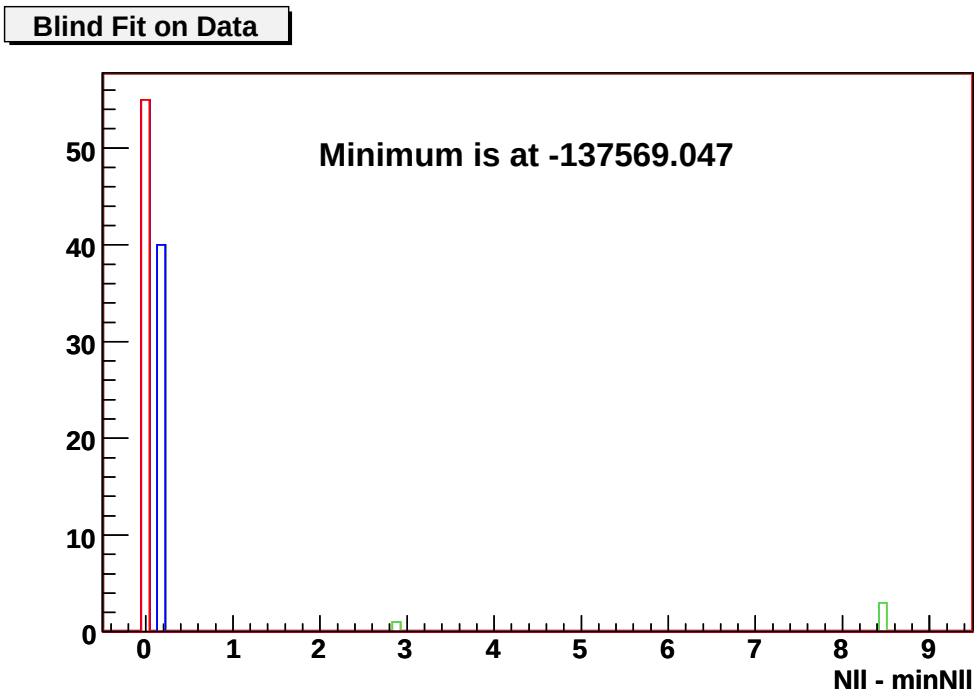

Figure 5.13: Spectrum of $NLL_{\min}$ for all the blind fits attempted with randomized input parameters.

solution-1 in Figure 5.20. The projection plots are presented for *solution-1* in Figure 5.21 (likelihood ratio), Figure 5.22 (m'_{ES}, $\Delta E'$ and NN'), Figure 5.23 (Dalitz invariant mass spectra), and Figure 5.24 ($m_{K^0_S\pi^0}$ in detail in the region of the $\bar{D}^0$). Similar constructive interference between the charged $K^0_S\pi$ resonances for B^+ and B^- can be seen in the signal-enriched projection plots for $m_{K^0_S\pi^+}$ separately for helicity angles with positive and negative cosines Figure 5.25.

5.6 Comments on the data fits

All the fits performed on pure and embedded toys, as well as the fit on the full Monte Carlo sample, show a good agreement between the fitted distributions and the simulated data. A proof of consistency is given by the projection plots (from Figure 5.9 to Figure 5.12) and the pull distributions (Table A.7 and Figure A.4). Moreover, the fit gives negligible biases on signal parameters even if the expected number of backgrounds events is wrong.

Unfortunately, fitting real data gives some inconsistencies. For the CP-blind fit, by

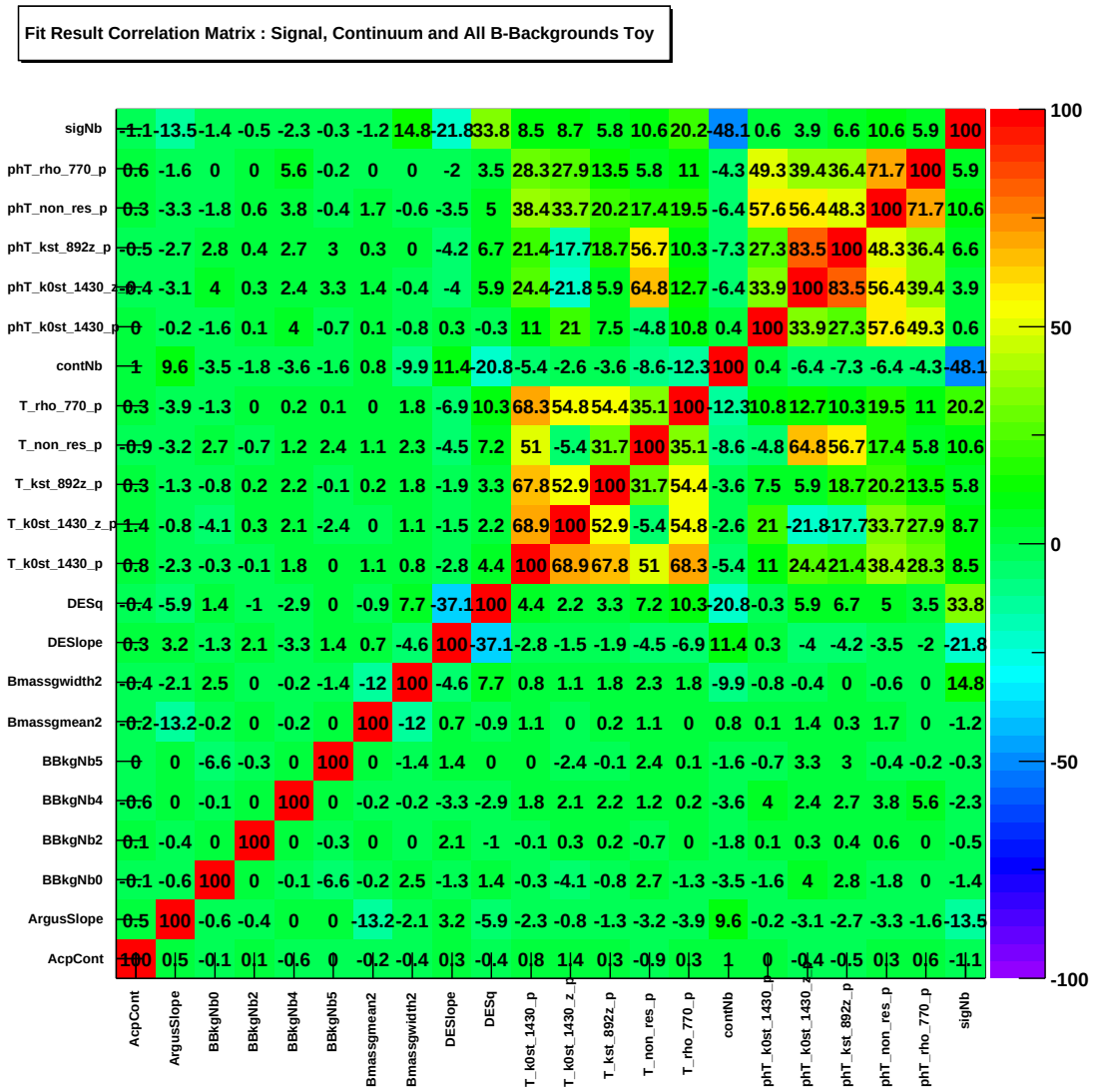

Figure 5.14: Correlation matrix for the CP-blind fit (*solution-1*).

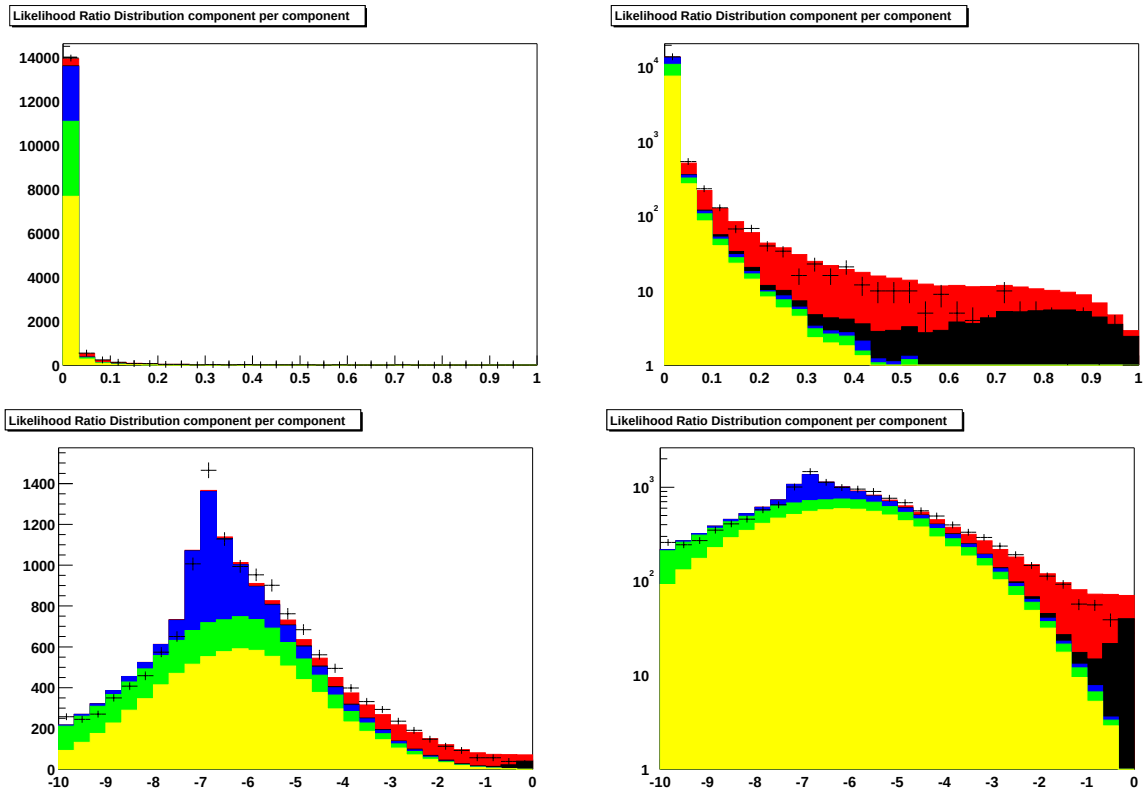

Figure 5.15: Likelihood ratio for the CP-blind fit (*solution-1*). The data are shown as point with error bars. The color code depicts the continuum (yellow), B background (green), $\bar{D}^0$ (blue), signal self cross feed (black), and truth-matched events (red) respectively. The various linear and log scales focus on where the signal dominates over the background and vice versa.

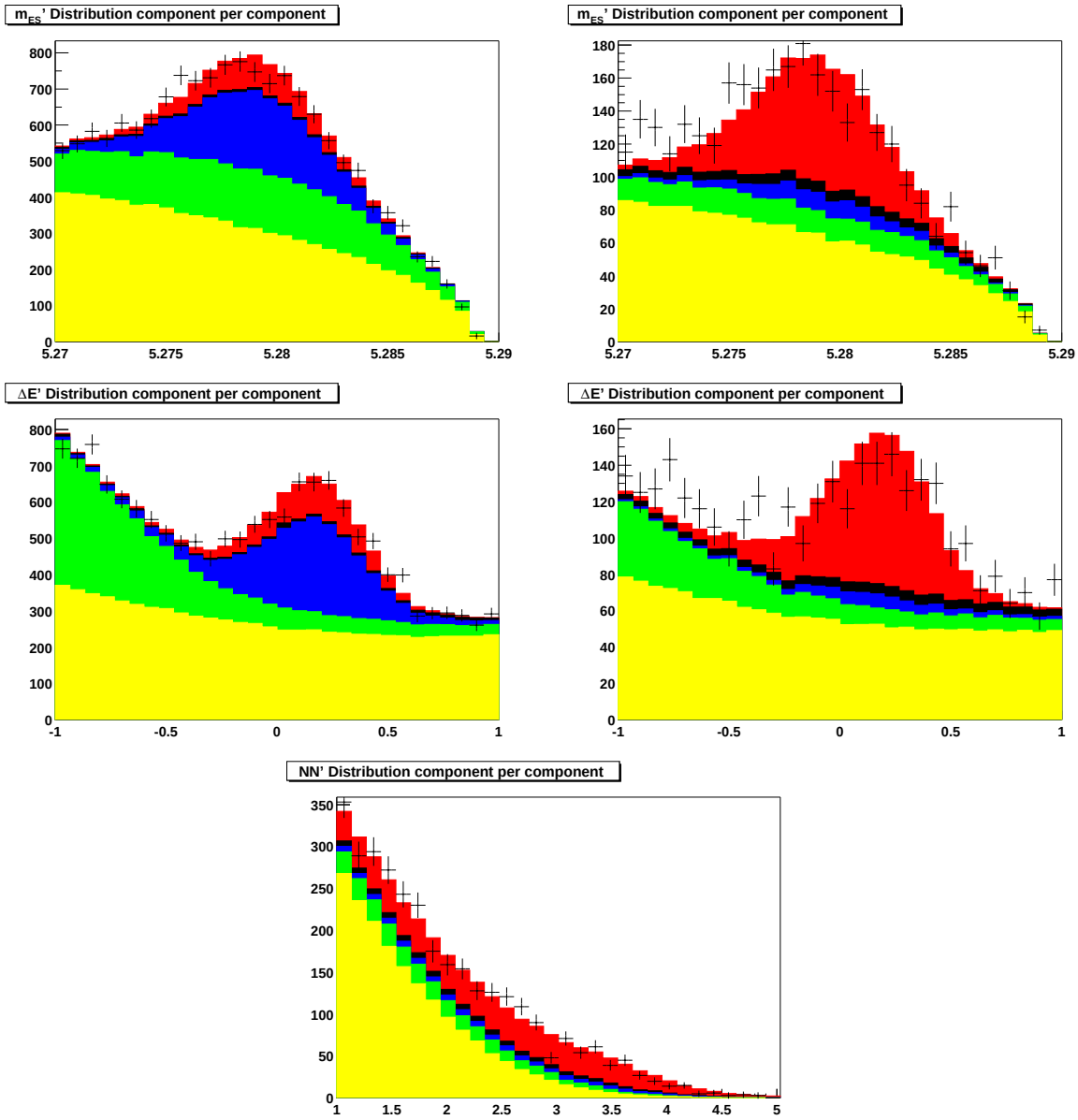

Figure 5.16: (top) m_{ES}, (middle) $\Delta E'$ and (bottom) NN' distributions for CP-blind fit (*solution-1*). The data are shown as points with error bars (all the data on the left, after a cut on R (computed excluding the plotted variable) to enhance signal on the right). The color code depicts the continuum (yellow), B background (green), $\bar{D}^0$ (blue), signal self cross feed (black), and truth-matched events (red) respectively.

	Solution-1		Solution-2	
Floating Parameter	Final Value	Error	Final Value	Error
Signal yield	1252	65	1258	70
Continuum yield	8128	108	8128	112
Continuum A_{CP}	-0.028	0.013	-0.028	0.014
Category #0 yield	2532	53	2527	54
Category #2 yield	321	20	322	20
Category #4 yield	7.9	4.8	7.8	6.8
Category #5 yield	237	28	235	28
Argus slope	-5.01	1.22	-5.00	1.19
B mass (MeV/c^2)	5279.36	0.075	5279.36	0.073
B mass width (MeV/c^2)	2.69	0.054	2.69	0.054
ΔE slope (GeV/$c^{2^{-1}}$)	-0.281	0.023	-0.281	0.025
ΔE intercept	0.214	0.046	0.214	0.050
$K^*(1430)^-$ (amp)	38.9	5.5	39.5	4.9
$K^*(1430)^+$ (amp)	24.4	4.4	24.6	4.6
$\bar{K}^*(1430)^0$ (amp)	35.2	5.0	35.9	4.6
$K^*(1430)^0$ (amp)	19.1	4.2	33.4	4.4
$K^*(892)^-$ (amp)	0.48	0.13	0.49	0.12
$\bar{K}^*(892)^0$ (amp)	0.53	0.13	0.54	0.16
$K^*(892)^0$ (amp)	0.69	0.13	0.65	0.13
$\overline{N.R.}$ (amp)	7.89	3.34	7.97	3.06
$N.R.$ (amp)	18.8	3.7	15.0	2.7
ρ^- (amp)	0.63	0.12	0.64	0.13
ρ^+ (amp)	0.73	0.13	0.75	0.13
$K^*(1430)^-$ (phase)	4	30	3	26
$K^*(1430)^+$ (phase)	-12	13	-16	17
$\bar{K}^*(1430)^0$ (phase)	-20	52	-21	47
$K^*(1430)^0$ (phase)	37	31	-133	25
$\bar{K}^*(892)^0$ (phase)	-155	60	-154	53
$K^*(892)^0$ (phase)	-70	35	80	35
$\overline{N.R.}$ (phase)	-92	52	-93	48
$N.R.$ (phase)	133	13	-135	24.
ρ^- (phase)	-153	65	-153	54
ρ^+ (phase)	94	29	-81	30

Table 5.7: Result of the nominal fit on data. The two almost degenerate solutions have $NLL_1 = -137575.3$, and $NLL_2 = -137574.8$. The phase angles are expressed in degrees. The K^{*+}isobar is the reference i.e. all amplitudes are measured with respect to $c(B^+ \to K^{*+}\pi^0) = 0.747$, and all B^+(resp. B^-) phases are differences with respect to $\phi(B^+ \to K^{*+}\pi^0)$ (resp. $\bar{\phi}(B^- \to K^{*-}\pi^0)$) which are set to zero.

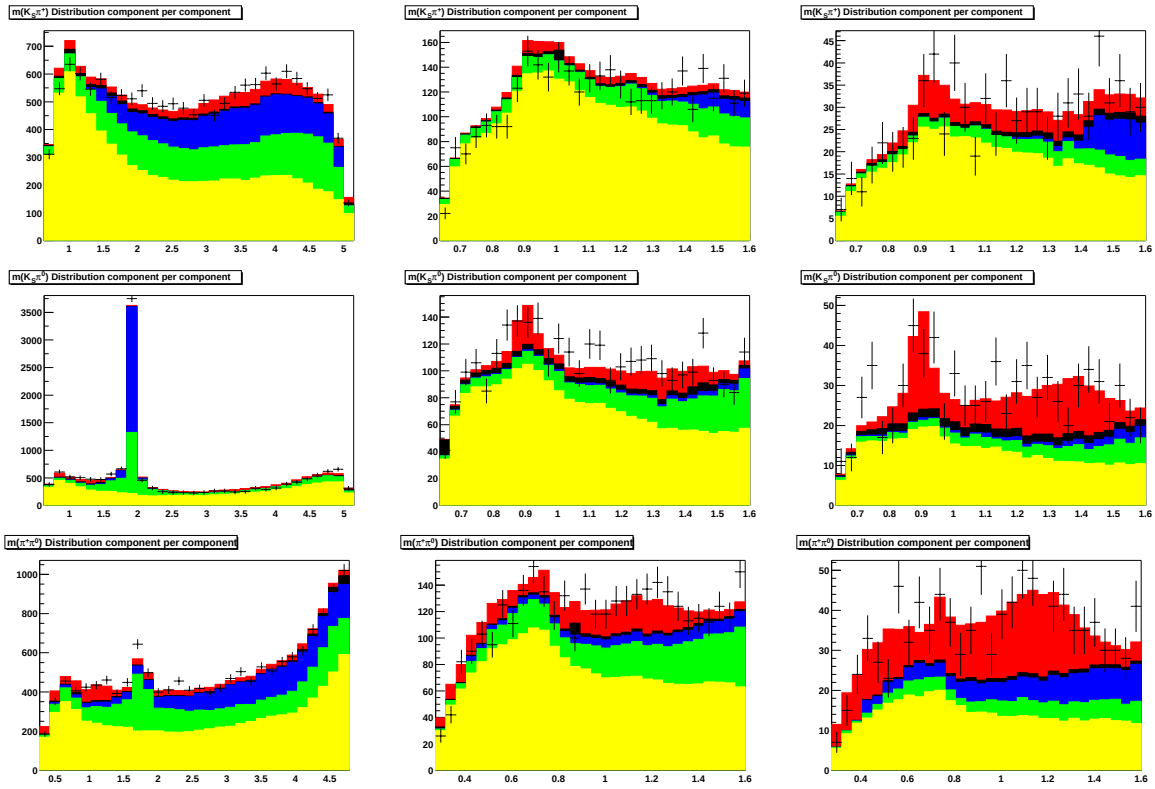

Figure 5.17: Distributions for the CP-blind fit (*solution-1*). (Top) $K^0_S\pi^+$ invariant mass all events (left), $m \leq 1.6$ GeV/c^2 (center) and for a sample enriched in signal by a cut on R (right). (Middle) the same for the $K^0_S\pi^0$ invariant mass. (Bottom) the same for the $\pi^-\pi^0$ invariant mass.
The data are shown as points with error bars. The color code depicts the continuum (yellow), B background (green), $\bar{D}^0$ (blue), signal self cross feed (black), and truth-matched events (red) respectively. The $\bar{D}^0$ mass peak which sticks out of the top-left plot is shown in detail in Figure 5.18.

	Solution-1		Solution-2	
Resonance	FF	A_{CP}	FF	A_{CP}
$K^*(892)^\pm$	0.0838 ± 0.0165	-0.421 ± 0.308	0.0805 ± 0.0147	-0.406 ± 0.281
$K^*(892)^0$	0.0816 ± 0.0348	-0.251 ± 0.324	0.0742 ± 0.0361	-0.180 ± 0.397
$N.R.$	0.1322 ± 0.0599	-0.702 ± 0.282	0.0867 ± 0.0325	-0.558 ± 0.418
$\rho(770)^\pm$	0.1104 ± 0.0418	-0.147 ± 0.251	0.1103 ± 0.0391	-0.152 ± 0.273
$K^*(1430)^\pm$	0.3268 ± 0.0806	0.435 ± 0.159	0.3202 ± 0.0743	0.440 ± 0.145
$K^*(1430)^0$	0.2496 ± 0.0706	0.546 ± 0.183	0.3555 ± 0.0757	0.070 ± 0.137
Total	0.985 ± 0.063	0.020 ± 0.281	1.0274 ± 0.1238	-0.786 ± 0.725

Table 5.8: Fitting fractions and A_{CP}'s parameters for the two solutions of the nominal fit on data.

looking at the $K^0_S\pi^+$ invariant mass distribution, we see a discrepancy in the $K^*(892)^+$ peak (Figure 5.17, first row) since the data points are under the fitted distributions. This is probably due to a wrong parametrization of the continuum PDF around the $K^*(892)^+$

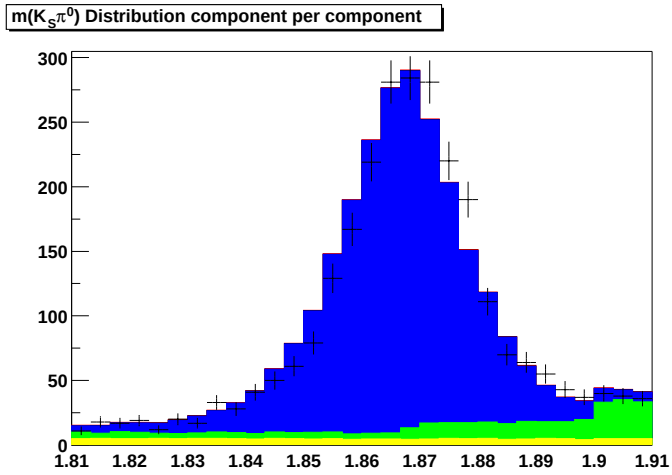

Figure 5.18: $K^0_S\pi^0$ invariant mass zoomed in the $\bar{D}^0$ mass region for the CP-blind fit (*solution-1*). The color code depicts the continuum (yellow), B background (green), $\bar{D}^0$ (blue), signal self cross feed (black), and truth-matched events (red) respectively.

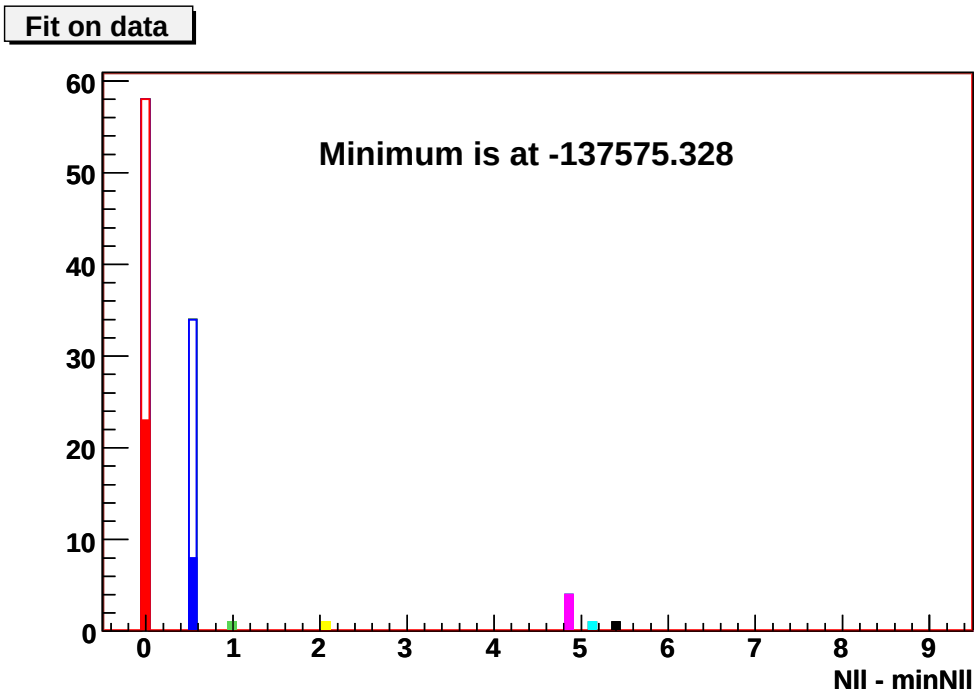

Figure 5.19: Spectrum of NLL_{min} for nominal 100 fits obtained by randomizing the initialization values of the fit parameters.

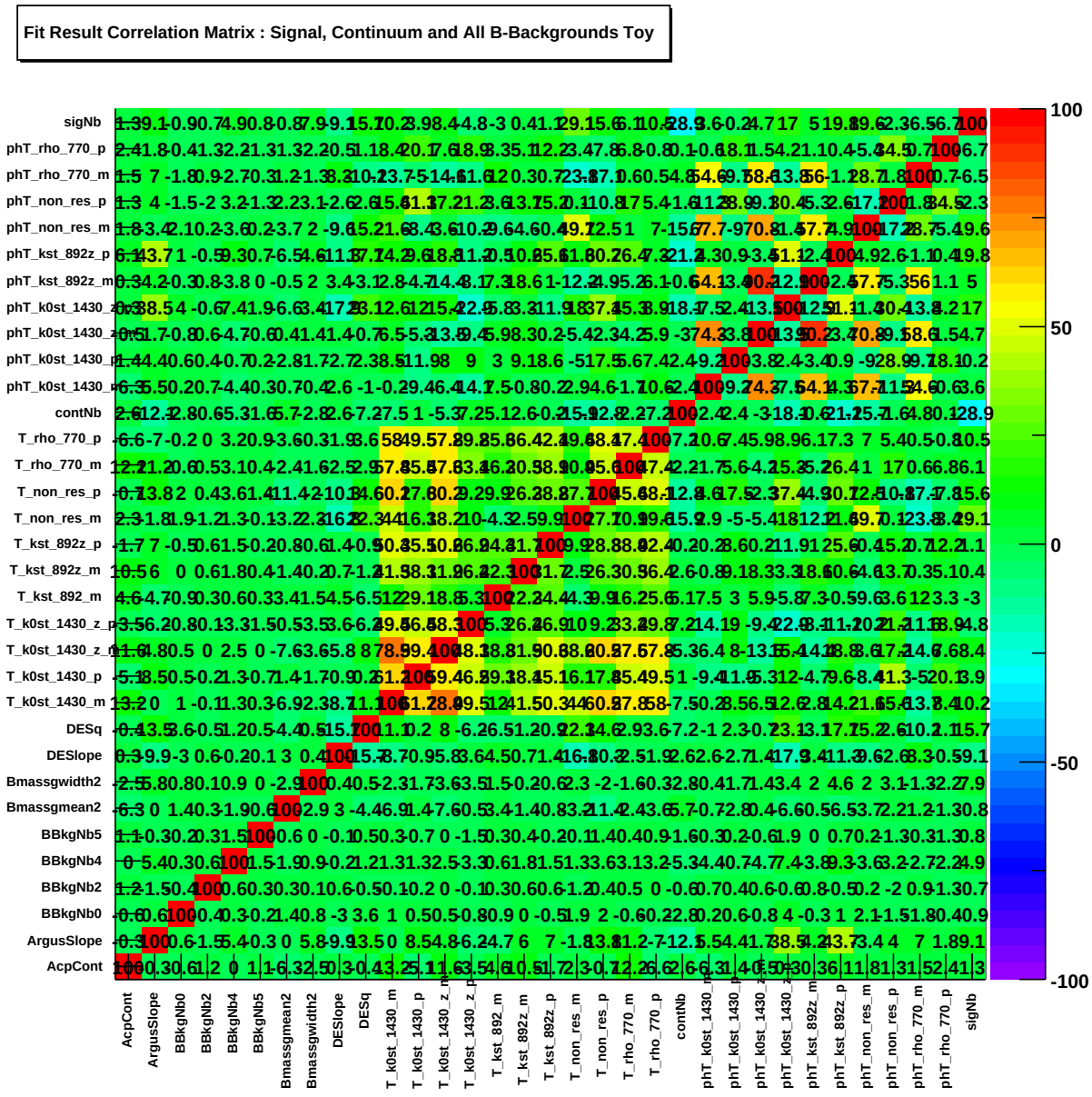

Figure 5.20: Correlation matrix for the nominal fit (*solution-1*).

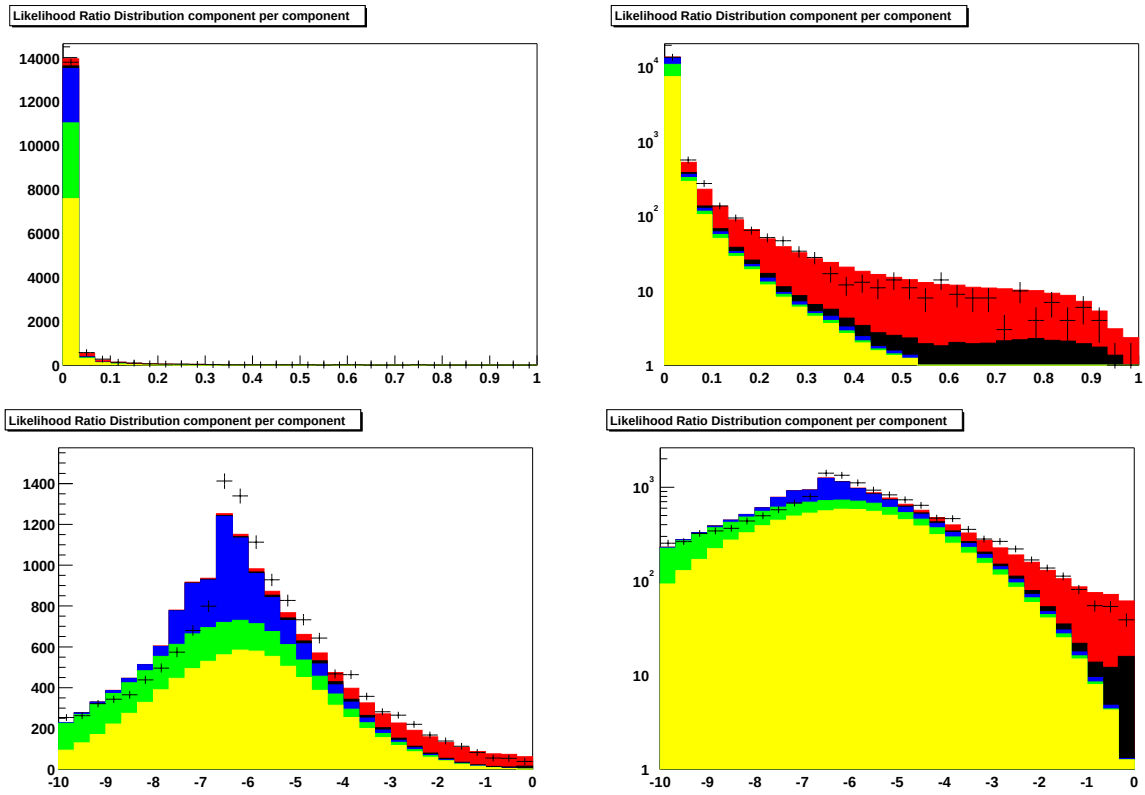

Figure 5.21: Likelihood ratio for the nominal fit (*solution-1*). The data are shown as point with error bars. The color code depicts the continuum (yellow), B background (green), $\bar{D}^0$ (blue), signal self cross feed (black), and truth-matched events (red) respectively. The various linear and log scales focus on where the signal dominates over the background and vice versa.

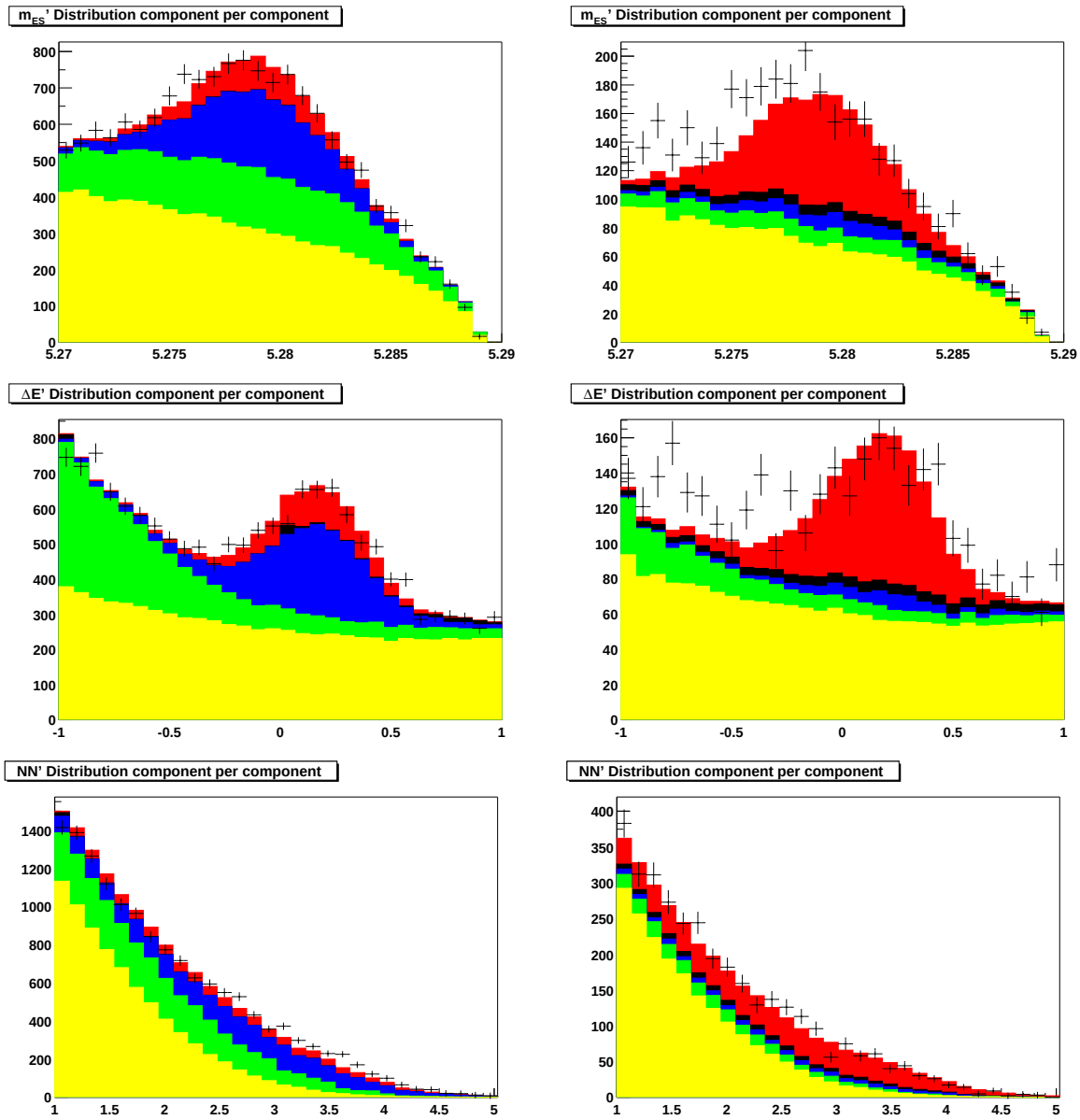

Figure 5.22: (top) m_{ES}, (middle) $\Delta E'$ and (bottom) NN' distributions for the nominal fit on data (*solution-1*). The data are shown as points with error bars (all the data on the left, after a cut on R (computed excluding the plotted variable) to enhance signal on the right). The color code depicts the continuum (yellow), B background (green), $\bar{D}^0$(blue), signal self cross feed (black), and truth-matched events (red) respectively.

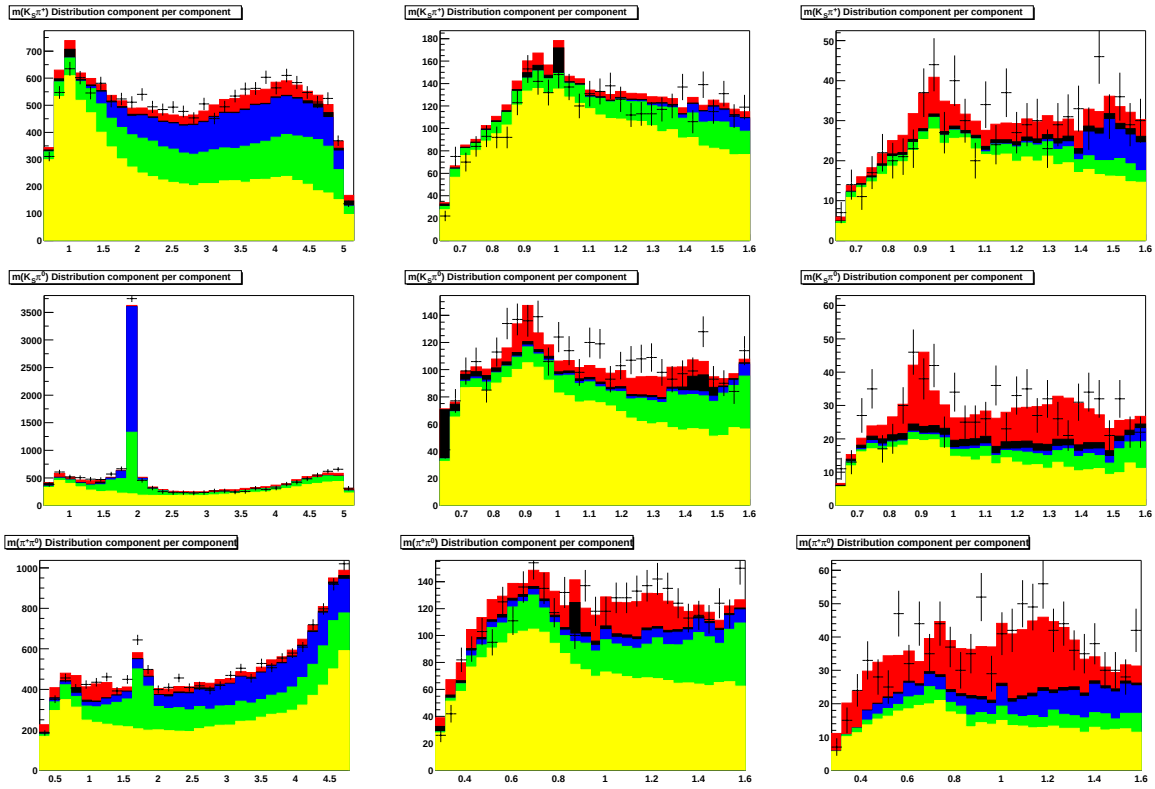

Figure 5.23: Distributions for the nominal fit on data (*solution-1*). (Top) $K^0_S\pi^+$ invariant mass all events (left), $m \leq 1.6$ GeV/c^2 (center) and for a sample enriched in signal by a cut on R (right). (Middle) the same for the $K^0_S\pi^0$ invariant mass. (Bottom) the same for the $\pi^-\pi^0$ invariant mass.
The data are shown as point with error bars. The color code depicts the continuum (yellow), B background (green), $\bar{D}^0$ (blue), signal self cross feed (black), and truth-matched events (red) respectively. The $\bar{D}^0$ mass peak which sticks out of the top-left plot is shown in detail in Figure 5.24.

peak. The m_{ES} and $\Delta E'$ distributions have some problems as well (in particular in the signal enhanced plots of Figure 5.16). The same discrepancies still occur in the *solution-1* nominal fit.

Further studies are in progress in order to understand these discrepancies. For instance, tighter selection criteria should reduce significantly the backgrounds and therefore improve the fit accuracy, although this could result in increased uncertainties. For the time being, we complete the analysis and evaluate systematic uncertainties for the current selection criteria in order to give an estimate of the precision which can be attained with the *BABAR* dataset.

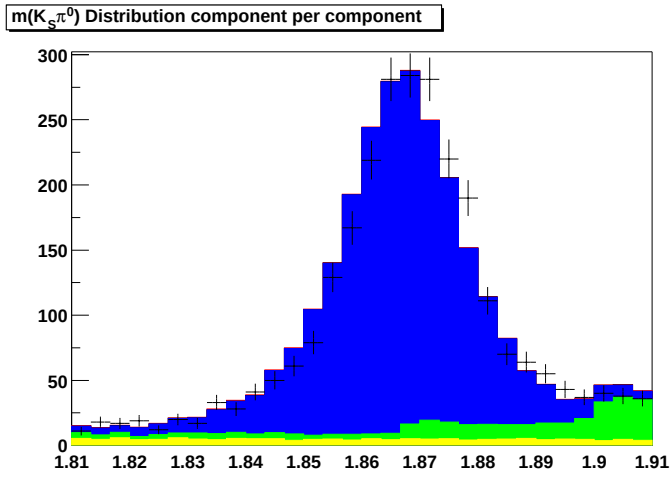

Figure 5.24: $K^0_S\pi^0$ invariant mass zoomed in the $\bar{D}^0$ mass region for the nominal fit on data (*solution-1*). The color code depicts the continuum (yellow), B background (green), $\bar{D}^0$ (blue), signal self cross feed (black), and truth-matched events (red) respectively.

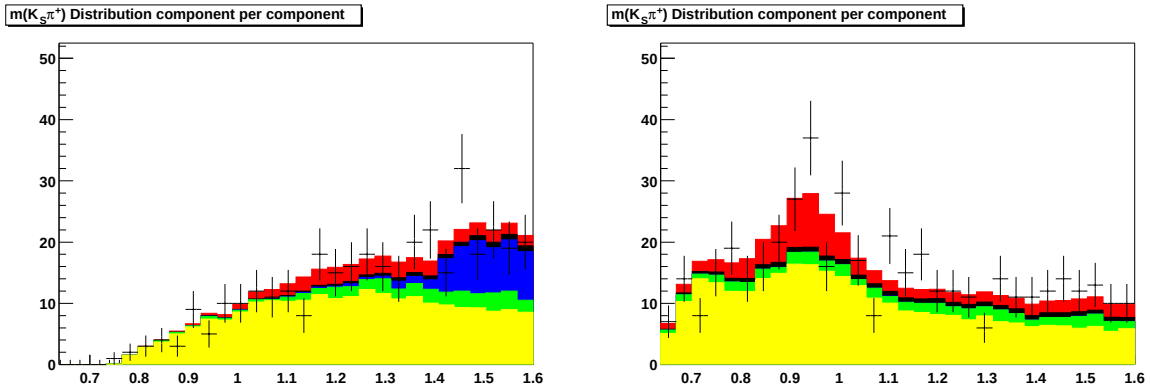

Figure 5.25: Nominal fit on data (*solution-1*) signal-enriched spectra of $m_{K^0_S\pi^+}$ in the low-mass resonance region and different ranges of the helicity angle, $\theta_{K^0_S\pi^+}$. (a) $0° < \theta_{K^0_S\pi^+} < 90°$, (b) $90° < \theta_{K^0_S\pi^+} < 180°$. The data sample is enriched in signal events. An interference between the vector and scalar K^{*+} is apparent through the opposite forward-backward asymmetries below and above the $K^*(892)$.

Chapter 6

Systematics

Several sources of systematic uncertainties affect the fitting fractions, CP-asymmetries, isobar phases and selection efficiencies.

- *Detector related effects*, concerning the reconstruction of the particles, estimated in Section 6.1.
- *Signal model uncertainties*, estimated in Section 6.2 by varying the isobar contents of the signal, adding or removing isobar components in the decay amplitudes.
- *Fit model uncertainties*, estimated by varying the fixed parameters in the PDFs within the measured uncertainties or conservatively chosen ranges. We consider in turn, the PDF shape parameters in Section 6.3, the B-background properties (fixed yields and A_{CP}) in Section 6.4, and the resonance lineshape parameters (masses, widths, barrier factors) in Section 6.5. We list in Table A.8, Table A.9, and Table A.10 the parameters `p` of the PDFs which are fixed in the nominal fit together with the range [`p-lo`, `p-hi`] $\equiv$ p$\pm\delta p$ over which we vary them to determine systematic uncertainties. The nominal fit is repeated for each `p-lo`/`p-hi` value and we record the deviations of the fitted parameters and the physical measurements which derive from them. We separately tabulate the deviations for the isobar fractions FF, the A_{CP}'s and the phases ϕ when relevant.
- The uncertainty associated to the distortion of the *Dalitz plot PDF* distribution induced by the B meson mass constraint on continuum events is estimated in Section 6.6

- The intrinsic *fit bias* is covered in Section 6.7.

Table 6.2 presents a summary of all the systematic uncertainties, except the uncertainties related to the detector effects that are in summarized Table 6.1.

6.1 Detector related effects

6.1.1 Charged particle tracking

Any differences between data and Monte Carlo simulation can potentially lead to a distortion in the distribution of the kinematical variables under study, as well as in the efficiency calculations.

To assign a systematic uncertainty on the charged particle tracking, a common prescription within *BABAR* measurements has been followed. No correction has been applied to Monte Carlo tracks, but a systematic uncertainty per track has been assigned.

The *BABAR* task force for the tracking efficiency [68] recommends a systematic uncertainty of 0.8% per charged track to be applied, which translates into a corresponding systematic uncertainty due to tracking efficiency being applied to each branching fraction measurement.

6.1.2 K_S reconstruction

Correction factors are needed for the tracking of the K_S particles, to correct for different reconstruction efficiencies in data and Monte Carlo. Corrections are necessary for the transverse momentum, the polar angle of the track in the laboratory frame and the POCA of the track in the xy plane.

The reconstruction efficiency in MC and data is determined by using a large semi-inclusive sample of K_S candidates [69]. The data/MC K_S reconstruction efficiency corrections are determined with a statistical error of 0.6-1.0%. Further studies indicate that the systematic uncertainty is about 1.5% which leads to a $\sim$1.8% total uncertainty on the corrections of the K_S reconstruction efficiency.

6.1.3 Reconstruction of neutral particles

Differences between data and Monte Carlo simulation in the photon detection efficiency and resolution, as well as additional energy depositions in the EMC, can impact the distributions of the kinematic variables used to reconstruct neutral pions in this analysis.

Two different control samples are used to check for disagreements between data and Monte Carlo simulation in efficiency and energy resolution. The study is performed using the τ hadronic decays that represent an abundant source of neutral pions. The $\tau \to e\nu\bar{\nu}$ decay is identified in $e^+e^- \to \tau^+\tau^-$ events. The ratio $R = N(\tau \to h^\pm\pi^0\nu_\tau)/N(\tau \to h^\pm\pi^0\pi^0\nu_\tau)$ is computed both for data and Monte Carlo as a function of the π^0 energy in order to evaluate possible differences in efficiency. The agreement has been found to be good and the ratio is compatible with the unity in the full range. A systematic uncertainty of 3% per neutral pion is assigned, due to uncertainties in the hadronic interactions in the EMC, to the photon background being not perfectly modeled in the Monte Carlo, and to the uncertainty in the τ branching fractions in $\pi\nu_\tau$ and $\rho\nu_\tau$ final states. The corresponding systematic uncertainty to each branching fraction measurement is therefore 3%.

The resolution has been studied taking π^0s from both $\tau \to h^\pm\pi^0\nu_\tau$ and $\tau \to h^\pm\pi^0\pi^0\nu_\tau$ decays. The π^0 mass is fitted in energy bins and the resolution (corresponding to the σ of a Gaussian fit) is then compared between data and Monte Carlo. The Monte Carlo resolution is changed by applying a smearing factor such to be identical to data. Similar corrections are applied on Monte Carlo to take into account differences in the energy scale and effects due to energy deposits close to crystal boundaries and to the edges between the barrel and the endcap of the EMC. These factors are determined as well with control samples such as $\mu\mu\gamma$ and $B \to K^*(K^+\pi^-)\gamma$ decays. All corrections turn out to be small.

Effect	systematic error [%]
Charged particle tracking (π^+)	0.8
K_S reconstruction	1.8
Neutral reconstruction (π^0)	3.0
Total error ($\Delta\epsilon$)	**3.6**

Table 6.1: Summary of the relative systematic uncertainties on the branching fractions due the detector related effects.

6.2 Extra Resonances in the signal model

Variants of the nominal fit in which one resonance component is removed or one less significant mode is added result in negative loglikelihood changes by amounts given in Table A.11 The removal of any component of the signal model result in significantly worse fits. On the contrary, when other resonances are added, the significance of the fit does not vary appreciably. Those fits where one adds in turn less significant channels one at a time to the nominal model give the results gathered in Table A.12. The positive (negative) systematic uncertainties on branching fractions and asymmetries are the averages of the positive (negative) variations with respect to the nominal results.

6.3 Shape parameters

Each of the fixed parameters of the m_{ES}, $\Delta E'$, NN' and $\bar{D}^0$ mass PDFs, is varied from `p-lo` to `p-hi`. The deviations of the isobar fractions are shown in Table A.13, Table A.14, Table A.15 and Table A.16 Those of the A_{CP}'s can be seen in Table A.17, Table A.18, Table A.19 and Table A.20. The systematic uncertainties on the results are given by the sum in quadrature of the different effects.

6.4 B-background

All the yields and A_{CP}'s for all the B-background categories from #1 to #7, are varied from `p-lo` to `p-hi`. The deviations of the isobar fractions are shown in Table A.21, and those of the A_{CP}'s in Table A.22. Again, the systematic uncertainty is the sum in quadrature of the resulting effects.

6.5 Lineshapes

In principle, the uncertainty due to the lineshapes of the subresonant structures should be estimated by varying the masses, widths and barrier factors within their errors from the PDG [40]. For this thesis we assume that these systematic uncertainties are small, as in the $B^0 \to K^+\pi^-\pi^0$ Dalitz analysis [66], and we neglect them. This assumption is

probably not well established, so this issue has to be revisited in further studies.

6.6 Continuum Dalitz plot PDF

We use previous analyses as a reference to guess the systematic uncertainty due to inaccuracies in the parametrization of the Dalitz plot PDF for the continuum. The resulting uncertainties are reported in Table 6.2.

6.7 Fit Bias

The difference between fitted values and the generation ones, observed in the embedded fits (Table A.7), is taken as systematic uncertainty due to biases in the fit procedure.

6.8 Systematics Summary

All systematic uncertainties but the detector related ones are reported in Table 6.2, and used in the next chapter to evaluate the systematic errors on the branching ratios.

6.9 Branching ratio uncertainties

The sources of systematic uncertainty on the branching ratio $\mathcal{B}_i$ of mode i can be determined from:

$$\mathcal{B}_i = \frac{\mathrm{FF}_i N_{\mathrm{sig}}}{\epsilon_i N_{B^+B^-}} \tag{6.1}$$

where ϵ_i is the total efficiency, N_{sig} the total number of signal events and $N_{B^+B^-}$ the numbers of B^+B^- pairs in the data. Each of the variables on the right hand side is a source of statistical and systematic uncertainty. The sum of the statistical and systematic uncertainties on $N_{B^+B^-}$ is found to be 1.1% [70]. The total systematic uncertainties for ϵ_i and FF_i are reported in Tables 6.2 and 6.1.

		ΔFF (%)	ΔA_{CP}	$\Delta\phi$ (°)
$(K\pi)_0^{*+}\pi^0$	Dalitz plot model	$^{+9.4}_{-4.6}$	$^{+0.12}_{0.17}$	
	Shape parameters	±1.1	$^{+0.06}_{-0.05}$	
	B background	$^{+0.98}_{-1.13}$	$^{+0.04}_{-0.05}$	
	Continuum DP PDF	±1.0		
	Fit bias	±4.8	±0.07	±20
	Total	$^{+10.7}_{-6.9}$	$^{+0.16}_{-0.20}$	–
$(K\pi)_0^{*0}\pi^+$	Dalitz plot model	$^{+7.4}_{-0.9}$	$^{-0.03}_{-0.53}$	
	Shape parameters	$^{+0.69}_{-0.94}$	$^{+0.03}_{-0.05}$	
	B background	$^{+1.35}_{-0.36}$	$^{+0.04}_{-0.05}$	
	Continuum DP PDF	±1.0		
	Fit bias	±1.9	±0.02	±7
	Total	$^{+7.9}_{-2.5}$	$^{+0.06}_{-0.54}$	–
$K^{*+}(892)\pi^0$	Dalitz plot model	±1.1	$^{+0.07}_{-0.01}$	
	Shape parameters	$^{+0.96}_{-0.84}$	±0.02	
	B background	$^{+0.12}_{-1.98}$	±0.01	
	Continuum DP PDF	±1.0		
	Fit bias	±0.5	±0.02	
	Total	$^{+1.8}_{-2.7}$	$^{+0.08}_{-0.03}$	reference
$K^{*0}(892)\pi^+$	Dalitz plot model	$^{+0.5}_{-1.6}$	$^{+0.11}_{-0.03}$	
	Shape parameters	±1.0	±0.03	
	B background	$^{+0.19}_{-0.17}$	$^{+0.2}_{-0.03}$	
	Continuum DP PDF	±1.0		
	Fit bias	±1.0	±0.08	±13
	Total	$^{+1.8}_{-2.4}$	±0.09	–
NR	Dalitz plot model	$^{+2.1}_{-8.0}$	$^{+0.21}_{-0.03}$	
	Shape parameters	$^{+2.7}_{-4.1}$	$^{+0.13}_{-0.10}$	
	B background	$^{+1.0}_{-0.9}$	$^{+0.03}_{-0.06}$	
	Continuum DP PDF	±1.0		
	Fit bias	±1.0	±0.03	±10
	Total	$^{+3.8}_{-10.3}$	$^{+0.25}_{-0.13}$	–
$\rho(770)^+K_S^0$	Dalitz plot model	$^{+0.4}_{-1.2}$	$^{0.42}_{-0.02}$	
	Shape parameters	±2.0	±0.04	
	B background	±0.14	±0.03	
	Continuum PDF	±1.0		
	Fit bias	±1.5	±0.09	±2
	Total	$^{+2.7}_{-3.0}$	$^{+0.43}_{-0.10}$	–

Table 6.2: Summary of the (absolute) systematic uncertainties. The systematic uncertainties are equal for the phases ϕ and $\overline{\phi}$. All phases ϕ are referenced to $\phi_{K^{*+}(892)\pi^0}$ and $\overline{\phi}$ to $\phi_{K^{*-}(892)\pi^-}$.

Chapter 7

Conclusions

7.1 Conclusions

We obtain 1252 ± 65 (statistical error) $^{+18}_{-13}$ (systematical error) charmless signal events from the fit to the data sample (*solution-1* in Table 5.7). The inclusive charmless signal efficiency is estimated to be 12.34% with the observed Dalitz plot structure. We measure the inclusive charmless branching fraction to be:

$$\mathcal{B}(B^+ \to K_S\pi^+\pi^0) = (28.13 \ \pm 1.49\ ^{+1.73}_{-1.46}) \times 10^{-6} \tag{7.1}$$

where the first error is statistical and the second systematical.

The branching ratios for all the decays of the signal model considered, are listed in Table 7.1.

Mode	B.R. $[\times 10^{-6}]$
$B^+ \to K^*(892)^+\ \pi^0$	$2.34 \pm 0.47\ ^{+0.51}_{-0.76}$
$B^+ \to K^*(892)^0\ \pi^+$	$2.33 \pm 1.00\ ^{+0.52}_{-0.70}$
$B^+ \to K_S\pi^+\pi^0$ N.R.	$3.53 \pm 1.61\ ^{+1.02}_{-2.75}$
$B^+ \to K_S\ \rho(770)^+$	$3.11 \pm 1.19\ ^{+0.77}_{-0.85}$
$B^+ \to K^*(1430)^+\ \pi^0$	$9.12 \pm 2.30\ ^{+3.01}_{-1.95}$
$B^+ \to K^*(1430)^0\ \pi^+$	$7.14 \pm 2.05\ ^{+2.28}_{-0.76}$

Table 7.1: Branching ratios obtained from the nominal fit on data including statistical and systematical uncertainties.

We also obtain 2532 ± 53 events for $B^+ \to \bar{D}^0\pi^+$, that was our category #0 of B-background, that correspond to a $\mathcal{B}(B^+ \to \bar{D}^0(\to K_S\pi^0)\ \pi^+) = (56.88 \pm 1.35) \times 10^{-6}$, where the error is statistical only.

The results obtained in this thesis represent a first attempt in measuring branching fractions and CP asymmetries of the resonant structures involved in the $K^0_S\pi^+\pi^0$ decay, and show the potential capabilities of the *BABAR* dataset. Their order of magnitude agrees with both theoretical expectations and with isospin-conjugate decays.

The current measurements exhibit a discrepancy between some fit results and the actual data. As shown in Chapter 5, the projection plots for the $K^0_S\pi^-$ invariant mass show a discrepancy in the $K^*(892)^+$ region both in the CP-blind fit and in the nominal one. Discrepancies are present also in m_{ES} and $\Delta E'$ distributions. This behaviour is possibly due to backgrounds being not correctly estimated and/or parametrized, in particular the continuum background.

The above problems might be cured by using tighter requirements for ΔE. Preliminary studies show that backgrounds can be reduced as much as 50% at the expense of small signal inefficiencies. Tightening the cut on the Neural Network will also decrease the amount of continuum events. In any case a better parametrization of the Dalitz plot PDF for continuum events is necessary, in order to take care of all the complex structures. In general, simplifying the fit and reducing the number of categories that need to be parametrized should help in making it more robust and reliable. As stated before, the results shown in these thesis have not been internally reviewed by the *BABAR* collaboration; therefore, they should not be regarded as official *BABAR* results.

Appendix A

A.1 Toy studies

We build three histograms for each parameter (isobar amplitudes, isobar phases and yields): the residue (reconstructed - generated value), the standard deviation, and the pull (residue/standard deviation).

Resonance	Pull Amplitude		Pull Phase	
	μ	σ	μ	σ
$\rho(770)^+$	-0.24	1.00	-0.13	1.06
$\rho(770)^-$	-0.29	0.98	-0.16	1.07
$K^*(892)^-$	-0.10	0.96	none	none
$K^*(892)^0$	-0.05	0.99	-0.008	1.21
$\bar{K}^*(892)^0$	-0.06	1.00	-0.08	1.02
$K^*(1430)^+$	-0.08	0.93	0.07	1.02
$K^*(1430)^-$	-0.10	0.95	0.06	0.99
$K^*(1430)^0$	-0.22	0.97	-0.11	1.19
$\bar{K}^*(1430)^0$	-0.20	1.00	-0.14	1.07
$N.R.$	-0.11	0.95	-0.25	1.13
$\overline{N.R.}$	-0.1 1	0.98	-0.21	1.03
Resonance	Residue Amplitude		Residue Phase	
	μ	σ	μ	σ
$\rho(770)^+$	-0.0001	0.20	-3.81	22.21
$\rho(770)^-$	-0.009	0.19	-4.34	23.78
$K^*(892)^-$	0.009	0.13	none	none
$K^*(892)^0$	0.02	0.16	0.64	31.41
$\bar{K}^*(892)^0$	0.02	0.16	-1.02	26.14
$K^*(1430)^+$	0.90	5.60	0.61	11.42
$K^*(1430)^-$	0.73	5.25	0.54	11.30
$K^*(1430)^0$	0.12	6.08	-0.90	30.85
$\bar{K}^*(1430)^0$	0.29	6.19	-2.53	26.15
$N.R.$	0.05	3.19	-3.66	17.79
$\overline{N.R}$	0.07	3.04	-3.10	16.08

Table A.1: Signal only Pure Toys. Pull and residue mean and σ for the amplitudes and phases.

Resonance	Pull Amplitude		Pull Phase	
	μ	σ	μ	σ
$\rho(770)^+$	-0.23	0.91	-0.23	1.08
$\rho(770)^-$	-0.30	0.96	-0.25	1.11
$K^*(892)^-$	-0.11	0.92	none	none
$K^*(892)^0$	-0.06	0.88	-0.05	1.19
$\bar{K}^*(892)^0$	-0.04	0.88	-0.12	1.15
$K^*(1430)^+$	-0.11	0.93	0.09	1.08
$K^*(1430)^-$	-0.11	0.93	0.05	1.05
$K^*(1430)^0$	-0.19	0.94	-0.13	1.16
$\bar{K}^*(1430)^0$	-0.25	0.98	-0.16	1.14
$N.R.$	-0.12	0.94	-0.30	1.13
$\overline{N.R.}$	-0.11	0.97	-0.33	1.06
Resonance	Residue Amplitude		Residue Phase	
	μ	σ	μ	σ
$\rho(770)^+$	-0.006	0.18	-6.36	24.74
$\rho(770)^-$	-0.02	0.19	-6.58	24.09
$K^*(892)^-$	0.008	0.12	none	none
$K^*(892)^0$	0.02	0.15	-0.54	32.28
$\bar{K}^*(892)^0$	0.02	0.15	-2.41	32.28
$K^*(1430)^+$	0.60	5.50	0.86	12.29
$K^*(1430)^-$	0.62	5.07	0.31	11.83
$K^*(1430)^0$	0.07	5.82	-2.84	31.14
$\bar{K}^*(1430)^0$	-0.22	6.05	-4.10	31.96
$N.R.$	0.05	3.22	-4.77	18.13
$\overline{N.R.}$	0.08	3.29	-4.93	16.84
Resonance	Pull		Residue	
	μ	σ	μ	σ
Signal yield	0.02	1.00	0.96	35.71
D^0 yield	-0.04	0.97	-1.17	48.25

Table A.2: Signal + D0 Pure Toys. Pull and residue mean and σ for the amplitudes and phases.

Resonance	Pull Amplitude		Pull Phase	
	μ	σ	μ	σ
$\rho(770)^+$	-0.20	0.91	-0.19	1.13
$\rho(770)^-$	-0.24	0.99	-0.33	1.14
$K^*(892)^-$	-0.10	0.94	none	none
$K^*(892)^0$	-0.02	0.90	0.00	1.27
$\bar{K}^*(892)^0$	-0.02	0.87	-0.16	1.30
$K^*(1430)^+$	-0.03	0.88	-0.009	1.01
$K^*(1430)^-$	-0.03	0.89	-0.09	0.99
$K^*(1430)^0$	-0.22	0.96	-0.21	1.24
$\bar{K}^*(1430)^0$	-0.20	0.99	-0.23	1.39
$N.R.$	-0.03	0.97	-0.45	1.10
$\overline{N.R.}$	-0.08	0.93	-0.42	1.11
Resonance	Residue Amplitude		Residue Phase	
	μ	σ	μ	σ
$\rho(770)^+$	0.02	0.27	-8.70	42.21
$\rho(770)^-$	0.01	0.28	-13.75	43.60
$K^*(892)^-$	0.01	0.20	none	none
$K^*(892)^0$	0.05	0.22	0.91	51.28
$\bar{K}^*(892)^0$	0.04	0.21	-3.43	53.59
$K^*(1430)^+$	2.32	8.07	-0.99	17.83
$K^*(1430)^-$	2.19	7.79	-2.52	17.50
$K^*(1430)^0$	0.36	8.32	-6.36	50.05
$\bar{K}^*(1430)^0$	0.53	8.71	-6.68	54.38
$N.R.$	0.44	5.02	-12.56	31.20
$\overline{N.R.}$	0.11	4.67	-9.84	36.80
Resonance	Pull		Residue	
	μ	σ	μ	σ
Signal yield	0.39	0.95	21.23	50.18
Continuum yield	-0.17	0.95	-14.85	90.36
A_{CP} continuum	-0.07	0.99	-0.001	0.01

Table A.3: Signal + continuum Pure Toys. Pull and residue mean and σ for the amplitudes, phases and yields.

Resonance	Pull Amplitude		Pull Phase	
	μ	σ	μ	σ
$\rho(770)^+$	-0.31	1.00	-0.19	1.25
$\rho(770)^-$	-0.27	0.96	-0.25	1.23
$K^*(892)^-$	-0.18	0.91	none	none
$K^*(892)^0$	-0.05	0.88	-0.18	1.30
$\bar{K}^*(892)^0$	-0.06	0.89	-0.17	1.38
$K^*(1430)^+$	-0.01	0.90	-0.03	1.08
$K^*(1430)^-$	0.04	0.90	0.01	0.99
$K^*(1430)^0$	-0.32	0.99	-0.19	1.28
$\bar{K}^*(1430)^0$	-0.36	1.06	-0.22	1.39
$N.R.$	-0.003	0.92	-0.47	1.17
$\overline{N.R.}$	-0.04	1.03	-0.53	1.21
Resonance	Residue Amplitude		Residue Phase	
	μ	σ	μ	σ
$\rho(770)^+$	0.002	0.27	-8.25	51.09
$\rho(770)^-$	0.009	0.27	-10.39	51.88
$K^*(892)^-$	0.001	0.18	none	none
$K^*(892)^0$	0.04	0.21	-5.30	60.77
$\bar{K}^*(892)^0$	0.04	0.20	-4.74	64.73
$K^*(1430)^+$	2.17	7.89	-1.23	18.78
$K^*(1430)^-$	2.50	7.81	-0.90	17.93
$K^*(1430)^0$	-0.36	8.08	-6.73	59.36
$\bar{K}^*(1430)^0$	-0.44	8.94	-8.47	64.32
$N.R.$	0.62	5.23	-13.34	36.55
$\overline{N.R.}$	0.23	5.54	-14.85	39.10
Resonance	Pull		Residue	
	μ	σ	μ	σ
Signal yield	0.43	1.00	25.60	57.37
Continuum yield	-0.13	0.97	-16.22	125.01
A_{CP} continuum	-0.03	1.08	-0.0005	0.02
D^0 yield	-0.06	1.00	-2.54	51.86
Category #1	-0.006	0.97	0.30	34.85
Category #2	-0.01	1.04	0.20	23.78
Category #3	0.05	0.98	5.44	71.42
Category #4	-0.23	1.14	-2.10	17.60
Category #5	-0.02	0.99	0.16	50.66
Category #6	-0.14	0.99	-18.23	141.45
Category #7	0.02	1.01	3.28	85.85

Table A.4: Full model Pure Toys. Pull and residue mean and σ for the amplitudes, phases and yields.

Resonance	Pull Amplitude		Pull Phase	
	μ	σ	μ	σ
$\rho(770)^+$	0.01	0.93	0.43	0.97
$\rho(770)^-$	0.03	0.95	0.33	0.97
$K^*(892)^-$	-0.05	0.95	none	none
$K^*(892)^0$	-0.001	0.89	0.51	1.09
$\bar{K}^*(892)^0$	0.02	0.96	0.49	1.07
$K^*(1430)^+$	-0.03	0.97	0.15	1.06
$K^*(1430)^-$	-0.01	0.96	-0.02	1.01
$K^*(1430)^0$	-0.21	0.97	0.25	1.01
$\bar{K}^*(1430)^0$	-0.17	0.96	0.25	1.08
$N.R.$	-0.39	1.00	0.13	0.99
$\overline{N.R.}$	-0.48	1.06	-0.05	1.09
Resonance	Residue Amplitude		Residue Phase	
	μ	σ	μ	σ
$\rho(770)^+$	0.05	0.20	7.30	19.33
$\rho(770)^-$	0.05	0.20	5.46	18.84
$K^*(892)^-$	0.02	0.13	none	none
$K^*(892)^0$	0.03	0.15	13.06	26.81
$\bar{K}^*(892)^0$	0.04	0.16	13.31	27.85
$K^*(1430)^+$	1.27	5.76	1.43	11.68
$K^*(1430)^-$	1.21	5.52	-0.40	11.96
$K^*(1430)^0$	0.05	5.92	6.95	25.47
$\bar{K}^*(1430)^0$	0.32	5.92	6.55	28.14
$N.R.$	-0.80	3.09	2.05	15.82
$\overline{N.R.}$	-1.03	3.09	-1.32	18.09

Table A.5: Signal only embedded fits. Pull and residue mean and σ for the amplitudes and phases.

Resonance	Pull Amplitude		Pull Phase	
	μ	σ	μ	σ
$\rho(770)^+$	-0.07	0.87	0.04	1.11
$\rho(770)^-$	-0.03	0.93	-0.06	0.98
$K^*(892)^-$	-0.11	0.95	none	none
$K^*(892)^0$	0.01	0.87	0.11	1.25
$\bar{K}^*(892)^0$	0.04	0.89	0.17	1.12
$K^*(1430)^+$	0.01	0.91	0.02	0.99
$K^*(1430)^-$	0.05	0.86	-0.01	1.04
$K^*(1430)^0$	-0.22	0.95	0.02	1.21
$\bar{K}^*(1430)^0$	-0.14	0.91	0.05	1.15
$N.R.$	-0.07	0.97	-0.14	1.00
$\overline{N.R.}$	-0.09	0.92	-0.20	1.07
Resonance	Residue Amplitude		Residue Phase	
	μ	σ	μ	σ
$\rho(770)^+$	0.06	0.28	-0.57	38.55
$\rho(770)^-$	0.07	0.29	-3.44	32.74
$K^*(892)^-$	0.02	0.19	none	none
$K^*(892)^0$	0.05	0.21	5.79	46.14
$\bar{K}^*(892)^0$	0.06	0.22	7.56	45.10
$K^*(1430)^+$	2.46	8.37	-0.76	16.74
$K^*(1430)^-$	2.52	7.67	-0.74	17.80
$K^*(1430)^0$	0.50	8.63	1.59	45.81
$\bar{K}^*(1430)^0$	1.12	8.63	2.92	43.55
$N.R.$	0.21	4.84	-4.43	31.20
$\overline{N.R.}$	0.08	4.87	-5.69	29.29
Resonance	Pull		Residue	
	μ	σ	μ	σ
Signal yield	0.32	0.99	18.03	52.64
Continuum yield	-0.26	1.00	-24.37	94.27
A_{CP} continuum	0.02	0.99	0.0003	0.01

Table A.6: Signal+continuum embedded fits. Pull and residue mean and σ for the amplitudes, phases and yields.

Resonance	Pull Amplitude		Pull Phase	
	μ	σ	μ	σ
$\rho(770)^+$	-0.11	1.04	0.10	1.15
$\rho(770)^-$	-0.06	0.99	0.02	1.05
$K^*(892)^-$	-0.11	0.91	none	none
$K^*(892)^0$	-0.01	0.92	0.21	1.31
$\bar{K}^*(892)^0$	0.04	0.96	0.14	1.18
$K^*(1430)^+$	0.05	0.97	0.04	1.06
$K^*(1430)^-$	0.08	0.91	-0.006	0.99
$K^*(1430)^0$	-0.31	1.08	0.13	1.31
$\bar{K}^*(1430)^0$	-0.24	1.04	0.04	1.24
$N.R.$	-0.03	1.01	-0.28	1.27
$\overline{N.R.}$	-0.08	0.93	-0.27	1.16
Resonance	Residue Amplitude		Residue Phase	
	μ	σ	μ	σ
$\rho(770)^+$	0.08	0.33	1.42	42.61
$\rho(770)^-$	0.09	0.31	-1.17	39.16
$K^*(892)^-$	0.03	0.18	none	none
$K^*(892)^0$	0.06	0.23	12.34	59.55
$\bar{K}^*(892)^0$	0.07	0.24	7.03	55.49
$K^*(1430)^+$	3.54	9.43	-0.49	18.84
$K^*(1430)^-$	3.57	8.80	-0.97	17.89
$K^*(1430)^0$	0.46	9.55	6.44	59.66
$\bar{K}^*(1430)^0$	1.14	9.94	1.82	56.92
$N.R.$	0.71	5.97	-9.88	42.64
$\overline{N.R.}$	0.24	5.27	-7.15	36.21
Resonance	Pull		Residue	
	μ	σ	μ	σ
Signal yield	0.58	0.98	33.47	56.19
Continuum yield	0.09	1.03	11.10	131.95
A_{CP} continuum	0.06	0.97	0.0008	0.01
D^0 yield	0.07	0.97	3.86	51.00
Category #1	-0.009	1.00	0.38	36.00
Category #2	0.02	1.04	1.15	23.59
Category #3	-0.06	1.02	-2.21	74.37
Category #4	-0.87	1.22	-11.40	16.29
Category #5	-0.02	1.03	0.03	52.57
Category #6	-0.32	1.01	-43.62	142.82
Category #7	0.11	1.00	9.76	85.92

Table A.7: Full model Embedded Fits. Pull and residue mean and σ for the amplitudes, phases and yields.

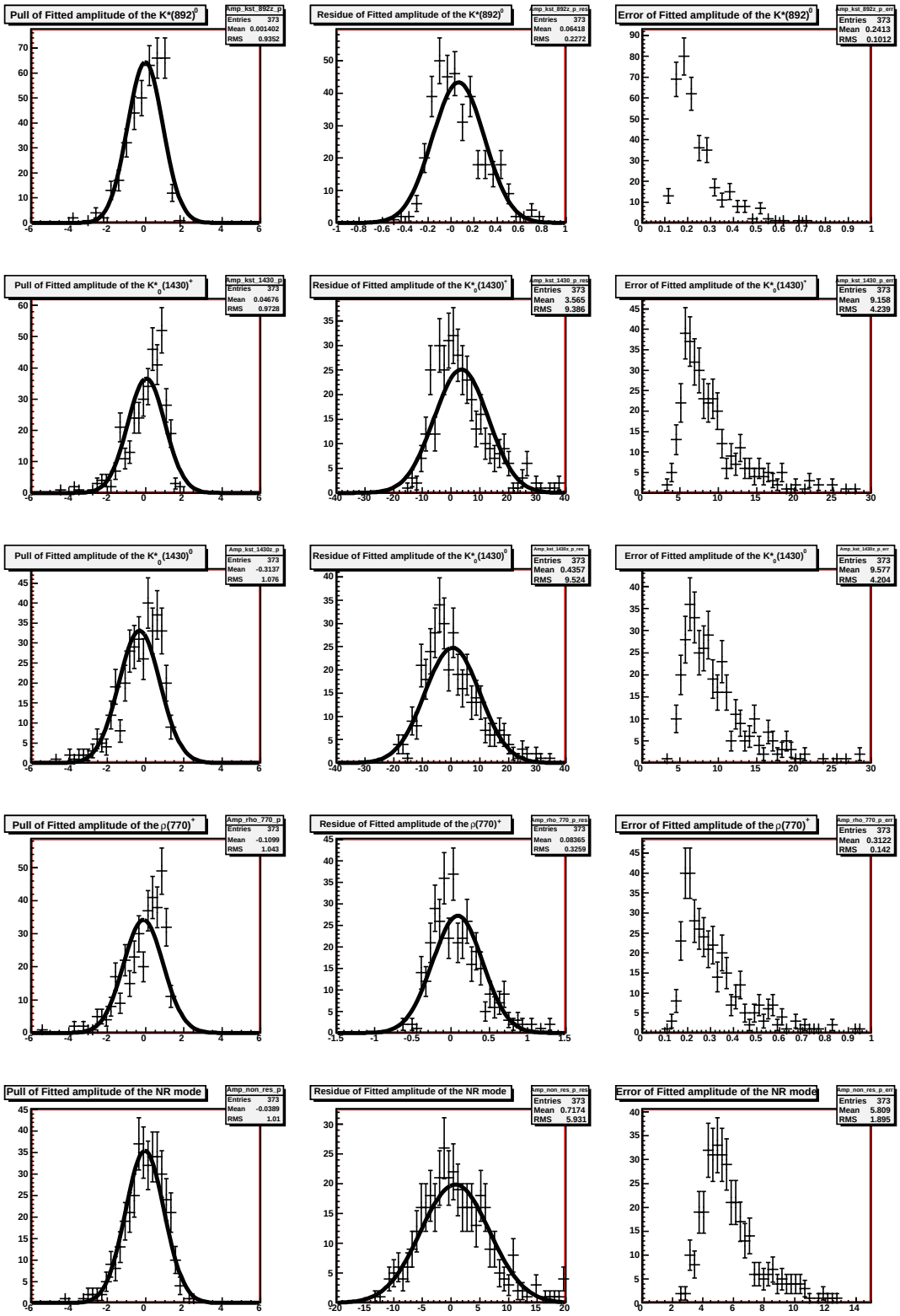

Figure A.1: Embedded Fits histograms for the full model fit model. The amplitude pull (left), residue (middle) and standard deviation (right) histograms are presented.

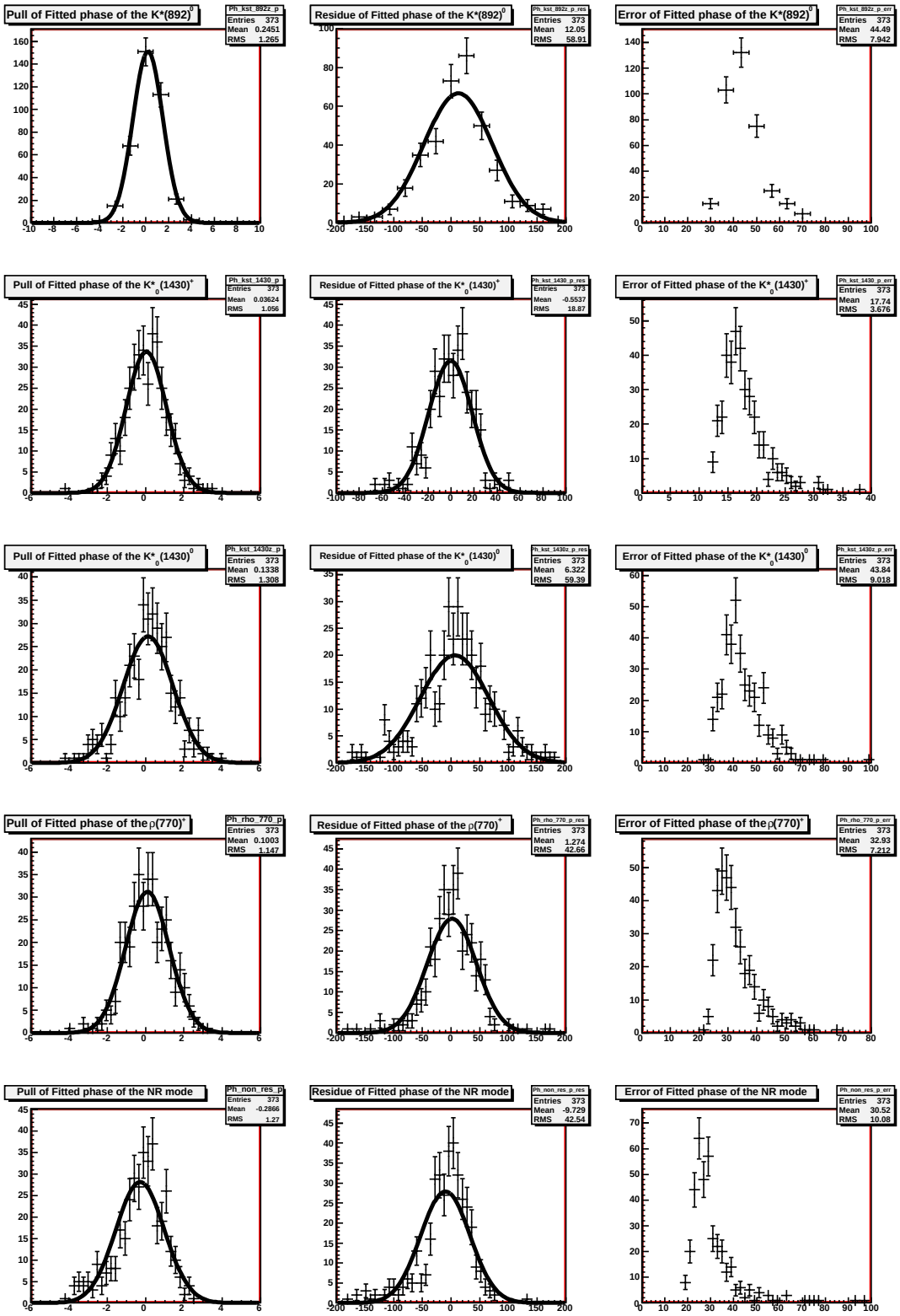

Figure A.2: Embedded Fits histograms for the full model fit model. The phase pull (left), residue (middle) and standard (right) deviation histograms are presented.

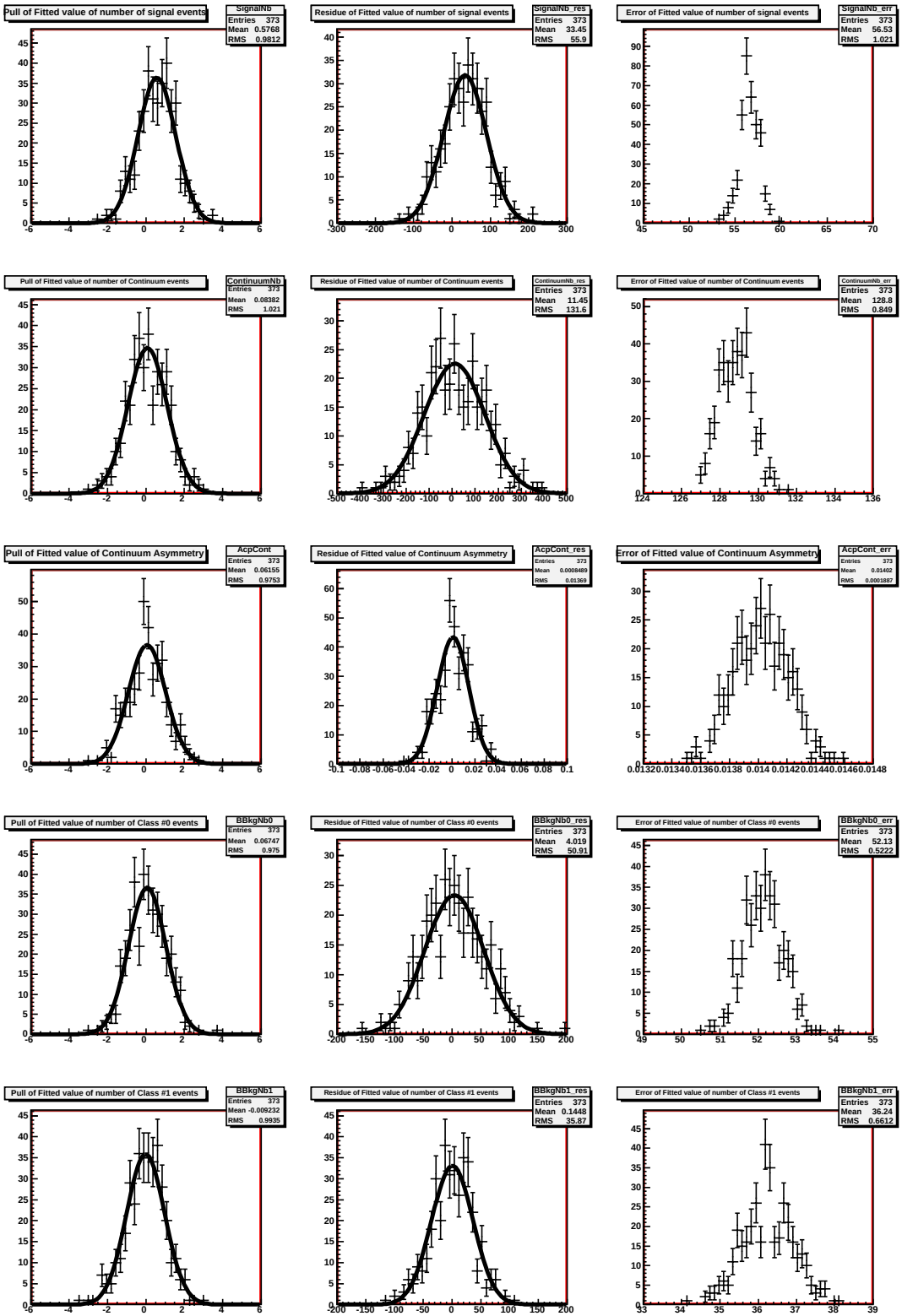

Figure A.3: Embedded Fits histograms for the full model fit model. The yields (part-1) pull (left), residue (middle) and standard deviation (right) histograms are presented. From top to bottom: signal yield, continuum yield, A_{CP}, category #0 yield, category #1 yield.

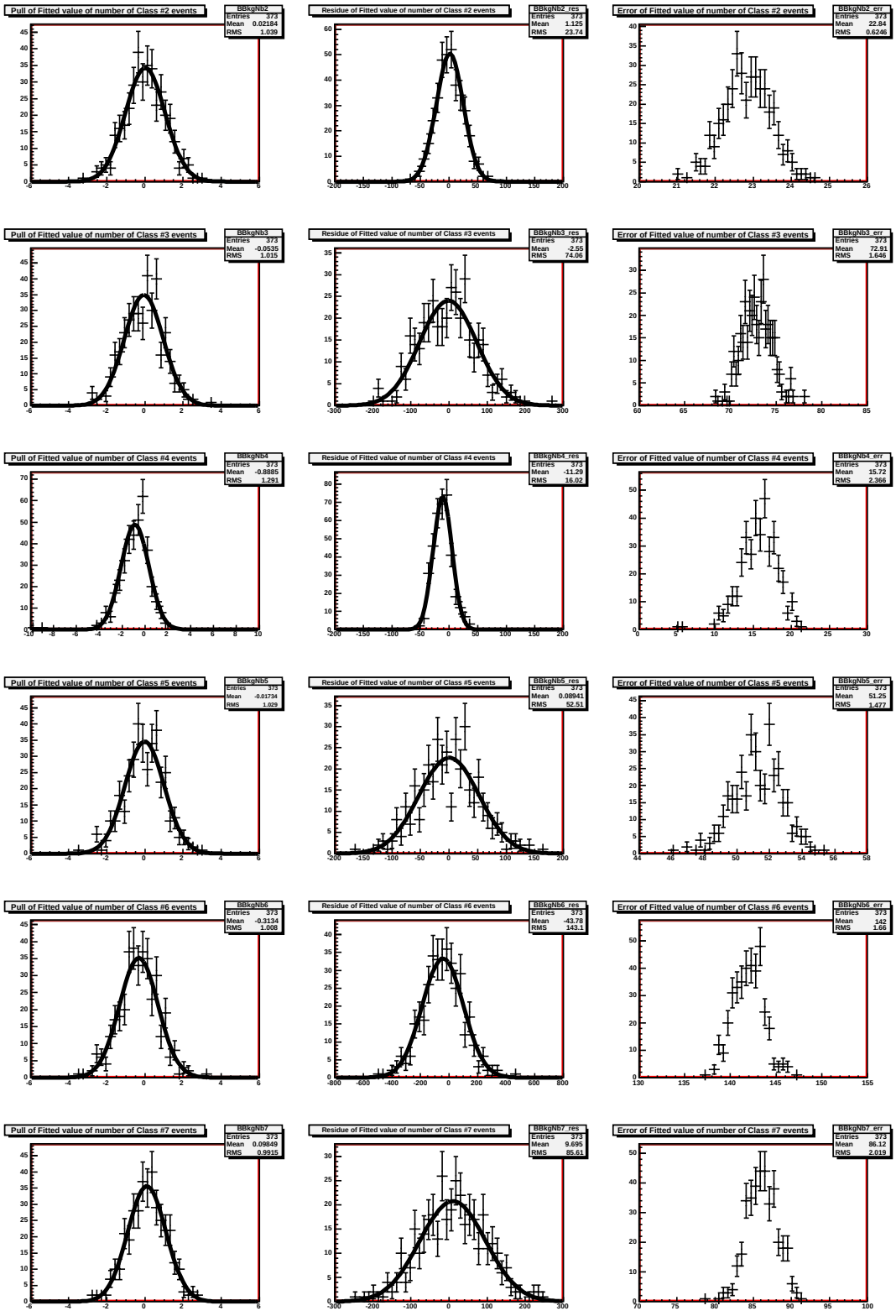

Figure A.4: Embedded Fits histograms for the full model fit model. The yields (part-2) pull (left), residue (middle) and standard deviation (right) histograms are presented. From top to bottom: category #2 yield, category #3 yield, category #4 yield, category #5 yield, category #7 yield, category #7 yield.

A.2 Systematics

Parameters	name	nominal value	variation
Yields of Bbackground labelled as in Table 4.8			
(category #1)	BBkg1Nb	726.0	
(category #3)	BBkg3Nb	593.0	
(category #6)	BBkg6Nb	1266.0	
(category #7)	BBkg7Nb	366.0	
Yields of Bbackground labelled as in Table 4.8			
(category #0, $D^0\pi^+$)	AcpD0	-0.008	$\pm$0.008
(category #1)	AcpBBkg1	0.00	$\pm$0.2
(category #2)	AcpBBkg2	0.00	$\pm$0.2
(category #3)	AcpBBkg3	0.00	$\pm$0.5
(category #4)	AcpBBkg4	0.00	$\pm$0.5
(category #5)	AcpBBkg5	0.00	$\pm$0.2
(category #6)	AcpBBkg6	0.00	$\pm$0.5
(category #7)	AcpBBkg7	0.00	$\pm$0.2
Average SCF fraction			
f_{SCF}	FracSCF	0.1948	$\pm$0.05
Slopes with $m_{K^0_S\pi^+}$ of the coefficients of the $\Delta E'$ PDF			
	DEgfrGSlope	-1.80242e-03	$\pm 5.75843e-04$
	DEgmeanGSlope	6.49573e-03	$\pm 4.11395e-04$
	DEgwidthGSlope	-2.39242e-04	$\pm 5.10273e-04$
	DEgmeanBGSlope	-5.69833e-03	$\pm 1.58900e-04$
	DEgwidthBGLSlope	-2.22262e-03	$\pm 2.01998e-04$
	DEgwidthBGRSlope	1.54990e-03	$\pm 1.21750e-04$
	Bmassgmean1	5.27629e+00	$\pm 2.14776e-04$
	Bmassgwidth1	3.32923e-03	$\pm 6.28923e-05$
	Bmassgfrac	1.92333e-01	$\pm 1.58069e-02$

Table A.8: List of the fixed parameters p of the nominal fit (part-1), their nominal values and their excursions $\pm\delta p$ used to estimate the systematics.

Parameters	name	nominal value	variation
Signal NN'; parameter names starting with Sig (Comb) refer to the TM(SCF) PDFs			
	SigNnOutgmeanBG1	3.55133e-01	$\pm 1.18852e-01$
	SigNnOutgwidth1L	1.31586e+00	$\pm 3.76766e-02$
	SigNnOutgwidth1R	2.04224e+00	$\pm 5.78780e-02$
	SigNnOutgmeanBG2	3.33897e+00	$\pm 1.77503e-02$
	SigNnOutgwidth2L	2.89873e+00	$\pm 1.45264e-02$
	SigNnOutgwidth2R	5.23995e-01	$\pm 1.15117e-02$
	SigNnOutgmean	2.03401e+00	$\pm 3.62319e-02$
	SigNnOutgwidth	1.16952e+00	$\pm 2.33948e-02$
	SigNnOutgfrac1	2.78977e-01	$\pm 2.40856e-02$
	SigNnOutgfrac2	7.02602e-01	$\pm 6.66352e-03$
	CombNnOutgmeanBG1	1.62968e+00	$\pm 5.31113e-02$
	CombNnOutgwidth1L	1.80378e+00	$\pm 4.74981e-02$
	CombNnOutgwidth1R	1.27862e+00	$\pm 2.50272e-02$
	CombNnOutgmeanBG2	3.22324e+00	$\pm 1.08591e-01$
	CombNnOutgwidth2L	3.22653e+00	$\pm 9.05983e-02$
	CombNnOutgwidth2R	4.87662e-01	$\pm 6.46050e-02$
	CombNnOutgfrac1	7.12075e-01	$\pm 3.75946e-02$
Parameters of the PDF of NN' in the continuum.			
	ContNnOutgmeanBG1	-1.19654e+00	$\pm 1.10357e+00$
	ContNnOutgmeanBG1Slope	1.23977e-01	$\pm 1.85078e+00$
	ContNnOutgmeanBG1Sq	6.07458e-02	$\pm 6.47811e-01$
	ContNnOutgwidth1L	1.36699e+00	$\pm 1.10357e+00$
	ContNnOutgwidth1LSlope	1.25267e-02	$\pm 1.85078e+00$
	ContNnOutgwidth1LSq	5.86307e-02	$\pm 6.47811e-01$
	ContNnOutgwidth1R	1.14607e+00	$\pm 1.10357e+00$
	ContNnOutgwidth1RSlope	-3.07741e-01	$\pm 1.85078e+00$
	ContNnOutgwidth1RSq	1.91450e-01	$\pm 6.47811e-01$
	ContNnOutgmeanBG2	3.68799e-02	$\pm 1.10357e+00$
	ContNnOutgmeanBG2Slope	2.22668e-01	$\pm 1.85078e+00$
	ContNnOutgmeanBG2Sq	1.44596e-01	$\pm 6.47811e-01$
	ContNnOutgwidth2L	2.62563e+00	$\pm 3.33333e-01$
	ContNnOutgwidth2RSlope	-6.12642e-02	$\pm 1.85078e+00$
	ContNnOutgwidth2RSq	-1.69518e-03	$\pm 6.47811e-01$
	ContNnOutgfrac1	5.44574e-01	$\pm 3.33333e-01$

Table A.9: List of the fixed parameters p of the nominal fit (part-2), their nominal values and their excursions $\pm\delta p$ used to estimate the systematics.

Parameters	name	nominal value	variation
Parameters for the $K^0_S\pi^0$ invariant mass for the $B^+ \to D^0\pi^+$ TM events.			
	DMassgmean1	6.49843e-01	$\pm 7.28453e-01$
	DMassgmean2	6.49843e-01	$\pm 7.28453e-01$
	DMassgwidth1	3.42583e-03	$\pm 1.18501e+00$
	DMassgwidth2	1.11956e-03	$\pm 1.18501e+00$
	DMassgfrac1	2.47196e-01	$\pm 3.53553e-01$
	DMassgmean1Slope	7.03222e-04	$\pm 1.58006e+00$
	DMassgmean2Slope	7.03222e-04	$\pm 1.58006e+00$
	DMassgwidth1Slope	-1.53522e-02	$\pm 6.82303e+00$
	DMassgwidth2Slope	9.15555e-05	$\pm 6.82303e+00$
	DMassgwidth1Sq	2.75490e-02	$\pm 8.19038e+00$
	DMassgwidth2Sq	2.31165e-03	$\pm 8.19038e+00$
Coefficients of the TM $B^+ \to D^0\pi^+$ helicity polynomial (Section 4.7.1).			
	A1	130.279	
	A2	-536.806	
	A3	4722.037	
	A4	-11710.63	
	A5	10875.29	
	A6	-3480.17	
Average SCF fraction for $B^+ \to D^0\pi^+$ events.			
	combFrac0	0.1094	
Parameters for the $K^0_S\pi^0$ invariant mass for the $B^+ \to D^0\pi^+$ SCF events.			
	DMassSCFgmean1	6.50234e-01	$\pm 1.26719e+00$
	DMassSCFgmean2	6.79801e-01	$\pm 1.03194e+00$
	DMassSCFgwidth1	7.39490e-03	$\pm 1.04269e+00$
	DMassSCFgwidth2	8.60310e-02	$\pm 1.03194e+00$
	DMassSCFgfrac1	4.63197e-01	$\pm 3.16228e-01$
	DMassSCFgmean1Slope	7.06864e-03	$\pm 9.74463e+00$
	DMassSCFgmean2Slope	-1.13098e-01	$\pm 4.810e+00$
	DMassSCFgwidth1Slope	-5.45934e-02	$\pm 4.66061e+00$
	DMassSCFgwidth2Slope	-3.02707e-01	$\pm 4.81080e+00$
	DMassSCFgmean1Sq	-5.60786e-02	$\pm 2.20204e+01$
	DMassSCFgmean2Sq	1.06191e-01	$\pm 4.67882e+00$
	DMassSCFgwidth1Sq	1.04101e-01	$\pm 4.28565e+00$
	DMassSCFgwidth2Sq	2.74902e-01	$\pm 4.67882e+00$
	DMassSCFgmean1Cub	1.02391e-01	$\pm 1.46926e+01$

Table A.10: List of the fixed parameters p of the nominal fit (part-3), their nominal values and their excusions $\pm\delta p$ used to estimate the systematics.

Mode	ΔLL
Removals	
$K^{*+}(892)$	+27.4
$K^{*0}(892)$	+18.9
$\rho(770)^{+}$	+16.5
$K^{*+}(1430)$	+82.8
$K^{*0}(1430)$	+51.8
$N.R.$	+19.0
Additions	
$\rho^{+}(1450)$	−9.8
$\rho^{+}(1700)$	−11.8
$K^{*+}(1680)$	−7.7
$K^{*0}(1680)$	−1.8
$K_2^{*+}(1430)$	−6.8
$K_2^{*0}(1430)$	−6.8

Table A.11: Change in the negative loglikelihood when one component of the nominal fit is removed or when an extra component is added. We recall that $NLL_{\text{fit}} = -135785.8$

Resonance	FF	A_{CP}
adding $\rho(1450)^+$: minNll is -137585.1		
k-892	0.0745525 ± 0.0124305	-0.359228 ± 0.245006
k-892z	0.0609055 ± 0.0203565	-0.140965 ± 0.320509
non-res	0.0778137 ± 0.0233315	-0.732541 ± 0.289234
rho-770	0.132499 ± 0.0406047	0.268534 ± 0.30139
k0st-1430	0.275454 ± 0.0411021	0.550388 ± 0.131778
k0st-1430z	0.319624 ± 0.0373398	0.0491923 ± 0.147859
rho-1450	0.0810019 ± 0.0377285	-0.305867 ± 0.490625
adding $\rho(1700)^+$: minNll is -137587.1		
k-892	0.0728034 ± 0.0174092	-0.383141 ± 0.356828
k-892z	0.061489 ± 0.0323944	-0.148309 ± 0.391245
non-res	0.0743962 ± 0.0324914	-0.708228 ± 0.359202
rho-770	0.136547 ± 0.0542734	0.0909656 ± 0.301542
k0st-1430	0.280208 ± 0.0783822	0.538025 ± 0.138071
k0st-1430z	0.319863 ± 0.0785238	0.0496117 ± 0.152594
rho-1700	0.067979 ± 0.0360018	-0.143528 ± 0.493515
adding $K^*(1680)^+$: minNll is -137583.0		
k-892	0.0890521 ± 0.0153188	-0.346406 ± 0.252777
k-892z	0.0741537 ± 0.0284257	-0.154479 ± 0.331228
non-res	0.0499781 ± 0.0247612	-0.607742 ± 0.430524
rho-770	0.128397 ± 0.0403876	-0.0530455 ± 0.264701
k0st-1430	0.285705 ± 0.0593621	0.269263 ± 0.196945
k0st-1430z	0.312346 ± 0.0617818	0.0189477 ± 0.165571
kst-1680	0.0593835 ± 0.0268124	-0.210072 ± 0.421273
adding $K^*(1680)^0$: minNll is -137577.1		
k-892	0.0735715 ± 0.0143464	-0.408578 ± 0.297719
k-892z	0.0605907 ± 0.0277182	-0.166129 ± 0.386703
non-res	0.0981159 ± 0.0523025	-0.571336 ± 0.36065
rho-770	0.132403 ± 0.0486726	-0.161635 ± 0.278476
k0st-1430	0.306253 ± 0.0748795	0.480442 ± 0.168709
k0st-1430z	0.339784 ± 0.0801696	0.0672542 ± 0.149685
kst-1680z	0.0169609 ± 0.0197191	0.098054 ± 1.21898
adding $K_2^*(1430)^+$: minNll is -137582.1		
k-892	0.0671762 ± 0.0129164	-0.350027 ± 0.278946
k-892z	0.0815831 ± 0.0240119	-0.279618 ± 0.303606
non-res	0.083103 ± 0.034225	-0.50128 ± 0.441163
rho-770	0.120897 ± 0.0297025	-0.12474 ± 0.277773
k0st-1430	0.394284 ± 0.0424971	0.121373 ± 0.118355
k0st-1430z	0.255485 ± 0.0377351	0.4414 ± 0.151939
k2st-1430	0.0453833 ± 0.0255308	-0.152192 ± 0.529575
adding $K_2^*(1430)^0$: minNll is -137582.1		
k-892	0.0758547 ± 0.0135693	-0.41464 ± 0.275023
k-892z	0.0663721 ± 0.0271823	-0.183948 ± 0.33073
non-res	0.150813 ± 0.0577377	-0.593571 ± 0.295639
rho-770	0.131345 ± 0.0467461	-0.15955 ± 0.257454
k0st-1430	0.316638 ± 0.073282	0.449848 ± 0.180037
k0st-1430z	0.236389 ± 0.0798732	0.421175 ± 0.260527
k2st-1430z	0.0548612 ± 0.028942	-0.313114 ± 0.481007

Table A.12: Variants of the nominal fit including resonances in the nominal model. The fractions do not sum to 100% because of interference.

Δ parameter	$K*(892)^+$	$K*(892)^0$	$K*_0(1430)^+$	$K*_0(1430)^0$	$\rho(770)^+$	$N.R.$	$total$
combFrac-high	0.00017218	-0.00456563	0.00146442	0.00105074	-0.00145012	0.00433666	0.00100825
combFrac-low	-0.000456427	0.0035686	-0.00303782	-0.000544168	0.00085059	-0.00160112	-0.00122034
DEgfrG-high	-0.000609331	-1.68867e-07	-0.000188588	3.49745e-05	-3.2925e-05	0.000878342	8.23033e-05
DEgfrG-low	-0.000232659	-5.29307e-05	-0.000887752	0.000135196	8.48946e-05	0.00100985	5.66008e-05
DEgfrGSlope-high	-0.000405226	0.000272565	-0.00136597	0.000219323	8.22709e-05	0.0010348	-0.000162233
DEgfrGSlope-low	-0.000121811	-0.000326367	4.14076e-05	-6.36394e-05	-3.66555e-05	0.000743365	0.0002363
DEgmeanG-high	-0.000250152	-8.88127e-05	-0.000903062	4.73013e-05	0.000150019	0.00107548	3.0776e-05
DEgmeanG-low	-0.000534111	6.46253e-05	-0.000143715	0.000148445	-8.46952e-06	0.000556363	8.31375e-05
DEgmeanGSlope-high	-0.000493942	-0.000130354	-0.000413584	5.97135e-05	0.000172065	0.00094911	0.000143009
DEgmeanGSlope-low	-0.000573846	0.000125869	-0.000297441	0.00019872	5.96948e-05	0.000574769	8.77653e-05
DEgwidthG-high	-0.000150532	-7.21756e-05	-0.0010368	3.40554e-05	1.83261e-05	0.0010962	-0.00011092
DEgwidthG-low	-0.000246397	-2.12762e-05	-0.000550965	7.76817e-05	2.84027e-05	0.000855238	0.000142684
DEgwidthGSlope-high	-0.000648774	3.627e-05	-0.000814281	0.000215881	0.000152299	0.0010968	3.81991e-05
DEgwidthGSlope-low	-0.000164104	-8.75913e-05	-0.000300449	2.89666e-05	-3.24065e-05	0.000729985	0.000174401
DEgmeanBG-high	-0.000551343	-0.000184829	-0.000920592	1.8782e-05	0.000397094	0.00131869	7.7805e-05
DEgmeanBG-low	-0.000497103	0.000159445	-6.29863e-05	0.000181083	-8.61443e-05	0.000458172	0.000152466
DEgmeanBGSlope-high	-0.000258166	-0.000357224	-0.00107893	2.4805e-05	0.000231263	0.00143351	-4.73443e-06
DEgmeanBGSlope-low	-0.000507801	0.000274101	-0.000109177	0.000156197	-4.70342e-05	0.000340344	0.000106629
DEgwidthBGL-high	-0.00025387	0.000115086	-0.000448757	2.2616e-05	3.15947e-06	0.000639277	7.75113e-05
DEgwidthBGL-low	-0.000254777	-0.000140405	-0.00123978	0.000226331	5.53359e-05	0.00127298	-8.03159e-05
DEgwidthBGLSlope-high	-0.000502375	0.000514747	-0.000620311	5.53301e-05	6.71579e-05	0.000347551	-0.0001379
DEgwidthBGLSlope-low	-0.000198035	-0.000488954	-0.00051221	1.56887e-05	4.40491e-05	0.00133323	0.000193769
DEgwidthBGR-high	-0.000402064	-0.000113022	-0.000774549	2.37543e-05	0.000346383	0.000922446	2.94807e-06
DEgwidthBGR-low	-0.000165879	0.00011747	-0.000562489	0.000118716	-0.00022715	0.00083011	0.000110779
DEgwidthBGRSlope-high	-0.000620903	-0.000140827	-0.000872671	0.000208498	0.000303531	0.00115738	3.50105e-05
DEgwidthBGRSlope-low	-0.000449749	9.44698e-05	-6.92609e-05	2.23638e-05	-8.2846e-05	0.000716565	0.000231543
Bmassgmean1-high	-0.000181055	-5.54546e-05	-0.000410728	0.000129398	-6.02076e-05	0.000594448	1.64e-05
Bmassgmean1-low	-0.000334446	-6.67276e-05	-0.00135029	-6.52129e-05	0.000242955	0.00168998	0.000116249
Bmassgwidth1-high	-0.000318738	-2.85551e-05	-0.000567668	6.62913e-05	4.62436e-05	0.000825047	2.26205e-05
Bmassgwidth1-low	-0.000462266	-9.01701e-06	-0.000514497	0.000128408	5.97613e-05	0.000928151	0.000130541
Bmassgfrac-high	-0.00035423	-5.03691e-05	-0.00133008	-4.49598e-05	0.00022631	0.00169133	0.000137997
Bmassgfrac-low	-0.000197235	-8.0234e-05	-0.000501422	9.95948e-05	-5.34737e-06	0.000701212	1.6569e-05
sqrt(quadratic sum high)	0.00167623	0.00462922	0.00360414	0.00113079	0.00163436	0.00595983	0.00106629
sqrt(quadratic sum low)	0.00147745	0.00364217	0.0038726	0.000735363	0.000934489	0.00389559	0.00133753

Table A.13: Systematic deviations of the isobar fractions in *solution-1* when each of the fixed parameters of the m'_{ES} and $\Delta E'$ signal PDFs is varied upwards to $p-hi$ (resp. downwards to $p-lo$) by its estimated error or a covering range devised to be conservative. The *total* upwards (resp. downward) deviations quoted in the last two rows are obtained by summing all upwards (resp. downwards) deviations in quadrature.

Δ parameter	$K*(892)^+$	$K*(892)^0$	$K*_0(1430)^+$	$K*_0(1430)^0$	$\rho(770)^+$	$N.R.$	$total$
ContNnOutgmeanBG1-high	0.000422087	0.000357033	0.00111682	0.000297816	-0.0031437	-0.000187084	-0.00113703
ContNnOutgmeanBG1-low	0.00124396	0.00100659	0.00229939	0.000813466	-0.00547985	-0.00253001	-0.00264646
ContNnOutgmeanBG1Slope-high	0.000479219	-6.40494e-05	0.00168111	0.000437523	-0.00378735	0.000187344	-0.00106621
ContNnOutgmeanBG1Slope-low	0.0014363	0.0011754	0.00158698	0.00108476	-0.00498142	-0.00292289	-0.00262087
ContNnOutgmeanBG1Sq-high	0.000331115	0.000656901	0.0028956	6.06269e-05	-0.00449511	-0.00108093	-0.00163179
ContNnOutgmeanBG1Sq-low	0.00144719	0.00120297	0.00144631	0.00110166	-0.00446955	-0.00327002	-0.00254145
ContNnOutgwidth1L-high	0.00103192	0.000734851	0.00165635	0.000716024	-0.00459771	-0.00154298	-0.00200154
ContNnOutgwidth1L-low	0.000942838	0.000652888	0.00170029	0.000591278	-0.00443703	-0.00126231	-0.00181204
ContNnOutgwidth1LSlope-high	0.0010438	0.000751977	0.00165431	0.000730582	-0.00453914	-0.00163661	-0.00199508
ContNnOutgwidth1LSlope-low	0.000927582	0.00063294	0.0017129	0.000570591	-0.00449764	-0.00116162	-0.00181525
ContNnOutgwidth1LSq-high	0.00109712	0.00081801	0.00170259	0.000808219	-0.00444634	-0.00203666	-0.00205706
ContNnOutgwidth1LSq-low	0.00085493	0.000547949	0.00167711	0.000464086	-0.00460566	-0.000664321	-0.00172591
ContNnOutgwidth1R-high	0.000987333	0.000693213	0.00168547	0.000654531	-0.00451776	-0.00141144	-0.00190866
ContNnOutgwidth1R-low	0.00140352	0.0013312	0.00294852	0.00103173	-0.00681656	-0.00343703	-0.00353862
ContNnOutgwidth1RSlope-high	0.0002501	8.86991e-05	0.0023436	9.71056e-05	-0.00231411	-0.00170097	-0.00123557
ContNnOutgwidth1RSlope-low	0.000987333	0.000693213	0.00168547	0.000654531	-0.00451776	-0.00141144	-0.00190866
ContNnOutgwidth1RSq-high	0.000624104	0.000206947	0.00194625	0.00040074	-0.00317913	-0.00185522	-0.00185631
ContNnOutgwidth1RSq-low	0.00186515	0.00167003	0.000743606	0.00126888	-0.00475574	-0.00400351	-0.00321159
ContNnOutgmeanBG2-high	0.00137474	0.00108785	0.00210111	0.000962936	-0.00556756	-0.00264358	-0.00268449
ContNnOutgmeanBG2-low	0.000428337	0.00071072	0.0021741	0.00100841	-0.00343499	-0.00243585	-0.00154927
ContNnOutgmeanBG2Slope-high	0.0015511	0.00131111	0.00189561	0.00107088	-0.00497856	-0.00350678	-0.00265664
ContNnOutgmeanBG2Slope-low	0.000289434	0.000590779	0.00211924	0.000311667	-0.00409284	-0.000927505	-0.00170923
ContNnOutgmeanBG2Sq-high	0.00365565	0.00383385	0.00204939	0.00221762	-0.00376294	-0.013651	-0.00565742
ContNnOutgmeanBG2Sq-low	-0.0018237	-0.00255301	-0.000134921	-0.00180163	-0.00572962	0.0130521	0.00100922
ContNnOutgwidth2L-high	0.000953805	0.000677772	0.00178075	0.000595493	-0.00449538	-0.00135906	-0.00184662
ContNnOutgwidth2L-low	0.000996298	0.000701612	0.00168134	0.00066717	-0.00453099	-0.00144223	-0.0019268
ContNnOutgwidth2R-high	0.00147574	0.00141234	0.0033689	0.00102822	-0.00657122	-0.00395025	-0.00323627
ContNnOutgwidth2R-low	0.000248322	8.93901e-05	0.000529231	0.000203485	-0.00241602	0.000471951	-0.000873639
ContNnOutgwidth2RSlope-high	0.00173047	0.00173259	0.00291017	0.00105171	-0.00557406	-0.00492937	-0.00307847
ContNnOutgwidth2RSlope-low	-7.67078e-05	-0.000357569	0.00181586	7.61504e-05	-0.0033653	0.00118311	-0.000724452
ContNnOutgwidth2RSq-high	0.00756715	0.00776384	-0.000246636	0.00172275	-0.00654688	-0.0203294	-0.0100692
ContNnOutgwidth2RSq-low	-0.00674915	-0.00864528	-0.00437226	-0.00515706	-0.00768954	0.0374179	0.00480461
ContNnOutgfrac1-high	0.000708661	0.000520212	0.00231115	0.000414022	-0.00418828	-0.00132572	-0.00155995
ContNnOutgfrac1-low	0.00115087	0.000862377	0.00161973	0.000887806	-0.00479119	-0.00197123	-0.00224164
sqrt(quadratic sum high)	0.00931708	0.00929911	0.0085766	0.00390269	0.0191474	0.0260999	0.0141202
sqrt(quadratic sum low)	0.00813249	0.0096693	0.00824642	0.00626748	0.0201642	0.0405425	0.00978867

Table A.14: Systematic deviations of the isobar fractions in *solution-1* when each of the fixed parameters of the continuum NN' PDF is varied upwards to $p-hi$ (resp. downwards to $p-lo$) by its estimated error or a covering range devised to be conservative. The *total* upwards (resp. downward) deviations quoted in the last two rows are obtained by summing all upwards (resp. downwards) deviations in quadrature.

Δ parameter	$K*(892)^+$	$K*(892)^0$	$K*_0(1430)^+$	$K*_0(1430)^0$	$\rho(770)^+$	$N.R.$	$total$
SigNnOutgmeanBG1-high	0.000348665	9.2339e-05	-7.43292e-06	-0.000114262	-0.000466485	4.70482e-06	-0.000142471
SigNnOutgmeanBG1-low	0.000163239	-5.29929e-05	-0.000369265	-5.58726e-05	0.000230892	0.000289021	0.000205022
SigNnOutgwidth1L-high	0.000253638	1.64102e-05	-0.000185673	-0.000105445	-0.000114271	0.00016369	2.83489e-05
SigNnOutgwidth1L-low	0.000253638	1.64102e-05	-0.000185673	-0.000105445	-0.000114271	0.00016369	2.83489e-05
SigNnOutgwidth1R-high	0.000332787	8.36528e-05	-4.41518e-06	-9.64077e-05	-0.000508775	-8.45241e-05	-0.000277682
SigNnOutgwidth1R-low	0.000150841	-7.0364e-05	-0.000396865	-6.95625e-05	0.000321641	0.000355646	0.000291337
SigNnOutgmeanBG2-high	0.000295404	8.64965e-05	-0.000223115	-3.18862e-05	-0.000406615	0.000114256	-0.00016546
SigNnOutgmeanBG2-low	0.000219683	-4.08167e-05	-0.000189713	-0.000132606	0.000178106	0.00018475	0.000219402
SigNnOutgwidth2L-high	0.000247459	1.45053e-05	-0.000198602	-0.000101387	-9.44563e-05	0.000166924	3.44425e-05
SigNnOutgwidth2L-low	0.00025983	1.82318e-05	-0.000172283	-0.000109421	-0.000134316	0.000160386	2.24278e-05
SigNnOutgwidth2R-high	0.000249395	3.00483e-05	-0.000200768	-5.66583e-05	-0.00029037	6.45503e-05	-0.000203803
SigNnOutgwidth2R-low	0.000230413	-2.13887e-05	-0.000201137	-0.000105745	0.000101028	0.000184674	0.000187846
SigNnOutgmean-high	0.000332721	6.95841e-05	-3.26705e-06	-9.179e-05	-0.0004481	2.45301e-05	-0.000116322
SigNnOutgmean-low	0.000176162	-3.21785e-05	-0.000377258	-8.05169e-05	0.000220042	0.000274695	0.000180946
SigNnOutgwidth-high	0.000262823	2.05555e-05	-0.000116791	8.87195e-07	-0.000311651	-5.50984e-05	-0.000199275
SigNnOutgwidth-low	0.000219083	-1.04494e-05	-0.000301107	-0.00016475	0.000121399	0.000321421	0.000185596
SigNnOutgfrac1-high	0.000202068	4.79545e-06	-0.000315873	-6.22978e-05	8.57803e-05	0.000138875	5.33476e-05
SigNnOutgfrac1-low	0.00031031	4.49597e-05	-9.35755e-05	-0.000130546	-0.0003206	0.000182283	-7.16936e-06
SigNnOutgfrac2-high	0.000259324	1.46033e-05	-0.000173757	-8.13216e-05	-0.000157297	0.00014259	4.1414e-06
SigNnOutgfrac2-low	0.000247717	1.77191e-05	-0.000196277	-0.000129145	-7.10949e-05	0.000184763	5.36823e-05
CombNnOutgmeanBG1-high	0.000360363	-9.56979e-05	0.000303311	2.65503e-05	-0.000597419	5.36851e-06	2.47618e-06
CombNnOutgmeanBG1-low	0.000149896	0.00013611	-0.000682425	-0.000195546	0.00036547	0.000285374	5.88788e-05
CombNnOutgwidth1L-high	0.00025168	1.95787e-05	-0.000193561	-0.000106011	-0.000107748	0.000164411	2.83488e-05
CombNnOutgwidth1L-low	0.000255749	1.29794e-05	-0.000177128	-0.000104821	-0.000121317	0.000162908	2.83705e-05
CombNnOutgwidth1R-high	0.000334917	-5.12184e-05	0.000177807	5.65346e-05	-0.00046977	-4.5508e-05	2.76339e-06
CombNnOutgwidth1R-low	0.000176792	0.000107273	-0.000605464	-0.000232804	0.000242529	0.00035098	3.93061e-05
CombNnOutgmeanBG2-high	0.000405832	-0.000116283	0.000538804	4.86233e-05	-0.00071892	-0.000153341	4.71634e-06
CombNnOutgmeanBG2-low	0.000114876	0.000167423	-0.000868245	-0.0001884	0.000510954	0.000351302	8.79085e-05
CombNnOutgwidth2L-high	0.000248651	2.41744e-05	-0.000211541	-0.000108456	-8.91955e-05	0.0001657	2.93333e-05
CombNnOutgwidth2L-low	0.000258996	7.9303e-06	-0.00015743	-0.000102089	-0.000141447	0.000161488	2.74492e-05
CombNnOutgwidth2R-high	0.000358597	-0.000111231	0.000342683	5.20653e-05	-0.000493928	-0.000177183	-2.89964e-05
CombNnOutgwidth2R-low	0.000120558	0.000122535	-0.000801668	-0.000207649	0.000347054	0.00044357	2.44011e-05
CombNnOutgfrac1-high	0.000218886	8.52046e-05	-0.000465025	-0.00011163	0.000192387	0.000143742	6.35647e-05
CombNnOutgfrac1-low	0.000266304	-8.07599e-05	3.22085e-05	-9.82448e-05	-0.000382172	0.000160324	-0.00010234
sqrt(quadratic sum high)	0.00122622	0.000275304	0.00106654	0.000333667	0.00157261	0.000504438	0.000480618
sqrt(quadratic sum low)	0.000896738	0.000306263	0.00173226	0.000573825	0.00107493	0.00108629	0.000554192

Table A.15: Systematic deviations of the isobar fractions in *solution-1* when each of the fixed parameters of the NN' signal PDFs is varied upwards to $p-hi$ (resp. downwards to $p-lo$) by its estimated error or a covering range devised to be conservative. The *total* upwards (resp. downward) deviations quoted in the last two rows are obtained by summing all upwards (resp. downwards) deviations in quadrature.

Δ parameter	$K*(892)^+$	$K*(892)^0$	$K*_0(1430)^+$	$K*_0(1430)^0$	$\rho(770)^+$	$N.R.$	$total$
DMassgmean1-high	-4.7933e-05	-8.74412e-05	-0.00028554	0.00111271	3.12533e-06	-0.000364207	0.000330716
DMassgmean1-low	-4.97853e-05	-7.61143e-05	-0.000315855	0.00120304	-6.80022e-05	-0.00033719	0.00035609
DMassgmean2-high	-7.14867e-05	-0.000146856	-0.000608979	0.00124824	2.2558e-05	-0.000243158	0.000200319
DMassgmean2-low	-7.14891e-05	-0.000146861	-0.000608999	0.00124825	2.25553e-05	-0.000243143	0.000200318
DMassgwidth1-high	2.40094e-05	2.21492e-06	0.000376864	-0.000215688	8.98128e-05	-4.91372e-05	0.000228076
DMassgwidth1-low	-1.48307e-05	7.759e-06	-0.000142479	8.23456e-05	-2.09933e-05	3.45148e-05	-5.36839e-05
DMassgwidth2-high	0.000483478	0.000239724	0.00207494	-0.00242991	0.00112712	-0.00126552	0.000229836
DMassgwidth2-low	-4.30822e-05	-6.92901e-05	-0.000215076	0.00114236	-5.311e-05	-0.000439898	0.0003219
DMassgfrac1-high	1.80958e-05	-2.25898e-06	0.000292898	-7.08473e-05	2.48701e-05	-8.95283e-05	0.000173229
DMassgfrac1-low	-4.65668e-05	-8.03434e-05	-0.000241293	0.00115905	-2.4581e-05	-0.000366652	0.000399614
DMassgmean1Slope-high	-6.84218e-06	-9.61314e-05	-1.4318e-05	0.000774857	4.49391e-05	-7.564e-05	0.000626864
DMassgmean1Slope-low	-6.58515e-06	8.4495e-06	0.000707772	0.000161831	8.29182e-06	-0.000529408	0.000350351
DMassgmean2Slope-high	-4.89281e-05	-0.00014548	-0.000454666	0.00115677	4.7106e-05	-0.000241727	0.000313078
DMassgmean2Slope-low	-5.36172e-05	-0.000119272	-0.000430271	0.00123691	-2.65857e-05	-0.00039681	0.000210352
DMassgwidth1Slope-high	0.000103713	0.000121652	0.00112255	-0.000769638	0.000319112	-0.000674973	0.000222421
DMassgwidth1Slope-low	7.62348e-05	8.63282e-05	0.00105368	-0.000709951	0.000243696	-0.000530423	0.000219564
DMassgwidth2Slope-high	0.000207771	0.000217359	0.00167369	-0.00149517	0.000438218	-0.000744955	0.000296906
DMassgwidth2Slope-low	0.000186174	0.000184235	0.00154886	-0.00133603	0.000383714	-0.000678076	0.000288878
DMassgwidth1Sq-high	0.000226322	0.000350687	0.000687236	-0.000296841	0.000400157	-0.00119695	0.000170616
DMassgwidth1Sq-low	0.000224819	0.000349865	0.000689074	-0.00029389	0.000398163	-0.00119744	0.000170587
DMassgwidth2Sq-high	0.000979438	0.000307215	0.00106145	-0.00241174	0.00113621	-0.000923963	0.000148608
DMassgwidth2Sq-low	0.000974683	0.000308867	0.00107602	-0.0024115	0.00112904	-0.000925926	0.000151187
combFrac0-high	-9.79827e-05	-0.000748848	0.00300482	-0.000271181	-0.00202189	0.00215378	0.0020187
combFrac0-low	-0.00098045	0.000730871	-0.00429715	0.000488003	0.00238454	-0.000298886	-0.00197307
sqrt(quadratic sum high)	0.00114828	0.000978405	0.0044589	0.00441551	0.00266774	0.00313107	0.00224484
sqrt(quadratic sum low)	0.00142023	0.000919971	0.00498887	0.00395545	0.00270845	0.00201528	0.00216258

Table A.16: Systematic deviations of the isobar fractions in *solution-1* when each of the fixed parameters of the $\bar{D}^0$ mass PDFs is varied upwards to $p-hi$ (resp. downwards to $p-lo$) by its estimated error or a covering range devised to be conservative. The *total* upwards (resp. downward) deviations quoted in the last two rows are obtained by summing all upwards (resp. downwards) deviations in quadrature.

Δ parameter	$K*(892)^+$	$K*(892)^0$	$K*_0(1430)^+$	$K*_0(1430)^0$	$\rho(770)^+$	$N.R.$	$total$
combFrac-high	-0.000207143	-0.0150952	0.00988314	0.000239922	-0.00464304	0.0139119	-0.000364884
combFrac-low	0.00476265	0.0152945	0.00116635	-0.000419073	0.00638622	-0.013382	0.00146362
DEgfrG-high	0.00511532	0.000688937	0.00185865	-0.000400723	0.00119299	0.00320823	0.000442499
DEgfrG-low	0.00169053	0.000988645	0.00519018	-7.50108e-05	0.000438574	-0.000167091	0.000356807
DEgfrGSlope-high	0.00257491	0.00150233	0.00421855	-0.000717993	0.00145463	0.000552992	0.0001294
DEgfrGSlope-low	0.00217845	0.000469881	0.00316077	0.000106641	0.000210603	0.00179047	0.000446777
DEgmeanG-high	0.00212577	0.00159769	0.00488039	-0.000260698	0.000838679	0.0004478	0.000309533
DEgmeanG-low	0.00423478	0.000150082	0.00196927	-8.34555e-05	0.000817267	0.00219386	0.000698658
DEgmeanGSlope-high	0.00379674	0.00138787	0.0033439	-0.000391577	0.000534953	0.00176411	0.000417187
DEgmeanGSlope-low	0.00400681	-0.000201141	0.0023855	-7.62518e-05	0.00121196	0.00199039	0.00075479
DEgwidthG-high	0.00208619	0.00170477	0.00457011	-0.000294548	0.000608143	0.000109874	9.85104e-05
DEgwidthG-low	0.00189066	0.000639793	0.00393586	-0.0002402	0.00108821	0.00171589	0.000410551
DEgwidthGSlope-high	0.00431001	0.0013684	0.00356557	-0.000413727	0.00066308	0.00141532	0.000326501
DEgwidthGSlope-low	0.00215836	0.000289057	0.00330444	-0.000257492	0.00111578	0.00220194	0.000440435
DEgmeanBG-high	0.00475161	0.00368139	0.0046837	-0.000588548	4.87446e-06	0.00102541	0.000255999
DEgmeanBG-low	0.00318789	-0.00205196	0.00185804	2.90137e-05	0.00173291	0.00272808	0.000724727
DEgmeanBGSlope-high	0.00230246	0.00567254	0.00552226	-0.000521047	-0.000932403	0.000348668	0.00013486
DEgmeanBGSlope-low	0.00387576	-0.00367844	0.00190962	0.000212366	0.00258448	0.00228207	0.000851854
DEgwidthBGL-high	0.0017115	-0.00121463	0.00272622	-0.000574236	0.00223012	0.00245805	0.00025819
DEgwidthBGL-low	0.00300847	0.003073	0.00633083	-0.000596599	-0.000332007	-0.000255884	0.00036055
DEgwidthBGLSlope-high	0.00332663	-0.00301644	0.0017091	-0.00129011	0.00338014	0.00099973	0.000143594
DEgwidthBGLSlope-low	0.00222397	0.00449564	0.00491385	0.000321759	-0.00126362	0.00142633	0.000410003
DEgwidthBGR-high	0.00365829	0.00234052	0.0036382	-0.000829452	0.000837382	0.000940607	0.000244122
DEgwidthBGR-low	0.00159908	-0.000461502	0.0038024	0.000182847	0.00111884	0.00171335	0.000436692
DEgwidthBGRSlope-high	0.00418583	0.00327622	0.00399042	-0.00105627	0.000123744	0.00145078	0.000278142
DEgwidthBGRSlope-low	0.00371948	-0.00181502	0.00250487	0.000461756	0.00172006	0.0026487	0.000629807
Bmassgmean1-high	0.00222823	6.96747e-06	0.00452283	-0.00152948	-0.000404336	0.000702202	0.000301229
Bmassgmean1-low	0.00205029	0.00248901	0.004913	0.00106717	0.00228797	0.00192876	0.000185462
Bmassgwidth1-high	0.00241957	0.00104452	0.00288469	-0.000176214	0.00105605	0.00108142	0.000248164
Bmassgwidth1-low	0.00372691	0.000565971	0.00385416	-0.000477367	0.000610426	0.00193994	0.000467662
Bmassgfrac-high	0.00230715	0.0021881	0.00535036	0.000874571	0.00193362	0.0020541	0.000233074
Bmassgfrac-low	0.00220906	0.000334197	0.00459229	-0.00134944	-0.000110759	0.000763405	0.000280029
sqrt(quadratic sum high)	0.0127915	0.0178395	0.0183542	0.00296037	0.00706388	0.0150517	0.00111645
sqrt(quadratic sum low)	0.0122904	0.0171233	0.0150468	0.00206619	0.00817349	0.0152199	0.00252138

Table A.17: Systematic deviations of the CP-asymmetries in *solution-1* when each of the fixed parameters of the m'_{ES} and $\Delta E'$ signal PDFs is varied upwards to $p-hi$ (resp. downwards to $p-lo$) by its estimated error or a covering range devised to be conservative. The *total* upwards (resp. downward) deviations quoted in the last two rows are obtained by summing all upwards (resp. downwards) deviations in quadrature.

Δ parameter	$K*(892)^+$	$K*(892)^0$	$K*_0(1430)^+$	$K*_0(1430)^0$	$\rho(770)^+$	$N.R.$	$total$
ContNnOutgmeanBG1-high	-0.00086753	0.000168548	-0.00363433	-0.00123423	-0.0059016	-0.00150872	-0.000667539
ContNnOutgmeanBG1-low	-0.00184759	9.06724e-05	-0.0103094	-0.00441789	-0.0105071	-0.00977236	-0.00163095
ContNnOutgmeanBG1Slope-high	-0.00248189	-0.00332939	-0.0051929	-0.000348457	-0.00620509	0.000843479	-0.000789924
ContNnOutgmeanBG1Slope-low	-0.00176135	0.00053487	-0.00831196	-0.00597857	-0.0097222	-0.0117293	-0.00169243
ContNnOutgmeanBG1Sq-high	0.000802058	0.00646781	-0.0110301	-0.00350335	-0.0046014	0.00039555	-0.0005253
ContNnOutgmeanBG1Sq-low	-0.00148325	0.000573243	-0.00806653	-0.00626162	-0.0088827	-0.0128417	-0.00162802
ContNnOutgwidth1L-high	-0.00181218	0.000114508	-0.00715385	-0.00320596	-0.00821554	-0.00634982	-0.00122081
ContNnOutgwidth1L-low	-0.00183281	-7.93346e-05	-0.00703215	-0.00232388	-0.00787229	-0.00508836	-0.00110127
ContNnOutgwidth1LSlope-high	-0.00178171	0.000124653	-0.0072009	-0.00330773	-0.0081664	-0.0065416	-0.00121776
ContNnOutgwidth1LSlope-low	-0.00186042	-0.000104352	-0.00701577	-0.0021882	-0.00792125	-0.00485375	-0.00110191
ContNnOutgwidth1LSq-high	-0.00168695	0.000165694	-0.00758038	-0.00391952	-0.00814213	-0.00757166	-0.00124705
ContNnOutgwidth1LSq-low	-0.00197238	-0.000214182	-0.00664282	-0.00138835	-0.00791978	-0.00347911	-0.00106439
ContNnOutgwidth1R-high	-0.00180023	4.87591e-06	-0.00713976	-0.00276812	-0.00805757	-0.00572227	-0.00116413
ContNnOutgwidth1R-low	-0.000587994	0.00156399	-0.0147411	-0.00650933	-0.0141575	-0.0123963	-0.00219891
ContNnOutgwidth1RSlope-high	-0.000107948	-0.000100261	-0.00888496	-0.00114989	-0.00432598	-0.00552757	-0.000684009
ContNnOutgwidth1RSlope-low	-0.00180023	4.87591e-06	-0.00713976	-0.00276812	-0.00805757	-0.00572227	-0.00116413
ContNnOutgwidth1RSq-high	-0.00236736	-0.000851187	-0.00602354	-0.0031026	-0.00516728	-0.0119887	-0.00129481
ContNnOutgwidth1RSq-low	-0.00146741	0.00130735	-0.00733639	-0.00807891	-0.010312	-0.0193904	-0.00227342
ContNnOutgmeanBG2-high	-0.0015464	0.00120123	-0.0095154	-0.00508468	-0.0105729	-0.0103773	-0.0015524
ContNnOutgmeanBG2-low	0.00122403	0.00614255	-0.0102202	-0.012899	-0.00128474	0.000952243	-0.00132725
ContNnOutgmeanBG2Slope-high	-0.00140597	0.00109271	-0.00959829	-0.00594089	-0.0100529	-0.0132943	-0.00168152
ContNnOutgmeanBG2Slope-low	0.00172769	0.00714496	-0.00952229	-0.00829978	-0.00159835	0.00139849	-0.00109131
ContNnOutgmeanBG2Sq-high	0.00262584	0.00401959	-0.0221622	-0.0179481	-0.0139966	-0.0573769	-0.00427971
ContNnOutgmeanBG2Sq-low	-0.00464643	-0.00391508	0.00739032	0.0161908	-0.00295852	0.0354951	0.00117735
ContNnOutgwidth2L-high	-0.00192737	-8.33976e-05	-0.00730844	-0.00234028	-0.00806303	-0.00536899	-0.00111458
ContNnOutgwidth2L-low	-0.00179759	2.48884e-05	-0.00715205	-0.00285881	-0.00808662	-0.00585137	-0.00117512
ContNnOutgwidth2R-high	0.000685134	0.00335277	-0.0157912	-0.00563757	-0.0135578	-0.0120427	-0.00163153
ContNnOutgwidth2R-low	-0.00221183	-0.0014263	-0.00173073	-0.00104933	-0.00407527	0.00032493	-0.000743475
ContNnOutgwidth2RSlope-high	0.00071753	0.00267706	-0.0156553	-0.0058644	-0.0124818	-0.0162922	-0.0019177
ContNnOutgwidth2RSlope-low	-0.0021254	-0.00253353	-0.00562912	0.00140455	-0.0055277	0.00614738	-0.000398897
ContNnOutgwidth2RSq-high	0.00692831	0.0091102	-0.0338605	-0.0174346	-0.021282	-0.105716	-0.00688769
ContNnOutgwidth2RSq-low	-0.00980946	-0.0145361	0.0326588	0.042494	0.010764	0.0878252	0.00541459
ContNnOutgfrac1-high	-0.000569688	-0.000272282	-0.00997573	-0.0010923	-0.00811466	-0.00258514	-0.00100447
ContNnOutgfrac1-low	-0.00195328	0.000441849	-0.00727128	-0.00441206	-0.00865643	-0.00817404	-0.00135889
sqrt(quadratic sum high)	0.0094871	0.0131915	0.0543717	0.0287958	0.041683	0.124695	0.00943175
sqrt(quadratic sum low)	0.0128032	0.0181356	0.0464799	0.0505545	0.0340481	0.100682	0.00779034

Table A.18: Systematic deviations of the CP-asymmetries in *solution-1* when each of the fixed parameters of the continuum NN' PDF is varied upwards to $p-hi$ (resp. downwards to $p-lo$) by its estimated error or a covering range devised to be conservative. The *total* upwards (resp. downward) deviations quoted in the last two rows are obtained by summing all upwards (resp. downwards) deviations in quadrature.

Δ parameter	$K*(892)^+$	$K*(892)^0$	$K*_0(1430)^+$	$K*_0(1430)^0$	$\rho(770)^+$	$N.R.$	$total$
SigNnOutgmeanBG1-high	-0.00142514	-0.00176182	0.000393515	0.00106481	0.000198869	-0.000709471	0.00013645
SigNnOutgmeanBG1-low	-0.00197811	-0.000719299	0.00140534	0.000162671	-0.000139812	0.000285065	-0.000291503
SigNnOutgwidth1L-high	-0.00164303	-0.00125916	0.000853215	0.000718097	1.25548e-05	-0.000309822	-9.26576e-05
SigNnOutgwidth1L-low	-0.00164303	-0.00125916	0.000853215	0.000718097	1.25548e-05	-0.000309822	-9.26576e-05
SigNnOutgwidth1R-high	-0.00197222	-0.00185718	0.000201913	0.000755978	-1.07731e-05	-0.00161185	-3.34903e-05
SigNnOutgwidth1R-low	-0.00195602	-0.000844594	0.00139773	0.000156812	-8.13951e-05	0.00084385	-0.000365599
SigNnOutgmeanBG2-high	-0.00173498	-0.0015861	0.00137077	-2.04805e-05	3.7591e-05	-0.000932245	-8.36441e-05
SigNnOutgmeanBG2-low	-0.00170651	-0.000816933	0.000592319	0.00119089	-9.85522e-05	0.000419707	-7.19582e-05
SigNnOutgwidth2L-high	-0.0016698	-0.00117635	0.00089653	0.000671977	-4.26224e-05	-0.000316968	-0.000106508
SigNnOutgwidth2L-low	-0.00161685	-0.00134551	0.000807516	0.000765185	6.91315e-05	-0.000300049	-7.8889e-05
SigNnOutgwidth2R-high	-0.00218955	-0.00167806	0.000961458	-3.82581e-05	-0.00018143	-0.00127904	-0.000259673
SigNnOutgwidth2R-low	-0.00189962	-0.00108336	0.000713614	0.000955299	-6.3666e-05	0.000269831	-0.000130746
SigNnOutgmean-high	-0.0015192	-0.00215948	0.000365495	0.00083047	0.000477822	-0.000372257	8.58395e-05
SigNnOutgmean-low	-0.00188315	-0.000319364	0.0014335	0.000408421	-0.000397164	-5.0245e-05	-0.000242447
SigNnOutgwidth-high	-0.00228629	-0.00188536	0.00055699	-0.000145031	-6.37976e-05	-0.00124768	-0.000238679
SigNnOutgwidth-low	-0.00180155	-0.000905262	0.00119716	0.00106189	-0.000175723	0.000250483	-0.000154281
SigNnOutgfrac1-high	-0.00160243	7.77475e-05	0.00118891	0.000388478	-0.000797113	-0.000648167	-0.000153929
SigNnOutgfrac1-low	-0.00183486	-0.00252394	0.000712646	0.000848759	0.000658048	-1.21248e-05	-6.23528e-05
SigNnOutgfrac2-high	-0.00169021	-0.00145777	0.00084903	0.000564283	0.000177998	-0.000395778	-9.60166e-05
SigNnOutgfrac2-low	-0.00159945	-0.00107063	0.000849699	0.00087408	-0.000149476	-0.000213129	-9.03215e-05
CombNnOutgmeanBG1-high	-0.0016497	-0.00157541	-2.2258e-05	0.000760386	0.00072754	0.000155857	0.000169012
CombNnOutgmeanBG1-low	-0.0017682	-0.0008847	0.00181682	0.000462408	-0.000725512	-0.000599761	-0.000332404
CombNnOutgwidth1L-high	-0.00165968	-0.00127202	0.00086228	0.000705437	-4.12465e-05	-0.000313563	-0.000106359
CombNnOutgwidth1L-low	-0.00162513	-0.00124547	0.000843283	0.00073179	7.07175e-05	-0.000305573	-7.78841e-05
CombNnOutgwidth1R-high	-0.00193182	-0.00183602	0.000127144	0.000242842	-0.0002777	0.000179021	-7.81121e-05
CombNnOutgwidth1R-low	-0.00150406	-0.000565365	0.00180574	0.00089641	0.000113097	-0.000819117	-0.000136744
CombNnOutgmeanBG2-high	-0.00247856	-0.00366619	-0.00143033	0.000647167	-0.00139238	0.000587308	-0.000436414
CombNnOutgmeanBG2-low	-0.000935503	0.00144416	0.0030824	0.000236224	0.00147742	-0.000780183	0.000285337
CombNnOutgwidth2L-high	-0.0016709	-0.00125595	0.000901524	0.00067501	-8.2233e-05	-0.000325552	-0.00011932
CombNnOutgwidth2L-low	-0.00161362	-0.00126426	0.000799668	0.00076497	0.000115441	-0.000291123	-6.40043e-05
CombNnOutgwidth2R-high	-0.00276485	-0.00327379	-0.000923266	-8.97413e-05	-0.00111146	4.24943e-05	-0.000587619
CombNnOutgwidth2R-low	-0.00120011	0.000904377	0.00296373	0.000842866	0.00118938	-0.00110158	0.00027527
CombNnOutgfrac1-high	-0.00176851	-0.001027	0.00147116	-2.21045e-05	-0.000510237	-0.000329356	-0.000303277
CombNnOutgfrac1-low	-0.00214053	-0.00177941	0.000265815	0.00106481	0.000369844	-0.000976444	-0.000120815
sqrt(quadratic sum high)	0.00781585	0.00771135	0.00370735	0.00242328	0.00224159	0.00296493	0.00094831
sqrt(quadratic sum low)	0.0070584	0.00502268	0.00609544	0.00320936	0.00223171	0.00230728	0.000813319

Table A.19: Systematic deviations of the CP-asymmetries in *solution-1* when each of the fixed parameters of the NN' signal PDFs is varied upwards to $p-hi$ (resp. downwards to $p-lo$) by its estimated error or a covering range devised to be conservative. The *total* upwards (resp. downward) deviations quoted in the last two rows are obtained by summing all upwards (resp. downwards) deviations in quadrature.

Δ parameter	$K*(892)^+$	$K*(892)^0$	$K*_0(1430)^+$	$K*_0(1430)^0$	$\rho(770)^+$	$N.R.$	$total$
DMassgmean1-high	0.000364702	0.000572368	0.00049651	-0.00493085	7.75656e-05	0.00105946	-0.000133482
DMassgmean1-low	0.000335641	0.00045506	0.000597255	-0.00485099	-2.52324e-06	0.0010766	-0.000117183
DMassgmean2-high	0.000652626	0.000152697	0.00081718	-0.00481869	0.000278024	0.00122338	-0.000130669
DMassgmean2-low	0.000652643	0.000152683	0.000817208	-0.0048187	0.000278032	0.00122341	-0.000130673
DMassgwidth1-high	-5.77826e-05	-5.61822e-05	-0.000869118	-0.000594057	5.49217e-05	0.00189845	-8.96171e-05
DMassgwidth1-low	0.000123588	-0.000221564	0.000445657	-0.000337319	3.87683e-05	-5.08188e-05	-1.13188e-05
DMassgwidth2-high	0.000871163	-0.000354059	-0.00240919	-0.00200211	0.00105646	-0.00297957	-0.000113917
DMassgwidth2-low	0.000315631	0.000423378	0.000239508	-0.00477978	4.45713e-05	0.00146068	-9.94705e-05
DMassgfrac1-high	-8.9675e-05	7.88551e-05	-0.000747962	-0.000106411	2.91292e-06	0.000835473	-7.04859e-06
DMassgfrac1-low	0.000277608	0.000562788	0.000432083	-0.00484669	-7.00545e-06	0.00128454	-0.000116311
DMassgmean1Slope-high	0.000163451	0.000653636	0.000438022	-0.00445824	-0.000143687	0.00223638	-8.10552e-05
DMassgmean1Slope-low	0.000168688	-7.9801e-05	-0.00240733	-0.000748875	0.000403229	0.00145235	0.000141186
DMassgmean2Slope-high	0.000589899	0.000195915	0.000698362	-0.00479219	8.64187e-05	0.00147229	-0.000133671
DMassgmean2Slope-low	0.000544043	0.000257531	0.000389452	-0.00479939	0.000651712	0.00110465	-5.39961e-05
DMassgwidth1Slope-high	0.00050473	0.00064473	-0.00221485	-0.00320972	0.000371254	0.00373806	-1.89451e-06
DMassgwidth1Slope-low	0.00044573	0.000648825	-0.00222267	-0.00325978	0.000293266	0.00404114	-5.19089e-05
DMassgwidth2Slope-high	0.000554319	0.000307064	-0.00224724	-0.0016753	0.000435309	0.00455982	0.000101995
DMassgwidth2Slope-low	0.000549527	0.000400265	-0.00217149	-0.00204687	0.00039461	0.00456018	0.000115029
DMassgwidth1Sq-high	0.000384628	-6.93811e-05	-0.0022358	-0.00329243	0.00101177	0.0083471	0.000361019
DMassgwidth1Sq-low	0.000382409	-7.00296e-05	-0.00224142	-0.00329389	0.00100826	0.00823802	0.000358361
DMassgwidth2Sq-high	0.000427383	-0.00190538	-0.00123927	-0.000884953	0.000897851	0.00771063	-0.000146209
DMassgwidth2Sq-low	0.000435575	-0.00188123	-0.00128414	-0.000965233	0.000892255	0.00768809	-0.000156487
combFrac0-high	0.00312682	0.00147751	0.00283503	0.00258642	-0.00179827	0.0152352	0.00166886
combFrac0-low	0.00624679	0.000342779	0.00407925	-0.00341771	0.00410047	-0.0119717	-0.000579104
sqrt(quadratic sum high)	0.00351761	0.00269806	0.00576546	0.0112325	0.00257322	0.0204688	0.00174
sqrt(quadratic sum low)	0.00639641	0.00225627	0.00635477	0.0124529	0.00442	0.0178099	0.0007625

Table A.20: Systematic deviations of the CP-asymmetries in *solution-1* when each of the fixed parameters of the $\bar{D}^0$ mass PDFs is varied upwards to $p-hi$ (resp. downwards to $p-lo$) by its estimated error or a covering range devised to be conservative. The *total* upwards (resp. downward) deviations quoted in the last two rows are obtained by summing all upwards (resp. downwards) deviations in quadrature.

Δ parameter	$K*(892)^+$	$K*(892)^0$	$K*_0(1430)^+$	$K*_0(1430)^0$	$\rho(770)^+$	$N.R.$	$total$
Category #1-high	-0.000262104	1.86592e-05	-0.000931598	0.000132782	8.62106e-06	0.000966031	-6.76083e-05
Category #1-low	-0.00029605	-8.07466e-06	-0.000984655	0.000140082	5.70292e-05	0.00106231	-2.93559e-05
Category #3-high	-0.000278149	0.000104085	-0.000628403	0.000247832	7.95906e-05	0.000622513	0.000147469
Category #3-low	-0.000244807	-0.000165418	-0.0010449	-4.57519e-05	-1.01164e-05	0.00137866	-0.000132335
Category #6-high	-0.000288749	-1.70876e-05	-0.0012942	-0.000669947	0.000434002	0.00246854	0.00063256
Category #6-low	-0.000455546	-6.08474e-05	-0.000160127	0.000831822	-0.00028013	-0.000346143	-0.000470972
Category #7-high	-0.000356424	-6.25145e-06	-0.000120141	-0.000659866	0.000212621	0.001668	0.000737942
Category #7-low	-0.000355002	-5.23359e-05	-0.0012809	0.000895147	-4.74532e-05	0.000189946	-0.000650594
Acp0-high	-0.000332456	-7.54293e-05	-0.000733566	1.99377e-05	0.000111398	0.00100884	-1.27753e-06
Acp0-low	-0.000517074	1.58614e-05	-0.000638195	0.000112742	0.000159177	0.00105371	0.000186226
Acp1-high	-0.000467605	-6.69627e-05	-0.000824862	-0.000386773	0.000165032	0.00152243	-5.87449e-05
Acp1-low	-0.000248776	5.76386e-06	-0.000369839	0.000658366	3.15486e-05	0.000228877	0.000305941
Acp2-high	-0.000499133	-0.000248426	-0.00241604	-0.000287827	4.17384e-05	0.0034752	6.55074e-05
Acp2-low	-0.000100712	0.000157832	0.00190453	0.000482051	2.18485e-05	-0.00200958	0.000455971
Acp3-high	9.11967e-05	0.000381461	-0.00223767	-0.000681447	-0.000202861	0.000451451	-0.00219787
Acp3-low	-0.000835798	-0.000938106	-0.000240714	0.000246715	1.2288e-05	0.00407645	0.00232084
Acp4-high	-0.000455769	0.000167149	-0.000267593	0.000200531	1.34673e-05	0.00043569	9.34744e-05
Acp4-low	-0.000261623	-0.000298772	-0.00111704	-0.000246081	0.000412646	0.00151074	-1.33066e-07
Acp5-high	-0.00025769	-0.000137895	-0.00106562	-0.000171014	6.92734e-05	0.00143799	-0.000124961
Acp5-low	-0.000351186	4.94535e-05	-0.000370637	0.000552799	6.07918e-05	0.000296162	0.000237384
Acp6-high	-0.000165014	-0.00178465	-0.00886609	-6.90598e-05	-0.00121637	0.00803939	-0.00406179
Acp6-low	-0.00137482	0.00133935	0.0108848	0.00298827	-0.00118894	-0.00699115	0.00565754
Acp7-high	-0.000322199	-0.000140955	-0.0010936	-0.000314635	5.71888e-05	0.0012957	-0.000518502
Acp7-low	-0.000564788	0.00010548	3.95457e-05	0.00105444	9.20235e-05	6.85672e-05	0.000795268
sqrt(quadratic sum high)	0.00116116	0.00186567	0.00979928	0.00135415	0.00134548	0.00971501	0.00475402
sqrt(quadratic sum low)	0.0019799	0.00168399	0.0113059	0.00355838	0.00130654	0.00873239	0.0062516

Table A.21: Systematic deviations of the isobar fractions in *solution-1* when each of the fixed B-background yields and A_{CP} are varied upwards to $p-hi$ (resp. downwards to $p-lo$) by its estimated error or a covering range devised to be conservative. The *total* upwards (resp. downward) deviations quoted in the last two rows are obtained by summing all upwards (resp. downwards) deviations in quadrature.

Δ parameter	$K*(892)^+$	$K*(892)^0$	$K*_0(1430)^+$	$K*_0(1430)^0$	$\rho(770)^+$	$N.R.$	$total$
Category #1-high	0.00249326	0.000725217	0.00483313	-0.000672566	0.00106286	0.000808736	0.000323593
Category #1-low	0.00240377	0.000832262	0.0052086	-0.000811733	0.00110026	0.00104217	0.000296871
Category #3-high	0.00148544	-0.000185472	0.00433813	-0.001142	0.00119529	0.00183218	0.000377458
Category #3-low	0.00313324	0.00212929	0.00480302	0.000116885	0.000661446	0.000365875	0.000213448
Category #6-high	0.00327233	0.00298974	0.00882344	0.00317916	0.00112188	0.00163874	0.000647793
Category #6-low	0.00297897	-0.00080238	-0.000539891	-0.00382062	0.000594979	0.00142564	4.79409e-05
Category #7-high	0.00281075	0.00222369	0.00417964	0.00243542	0.00133032	0.00306368	0.000520292
Category #7-low	0.00353696	0.000191386	0.00371341	-0.00364549	0.000483896	-0.000324143	0.000214565
Acp0-high	0.00309391	0.00218912	0.0034619	0.000923216	0.00215236	0.000198328	0.000766627
Acp0-low	0.00389216	-5.3399e-05	0.00443891	-0.00158015	-0.000476615	0.00305033	-8.55551e-05
Acp1-high	0.00352562	0.00106154	0.00267878	0.002892	-0.0030386	-0.00150827	-0.000176059
Acp1-low	0.00237716	0.00085074	0.00473999	-0.004031	0.00504207	0.00548815	0.00105349
Acp2-high	0.00181686	0.000334813	0.0142666	0.000931641	-0.00348503	0.00253647	1.0068e-05
Acp2-low	0.0027451	0.00133421	-0.0091063	-0.00192004	0.00532538	0.00372641	0.00076811
Acp3-high	0.00864128	-0.00582846	-0.00147705	-0.00419706	-0.0210204	-0.00581908	-0.00487726
Acp3-low	-0.00339003	0.0118126	0.0138449	0.00618545	0.0221868	0.0110821	0.00528841
Acp4-high	0.0046657	0.00130613	0.0027527	-0.000740619	0.00538396	0.00132772	0.00145722
Acp4-low	0.00169683	0.00140781	0.00506748	0.000504404	-0.0022323	0.000623972	-0.000557791
Acp5-high	0.00217325	0.00191276	0.0042159	0.00225214	-0.000888778	-0.00125183	0.000319073
Acp5-low	0.00284145	6.30855e-05	0.00386338	-0.00388272	0.00290637	0.00524677	0.000482903
Acp6-high	-2.46942e-05	0.0167664	0.0351549	0.0328431	-0.00539338	-0.0314394	0.0119878
Acp6-low	0.00516298	-0.0247515	-0.042041	-0.0501303	0.00593351	0.0614386	-0.0122323
Acp7-high	0.00447428	0.000925487	-0.00046752	0.00835166	-0.000837616	-0.00627838	0.00114256
Acp7-low	0.00351458	0.000717179	0.00670033	-0.0118351	0.00301171	0.0130285	-9.36488e-05
sqrt(quadratic sum high)	0.0131726	0.0184873	0.0402966	0.0346343	0.0230873	0.0330133	0.0131371
sqrt(quadratic sum low)	0.0112592	0.027624	0.0472652	0.0525138	0.0246213	0.0644348	0.0134179

Table A.22: Systematic deviations of the CP-asymmetries in *solution-1* when each of the fixed B-background yields and A_{CP} are varied upwards to $p-hi$ (resp. downwards to $p-lo$) by its estimated error or a covering range devised to be conservative. The *total* upwards (resp. downward) deviations quoted in the last two rows are obtained by summing all upwards (resp. downwards) deviations in quadrature.

Bibliography

[1] G. C. Wick, A.S. Wightman, E. P. Wigner, The Intrinsic Parity of Elementary Particles, Phys. Rev. 88 Issue 1 (1952) 101-105.

[2] T. D. Lee e C. N. Yang, Question of Parity Conservation in Weak Interaction, Phys. Rev. 104 (1956).

[3] R. L. Garwin, Lederman L. M., M. Weinrich, Observation of the Failure of Conservation of Parity and Charge Conjugation in Meson Decays: The Magnetic Moment of the Free Muon, Phys. Rev. 105 (1957) 1415.

[4] C. S. Wu, E. Ambler, R. W. Hayward, D. D. Hoppes, R. P. Hudson, Experimental Test of Parity Conservation in Beta Decay, Phys. Rev. 105 (1957) 1413.

[5] M. Goldhaber, L. Grodzins, A. W. Sunyar, Helicity of Neutrinos, Phys. Rev. 109 (1958) 1015.

[6] J. H. Christenson, J.W. Cronin, V.L. Fitch, R. Turlay, Evidence for the 2π Decay of the K_L Meson, Phys. Rev. Lett. 13 (1964) 138.

[7] A. D. Sakharov, CP violation and baryonic asymmetry of the Universe, ZhETF Pis. Red. 5, 32-35 (1967), traduzione in JETP Lett. 5, 24-27 (1967).

[8] V. Weisskopf e E. Wigner, Z. Für Physik 63 (1930) 54.

[9] G. C. Branco, L. L., J. P. Silva, CP Violation, Oxford U. P., New York (1999).

[10] C. Jarlskog ed., CP Violation, World Scientific (1998).

[11] N. Cabibbo, Unitary Symmetry and Leptonic Decays, Phys. Rev. Lett. 10 (1963) 531.

[12] M. Kobayashi e T. Maskawa, CP-Violation in the Renormalizable Theory of Weak Interaction, Prog. Theor. Phys. 49 (1973) 652.

[13] P. F. Harrison, H. R. Quinn, The *BABAR* Physics Book, SLAC-R-0504 (1998).

[14] L. Wolfenstein, Pametrization of the Kobayashi-Maskawa matrix, Phys. Rev. Lett. 51 (1983) 1945.

[15] *BABAR* Collaboration, B. Aubert *et al.*, arXiv:0803.4451 (submitted to PRD).

[16] Belle Collaboration, A. Garmash *et al.*, Phys. Rev. Lett. 96, 251803 (2006).

[17] CLEO Collaboration, C. P. Jessop *et al.*, Phys. Rev. Lett. 85, 2881-2885 (2000).

[18] *BABAR* Collaboration, B. Aubert *et al.*, Phys. Rev. **D**71, 111101 (2005).

[19] Belle Collaboration, A. Garmash *et al.*, Phys. Rev. **D**71, 092003 (2005).

[20] *BABAR* Collaboration, B. Aubert *et al.*, Phys. Rev. **D**72, 072003 (2005).

[21] CLEO Collaboration, E. Eckhart *et al.* Phys. Rev. Lett. 89, 251801 (2002).

[22] *BABAR* Collaboration, B. Aubert *et al.*, Phys. Rev. **D**76,011103 (2007).

[23] CLEO Collaboration, D. M. Asner *et al.*, Phys. Rev. **D**53, 1039 (1996).

[24] Q. Changa, X.-Q. Li, Y.-D. Yanga, [arXiv:0807.4295v4].

[25] C. W. Chiang, [arXiv:0809.0841v2].

[26] H. Y. Cheng, *et al.*, Phys. Rev. **D**76, 094006 (2007).

[27] C. K. Chua, [arXiv:0712.4187v3].

[28] The Belle Collaboration, Nature **452**, 332-335 (2008).

[29] Heavy Flavor Averaging Group (HFAG), E. Barberio *et al.*, Averages of b-hadron and c-hadron Properties at the End of 2007. [arXiv:0808.1297].

[30] M. Bona *et al.*, UTfit Collaboration [arXiv:hep-ph/0606167], [http://www.utfit.org].

[31] N. G. Deshpande, N. Sinha, and R. Sinha, Weak phase γ using isospin analysis and time dependent asymmetry in $B_d \to K^0_S\pi^+\pi^-$. Phys. Rev. Lett. 90:061802, (2003).

[32] M. Gronau, D. Pirjol, A. Soni, and J. Zupan, Improved method for CKM constraints in charmless three-body B and Bs decays. Phys. Rev. **D**75:014002, (2007).

[33] M. Ciuchini, M. Pierini, and L. Silvestrini, New bounds on the CKM matrix from $B \to K\pi\pi$ Dalitz plot analyses. Phys. Rev. **D**74:051301, (2006).

[34] H. J. Lipkin, Y. Nir, H. R. Quinn, and A. Snyder, Penguin trapping with isospin analysis and CP asymmetries in B decays. Phys. Rev. **D**44:1454-1460, (1991).

[35] R. H. Dalitz, Phil. Mag. 44, 1068 (1953).

[36] E. Fabri, *Nuovo Cimento* 11, 479 (1954).

[37] G. N. Fleming, Recoupling Effects in the Isobar Model. I. General Formalism for Three-Pion Scattering. Phys. Rev., 135(2B):B551-560, (1964).

[38] D. J. Herndon, P. Söding, and R. J. Cashmore. Generalized isobar model formalism. Phys. Rev. **D**11, 11:3165-3182, (1975).

[39] D. Asner, Charm Dalitz plot analysis formalism and results (expanded RPP-2004 version). 2003. Unpublished. hep-ex/0410014.

[40] C. Amsler *et al.*, Review of Particle Physics, Physics Letters **B** 667, 1 (2008).

[41] J. D. Jackson, Remarks on the phenomenological analysis of resonances. *Nuov. Cim.*, 34:1644-1666, (1964).

[42] G.J. Gounaris and J.J. Sakurai, Phys. Rev. Lett. 21, 244 (1968).

[43] E. Ben-Haim *et al.*, Study of $B^0 \to K^0_S\pi^+\pi^-$ time dependent Dalitz plot. *BABAR* Analysis Document #1387v6. Unpublished.

[44] D. Aston *et al.*, A Study of $K^-\pi+$ Scattering in the Reaction $K^-p \to K^-\pi^+n$ at 11 *GeV/c. Nucl. Phys.*, B 296:49 (1988).

[45] J. Blatt and V. E. Weisskopf, Theoretical Nuclear Physics. J. Wiley (New York) (1952).

[46] C. Zemach, Phys. Rev, 133, B1201 (1964).

[47] *BABAR* Technical Design Report, SLAC-R-457 (1995).

[48] B. Abuert *et al.*, (*BABAR* Collaboration), *Nucl. Instrum. Meth.*, A **479**: 1-116 (2002) [arXiv:hep-ex/0105044].

[49] B. Abuert *et al.*, (*BABAR* Collaboration), *The First Year of the BABAR experiment at PEP-II*, BABAR-CONF-00/17, Contribution to XXXth International Conference on High Energy Physics, Osaka (Japan) (2000).

[50] D. J. Lange, The EvtGen particle decay simulation package. *Nucl. Instrum. Meth.*, A **462**:152-155 (2001).

[51] T. Sjöstrand, High-energy physics event generation with PYTHIA 5.7 and JET-SET 7.4. *Comput. Phys. Commun*, 82:74 (1994).

[52] S. Agostinelli *et al.*, GEANT4: A simulation toolkit. *Nucl. Instrum. Meth.*, A **506**:250-303 (2003).

[53] P. Billoir, Track Fitting with Multiple Scattering: A New Method. Nucl. Instr. Meth., A225:352, 1984.

[54] W. Ford, Choice of Kinematic Variables in B Meson Reconstruction. *BABAR* Analysis Document #53. Unpublished.

[55] D. Lange *et al.*, A B Flavour tagging algorithm for CP violation measurements with the *BABAR* experiment. *BABAR* Analysis Document #1025. Unpublished.

[56] `TMVA`, Toolkit for Multivariate Data Analysis with ROOT, [http://tmva.sourceforge.net].

[57] R. Barlow, Statistics: A Guide to the Use of Statistical Methods in the Physical Sciences. Wiley, 1989.

[58] G. Cowan, Statistical Data Analysis. Oxford University Press, 1998.

[59] R. Aleksan *et al.*, Measurement of Branching Fractions and CP-Violating Asymmetries in $B^0 \to \rho^- h^+$ *BABAR* Analysis Document #350. Unpublished

[60] F. James and M. Roos, `MINUIT`, a system for function minimization and analysis of the parameter errors and correlations. *Comput. Phys. Commun.*, 10:343-367 (1975).

[61] F. James, `MINUIT`, Function Minimization and Error Analysis, Reference Manual. Unpublished. [wwwasdoc.web.cern.ch/wwwasdoc/minuit/minmain.html].

[62] `ROOT`, An Object Oriented Data Analysis Framework. [http://root.cern.ch/].

[63] P. F. . Harrison and H. R. . Quinn [BABAR Collaboration], "The BaBar physics book: Physics at an asymmetric B factory".

[64] K. Mishra *et al.*, Measurement of the CKM angle gamma in $B^- \to D^0 K^-$ decays using a D^0 Dalitz analysis of $D^0 \to \pi^+\pi^-\pi^0$. *BABAR* Analysis Document #1174. Unpublished.

[65] E. Ben-Haim, C. Bozzi *et al.*, $B^+ \to K_S\pi^+\pi^0$ Dalitz plot analysis.*BABAR* Analysis Document #1731v5. Unpublished.

[66] J. Chauveau *et al.*, Amplitude Analysis in $B^0 \to K^+\pi^-\pi^0$. *BABAR* Analysis Document #826v7. Unpublished.

[67] E. Ben-Haim *et al.*, Study of $B^0 \to K_S\pi^+\pi^-$ time dependent Dalitz plot. *BABAR* Analysis Document #1387v6. Unpublished.

[68] The *BABAR* Tracking Efficiency Task Force, [http://www.slac.stanford.edu/BFROOT/-www/Physics/TrackEfficTaskForce/TrackingTaskForce-2007.html]

[69] A. Telnov *et al.*, $K^0_S \to \pi^+\pi^0$ Reconstruction Efficiency in *BABAR* : Release-10 Data vs. SP4 Monte Carlo. *BABAR* Analysis Document #677. Unpublished.

[70] C. Hearty, Measurement of the Number of $\Upsilon(4S)$ Mesons Produced in Run 1 (B Counting) (2001). *BABAR* Analysis Document #134. Unpublished.